



**HAL**  
open science

# Elaboration of Metal Organic Framework - polymer composites for CO<sub>2</sub> capture by Pressure Swing Adsorption in the context of bio-CH<sub>4</sub> enrichment

Muhamad Tahriri Bin Rozaini

## ► To cite this version:

Muhamad Tahriri Bin Rozaini. Elaboration of Metal Organic Framework - polymer composites for CO<sub>2</sub> capture by Pressure Swing Adsorption in the context of bio-CH<sub>4</sub> enrichment. Chemical and Process Engineering. Ecole nationale supérieure Mines-Télécom Atlantique; Université de technologie de Petronas (1997-..; Seri Iskandar, Perak, Malaisie), 2024. English. NNT : 2024IMTA0429 . tel-04918911

**HAL Id: tel-04918911**

**<https://theses.hal.science/tel-04918911v1>**

Submitted on 29 Jan 2025

**HAL** is a multi-disciplinary open access archive for the deposit and dissemination of scientific research documents, whether they are published or not. The documents may come from teaching and research institutions in France or abroad, or from public or private research centers.

L'archive ouverte pluridisciplinaire **HAL**, est destinée au dépôt et à la diffusion de documents scientifiques de niveau recherche, publiés ou non, émanant des établissements d'enseignement et de recherche français ou étrangers, des laboratoires publics ou privés.

# THESE DE DOCTORAT DE

L'ÉCOLE NATIONALE SUPERIEURE  
MINES-TELECOM ATLANTIQUE BRETAGNE PAYS DE LA LOIRE –  
IMT ATLANTIQUE

en cotutelle avec

UNIVERSITI TEKNOLOGI PETRONAS  
SERI ISKANDAR - PERAK – MALAYSIA

ECOLE DOCTORALE N° 648  
*Sciences pour l'Ingénieur et le Numérique*  
Spécialité : Génie des procédés et bioprocédés

Par

**Muhamad Tahriri BIN ROZAINI**

**Elaboration of Metal Organic Framework - polymer composites for CO<sub>2</sub> capture by Pressure Swing Adsorption in the context of bio-CH<sub>4</sub> enrichment.**

Thèse présentée et soutenue à IMT Atlantique, Nantes, le 09/10/2024  
Unité de recherche : GEPEA UMR CNRS 6144  
Thèse N° : 2024IMTA0429

## Rapporteurs avant soutenance :

Guy DE WEIRELD Professeur, Faculté Polytechnique de Mons  
Xavier PY Professeur, Polytech Nantes

## Composition du Jury :

Président :	Conchi ANIA	Directrice de Recherche, CNRS
Examineurs :	Guy DE WEIRELD	Professeur, Faculté Polytechnique de Mons
	Xavier PY	Professeur, Polytech Nantes
	Igor BEZVERKHYY	Chercheur, Université de Bourgogne
	Hashim HASLENDIA	Professeure, Universiti Teknologi Malaysia
	Yin Fong YEONG	Professeur Associé, Universiti Teknologi PETRONAS
	Nik Abdul Hadi BIN SAPIAA	Professeur Associé, Universiti Teknologi PETRONAS
Dir. de thèse :	Pascaline PRÉ	Professeure, IMT Atlantique
Co-dir. de thèse :	Mohamad Azmi BIN BUSTAM	Professeur, Universiti Teknologi PETRONAS
Co-encadrant de thèse :	Denys GREKOV	Maitre-assistant, IMT Atlantique

Invité(s)

# Acknowledgement

I would like to express my sincere gratitude to AP. Dr Mohamad Azmi Bustam and Prof. Pascaline Pré for their exceptional care, kindness, patient guidance, enthusiastic encouragement, and invaluable advice throughout this three-year research journey. Their tireless assistance in every possible way is deeply appreciated, and I am profoundly grateful to have them as my supervisor.

I also extend my heartfelt thanks to my co-supervisor, Dr. Denys Grekov, for his kindness and patience. His guidance, insightful comments, and encouragement were instrumental throughout the research and the writing of this thesis. He was an excellent teacher, and his detailed explanations were immensely helpful. I would like also to thank my other co-supervisor, Dr Nik Abdul Hadi B Sapiaa@Md Nordin, for his guidance especially during the early stage of my thesis, which has immensely help me to properly define the research direction of my thesis.

I would like to thank the other members of my thesis committee, Dr. Igor BEZVERKHYY, Dr. Conchi ANIA, AP. Dr. Bawadi Bin Abdullah, and Dr. Sow Mun Serene Lock, for their valuable suggestions and immense knowledge. The discussions with them were always meaningful and encouraging.

My gratitude also goes to the staff of IMT Atlantique and Universiti Teknologi PETRONAS, especially Mr. Eric Chevrel and Mr. Suleiman Hakimi B. Zainal Abidin, for their valuable technical support, which greatly facilitated my experimental work on this research.

I am also grateful to my office mates: Dr. Morgane, Dr. Gaëtan, Dr. Emmanuel, Marie and Maëllia, as well as my fellow PhD friends: Dr. Ali, Dr. Ridha, Dubon, Shri, Yasser, Sasi, Florent, Luis, Angela and Delphine. All of you have been a major source of support in avoiding my PhD journey from becoming full of solitary moments.

Most importantly, I wish to acknowledge the support and great love of my family. They kept me going on and this work would not have been possible without their motivational support.

# RÉSUMÉ

Le procédé d'adsorption par variation de pression est l'une des techniques utilisées dans l'industrie pour séparer le CO<sub>2</sub> du biogaz afin de produire du biométhane. Cette technique d'adsorption est connue sous le nom d'adsorption modulée en pression (PSA) ou adsorption modulée en pression sous vide (VPSA), cette dernière impliquant l'utilisation d'un vide pour la régénération de l'adsorbant. Le mécanisme de l'adsorption dépend de la sélectivité à l'équilibre ou cinétique de l'adsorbant pour séparer le CO<sub>2</sub> et le CH<sub>4</sub>. Le VPSA garantit une régénération totale de l'adsorbant, rétablissant ainsi sa capacité de travail maximale, mais au prix d'une consommation énergétique supplémentaire liée à l'utilisation du vide. Le PSA est donc plus avantageux, mais il nécessite l'utilisation d'un adsorbant approprié capable de maintenir une capacité de travail élevée même lorsque la régénération est effectuée à pression ambiante.

L'un des adsorbants potentiels pouvant être utilisé dans le processus PSA pour la séparation CO<sub>2</sub>/CH<sub>4</sub> dans le biogaz est le HKUST-1. Ce matériau est l'un des MOFs fréquemment étudiés comme adsorbant pour la séparation CO<sub>2</sub>/CH<sub>4</sub> compte tenu de sa disponibilité commerciale et de grande capacité d'adsorption vis-à-vis du CO<sub>2</sub>. Néanmoins, les voies de synthèse actuelles mises en œuvre à l'échelle industrielle conduisent à l'obtention de poudres cristallines auxquelles des post-traitements de mise en forme sont nécessaires. La mise en forme de HKUST-1 par extrusion en utilisant deux liants thermoplastiques : TPU, (thermoplastic polyurethane) et PLA (polylactic acid) au caractère hydrophobe a été vérifié, dans le but de fabriquer un adsorbant avec une bonne tenue mécanique et une stabilité à l'humidité améliorée en vue de sa mise en œuvre dans un procédé de séparation CO<sub>2</sub>/CH<sub>4</sub>.

HKUST-1 en poudre a été mélangé avec 10 % en masse de PLA ou TPU, suivi par l'extrusion du mélange pour produire des composites, désignés respectivement HKUST-1/PLA et HKUST-1/TPU. La caractérisation par diffractométrie de rayons X (DRX), microscopie électronique à balayage (MEB) et analyse thermogravimétrique (ATG) a confirmé la préservation de la structure cristalline du MOF, ainsi que l'absence de dégradation thermique des composites. Les mesures d'isothermes d'adsorption CO<sub>2</sub>/CH<sub>4</sub> jusqu'à 10 bars à 298 K mettent en évidence une augmentation des capacités d'adsorption en CO<sub>2</sub> et CH<sub>4</sub> des deux composites, de l'ordre de 16-30% par rapport au HKUST-1. La prédiction par le modèle IAST des équilibres de co-adsorption pour un mélange équimolaire CO<sub>2</sub>/CH<sub>4</sub> à 298 K a permis d'évaluer leur sélectivité dans une gamme de pression jusqu'à 10 bar. Il se trouve que la sélectivité des composites est légèrement dégradée par rapport à l'adsorbant HKUST-1 pur.

HKUST-1 est connue pour sa sensibilité à l'humidité qui diminue sa capacité d'adsorption. L'étude de la stabilité des matériaux composites en conditions humides montre que l'adjonction du TPU confère au composite un caractère hydrophobe qui améliore sa résistance à sa dégradation en présence d'eau. Après un stockage prolongé des matériaux en conditions humides, HKUST-1/TPU et HKUST-1/PLA présentent respectivement des diminutions de 10% et 25% des capacités d'adsorption de CO<sub>2</sub>, contre 54% pour le HKUST-1 pur.

Une simulation du procédé de séparation par adsorption modulée en pression (PSA) appliquée à un mélange équimolaire CO<sub>2</sub>/CH<sub>4</sub> représentatif de la composition d'un biogaz, a été réalisée à l'aide du logiciel gPROMS, en

prenant en compte les propriétés d'équilibre mesurées pour le matériau adsorbant composite. Le modèle a été développé à partir de la simulation du cycle de Skarstrom d'une unité de taille industrielle, comportant deux colonnes adiabatiques, contenant un volume d'adsorbant de 3.6 m<sup>3</sup> pour un débit d'alimentation CO<sub>2</sub>-CH<sub>4</sub> de 0.07 kg/s à 298 K. Les valeurs hautes et basses de pression appliquées ont été définies à partir de la capacité maximale de travail de l'adsorbant mesurée à l'équilibre. Celle-ci permet d'opérer la désorption à pression atmosphérique sans requérir au vide, énergétiquement coûteux.

L'optimisation des paramètres du cycle amène la production d'un raffinat enrichi en CH<sub>4</sub> avec une pureté de 99.7%, mais associé à un taux de récupération très faible en méthane, inférieur à 7%. Afin d'améliorer les performances de l'unité PSA, une étape supplémentaire d'égalisation de pression a été introduite dans le cycle et cette nouvelle simulation a été faite en utilisant 4 colonnes. Dans ces conditions, les taux de récupération en CH<sub>4</sub> peuvent alors être significativement améliorés, jusqu'à 22.6%, mais restent cependant insuffisants par rapport aux spécifications de performances attendues de l'unité. Néanmoins, comme la séparation CO<sub>2</sub>/CH<sub>4</sub> a été simulée avec succès en utilisant le procédé PSA, il est évident que la consommation énergétique spécifique calculée pour ce travail serait inférieure à celle d'autres études utilisant le procédé VPSA.

Pour conclure, cette étude montre qu'il est possible de formuler des adsorbants composites à base de MOF mis en forme de granulats grâce à l'extrusion de mélanges contenant de faible fraction en masse de polymère. Il est démontré que l'adjonction du liant polymère peut permettre de formuler des adsorbants moins dégradables en présence d'humidité. La simulation des performances du composite pour la séparation CO<sub>2</sub>/CH<sub>4</sub> dans un procédé PSA montre qu'il est possible de produire du méthane enrichi avec une pureté de 99%, mais de faibles taux de récupération en CH<sub>4</sub> sont obtenus dus à la faible sélectivité de l'adsorbant.

Plusieurs perspectives peuvent être mises en avant pour cette étude. Tout d'abord, les protocoles de mise en forme devraient être étendus à d'autres adsorbants d'intérêt, tels que d'autres MOFs commerciaux, des zéolithes synthétiques ou des argiles échangées par cations. Ensuite, des analyses expérimentales de courbe de percée devraient être menées pour établir des modèles cinétiques d'adsorption pertinents et valider les résultats de simulation PSA de ce travail. Enfin, les performances simulées de séparation PSA pourraient être considérablement améliorées en utilisant des configurations de cycles plus complexes, comme l'ajout de plusieurs étapes d'égalisation de pression ou le recyclage du gaz résiduaire dans le flux d'alimentation.

# Table of Contents

Acknowledgement.....	1
RÉSUMÉ.....	2
List of abbreviations.....	9
List of symbols.....	12
List of Figures.....	15
List of tables.....	20
1. CHAPTER 1: INTRODUCTION.....	22
1.1. General introduction.....	22
1.2. Problem statement.....	22
1.3. Objectives of the study.....	23
1.4. Scopes of the study.....	23
2. CHAPTER 2: STATE-OF-THE-ART.....	25
2.1. Context of study.....	25
2.1.1. Greenhouse gas (GHG) emission: status and trends.....	25
2.1.2. Mitigation strategies.....	26
2.1.3. Biogas as a renewable energy.....	28
a) Biogas production.....	28
b) Biogas feedstock and composition.....	29
c) The outlook for biogas and biomethane.....	30
2.2. Biogas purification to biomethane.....	32
2.2.1. Biomethane specification for injection into French gas grid system.....	32
2.2.2. Biogas upgrading technologies.....	33
a) Principle.....	33
b) Comparison of process operating conditions and performances.....	37
c) Repartition of biogas upgrading technology employed in the European market.....	39
2.2.3. Biogas cleaning technologies.....	41
a) Removal of H <sub>2</sub> O.....	41
b) Removal of H <sub>2</sub> S.....	42

2.3.	Pressure Swing Adsorption (PSA) .....	42
2.4.	Metal-organic framework (MOFs) .....	47
2.4.1.	Introduction to MOFs structure and families .....	47
2.4.2.	Potential for HKUST-1 as an adsorbent for CO <sub>2</sub> /CH <sub>4</sub> separation .....	49
2.5.	Shaping technologies .....	52
2.5.1.	Post-synthesis shaping methods .....	52
a)	Pressing/compression .....	52
b)	Wet granulation .....	53
c)	Sol-gel .....	54
d)	Extrusion .....	55
e)	Additive manufacturing (3D printing) .....	55
2.5.2.	<i>In situ</i> shaping methods .....	57
a)	Wet impregnation/coating .....	57
2.5.3.	Impact of shaping methods on MOF's textural properties and CO <sub>2</sub> adsorption capacity .....	58
2.6.	Conclusion .....	63
3.	CHAPTER 3: Elaboration and Characterization of HKUST-1 composites .....	64
3.1.	Introduction to thermoplastics .....	64
3.2.	Choice of the binder .....	67
a)	PLA .....	68
b)	TPU .....	69
3.3.	Synthesis of HKUST-1 composites .....	70
3.3.1.	Materials .....	70
3.3.2.	Shaping process of HKUST-1 by extrusion .....	71
3.3.3.	Shaping of HKUST-1 by additive manufacturing .....	72
a)	HKUST-1 shaping method by FDM .....	72
b)	HKUST-1 shaping method by Fused Granulate Fabrication (FGF) .....	73
3.4.	Characterization methods .....	75
3.4.1.	X-ray diffraction (XRD) analysis .....	75
3.4.2.	Fourier transform infrared spectroscopy (FTIR) analysis .....	75
3.4.3.	Scanning electron microscopy (SEM) analysis .....	75

3.4.4.	Thermogravimetric analysis (TGA) .....	76
3.4.5.	Attrition test analysis.....	76
3.4.6.	N <sub>2</sub> /CO <sub>2</sub> adsorption/desorption isotherm analysis .....	76
3.4.7.	Water contact angle measurement.....	77
3.4.8.	H <sub>2</sub> O adsorption isotherm and ageing under humid atmosphere analysis.....	77
3.5.	Results.....	78
3.5.1.	Materials structure verification.....	78
a)	HKSUT-1 composites synthesized from extrusion.....	78
b)	HKSUT-1 composites synthesized from additive manufacturing .....	80
a)	Extruded HKUST-1 composites.....	80
b)	HKSUT-1 composites synthesized from additive manufacturing .....	82
3.5.3.	Thermal properties of materials.....	83
a)	Extruded HKUST-1 composites.....	83
b)	HKUST-1 composite synthesized from additive manufacturing .....	85
3.5.4.	Mechanical resistance.....	85
3.5.5.	Textural properties .....	86
a)	Extruded HKUST-1 composites.....	86
b)	HKUST-1 composite synthesized from additive manufacturing .....	89
3.5.6.	Ageing analysis and hydrophilicity .....	90
a)	Ageing of materials .....	90
b)	Characterization of hydrophobicity of thermoplastics.....	93
3.6.	Conclusion .....	94
4.	CHAPTER 4: Adsorption performance of materials .....	95
4.1.	Modelling of adsorption thermodynamics .....	95
4.1.1.	Generality .....	95
4.1.2.	Adsorption models for pure gas.....	98
a)	Adsorption models based on Gibbs isotherm.....	98
b)	Multilayer adsorption model .....	100
c)	Empirical adsorption models .....	101
4.1.3.	Heat of adsorption .....	105
4.1.4.	Adsorption models for gas mixture .....	108



a)	Ideal Adsorbed Solution Theory (IAST) .....	108
4.2.	Experimental methods.....	110
4.2.1.	Manometric measurement .....	110
a)	General approach.....	110
b)	Influence of temperature on manometric measurement.....	112
c)	Influence of high pressure on manometric measurement .....	114
d)	Materials and protocol for manometric measurement .....	117
4.2.2.	Fitting of adsorption model for pure gas isotherm .....	118
4.2.3.	Computation of adsorption heat .....	121
4.2.4.	Method for predicting co-adsorption isotherm using IAST model.....	122
4.3.	Results.....	124
4.3.1.	CO <sub>2</sub> and CH <sub>4</sub> adsorption isotherms .....	124
4.3.2.	Isosteric heat of adsorption.....	128
4.3.3.	CO <sub>2</sub> /CH <sub>4</sub> adsorption selectivity .....	130
4.4.	Conclusion .....	135
5.	CHAPTER 5: Simulation and optimization of PSA process for biogas upgrading .....	136
5.1.	Different configurations of PSA/VPSA cycle for biogas upgrading .....	136
5.1.1.	Skarstrom cycle .....	137
5.1.2.	Dual-stage (V)PSA process configuration.....	138
5.1.3.	VPSA with N <sub>2</sub> purging .....	142
5.1.4.	VPSA with off gas recycling .....	144
5.2.1.	Principle of diffusion.....	145
a)	External film diffusion .....	146
b)	Mesopore and macropore diffusion .....	147
c)	Micropore diffusion.....	149
5.2.2.	Kinetics model.....	150
a)	Fick's model.....	150
b)	Gradient of chemical potential .....	151
c)	Linear Driving Force (LDF) model .....	153
d)	Biporous Linear Driving Force (bi-LDF) model .....	153
5.3.1.	Column dynamic (mass, energy and momentum balances).....	154

a)	General assumptions.....	154
b)	Mass conservation equations .....	155
c)	Energy conservation equations.....	155
d)	Momentum conservation equations .....	156
e)	Boundary conditions .....	157
5.3.2.	Single column design .....	157
a)	Case 1: Model validation.....	157
b)	Case 2: PSA cycle for CO <sub>2</sub> /CH <sub>4</sub> separation in the context of biogas upgrading .....	158
5.3.3.	Cycle configuration .....	160
a)	Case 1: Model validation.....	160
b)	Case 2: PSA cycle for CO <sub>2</sub> /CH <sub>4</sub> separation in the context of biogas upgrading .....	161
5.3.4.	Operational/Isotherms/Mass and heat transfer parameters .....	164
a)	Case 1: Model validation.....	164
b)	Case 2: PSA cycle for CO <sub>2</sub> /CH <sub>4</sub> separation in the context of biogas upgrading .....	165
5.3.5.	Simulation performance criteria .....	166
a)	Case 1: Model validation.....	166
b)	Case 2: PSA cycle for CO <sub>2</sub> /CH <sub>4</sub> separation in the context of biogas upgrading .....	167
5.4.	Simulation results.....	168
5.4.1.	Case 1: Model validation.....	168
a)	Effect of heat transfer coefficient between bulk gas and adsorbent, $h_{f-ads}$ .....	169
b)	Effect of heat transfer coefficient between bulk gas and and wall, $h_{f-w}$ .....	170
c)	Effect of heat transfer coefficient between wall and external environment, $h_{w-ext}$ .....	172
d)	New breakthrough simulation with modified heat transfer coefficient parameters for $h_{f-w}$ and $h_{w-ext}$ .....	173
5.4.2.	Case 2: PSA cycle for CO <sub>2</sub> /CH <sub>4</sub> separation in the context of biogas upgrading .....	174
a)	Skarstrom cycle configuration .....	175
b)	Skarstrom + Pressure Equalization cycle .....	178
5.5.	Conclusion .....	181
GENERAL CONCLUSION AND PERSPECTIVES .....		183
References .....		186

# List of abbreviations

AC	Activated carbon
AD	Anaerobic digestion
AMP	2-amino-2-methyl-1-propanol
BBC	3,5-tris(4'-carboxy[1,1'biphenyl]-4-yl) benzoate
bcm	billion cubic metres
BDC	1,4-benzenedicarboxylate
BET	Brunauer–Emmett–Teller
BPDC	4,4-biphenyldicarboxylate
BTB	1,3,5-benzenetriyltribenzoate
BTC	1,3,5-benzenetricarboxylate
BTE	1,3,5-triscarboxyphenylethynyl
C	Carbon
CA	Cellulose acetate
CH <sub>4</sub>	Methane
CMS	Carbon molecular sieves
CNT	Carbon nanotubes
CO	Carbon monoxide
CO <sub>2</sub>	Carbon dioxide
Cu	Copper
CVD	Chemical vapor deposition
DEA	diethanolamine
DGA	diglycolamine
DHBDC/DOBDC	2,5-dioxido-1,4-benzenedicarboxylate
DLF	Dual-site Langmuir-Freundlich
DMF	Dimethylformamide
DMSO	Dimethyl sulfoxide
DR	Dubinín-Radushkevich
EBA	European Biogas Association
EDXS/EDS	Energy dispersive X-ray spectroscopy
RSS	Sum square error
ESA	Electrical swing adsorption
EU	European Union
FDM	Fused Deposition Modelling
FFI	Fossil fuel and industry
FGF	Fused Granulate Fabrication
FTIR	Fourier transform infrared spectroscopy
GDS	Gibbs Dividing surface
GHG	Greenhouse gas
GIE	Gas Infrastructure Europe
Gt	Gigatonne
GW	GigaWatt
H	Hydrogen

H <sub>2</sub>	Dihydrogen
H <sub>2</sub> BDC	Benzene-1,4-dicarboxylic acid
H <sub>2</sub> BPDC	4,4-biphenyldicarboxylic acid
H <sub>2</sub> DHBDC/H <sub>4</sub> DOBDC	2,5-dihydroxy-1,4-benzenedicarboxylic acid
H <sub>2</sub> NDC	1,4-naphthalenedicarboxylic acid
H <sub>2</sub> O	Water or humidity
H <sub>2</sub> PDC	Pyridine-2,6-dicaboxylic acid
H <sub>2</sub> S	Hydrogen sulfide
H <sub>3</sub> BBC	1,3,5-tris (4'-carboxy [1,1'biphenyl]-4-yl) benzene
H <sub>3</sub> BTB	1,3,5-tri(4carboxyphenyl) benzene
H <sub>3</sub> BTC	Benzene-1,3,5-tricarboxylic acid
H <sub>3</sub> BTE	1,3,5-triscarboxyphenylethynyl benzene
He	Helium
HKUST-1	Hong Kong University of Science and Technology-1
HPDC	Pyridine-2,6-dicaboxylic acid
HSs	linear hard segments
IAST	Ideal adsorption solution theory
IEA	International Energy Agency
ISDC	in situ dip coating
LBL	layer by layer
LSM	Least Square Method
MDEA	methyldiethanolamine
MEA	monoethanolamine
MIL	Matériaux de l'Institut Lavoisier
MMMs	mixed matrix membranes
MOFs	Metal organic frameworks
MRA	mesoporous $\rho$ -alumina
N	Nitrogen
N <sub>2</sub>	Notrogen gas
NDC	1,4-naphthalenedicarboxylate
NH <sub>3</sub>	ammonia
NMP	N-Methyl-2-pyrrolidone
O	Oxygen
O <sub>2</sub>	Oxygen gas
OS	One shot
PC	polycarbonate
PDMS	polydimethylsiloxane
PI	polyimide
PLA	poly-lactic acid
POME	palm oil mill effluent
PSA	Pressure Swing Adsorption
PSf	polysulphone
PVA	polyvinylalcohol
PVB	polyvinylbutyral

PZ	piperazine
ROP	ring-opening polymerization
SBU	Secondary Building Unit
SEM	Scanning electron microscopy
SiO <sub>2</sub>	Silicone dioxide
SSs	linear soft segments
TEA	triethanolamine
TGA	Thermogravimetric analysis
TPU	thermoplastic polyurethane
TS	Two-shot
TSA	Temperatute Swing adsorption
TWh	Terra Watt hour
UNFCC	United Nations Framework Convention on Climate Change
VOC	volatile organic compounds
VSA/VPSA	Vacuum Pressure Swing Adsorption
XRD	X-ray diffraction
ZIF	Zeolitic imidazolate framework

# List of symbols

$A$	solid specific surface area
$A_{\text{bed}}$	bed cross-sectional area
$C_{\text{BET}}$	BET constant
$C$	gas concentration in bulk phase
$C_s$	Concentration on the surface of adsorbent pellet
$C_{\text{pore}}$	concentration of gas in the pores of adsorbent
$C_{p,p}$	heat capacity of adsorbent particle
$C_{p,w}$	specific heat capacity of the wall material
$D_m$	molecular diffusivity of constituent $i$ in bulk gas phase
$D_{i,k}$	Knudsen diffusivity
$D_L$	axial dispersion coefficient
$D_{i,v}$	Poiseuille diffusivity
$D_{i,s}$	Micropore/surface diffusivity
$D_{i,s0}$	surface diffusivity at zero adsorption coverage
$D_i$	total diffusivity for internal diffusion
$D_0$	Fickian diffusivity in adsorbed phase at nearly zero adsorption coverage
$d_{\text{bed}}$	Diameter of bed
$d_p$	diameter of adsorbent particle
$E_l$	liquefaction energy of the adsorbate
$E_0$	characteristic energy of adsorption towards a reference adsorbate
$E_{a,s}$	activation energy related to surface diffusion
$f$	molecular friction coefficient
$H_f$	bulk gas phase mass specific enthalpy
$h_{f-w}$	heat transfer coefficient between gas phase and wall
$J$	diffusive flux
$K_H$	Henry's constant
$K_L$	Langmuir coefficient
$K_F$	Freundlich coefficient
$K_S$	Sips constant
$K_T$	Toth constant
$K_{DL,1} / K_{DL,2}$	Dual-site Langmuir constant representing the theoretical affinity parameter of adsorption site 1 or site 2-adsorbate
$k_{fi}$	mass transfer coefficient
$k_b$	Boltzmann constant
$k_{i,\text{mac-mes}}$	LDF coefficient for mass transfer through macro/mesopores for component $i$
$K_{\text{LDF}}$	global LDF mass transfer coefficient
$k_{i,\text{micro}}$	LDF coefficient for mass transfer for component $i$ through micropores
$l_w$	Wall thickness
$M$	Molecular weight of gas

$\dot{n}^{\text{in}}$	molar flow rate at the entrance of bed
$n_{\text{ex}}$	surface excess amount
$n_{\text{net}}$	net adsorption capacity of an adsorbent
$n_{\text{abs}}$	absolute adsorption capacity of an adsorbent
$n_{\text{ads}}$	amount of gas adsorbed by adsorbent
$n$	total amount of gas enclosed in the system
$P_0$	saturated vapor pressure
$P$	adsorption equilibrium pressure
$P_i^0(\pi)$	Hypothetical pressure of the pure component that gives the same spreading pressure on the surface
$q_{m1,i} / q_{m2,i}$	theoretical saturation capacity of gas component i per unit mass of adsorbent of site 1 and 2
$Q_{st}$	isosteric heat of adsorption
$q$	amount of adsorbate adsorbed per unit mass of adsorbent
$q_t$	total quantity of component i adsorbed in the mixture gas system
$q_i^0$	quantity of component i adsorbed when in equilibrium with the gas phase in the pure gas system
$q_M$	Monolayer adsorption capacity
$q_m$	maximum adsorption capacity
$\bar{q}_i$	average adsorbed amount for component i.
$q_{\text{eq}} _C$	adsorbed quantity in equilibrium with bulk phase
$q_{\text{eq}} _{C_{\text{pore}}}$	adsorbed quantity in equilibrium with gas phase concentration in the pores
$R$	Molar gas constant
$Re$	Reynold numbers
$R_p$	radius of adsorbent particle
$R^2$	Coefficient of determination
$R_{\text{pore}}$	radius of the pore
$Sc$	Schmidt numbers
$T$	Temperature
$T_{\text{ref}}$	Reference temperature
$T_{\text{ext}}$	temperature of the environment
$T_w$	temperature of wall
$u$	superficial velocity of gas
$V_D / V_d^g$	dead space volume
$V^s$	Volume of solid
$V$	Volume of adsorbate in adsorption space
$V^a$	Volume of adsorbed phase
$V^g$	Volume of gas phase region
$V_{\text{pore}}$	Pore volume of adsorbent
$V_{\text{cell}}$	Volume of sample cell
$WC$	Working capacity
$y_i / x_i$	mole fractions of species i in the gas phase and adsorbed phase, respectively
$Z$	Compressibility factor
$\theta$	fractional adsorption loading
$\kappa$	empirical heterogeneity factor of an adsorption system
$\beta$	similarity constant

$\pi$	Spreading pressure
$v_g$	Molar volume of gas phase
$\alpha_{A/B}^{IAST}$	IAST selectivity between gas component A and B
$\alpha_{CO_2/CH_4}^{eq}$	CO <sub>2</sub> /CH <sub>4</sub> equilibrium selectivity
$\alpha_{CO_2/CH_4}^{kin}$	CO <sub>2</sub> /CH <sub>4</sub> kinetic selectivity
$\mu$	dynamic viscosity of gas
$\sigma_{ij}$	collision diameter between molecules i and j
$\Omega_D$	dimensionless Lennard-Jones parameter
$\epsilon_{ij}$	maximum energy of attraction between molecules i and j
$\epsilon_{ads}$	adsorption potential
$\epsilon_{bed}$	inter particle void of adsorbent bed
$\epsilon_p$	Porosity an adsorbent particle
$\tau$	tortuosity factor of an adsorbent
$\rho_{bed}$	bed bulk density
$\rho_w$	mass density of wall material
$\rho_g$	density of gas
$\lambda_{eff}$	effective thermal conductivity
$\lambda_w$	thermal conductivity of the wall material
$\lambda_g$	thermal conductivity of gas mixture
$\lambda_p$	thermal conductivity of adsorbent particle
$\Delta H_{i,ads}$	heat of adsorption for component i on the adsorbent
$\Gamma$	surface concentration of adsorbed phase
$Y$	ratio of specific heat
$\delta$	mechanical efficiency of the compressor



# List of Figures

Figure 2-1: (a) Evolution of GHG emission by gas constituent from the year 1990 until 2019. (b) Evolution of GHG emission by sector from the year 1990 until 2019. Both graphs were taken from IPCC [2].	25
Figure 2-2: (a) Evolution of the atmospheric concentration for the three major well-mixed GHGs of CO <sub>2</sub> , CH <sub>4</sub> and N <sub>2</sub> O. (b) Evolution of global surface temperature. Both graphs were taken from IPCC [1].	26
Figure 2-3: Biochemical process for the production of biogas via AD. Figure reproduced from [24, 25].	28
Figure 2-4: (a) Evolution of energy production from biogas in France. (b) Evolution of energy production from biomethane injected into the French national gas grid system. Data extracted from [30].	30
Figure 2-5: Biogas demand (direct use and purified) in Malaysia [34].	31
Figure 2-6: Simplified process flow diagram of a recirculating water scrubber. Image reproduced from [39].	34
Figure 2-7: Simplified process flow diagram of an amine scrubber. Image reproduced from [39].	35
Figure 2-8: Simplified process flow diagram of a pressure swing adsorption unit. Image reproduced from [39].	36
Figure 2-9: Simplified process flow diagram of cryogenic separation. Image reproduced from [44].	36
Figure 2-10: Simplified process flow diagram of a membrane upgrading process. Image reproduced from [39].	37
Figure 2-11: (a) Distribution of upgrading technologies applied by biomethane plants in Europe [8] in 2016. (b) Distribution of upgrading technologies applied by biomethane plants in Europe [9] in 2020.	40
Figure 2-12: (a) Pressure profile for each step in Skarstrom cycle. (b) simplified schematic configuration of PSA units in the Skarstrom cycle.	44
Figure 2-13: HKUST-1 cubic metal–organic framework structure (left), and its secondary building unit (SBU) (right). Grey—carbon; light grey—hydrogen; red—oxygen; cyan—copper. In the right-hand figure, the larger green spheres indicate the exchangeable axial positions of the SBU [125].	50
Figure 2-14: (a). Comparison of CO <sub>2</sub> and CH <sub>4</sub> adsorption capacities for different adsorbents at 298 K and 1 bar. (b) Comparison of CO <sub>2</sub> and CH <sub>4</sub> adsorption capacities for different adsorbents at 298 K and 5 bar.	50
Figure 2-15 : Adsorbent Performance Indicator (API) of different adsorbent for equimolar CO <sub>2</sub> /CH <sub>4</sub> separation at 25 °C, 5 bar adsorption pressure and 1 bar regeneration pressure. Data taken from [138].	51
Figure 2-16: Schematic representation of the preparation procedure of MOF disk tablets by compression. Image reproduced from [142].	52
Figure 2-17: (a) Schematic representation of granulation method [144]. (b) Schematic diagram of shear wet granulator [145].	54
Figure 2-18: Schematic representation of the sol-gel method.	55
Figure 2-19: Schematic representation of the sol-gel method. Image taken from [144].	55
Figure 2-20: Schematic representation of additive manufacturing method for (a) FDM, (b)DIW, (c) SLS and (d)DLP. Image taken from [150].	56
Figure 2-21: Schematic representation of the wet impregnation/coating method. Image taken from [155].	58
Figure 3-1: Schematic structure of a thermoplastic. Image reproduced from [167].	64
Figure 3-2: Periodic Table of Thermoplastics created by Tangram Technology [168].	67

Figure 3-3: General routes of PLA production .....	68
Figure 3-4: Illustration of structural morphology of TPU. Image reproduced from [176]. .....	69
Figure 3-5: General routes of TPU production .....	70
Figure 3-6: Schematic figure of the shaping process for HKUST-1/polymer composite by extrusion .....	71
Figure 3-7 : Schematic figure for the shaping process of 3D printed HKUST-1/PLA by FDM.....	73
Figure 3-8: (a) FGF 3D printer used for the fabrication of 3D printed HKUST-1/TPU. (b) Printing of HKUST-1/TPU .....	74
Figure 3-9: (a) XRD of HKUST-1, HKUST-1/PLA and PLA. (b) XRD of HKUST-, HKUST-1/TPU and TPU. ....	78
Figure 3-10: (a) FTIR of HKUST-1, neat PLA and HKUST-1/PLA extrudate. (b) FTIR of HKUST-1, neat TPU and HKUST-1/TPU extrudate .....	79
Figure 3-11: (a) XRD of PLA, HKUST-1, HKUST-1/PLA and 3D printed HKUST-1/PLA. (b) FTIR of HKUST-1, neat PLA and 3D printed HKUST-1/PLA. ....	80
Figure 3-12: SEM image of (a) HKUST-1. (b) HKUST-1/PLA. (c) HKUST-1/TPU.....	81
Figure 3-13: (a) EDS mapping for HKUST-1/PLA. (b) EDS spectra for HKUST-1/PLA. c) EDS mapping for HKUST-1/TPU. (d) EDS spectra for HKUST-1/TPU (e) EDS spectra for HKUST-1 powder from study [198]. ....	82
Figure 3-14: SEM image of 3D printed HKUST-1/PLA.....	83
Figure 3-15: TGA profile for TPU, PLA, HKUST-1 and its composites. ....	84
Figure 3-16: TGA profiles for pristine HKUST-1, PLA and 3D printed HKUST-1//PLA. ....	85
Figure 3-17: N <sub>2</sub> adsorption isotherms for TPU and PLA. Filled and unfilled symbols signify adsorption and desorption branches respectively.....	87
Figure 3-18: N <sub>2</sub> adsorption isotherm plots for HKUST-1/TPU, HKUST-1/PLA and HKUST-1 in (a) linear scale and in (b) log scale .....	87
Figure 3-19: N <sub>2</sub> adsorption isotherms of HKUST-1 and solvent-washed HKUST-1. ....	89
Figure 3-20: (a) N <sub>2</sub> adsorption isotherms of HKUST-1, PLA and 3D printed HKUST-1/PLA. (b) CO <sub>2</sub> adsorption isotherms of HKUST-1 and 3D printed HKUST-1/PLA.....	90
Figure 3-21: H <sub>2</sub> O adsorption-desorption isotherm plots for HKUST-1-TPU, HKUST-1-PLA and HKUST-1 at 298 K. ....	91
Figure 3-22: Variation of H <sub>2</sub> O adsorption capacity for HKUST-1, HKUST-1-PLA and HKUST-1-TPU after multiple cycles of adsorption equilibrium. ....	92
Figure 3-23: Variations of (a) BET surface areas and (b) CO <sub>2</sub> adsorption capacities for HKUST-1, HKUST-1-PLA and HKUST-1-TPU extrudates stored in humid condition for 3 months. ....	93
Figure 3-24: Image of water drop onto the surface of PLA (left) and TPU (right).....	93
Figure 4-1: Different type of physical adsorption isotherm.....	96
Figure 4-2: (a) CO <sub>2</sub> adsorption isotherm on 13X at 298 K, 308 K and 323 K with DLF fitting (solid line), Sips fitting (dashed line) and Freundlich fitting (dotted line). (b) Q <sub>ST</sub> values in function of CO <sub>2</sub> loading amount determined from DLF, Sips and Freundlich model.....	107

Figure 4-3: Comparison between isosteric heat of adsorption $Q_{ST}$ , and calorimetric heat heats of adsorption, $\Delta H$ , for a different quantity of $CO_2$ adsorbed. ....	107
Figure 4-4: General configuration of manometric apparatus where the sample cell temperature equals to the reservoir temperature .....	110
Figure 4-5: Configuration of the manometric system taking into consideration the gradient of temperature between the sample cell and the gas reservoir .....	113
Figure 4-6: (a) Profile of gas density at standard gas-solid interface (b) Profile of gas density with introduction of GDS. ....	115
Figure 4-7: Illustration of Gibbs hyper-surface definitions by absolute, excess, and net adsorption. Dark shaded regions are not accessible by fluid molecules [271]. ....	116
Figure 4-8 : A schematic representation of the difference between excess and absolute adsorption capacities as a function of pressure at constant temperature [272]. ....	117
Figure 4-9: (a) Micromeritic 3Flex used in this work for adsorption isotherm measurement at pressure up to 1 bar. (b) SETARAM PCT-PRO used in this work for adsorption isotherm measurement at pressure up to 10 bar. ....	118
Figure 4-10: The method of calculation of isosteric heat of adsorption using Clausius–Clapeyron approach .....	122
Figure 4-11 : Workflow of IAST calculation assuming Langmuir isotherm model was used to describe pure gas adsorption isotherm. ....	123
Figure 4-12 : $CO_2$ adsorption isotherms on HKUST-1 (green square), HKUST-1/PLA (red circle), and HKUST-1/TPU (blue triangle), up to 10 bar at 298 K. Graph in inset represent $CO_2$ adsorption/desorption isotherm up to 1 bar where solid and open symbols represent the adsorption and desorption of $CO_2$ , respectively. ....	124
Figure 4-13: $CH_4$ adsorption isotherms on HKUST-1 (green square), HKUST-1/PLA (red circle), and HKUST-1/TPU (blue triangle), up to 10 bar at 298 K. Graph in inset represent $CH_4$ adsorption/desorption isotherm up to 1 bar where solid and open symbols represent the adsorption and desorption of $CH_4$ , respectively. ....	124
Figure 4-14 : Adsorption isotherms of $CH_4$ (open symbols) and $CO_2$ (solid symbols) at different temperatures for (a) HKUST-1, (b) HKUST-1/PLA, and (c) HKUST-1/TPU. The lines represent DSL model fitting. ....	125
Figure 4-15 : Molecule structure for (a) $CO_2$ adsorption and (b) $CH_4$ adsorption on HKUST-1 at different pressure and temperature. The light blue atoms represent $CO_2$ molecules and the yellow atoms represent $CH_4$ molecules that are adsorbed onto the structure. The open metal sites are represented by gray atoms whereas the red atoms represent the ligands. The image is reproduced from [16] .....	127
Figure 4-16 : Arrhenius plot for the calculation of $CO_2$ and $CH_4$ isosteric heat of adsorption for HKUST-1 (a-i and b-ii), HKUST-1/PLA (b-i and b-ii) and HKUST-1/TPU (c-i and c-ii) with the coefficient of determination, $R^2$ , for each amount adsorbed, $q$ , in $mmol \cdot g^{-1}$ .....	129
Figure 4-17: Isosteric heat of adsorption for HKUST-1 (green square), HKUST-1/PLA (red circle) and HKUST-1/TPU (blue triangle). Solid and open symbols represent $CO_2$ and $CH_4$ respectively. ....	130
Figure 4-18 : IAST-predicted co-adsorption isotherms for equimolar $CO_2/CH_4$ mixtures on HKUST-1 powder (green square), HKUST-1/PLA (red circle), HKUST-1/TPU (blue triangle) and 13X (black diamond) at 298 K as a function of total bulk pressure. Solid and open symbols represent $CO_2$ and $CH_4$ adsorption, respectively. ....	131

Figure 4-19 : IAST-predicted selectivities toward CO <sub>2</sub> and CH <sub>4</sub> for equimolar CO <sub>2</sub> /CH <sub>4</sub> mixtures on HKUST-1 (green square), HKUST-1/PLA (red circle), HKUST-1/TPU (blue triangle) and 13X (black diamond) at 298K as a function of total bulk pressure. ....	132
Figure 4-20: IAST-predicted selectivities toward CO <sub>2</sub> and CH <sub>4</sub> for equimolar CO <sub>2</sub> /CH <sub>4</sub> mixtures on (a) HKUST-1 (b) HKUST-1/PLA and (c) HKUST-1/TPU at different temperatures.....	132
Figure 5-1: Process Flow Diagram of a Skarstrom cycle configuration [285] .....	138
Figure 5-2: Dual-stage PSA scheme used to obtain purified streams of methane and carbon dioxide [286]. ....	139
Figure 5-3: Scheme of the cycle steps employed in the rectifying section of the PSA unit by Grande and Blom [286]. .....	140
Figure 5-4: Scheme of the cycle steps employed in the stripping section of the PSA unit by Grande and Blom [286]. .....	140
Figure 5-5: Scheme of the cycle steps employed in both the rectifying and stripping section of the VPSA unit by Augletti et al. [288].....	142
Figure 5-6: A simplified diagram of the pilot-scale four-column VPSA process with N <sub>2</sub> purging [287].....	143
Figure 5-7: Scheme of the cycle steps for the VPSA process with N <sub>2</sub> purging [287].....	143
Figure 5-8: Cycle representation based on a single bed sequence of 15 steps [289]. ....	144
Figure 5-9: (a) Schema of mass transfers from bulk gas phase to the adsorbent solid surface. (b) Concentration profile of gas component in bulk phase, film layer and inside adsorbent particle at the start of adsorption. ....	146
Figure 5-10: Representation of a different mechanism for internal diffusion.....	147
Figure 5-11: Representation of the mechanism for surface diffusion.....	149
Figure 5-12: Combination of internal diffusional resistance according to a resistor network model [290].....	150
Figure 5-13: Simplified scheme of an adsorption column used for the CO <sub>2</sub> /CH <sub>4</sub> breakthrough simulation [17]. ....	158
Figure 5-14: Simplified scheme of an adsorption column used for PSA simulation .....	159
Figure 5-15: Descriptive scheme of steps applied for the simulation of CO <sub>2</sub> /CH <sub>4</sub> breakthrough conducted by Asadi et al. [17].....	161
Figure 5-16: Descriptive scheme of Skarstrom cycle applied to the simulation of CO <sub>2</sub> /CH <sub>4</sub> separation using HKUST-1/PLA as adsorbent media. The arrows signify the flow of the gas stream. ....	162
Figure 5-17: Descriptive scheme of Skarstrom + Pressure Equalization cycle applied to the simulation of CO <sub>2</sub> /CH <sub>4</sub> separation using HKUST-1/PLA as adsorbent media. The arrows signify the flow of the gas stream. ....	163
Figure 5-18: (a) CO <sub>2</sub> breakthrough profile (b) Temperature profile along adsorbent bed. (c) Simplified scheme of the column showing the position of each thermocouple. t <sub>A</sub> and t <sub>R</sub> signifies adsorption time and regeneration time.....	168
Figure 5-19: (a) Fitting of CO <sub>2</sub> breakthrough profile for different h <sub>f-ads</sub> values. (b) Fitting of temperature profile throughout adsorbent bed for different h <sub>f-ads</sub> values.....	170
Figure 5-20: (a) Fitting of CO <sub>2</sub> breakthrough profile for different h <sub>f-w</sub> values. (b) Fitting of temperature profile throughout adsorbent bed for different h <sub>f-w</sub> values. ....	171
Figure 5-21: (a) Fitting of CO <sub>2</sub> breakthrough profile for different h <sub>w-ext</sub> values. (b) Fitting of temperature profile throughout adsorbent bed for different h <sub>w-ext</sub> values. ....	172

Figure 5-22: (a) Fitting of CO<sub>2</sub> breakthrough profile for simulation with modified heat transfer parameters. (b) Fitting of temperature profile throughout adsorbent bed for simulation with modified heat transfer parameters. .... 173

Figure 5-23: CO<sub>2</sub> breakthrough profile using HKUST-1/PLA as adsorbent media..... 175

Figure 5-24: Pressure profile (straight lines) and temperature profile (dotted lines), measured in the middle of adsorption column, for simulation 2.1-S. .... 176

Figure 5-25: (a) Evolution of pressure at the middle of adsorption column 1 from initial simulation cycle (S2.1-S) until CSS. (b) Evolution of temperature at the middle of adsorption column 1 from initial simulation cycle (S2.1-S) until CSS. .... 176

Figure 5-26: (a) Evolution of pressure at the middle of adsorption column 1 from initial simulation cycle (S2.2-S) until CSS. (b) Evolution of temperature at the middle of adsorption column 1 from initial simulation cycle (S2.2-S) until CSS. .... 177

Figure 5-27: (a) Simulated pressure and temperature (in the middle of the bed) profiles for a complete PSA cycle under CSS regime. .... 179

Figure 5-28: (a) Evolution of pressure and temperature (in the middle of adsorption column) from initial simulation cycle (S2.1-PE) until CSS. (b)..... 180

# List of tables

Table 2-1: Typical compositions of biogas according to the biomass source in volume percent basis (% vol.) .....	29
Table 2-2: Technical specification for biomethane quality for injection into French gas grid system [36].....	32
Table 2-3: Comparison of different biogas upgrading technologies [8, 38]. .....	38
Table 2-4: Advantages and limitations of biogas upgrading technologies [8, 38].....	40
Table 2-5: Sequences of PSA units in Skarstrom cycle.....	44
Table 2-6: Equilibrium and kinetic selectivity of adsorbents for CO <sub>2</sub> and CH <sub>4</sub> at 100 kPa [8]. .....	47
Table 2-7: Different types of carboxylate ligands used in the synthesis of MOFs. ....	47
Table 2-8: Different MOF families produced from divers SBUs and linkers.....	48
Table 2-9: BET surface area and CO <sub>2</sub> adsorption capacities reported for shaped MOF.....	60
Table 3-1 Comparison between properties of amorphous and semi-crystalline thermoplastic materials [167]. .....	65
Table 3-2: General properties of PLA and TPU .....	67
Table 3-3: Variation of PLA loading for the synthesis of HKUST-1 extrudate .....	72
Table 3-4: Variation of PLA loading for the fabrication of the filament and 3D printed composite .....	73
Table 3-5: Summary of HKUST-1/TPU printing tests .....	75
Table 3-6: Attrition percentage of HKUST-1/TPU, HKUST-1/PLA, 3D printed HKUST-1/PLA, conventional zeolite adsorbents and MOF extrudates. ....	86
Table 3-7: BET Surface areas, pore volumes of HKUST-1, HKUST-1/TPU and HKUST-1/PLA.....	88
Table 3-8: BET Surface area, pore volume of HKUST-1 and the respective solvent-washed HKUST-1.....	89
Table 3-9: BET Surface area, pore volume of HKUST-1, PLA and 3D printed HKUST-1/PLA. ....	90
Table 3-10: Average value of water contact angle on the surface of TPU and PLA. ....	93
Table 4-1: CO <sub>2</sub> heat of adsorption of HKUST-1 determine via direct and indirect approach. ....	107
Table 4-2 : Fitted parameters of different models for CO <sub>2</sub> and CH <sub>4</sub> adsorption isotherms of HKUST-1, HKUST-1/PLA and HKUST-1/TPU up to 10 bar at 273 K, 298 K and 323 K. ....	133
Table 5-1: Comparison of the operational parameters and CO <sub>2</sub> /CH <sub>4</sub> separation performance of a different configuration of PSA/VPSA process for biogas upgrading .....	137
Table 5-2: Separation performance for single-stage and dual-stage PSA unit by Grande and Blom [285].....	141
Table 5-3: Boundary conditions for each conservation equation.....	157
Table 5-4: Column design parameters and adsorbent properties for CO <sub>2</sub> /CH <sub>4</sub> breakthrough simulation [17]. ....	158
Table 5-5: Column design parameters and adsorbent properties for PSA simulation .....	159
Table 5-6: Initial conditions of Skarstrom PSA cycle for biogas upgrading .....	162
Table 5-7: Column's initial condition parameters for Skarstrom + PE configuration .....	164
Table 5-8: Operational/Isotherms/Mass and heat transfer parameters applied for the simulation of CO <sub>2</sub> /CH <sub>4</sub> breakthrough reported by Asadi et al. [17] .....	164
Table 5-9: Operational/Isotherms/Mass and heat transfer applied for the PSA simulation of CO <sub>2</sub> /CH <sub>4</sub> separation using HKUST-1/PLA.....	165

Table 5-10: Comparison between simulation results and experimental values of CO <sub>2</sub> /CH <sub>4</sub> breakthrough analysis reported by Asadi et al. [17] .....	168
Table 5-11: Impact of h <sub>f-ads</sub> on the simulated results.....	170
Table 5-12: Impact of h <sub>f-w</sub> on the simulated results .....	171
Table 5-13: Impact of h <sub>w-ext</sub> on the simulated results.....	172
Table 5-14: Comparison between simulation with modified heat transfer parameters, and experimental values of CO <sub>2</sub> /CH <sub>4</sub> breakthrough analysis as reported by Asadi et al. [17] .....	173
Table 5-15: Process performance for PSA simulation with Skarstrom configuration .....	175
Table 5-16: Impact of t <sub>PS</sub> to the performance criteria of PSA simulation.....	177
Table 5-17: Process performance for PSA simulation with Skarstrom+PE configuration .....	178
Table 5-18: Comparison of the operational parameters and CO <sub>2</sub> /CH <sub>4</sub> separation performance of this study with different PSA/VPSA process simulation studies for biogas upgrading. ....	180

# CHAPTER 1: INTRODUCTION

## 1.1. General introduction

The increasing trend of Greenhouse Gas (GHG) emission over past decades has undoubtedly contributed to the global warming [1]. Carbon dioxide (CO<sub>2</sub>) gas made up the bulk of GHG emission, whereby the majority of CO<sub>2</sub> was generated from the fossil fuel and industry (FFI) [2]. If GHG emission is left unchecked, it would lead to irreversible impact on natural systems such as the extinction of ~50% of tropical marine species, water scarcity for 4 billion people as well as concurrent heatwaves, droughts and flooding in global scale [1]. One of the strategies to mitigate CO<sub>2</sub> emission is to transition the use of energy source from fossil fuel to renewable energies with low carbon emission [3] [4] [5]. Biogas, which is produced from anaerobic digestion of organic waste, is one of the emerging renewable energies considered for energy transition. However, CO<sub>2</sub> as the major gas contaminant in biogas stream (20-50 % vol) [6] [7], needs to be removed to obtain biogas with high purity of methane (CH<sub>4</sub>), also known as biomethane. The process of removing CO<sub>2</sub> from biogas is known as biogas upgrading, and Pressure Swing Adsorption (PSA) is one of the technologies applied in industry for this process [8] [9]. In PSA, solid-state adsorbent such as zeolite, activate carbon (AC), alumina and carbon molecular sieves (CSM) are employed for biogas upgrading [10], where these adsorbents are capable to selectively adsorbed CO<sub>2</sub> over CH<sub>4</sub> in biogas.

In the past decades, a new family of porous solid called metal-organic framework (MOF) has emerged as a potential adsorbent for gas separation, such as CO<sub>2</sub>/CH<sub>4</sub> separation [11] [12]. MOFs are two- or three-dimensional porous crystalline materials with well-defined structures and superior surface areas of 1000–10 000 m<sup>2</sup>. g<sup>-1</sup> [13]. MOF structure is made up of metal nodes such as transition metals, alkaline earth elements, p-block elements, actinides or mix metals [14], linked together with organic ligands, such as polycarboxylates, phosphonates, sulfonates, imidazolates, amines, pyridyl, phenolates [15]. In this study, HKUST-1 (Hong Kong University of Science and Technology-1) was chosen as the model MOF as this MOF has been widely studied for CO<sub>2</sub>/CH<sub>4</sub> separation application as it shows a good CO<sub>2</sub>/CH<sub>4</sub> equilibrium selectivity [16, 17]. Additionally, HKUST-1 is one of the few commercially available [18] making the procurement of this MOF for this study relatively easy. The HKUST-1 is composed of copper nodes linked with BTC as the linker and was first reported by Chui *et al.* [19] as MOF with BET surface area = 692.2 m<sup>2</sup>. g<sup>-1</sup> and accessible porosity of 40.7%. However, HKUST-1 is also known for its instability in humid condition [20], which would lead to disintegration of its structural framework thus its capacity to selectively retain gas molecules.

## 1.2. Problem statement

Today, the application of HKUST-1 or MOFs in general as an adsorbent in industry is limited as they are often synthesized under powder form, which is not an ideal form for an adsorbent to be used inside an adsorption column. The powder form can cause operational issues, such as clogging and increased pressure drop across the column. To address this challenge, MOF powders must be shaped into larger solid-state forms. Various MOF shaping techniques reported in the literature can be categorized into two main approaches: *in situ* shaping, where shaping occurs simultaneously with MOF synthesis, and post-synthesis shaping, where the powder is synthesized first and then



shaped. Some post-synthesis shaping methods incorporate binding agents, which facilitate the aggregation of MOF particles by creating bonds between them, leading to the formation of larger agglomerates [21]. However, the use of binding agents generally results in a reduction in the MOF's BET surface area and adsorption capacity, as the binder can block the MOF pores [21]. Nevertheless, literature indicates that the impact of binders on MOF properties is highly dependent on both the type and quantity of the binding agent used. Therefore, understanding the influence of binding agents on MOFs is crucial for advancing MOF shaping techniques.

The present study aims to contribute to the field of MOF shaping by synthesizing HKUST-1/thermoplastic (PLA or TPU) composites for CO<sub>2</sub>/CH<sub>4</sub> adsorption across a wide range of pressures and temperatures. Therefore, it is essential to develop the most suitable shaping protocol for HKUST-1 powder. Following that, this study needs to better understand the impact of the proposed shaping protocol on the HKUST-1 intrinsic properties. Finally, the potential of shaped HKUST-1 produced in this study for the separation of CO<sub>2</sub>/CH<sub>4</sub> in the context of biogas upgrading needs to be well understood. Addressing these gaps in understanding related to the shaped HKUST-1 will be the central focus of this study.

### 1.3. Objectives of the study

The main goal of this study is to shape MOFs powder into a compact and less degradable adsorbent in order to improve the PSA's CO<sub>2</sub>/CH<sub>4</sub> separation performances. It is therefore interesting to determine the difference or similarity of the shaped composites with pristine HKUST-1 material. Following are the objectives of this study:

1. To develop preparation protocols for the production of HKUST-1/ thermoplastic composites.
2. To investigate HKUST-1/thermoplastic composites properties by relevant analysis methods.
3. To simulate the CO<sub>2</sub>/CH<sub>4</sub> separation performance of these composites in the context of biogas upgrading using the PSA process.

### 1.4. Scopes of the study

**Synthesis and characterization:** The pristine HKUST-1 powder used in this study was procured commercially and used as it is for its characterization and subsequent shaping. The shaping of HKUST-1/thermoplastic composites was done using post-synthesis shaping method (extrusion and additive manufacturing), with PLA and TPU as the binder. The synthesized materials were characterized for the studies of crystal structure (PXRD analysis), chemical functionalities (FTIR analysis), morphology (FESEM analysis), thermal stability (TG analysis) and pore textural properties (nitrogen physisorption analysis).

**Adsorption equilibria:** The synthesized materials in this study were tested for the equilibrium measurement of pure CO<sub>2</sub> and CH<sub>4</sub> at both low pressure (up to 1 bar) and medium pressure (up to 10 bar). The adsorption isotherms were also conducted at three different temperature of 273 K, 298 K and 323 K. For high-temperature adsorption conditions, the effect of temperature gradient of the instrument was taken into consideration.

**PSA simulation for CO<sub>2</sub>/CH<sub>4</sub> separation:** Simulation of CO<sub>2</sub>/CH<sub>4</sub> separation using HKUST-1/PLA composite as adsorbent. The simulation was conducted using equimolar mixture of CO<sub>2</sub>/CH<sub>4</sub>, which represent the composition of

cleaned biogas prior to biogas upgrading process, with adsorption pressure of 4 bar and temperature of 298 K. Additionally, the regeneration of adsorbent bed was simulated at atmospheric pressure without the use of vacuum. Lastly, the physical and thermodynamic properties of HKUST-1 composites obtained from this study were used to develop the simulation models, whereas kinetics parameters were taken from literature studies.

# CHAPTER 2: STATE-OF-THE-ART

## 2.1. Context of study

### 2.1.1. Greenhouse gas (GHG) emission: status and trends

According to the intergovernmental panel on climate change (IPCC), global GHG emissions, which originate from human activities, have been steadily increasing since the industrial revolution in the 19<sup>th</sup> century, reaching an all-time high of 59 GtCO<sub>2</sub>-eq in 2019 [1]. Figure 2-1-a breaks down the percentage of emission for different GHG constituents whereas Figure 2-1-b categorize the contribution of different sectors in terms of GHG emission. Carbon dioxide (CO<sub>2</sub>) gas made up the bulk of GHG emission in 2019, which was generated from the fossil fuel and industry (FFI) as well as from land use, land-use change and forestry (LULUCF), followed by methane (CH<sub>4</sub>) gas, nitrous oxide (N<sub>2</sub>O) and fluorinated gases (F-gases). Additionally, since 1990 until 2019, the energy and industry sectors accounts for more than half of the global GHG emission, followed by agriculture, forestry and other land use (AFOLU) sector, transport and building [2].

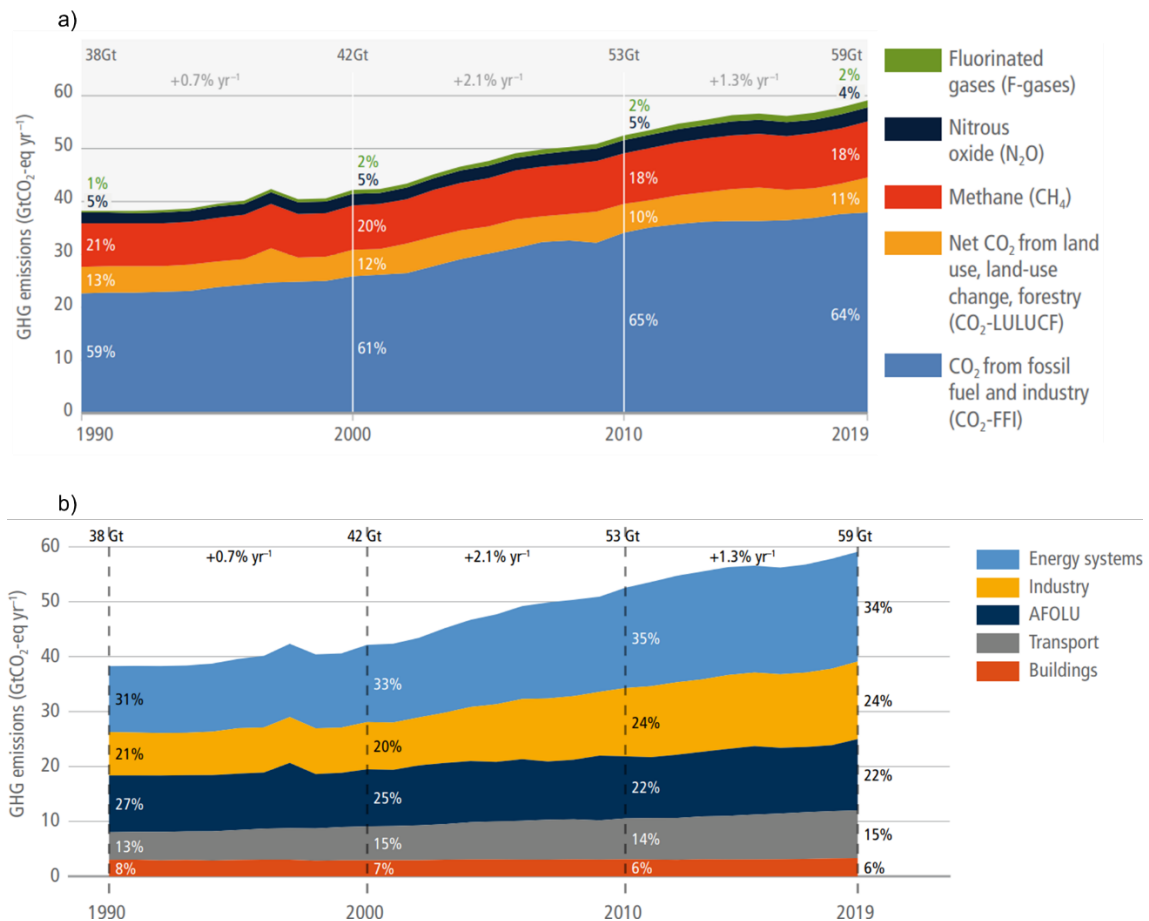


Figure 2-1: (a) Evolution of GHG emission by gas constituent from the year 1990 until 2019. (b) Evolution of GHG emission by sector from the year 1990 until 2019. Both graphs were taken from IPCC [2].

On one hand, this increase in GHG emission results in an increase in carbon dioxide (CO<sub>2</sub>), methane (CH<sub>4</sub>) as well as nitrous oxide (N<sub>2</sub>O) concentrations in atmosphere where in 2019, their concentrations are 410 parts per million, 1866 parts per billion and 332 parts per billion, respectively (Figure 2-2-a). On the other hand, the global surface temperature has been steadily increasing, where in 2020, it records an increase up to 1.1°C relative to the year of 1900 (Figure 2-2-b). This trend of increasing global temperature corroborates with the findings of increasing GHG concentration in atmosphere (e.g. CO<sub>2</sub>, CH<sub>4</sub> and N<sub>2</sub>O) for same the period. Thus, the IPCC has concluded in its 6<sup>th</sup> assessment report [1] that emission of GHG has unequivocally contributes to the global warming.

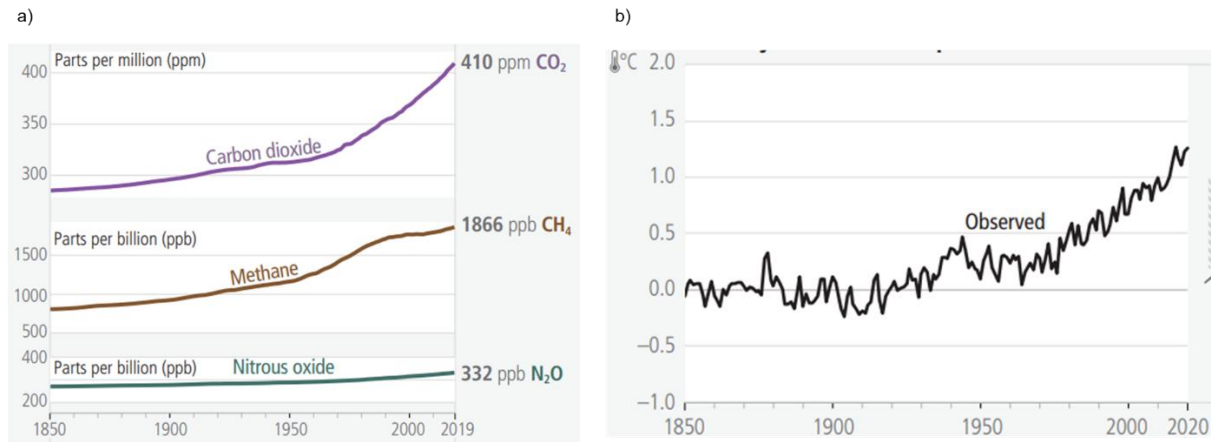


Figure 2-2: (a) Evolution of the atmospheric concentration for the three major well-mixed GHGs of CO<sub>2</sub>, CH<sub>4</sub> and N<sub>2</sub>O. (b) Evolution of global surface temperature. Both graphs were taken from IPCC [1].

Furthermore, IPCC has stated that the rise in global temperature leads to adverse impacts on human life ranging from heat-related mortality to mental health, biodiversity loss in ecosystems (forests, coral reefs, arctic regions), decrease in food and water security as well as mass waves of immigration from coastal cities due to sea level rise [1]. In the event of unabated GHG emissions leading to the increase in global temperature by 4°C relative to the year of 1900, IPCC has projected irreversible impacts on natural systems such as the extinction of ~50% of tropical marine species, water scarcity for 4 billion people as well as concurrent heatwaves, droughts and flooding in global scale [1].

### 2.1.2. Mitigation strategies

Aware of the potential harm brought by the increase in GHG emission, the United Nations Framework Convention on Climate Change (UNFCCC) was created in 1992 [3] by the United Nations (UN) to organize global efforts in stabilizing GHG concentrations at a level that would prevent dangerous anthropogenic (human induced) interference with the climate system. The convention outlined the commitments for all parties involved, placing major responsibilities on developed countries to implement national policies to limit anthropogenic emissions. Additionally, it established the structure, reporting requirements, and mechanisms for financial resources, fundamentally setting the scene for global climate policy.

During the 21<sup>st</sup> UNFCCC conference of the parties (COP-21) held in Paris in 2015, the Paris agreement [4] was adopted and entered into force in 2016. The main objective of the agreement is to limit the global temperature increase to 2 °C by 2100 and pursue efforts to limit the increase to 1.5 °C. The agreement introduced new binding

commitments, asking all parties to deliver nationally determined contributions (NDC) and to enforce national measures to achieve, and attempt to exceed such commitments. NDCs are milestones in GHG emission cuts that it strives to achieve and can be conditional, where international assistance is needed (technical or financial) or non-conditional, i.e. each country is capable of achieving with its current available means.

Strategies to mitigate GHG emission and limit the rise in global temperature to 2 °C revolves around the idea of limiting CO<sub>2</sub> emission and concentration in the atmosphere, which consist of three main climate mitigation approaches [5]: (1) conventional mitigation efforts, which employ decarbonization technologies and techniques that reduce CO<sub>2</sub> emission. (2) negative emissions technologies, which revolves around the technologies of carbon dioxide removal directly from the atmosphere. (3) radiative forcing geoengineering technologies, which revolves around the principle of altering the earth's radiation balance through the management of solar and terrestrial radiation. In this section, we will only focus on the explanation of the first approach.

As previously mentioned, CO<sub>2</sub> from fossil fuel and industry made up the bulk of GHG emission; hence, conventional mitigation technologies and efforts should be focused on both the supply and demand sides of energy. Within the power/energy sector, decarbonization can be achieved through the introduction of renewable energy, nuclear power as well as carbon capture, storage and utilization (CCUS) technologies [5].

According to the latest report prepared by the international energy agency (IEA), as of 2022, the total installed capacity of nuclear power in energy sector reaches up to 417 GW in 2022 and IEA projected for it to reach 482 GW, 557 GW and 622 GW by 2030, 2040 and 2050 respectively [22]. Nuclear energy is considered as a low-carbon solution for climate change mitigation, with lifecycle GHG emission from electricity supplied from nuclear energy estimated to be in the range of 1-220 gCO<sub>2</sub>eq/kWh, which is lower than that of coal source (675-1689 gCO<sub>2</sub>eq/kWh) and oil & gas (290-1689 gCO<sub>2</sub>eq/kWh) [23]. However, nuclear energy comes with a number of major disadvantages. First, the capital and operating costs associated with nuclear power development are quite significant. Moreover, risk of environmental radioactive pollution is a major problem related to nuclear power, which is mainly caused by the threat of reactor accidents as well as nuclear waste disposal [5].

Next, CCUS technologies involve separating and capturing CO<sub>2</sub> gases from processes that rely on fossil fuels such as coal, oil, or gas. The captured CO<sub>2</sub> is then transported and stored in geological reservoirs for extended periods. The primary objective is to reduce emission levels while continuing to utilize fossil fuel sources. There exist three CO<sub>2</sub> capturing technologies [5]: pre-combustion, post-combustion, and oxyfuel combustion, each with a specific process for extracting and capturing CO<sub>2</sub>. Once CO<sub>2</sub> is successfully captured, it is liquefied and transported via pipelines or ships to suitable storage sites. The use of CCUS is expected to reduce GHG emissions to 70–290 gCO<sub>2</sub>eq/kWh for coal source and 120–170 gCO<sub>2</sub>eq/kWh for gas source [23].

Lastly, IEA has reported that renewable energy installed capacity in the energy sector reaches 3629 GW in 2022 and it was projected to reach 8611 GW, 14965 GW and 19120 GW by 2030, 2040 and 2050 respectively [22]. Example of renewable energies are solar photovoltaic, wind power, hydropower, geothermal and bioenergy. The utilization of renewable energy is not only limited to the energy sector, as it can also be employed within the industry, transportation

and building sector [5]. Renewable energy sources are also considered as low carbon solution for climate change mitigation, with the following estimated lifecycle GHG emission for electricity [23]: solar photovoltaic (5–217 gCO<sub>2</sub>eq/kWh), wind power (7–56 gCO<sub>2</sub>eq/kWh), hydropower (2–70 gCO<sub>2</sub>eq/kWh), geothermal (6–79 gCO<sub>2</sub>eq/kWh), and bioenergy (90–480 gCO<sub>2</sub>eq/kWh).

In the context of this work, we are going to be focusing on one of the mitigation strategies to reduce CO<sub>2</sub> emissions, which is the scaling up of renewable energy, or more precisely, biogas.

### 2.1.3. Biogas as a renewable energy

Bioenergy from biogas has the potential to become a significant global renewable energy source as an attractive alternative to fossil fuels. In this subsection, the production of biogas, its feedstock and composition as well as its potential capacities will be briefly explained.

#### a) Biogas production

Biogas is an output of anaerobic digestion (AD), which involves the breakdown of organic matter through a different sequence of biochemical reactions in the absence of oxygen. Generally, four biochemical processes are involved in biogas production via AD: hydrolysis, acidogenesis, acetogenesis, and methanogenesis (Figure 2-3) [24, 25].

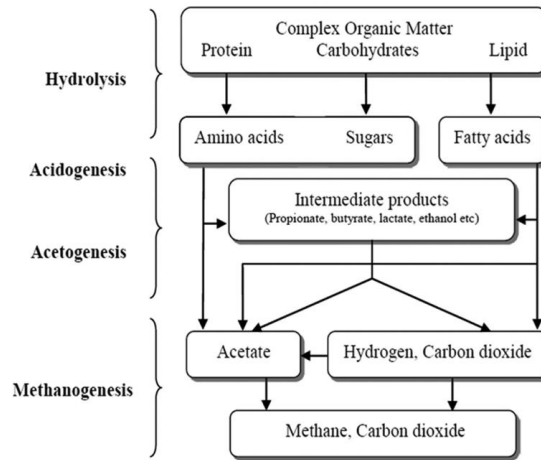


Figure 2-3: Biochemical process for the production of biogas via AD. Figure reproduced from [24, 25].

Hydrolysis in AD is the first step in the process, which involves the decomposition of complex organic polymeric materials such as carbohydrates, proteins and lipids into smaller, water-soluble compounds such as sugars, amino acids, and long-chain fatty acids by enzymes produced by the microorganisms [24].

Next, in the process of acidogenesis, the products of the previous hydrolysis stage are further broken down by a variety of microorganisms to produce weak acids (mostly organic acids) such as acetic acid, propionic acid, butyric acid (VFAs), lactic acid, alcohols, hydrogen and carbon dioxide (CO<sub>2</sub>) [24].

During the acetogenesis stage, which is the third process of AD, the products of the previous acidogenesis process are converted by acetate-forming bacteria into acetate, with hydrogen and carbon dioxide being the main products [24]. This step constitutes the final phase for fermentation of organic wastes prior to methanogenesis, which is the final steps of AD.

The final stage of AD process, which is methanogenesis, is very crucial as the majority of methane in a biogas composition is generated from it. During this stage, carbon dioxide-reducing and hydrogen-oxidizing methanogens convert hydrogen and carbon dioxide to obtain methane, while acetoclastic methanogens utilize acetate to produce methane [24].

b) Biogas feedstock and composition

The feedstock for AD in biogas production could be originated from renewable materials such as (1) agricultural waste, (2) industrial waste, (3) landfills waste and (4) sludge. Agricultural waste is animal residues, which include cow manure, swine manure, chicken manure, horse manure, elephant manure, fishery residue, and slaughterhouse waste [26]. Next, industrial waste originated from the food and beverage (F&B) industries, the agro-industrials (paper and cellulose industry), distilleries waste and refineries waste [26]. Meanwhile, landfills waste is made up of urban solid waste corresponds to food waste, paper, wood, plastic, metal, and glass. Finally, sludge used for AD could be obtained from liquid wastes such as brewery wastewater, palm oil mill effluent (POME), biodiesel wastewater, and bioethanol wastewater [27].

Biogas is primarily composed of methane (CH<sub>4</sub>) and carbon dioxide (CO<sub>2</sub>), with traces of various other gases such as hydrogen sulfide (H<sub>2</sub>S), ammonia (NH<sub>3</sub>), hydrogen (H<sub>2</sub>), nitrogen (N<sub>2</sub>), oxygen (O<sub>2</sub>), and carbon monoxide (CO), as well as saturated or halogenated carbohydrates [6, 7]. Additionally, the gas mixture may contain water vapor and solid particles, along with siloxanes. The composition of biogas varies based on the type of biomass used and operating conditions of the digestion process. Table 2-1 provides typical compositions of biogases obtained from different feedstock types. It can be observed that whatever the type of feedstock used, CO<sub>2</sub> is the predominant biogas impurity, with contents averaging 30–40 vol% and peaks up to 50 vol%).

Table 2-1: Typical compositions of biogas according to the biomass source in volume percent basis (% vol.)

<b>Components</b>	<b>Agricultural waste [6]</b>	<b>Industrial waste [7]</b>	<b>Landfills [6]</b>	<b>Sludge [7]</b>
Methane, CH <sub>4</sub>	50–80	50–70	45–65	50–80
Carbon dioxide, CO <sub>2</sub>	30–50	30–50	20–50	20–50
Hydrogen sulphide, H <sub>2</sub> S	0.70	0–8	0.10	0–1
Hydrogen, H <sub>2</sub>	0–2	0–2	0–5	0–5
Nitrogen, N <sub>2</sub>	0–1	0–1	0–3	0–3
Oxygen, O <sub>2</sub>	0–1	0–1	0–1	0–1
Carbon monoxide, CO	0–1	0–1	0–1	0–1
Ammonia, NH <sub>3</sub>	Traces	Traces	Traces	Traces
Siloxanes	Traces	Traces	Traces	Traces

Biogas can be directly burnt to produce heat and energy. However, the presence of noncombustible CO<sub>2</sub> in biogas decreases its calorific value. Therefore, biogas could be purified by removing its contaminants to obtain gas rich in

CH<sub>4</sub>, known as biomethane. Post-treatments of raw biogas include removal of moisture and acid gases like CO<sub>2</sub> and H<sub>2</sub>S, as well as trace components such as nitrogen, oxygen, hydrogen, carbon monoxide, ammonia, and siloxanes. The different technologies employed for the post-treatment of raw biogas are further explained in the section 2.2, page 32, of this chapter.

c) The outlook for biogas and biomethane

From the year 2010 until 2019, it was estimated that global biogas production has increased from 65 GW to 120 GW, in which 70% originated from Europe [28]. Moreover, by taking into account the current implemented policies, IEA has projected the global biogas production to reach 12.6 mt (million tonnes) and 26.7 mt in 2030 and 2050, respectively [22]. In addition to that, IEA has also projected that the production of biomethane, which is the purified version of biogas, will reach 7.2 mt and 40.8 mt in 2030 and 2050, respectively [22]. This reveals the huge potential for the market growth of biogas as well as biomethane. The current trend and potential outlook for biogas and biomethane production in France and Malaysia will be elaborated below:

❖ Biogas and biomethane outlook in France

Biogas adoption in world regions varies due to factors such as feedstock availability and supportive policies. Its production in Europe's energy transition is pivotal. Today, Germany stands out as the primary market, hosting two-thirds of Europe's biogas capacity [29]. France has also been actively advocating for biogas production, as could be seen from the increasing amount of energy production from biogas and biomethane in France (Figure 2-4), as reported by the French's Statistical Data and Studies Department (SDES) [30]. Production of biogas in France has been gradually increasing in the past decade, with its energy production reaching 14 TWh in 2022. Moreover, the production of biomethane, which is obtained after biogas up-grading, has also the same increasing trend as biogas. In 2022, around 7 TWh or energy was produced from biomethane that was injected into the French national gas grid. This means that in 2022, half of the biogas produced in energy sector was purified into biomethane before being subsequently injected into the national gas grid system.

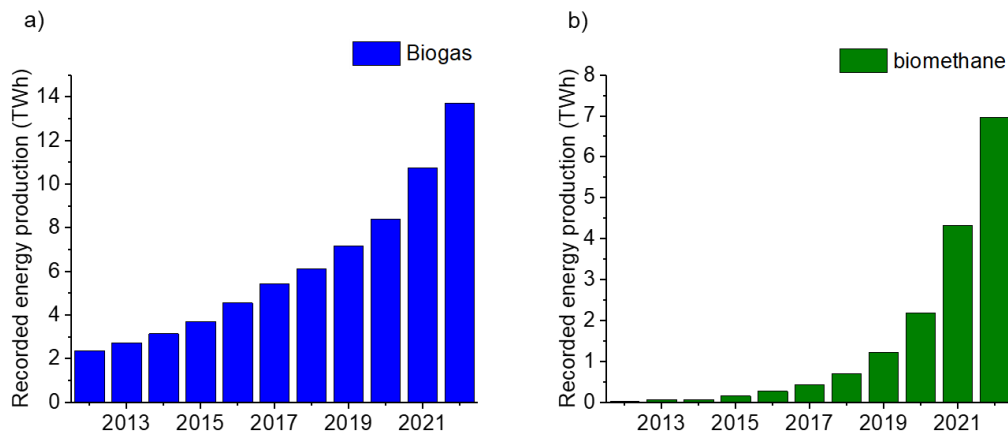


Figure 2-4: (a) Evolution of energy production from biogas in France. (b) Evolution of energy production from biomethane injected into the French national gas grid system. Data extracted from [30].



Based on the current trend for biogas and biomethane production, it could be seen that there the potential for biogas market in France is promising. In 2022, the European Union (EU) introduced the REPowerEU Plan with the aim of reducing its dependency on fossil natural gas supply from Russia due to the geopolitical crisis between Russia and Ukraine. The European Commission has set a target to produce 38 billion cubic meters (bcm) of biomethane, which originated from biogas produced by AD, annually in the EU by 2030, representing a tenfold increase of biomethane production since 2022 [31]. Similarly, by 2050, its production is even projected to rise up to 91 bcm annually [31]. Out of this, 18% of biomethane potential in 2030 and 2050 would be produced by France [31].

❖ Biogas and biomethane outlook in Malaysia

About 90% of Malaysia's electricity is today produced from coal and fossil natural gas [32]. On another hand, Malaysia's tropical climate offers abundant biomass resources that can be harnessed for biogas production. Potential biomass sources for biogas production include palm oil mill effluent (POME), agriculture waste, animal waste, municipal and sewage waste [33]. The growth for biogas and biomethane in Malaysia has recently shown promising development, though still in a very early stage, as illustrated in Figure 2-5 [34].

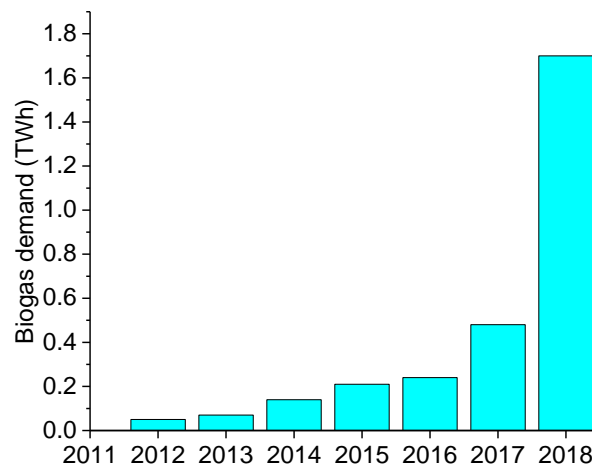


Figure 2-5: Biogas demand (direct use and purified) in Malaysia [34].

The growth of biogas market in Malaysia could support the enactment by the Malaysian parliament of the Renewable Energy Act 2011 [35], which allows the implementation of a special tariff system to catalyze the production of renewable energies. The rising demand for biomethane has so resulted in the operation of 125 fully functional biogas plants in 2020 [33], with the majority of these plants feeding the national gas grid. As the market for biogas is still in its infancy stage, an accurate prediction of its outlook is difficult. Nevertheless, Malaysian government needs to play a more active role in introducing incentives to promote the usage of its biomass sources, especially POME, for the production of biogas.

## 2.2. Biogas purification to biomethane

As previously mentioned, raw biogas could be further purified to eliminate its impurity, thus increasing its calorific value. The purified biogas is referred as biomethane and could be injected into a natural gas grid system, whereas the process of purifying biogas into methane by removing impurities is referred as biogas upgrading. In this section, the French's specification for the quality of biomethane injection into its national gas grid system will be presented followed by a brief explication of different biogas purification techniques for the removal of impurities in biogas.

### 2.2.1. Biomethane specification for injection into French gas grid system

Table 2-2 lists the technical specification of biomethane, which is based on the French standard NF EN 16723-1, for its integration into different type of French's gas grid system [36]: (1) Gaz Réseau Distribution France (GRDF), (2) TEREKA, (3) Storengy, (4) Réseau GDS (RGDS), (5) GRTgaz.

Table 2-2: Technical specification for biomethane quality for injection into French gas grid system [36]

Criteria	Unit	Type H <sup>1</sup> gas GRDF/RGDS	Type H <sup>1</sup> gas TEREKA/Storengy	Type H <sup>1</sup> gas GRTgaz	Type B <sup>2</sup> gas GRDF
<b>Higher calorific value (HCV)</b>	kWh. m <sup>-3</sup>		10.7 – 12.8		9.5 – 10.5
CH <sub>4</sub> composition	% vol	> 96.5	> 96	97.5	> 88.3
CO <sub>2</sub> composition	% vol	< 3.5	< 4	< 2.5	< 11.7
H <sub>2</sub> S composition	mg. m <sup>-3</sup>		< 5		
Total sulfur	mg. m <sup>-3</sup>		< 30		
H <sub>2</sub> composition	mg. m <sup>-3</sup>		< 6		
O <sub>2</sub> composition	% vol	< 0.75	< 0.7		< 3
NH <sub>3</sub> composition	mg. m <sup>-3</sup>		< 3		
Hg composition	µg. m <sup>-3</sup>	-	< 5		-
CO composition	% vol		< 2		
Siloxane composition	mg. m <sup>-3</sup>	-	< 5		
Cl composition	mg. m <sup>-3</sup>		< 1		
Dust	mg. m <sup>-3</sup>	-	< 5		-
H <sub>2</sub> O dew point	°C		< 5		
Gas temperature	°C	5 – 35	0 – 50	-	5 – 35

<sup>1</sup>gas with high HCV value. <sup>2</sup>gas with low HCV value.

In order to match the specifications for injection into natural gas grid, biogas needs to be purified and undergo several treatment processes to remove the main contaminant of biogas, which is CO<sub>2</sub>, as well as other contaminants such as moisture and harmful and/or toxic compounds (such as H<sub>2</sub>S, siloxanes, volatile organic compounds VOCs and NH<sub>3</sub>) until the obtention of biomethane with CH<sub>4</sub> purity > 97 %.

### 2.2.2. Biogas upgrading technologies

All gases except CH<sub>4</sub> contained in biogas are undesirable gases and are known as contaminants. For the biogas purification process, the first step is biogas cleaning and the second step is biogas upgrading. Biogas cleaning is performed to remove harmful or toxic components such as H<sub>2</sub>S, Si, CO, siloxanes, VOCs, and NH<sub>3</sub>, whereas biogas upgrading aims to increase the calorific value of biogas by removing CO<sub>2</sub>. This section starts with the principle behind each biogas upgrading technologies used in the context of CO<sub>2</sub> removal, followed by the comparison of each technology operating parameters as well as the repartition of each technology currently employed in industrial scale in the context of European market.

#### a) Principle

The established biogas upgrading technologies are derived from the natural gas purification industry. Currently, several separation technologies for biogas upgrading exist at commercial readiness level such: absorption, adsorption, cryogenic distillation and membrane. It should be highlighted that some of these processes could eliminate CO<sub>2</sub> along together with other traces of contaminants concurrently. The principle behind each biogas upgrading technologies employed in industry is further elaborated below.

#### ❖ Absorption

Gas-liquid absorption is a treatment process widely used in air treatment. In the case of biogas, this process can be used to remedy the presence of various compounds. Absorption process for biogas upgrading can be categorized into either physical or chemical scrubbing. A physical scrubbing operation relies on a separation dictated by the solubility differences between the gas components into the solvent. For separation of CO<sub>2</sub> from CH<sub>4</sub>, either water or organic solvents are employed for physical scrubbing.

One of the first solvents studied and used by industry was water, as the water-soluble compounds present in biogas absorb better into water than hydrophobic, apolar compounds such as the main target compound, methane. The solubility of CH<sub>4</sub> is 26 times lower than CO<sub>2</sub> in water at 298 K [10]. Figure 2-6 shows a schematic of a process flow diagram of a recirculating water scrubber. This operation is carried out in a packed column where pressurized biogas flows in countercurrent to the washing solution. The higher the pressure in the column and the lower the water temperature, the better the transfer of CO<sub>2</sub> from gas to liquid phase. Next, the CO<sub>2</sub> saturated water is transferred to the flash column, where the pressure is dropped to minimize methane loss by recirculating the desorbed gas to the feed stream. The water then leaves the flash tank and goes to the desorption column, where the pressure is further decreases and air came into contact with the water in a countercurrent direction. This promotes the desorption of CO<sub>2</sub> from water to air (solvent regeneration). Physical scrubbing using water for biogas upgrading also allows the removal of H<sub>2</sub>S in concurrent with CO<sub>2</sub> [10], though acidic properties of these compounds lower the pH of the water, making it is necessary to feed the process with fresh water to rebalance the pH.

Meanwhile, water could be replaced with organic solvents, which have significantly higher solubility of CO<sub>2</sub> in comparison to water. As an example, Selexol®, which is a trade name for an organic solvent of dimethyl ethers of polyethylene glycol, has the capacity to absorb at least three times more CO<sub>2</sub> than water at 30 bar and 333 K [37].

Organic solvents commonly used in physical scrubbing are mixtures of methanol and dimethyl ethers of polyethylene glycol [8]. Similar to water, H<sub>2</sub>S also could be co-absorbed with CO<sub>2</sub> using organic solvent. However, as the solubility of CO<sub>2</sub> and H<sub>2</sub>S in organic solvent is higher than in water, the regeneration of organic solvent requires a higher temperature condition to ensure total regeneration, which contributes to a higher electrical consumption: i.e. 0.32 kWh. Nm<sup>-3</sup> biogas for organics solvent vs 0.25 kWh. Nm<sup>-3</sup> biogas for water solvent [38].

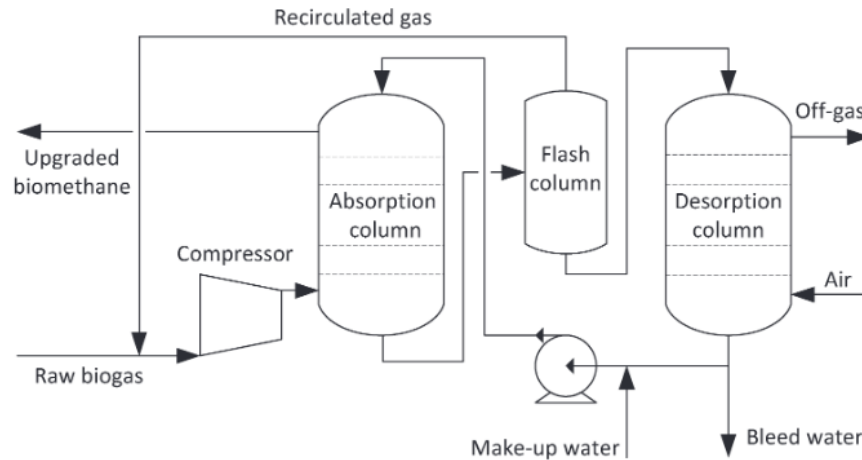


Figure 2-6: Simplified process flow diagram of a recirculating water scrubber. Image reproduced from [39].

Even higher loading and selectivity capacities are achieved when absorption is carried using a chemical solvent. Chemical scrubbing processes for biogas upgrading involve reversible chemical reactions between the absorbed gases and the solvent. Commonly used solvents for removing acid gases such as CO<sub>2</sub> and H<sub>2</sub>S are aqueous amine solutions such as mono-ethanolamine (MEA), diethanolamine (DEA) and methyldiethanolamine (MDEA) [8, 39, 40]. Figure 2-7 shows a schematic of biogas upgrading by amine scrubbing. The raw biogas at ambient pressure enters the absorption tank from the bottom, and an amine solvent enters through the top of the tank. During the counter-current flow, CO<sub>2</sub> reacts with the amine solvent, which leads to the temperature increases in the solvent as the reaction is exothermic [10]. The saturated amine solvent then goes to the heat exchanger, where it is heated until boiling point before entering the stripping column. The stripping column allows the separation of the two phases: desorbed CO<sub>2</sub> and boiling amine solvent.

Today, a common option is to use a mixture of MDEA and piperazine (PZ), which is sometimes called activated MDEA (aMDEA). It has a significantly higher absorption capacity compared to MDEA, the reason being that PZ acts as an activator in CO<sub>2</sub> capture by enhancing the CO<sub>2</sub> solubility and absorption rate of the MDEA solution of CO<sub>2</sub> as well as the absorption rate of the MDEA solution. [39, 41, 42].

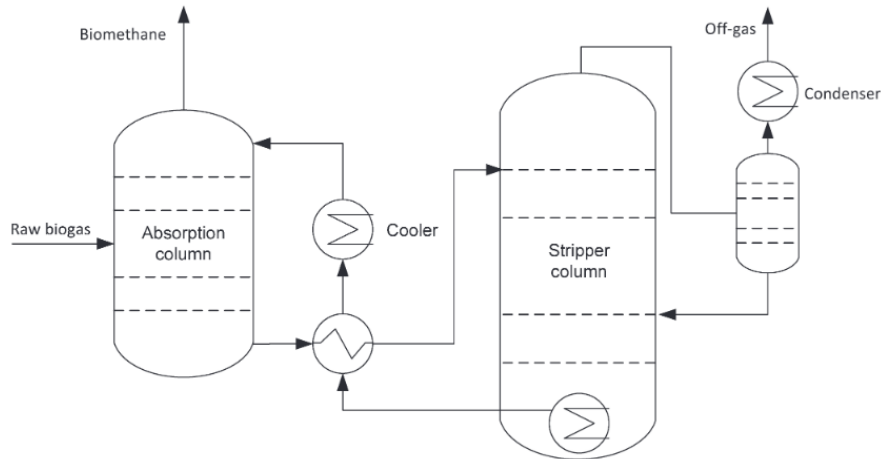


Figure 2-7: Simplified process flow diagram of an amine scrubber. Image reproduced from [39].

#### ❖ Adsorption

Gas separation via adsorption implies the selective transfer of molecules (adsorbate) on a solid surface (adsorbent), thanks to physical interactions (Van der Waal forces) [39]. In the context of biogas upgrading,  $\text{CO}_2$  in raw biogas is adsorbed by porous physical adsorbent such as activated carbons, zeolites (natural or synthetic) and silica gels [10]. This technique enables the selective adsorption of  $\text{CO}_2$  from biogas either through: (1) adsorption capacity of an adsorbent that adsorb larger amounts of  $\text{CO}_2$  than  $\text{CH}_4$  at equilibrium condition (adsorption equilibrium) or (2) adsorption kinetic of an adsorbent that adsorb  $\text{CH}_4$  molecules slower than  $\text{CO}_2$ . Further explanation regarding adsorbents used for biogas upgrading will be detailed in section 2.3, page 42.

Figure 2-8 shows the simplified process flow of the adsorption process frequently applied in the context of biogas upgrading, which is known as Pressure Swing Adsorption (PSA) [10]. In this process, there are four vertical columns that are used for adsorption, blowdown, purge, and pressurization sequences. These four columns allow the process to maintain continuous production of biomethane, as each vessel engages in different phase concurrently. First, compressed biogas enters the adsorption column and  $\text{CO}_2$  is captured by the means of adsorption on the surface of the adsorbent until saturation of the adsorbent occurs. Second, desorption of  $\text{CO}_2$  from the adsorbent occurs by stepwise depressurization of the adsorption column, which are under pressure to atmospheric pressure. Third, purge gas enters the adsorption column to push out any leftover  $\text{CO}_2$  accumulated inside the adsorption column. Finally, the adsorption column is pressurized using the feed biogas stream. The main feature of PSA is the blowdown step, where the desorption of  $\text{CO}_2$  occurs by decreasing the pressure inside the adsorption column to atmospheric pressure.

Meanwhile, another adsorption technique employed for biogas upgrading is the Vacuum Pressure Swing Adsorption (VPSA). VPSA also works on the same principle as PSA, where the only difference is that VPSA comes with a vacuum pump that makes the desorption process of  $\text{CO}_2$  under vacuum condition during blowdown sequence. It should be noted that there exist 2 more adsorption techniques for gas separation, though in the context of biogas upgrading, they are not employed in the industry and thus will not be further explained here. These techniques are called Temperature Swing Adsorption (TSA) and Electrical Swing Adsorption (ESA)

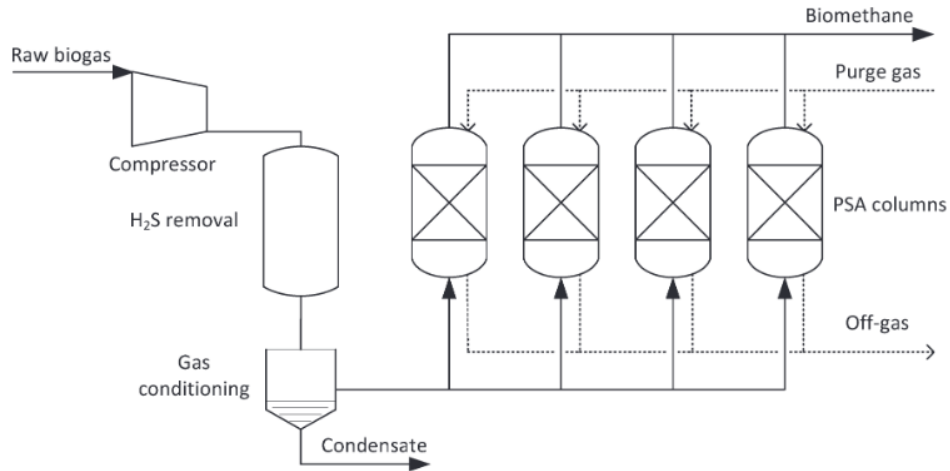


Figure 2-8: Simplified process flow diagram of a pressure swing adsorption unit. Image reproduced from [39].

❖ Cryogenic distillation

Cryogenic technology is popular for treating landfill gas, particularly for the removal of contaminants such as  $\text{CO}_2$  and  $\text{N}_2$  [8]. The process relies on the differences in the boiling points of the different gas components, which are  $-78.2^\circ\text{C}$  vs  $-161.5^\circ\text{C}$ , at 1 bar for  $\text{CO}_2$  and  $\text{CH}_4$ . It should be noted that this technique can be used to separate virtually all the constituents in biogas from methane (e.g.  $\text{CO}_2$ ,  $\text{NH}_3$ ,  $\text{H}_2\text{S}$ ,  $\text{O}_2$ ). Figure 2-9 shows the simplified diagram of such a process. Typically, the process must operate at high pressure and low temperature to effectively separate  $\text{CO}_2$  from  $\text{CH}_4$  and prevent  $\text{CO}_2$  freeze-out during the operation [43]. The cryogenic process comprises three main sections: compression, refrigeration, and distillation/separation. In the compression section, biogas is compressed in multi-stage compressors separated by water inter-coolers. The reason for this arrangement of alternate compression and cooling is to ensure the temperature of the biogas stream between compressor stages can be kept constant to maximize the compressor performance [43]. After leaving the last compressor, the high-pressure biogas is diverted into the refrigeration system to cool down the biogas close to the liquefaction temperature of  $\text{CO}_2$ . Finally, the pressurized and cooled biogas enters the distillation/separation column where biomethane is obtained as a final product and liquid  $\text{CO}_2$  is a valuable by-product.

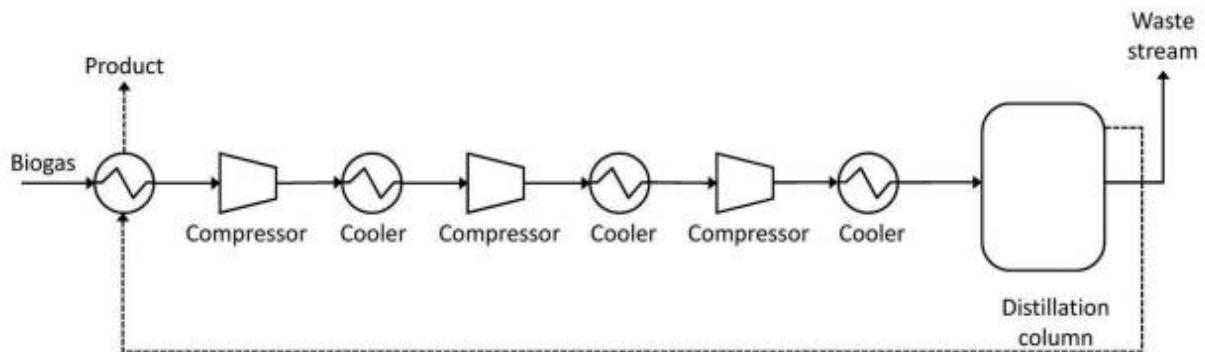


Figure 2-9: Simplified process flow diagram of cryogenic separation. Image reproduced from [44]

### ❖ Membrane separation

The principle behind membrane separation is based on the selective permeation of gas components through a semi-permeable membrane. Figure 2-10 shows the simplified process flow for membrane separation. It should be noted that for biogas application, separation of compounds is often limited to three species: methane, carbon dioxide and hydrogen sulfide [45]. However, it is recommended to clean the raw biogas by removing H<sub>2</sub>S from it, as to avoid deterioration, clogging of the membrane and to prolong the membrane life [44]. The cleaned biogas is then fed into the membrane module at high pressures, where gas types with higher permeability in biogas preferably pass the membrane to the low-pressure permeable side, while gas types with lower permeability accumulate on the high-pressure side and leave the membrane module as a retentate.

Different membrane shapes are available for this technique: flat, wound and hollow-fiber [44], The most commonly used membrane materials in this technique are polymeric membrane: polysulphone, polyimide, and cellulose acetate [8, 45], as these materials show higher selectivities between methane and carbon dioxide. Apart from that, inorganic membranes have excellent thermal stability, mechanical strength, and resistance against chemicals compared to polymeric membranes. The examples of this type of membrane are zeolite, silica, activated carbon, metal-organic framework, and carbon nanotubes [10]. Each type of membrane has their own advantages and limitations, which is not discussed in details here, though the most crucial aspect about the choice of membrane to be employed in biogas upgrading is its ability to resist harsh process conditions (e.g. high temperature and pressure) and chemically resistant to H<sub>2</sub>S present in raw biogas if it was not removed prior to the membrane separation process.

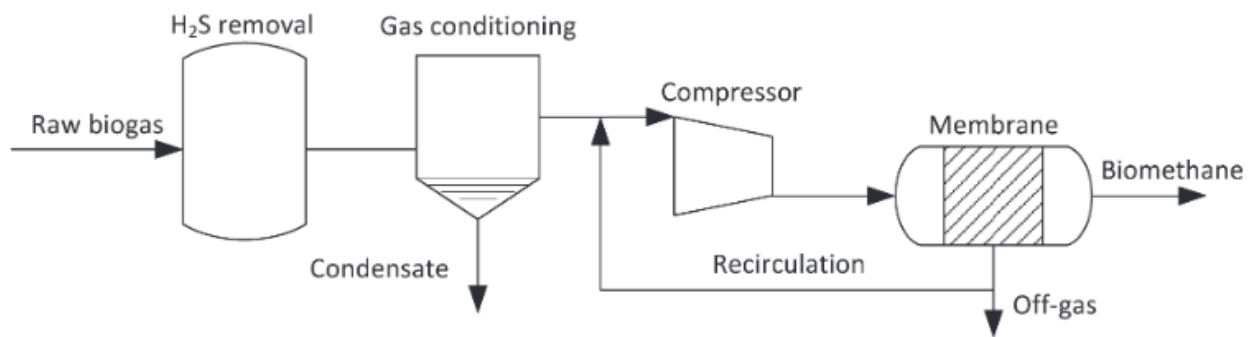


Figure 2-10: Simplified process flow diagram of a membrane upgrading process. Image reproduced from [39].

#### b) Comparison of process operating conditions and performances

Table 2-3 compares the operating conditions, CH<sub>4</sub> purity and loss as well as the energy consumption for different biogas upgrading technologies explained in Section 2.2.2-a, page 33. Each of the technique presented previously is able to produce biomethane with CH<sub>4</sub> purity > 97% vol, which is the requirement for biomethane injection into French national gas grid system. Furthermore, chemical absorption induces the lowest CH<sub>4</sub> losses thanks to the use of a chemical solvent that is very selective towards CO<sub>2</sub>. Meanwhile, physical absorption, PSA/VPSA and cryogenic distillation are characterized with comparable CH<sub>4</sub> losses, though are considered as less efficient than chemical

absorption. Lastly, membrane separation generates the largest CH<sub>4</sub> losses, as CH<sub>4</sub> is also able to permeate through the membrane together with CO<sub>2</sub> [8, 38].

Chemical absorption is the only biogas upgrading technique that is operated under ambient pressure, while the others operate under pressurized condition [8, 38]. Apart from that, chemical absorption and cryogenic distillation operates far from ambient temperature, with chemical absorption requires very high temperature (453 K) and cryogenic requires very low temperature (214-228 K) to separate CO<sub>2</sub> from biogas. Meanwhile, physical absorption, PSA/VPSA as well as membrane separation techniques operate at the temperature range closer to the ambient temperature. As a consequence, the electrical consumption of chemical absorption and cryogenic distillation both have the highest electrical consumption among other biogas upgrading technologies [8, 38]. This is followed by membrane separation technique, which consumed 0.5 kWh. Nm<sup>-3</sup> raw biogas due to its operation high pressure (20-36 bar), and chemical absorption technique, which consumed 0.42 kWh. Nm<sup>-3</sup> raw biogas due to its operation at high temperature (453 K) [8, 38], Lastly, the physical absorption and PSA/VPSA technique have comparable energy consumption as their operational pressure and temperature parameters closely resemble each other.

It should be noted here that the reported energy consumption for the PSA/VPSA separation technique in Table 2-3 has a wide range (0.16–0.43 kWh. Nm<sup>-3</sup> raw biogas) [8, 38], as in literature, there is often no distinction between both process by researchers and they are often grouped in the same category. As an example, in the study by Vilardi et al. [46], the authors simulate the biogas upgrading by “PSA” process, although the regeneration of the bed was actually operated under vacuum condition of 0.3 bar. Nevertheless, it is logical that PSA has a lower energy consumption than VPSA at the same operational temperature and adsorption pressure condition, as PSA does not require the use of a vacuum pump during regeneration of the adsorbent bed.

Table 2-3: Comparison of different biogas upgrading technologies [8, 38].

	Physical absorption	Chemical absorption	PSA/VPSA	Cryogenic	Membrane
	Water scrubber:				
Operational pressure (bar)	6-10	1	4-8	40	20-36
	Organic scrubber:				
	4-7				
	Water scrubber:				
Temperature (K)	293-313	453	278-303	214-228	298-333
	Organic				



	scrubber:				
	328-353				
	Water				
	scrubber:				
	1-3				
CH <sub>4</sub> loss (%)		0.04-0.1	1-3.5	0.5-3	0.5-20
	Organic				
	scrubber:				
	1.5-4				
	Water				
	scrubber:				
	95-98				
CH <sub>4</sub> purity (%)		> 98	> 96-98	99	90-97
	Organic				
	scrubber:				
	93-98				
	Water				
	scrubber:				
	0.25				
Energy consumption		0.42	0.16–0.43	0.2-0.79	0.5
(kWh.Nm <sup>-3</sup> raw biogas)					
	Organic				
	scrubber:				
	0.32				
Biogas cleaning	Not required	Required	Required	Recommended	Required

c) Repartition of biogas upgrading technology employed in the European market

Every biogas upgrading technology exhibits its own advantages and limitations relatively to others, as summarized in Table 2-4. PSA process, **which is the technology of interest in this work**, has many advantages, especially in terms of low negative environmental impacts, as the process does not involve the use of chemical products. In addition to that, the adsorption unit is also compact as well as easily scalable for medium and high production capacity of biomethane. However, in many cases, the raw biogas needs to be cleaned before being fed into the adsorption unit, which limits the attractiveness of adsorption compared to the physical absorption process. Moreover, high CH<sub>4</sub> loss during the adsorption process is another drawback of this process. Nevertheless, PSA could be regarded as a competitive technology for biogas upgrading, as a considerable amount of biomethane plants in Europe have adopted it as biogas upgrading technology. In study [8], it was reported that out of 503 plants, 18% of them use the PSA process for biogas upgrading (Figure 2-11-a). Similarly, in 2020, the European Biogas Association (EBA) and Gas Infrastructure Europe (GIE) [9] reported that 10% of 729 biomethane plants in Europe have adopted

PSA as biogas upgrading technology, and this percentage could be higher, as 38% of these plants did not provide the information of their chosen biogas upgrading technology (Figure 2-11-b). It could be said that PSA remains relevant today in the context of biogas upgrading.

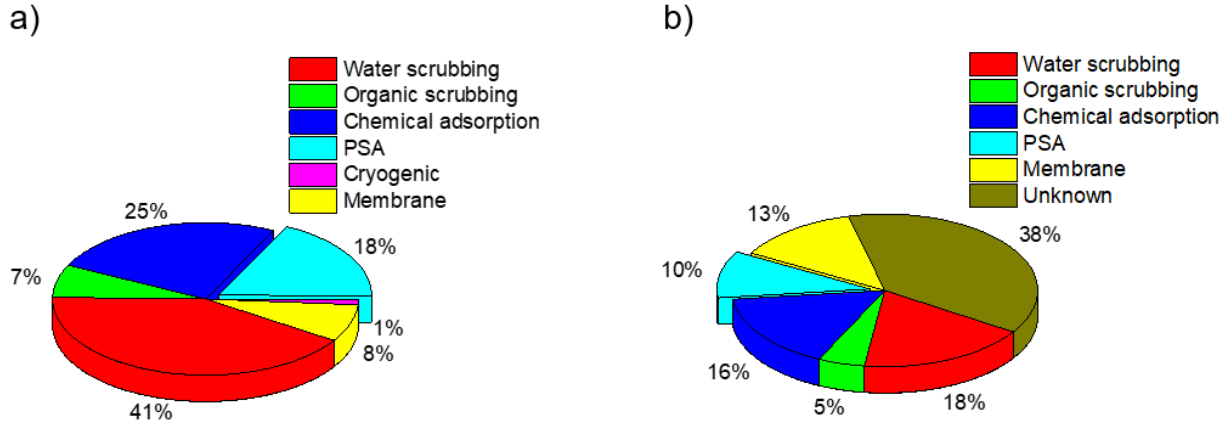


Figure 2-11: (a) Distribution of upgrading technologies applied by biomethane plants in Europe [8] in 2016. (b) Distribution of upgrading technologies applied by biomethane plants in Europe [9] in 2020.

Table 2-4: Advantages and limitations of biogas upgrading technologies [8, 38].

	Advantages	Limitation
<b>Physical absorption (water scrubbing)</b>	Easily scalable Inexpensive Easy to operate Co-removal of H <sub>2</sub> S No special chemical or equipment	High water demand even with regeneration H <sub>2</sub> S damages equipment Clogging due to bacterial growth Foaming possibility
<b>Physical absorption (organic scrubbing)</b>	Higher CO <sub>2</sub> solubility than water. Relatively low methane loss Co-removal of H <sub>2</sub> S and other impurities	Expensive investment and operation Difficult to operate Heating required for complete regeneration
<b>Chemical absorption</b>	Highest biomethane quality High CO <sub>2</sub> removal efficiency Low methane loss No gas pressurization required	High investment cost High heat requirement for regeneration Corrosion of equipment Salt precipitation Foaming possible
<b>PSA</b>	Dry process Relatively inexpensive Easily scalable Compact	High methane loss Complicated process control H <sub>2</sub> S and water pre-treatment required

<b>Cryogenic</b>	High biomethane purity Fewest methane losses Pure CO <sub>2</sub> as a by-product	High investment and operational cost Pre-treatment required High energy requirement Relatively new technology
<b>Membrane</b>	Simple and compact construction Easy operation and maintenance Modular configuration No chemical or heat demand High reliability	Multiple steps needed for high purity Medium to high methane losses Membrane replacement required in 1–5 years Clogging and fouling of membranes Expensive

### 2.2.3. Biogas cleaning technologies

As mentioned previously, biogas cleaning was carried out to get rid of harmful contaminants that can damage and corrodes the piping line, such as H<sub>2</sub>S and H<sub>2</sub>O, prior to the process of biogas upgrading. In this section, the technologies carried out for dehumidification of biogas and H<sub>2</sub>S removal from biogas will be briefly explained.

#### a) Removal of H<sub>2</sub>O

The biogas that leaves digesters in AD process is always saturated with water and this water must be dried if the biogas is to be used for grid injection or vehicle fuel. Other impurities, such as siloxanes and particles, can dissolve into water. When removing water vapor in raw biogas, certain impurities (e.g. Siloxane, H<sub>2</sub>S) would dissolve into the water, thus removing them simultaneously. The process of biogas dehumidification could be carried out through three different techniques: (1) condensation, (2) adsorption and (3) absorption

Raw biogas, which has 5% water at 308 K as saturated water vapor [10], can be removed by changing the pressure and temperature, which will then cause the condensation of water vapor, making it possible to physically separate water from biogas. Some examples of physical separation equipment that could be used to separate condensed water from biogas are: (1) cyclone separators, which utilize the centrifugal force to separate water droplets, (2) moisture traps, which use a pressure differential to create a low temperature and condense water, and (3) demisters, which separates water particles from biogas stream by a wired mesh with microspores 0.5–2 nm [47].

Next, water removal from biogas can be carried out using the adsorption technique. The dew point of biogas can be reduced to 233 K by using water adsorption in columns pressurized to 6–10 bar [10]. These columns are filled with silica, alumina, magnesium oxide, or activated carbon. To maintain continuous operation, two columns are required: one operates until it reaches saturation while the other undergoes regeneration at low pressure.

Lastly, the dehumidification of water in the biogas stream can be carried out by the absorption of water in glycol, a drying agent, which can lower the dew point of biogas from 268 K to 258 K [10]. However, the regeneration of glycol can only be carried out at a high temperature of 473 K, which would require high energy consumption.

## b) Removal of H<sub>2</sub>S

The removal of H<sub>2</sub>S from biogas can either be carried out during biogas production via anaerobic digestion (in situ desulphurization) or after biogas production (ex-situ desulphurization), though in this sub-section, we will only be focusing on the techniques for ex-situ desulphurization. H<sub>2</sub>S can be removed from the biogas stream through several ex-situ desulphurization methods such as: (1) physical and chemical absorption, (2) adsorption, (3) membrane separation and (4) bio trickling filtration (BTF).

As previously mentioned in section 2.2.2, water and organic scrubbing could be used to remove H<sub>2</sub>S in biogas as it is soluble in water as well as organic solvent [47]. The absorption process occurs in a high-pressure column in which the biogas is washed with either water or organic solvent, resulting in the transfer of H<sub>2</sub>S from gas to liquid solvent. The advantage of physical absorption is that CO<sub>2</sub> is also removed concurrently with H<sub>2</sub>S [10]. In addition to that, chemical absorption of H<sub>2</sub>S can be carried out with chemicals such as sodium hydroxide (NaOH), calcium hydroxide (Ca (OH)<sub>2</sub>), iron (II) chloride, iron (III) hydroxide, ethylenediaminetetraacetic acid, monoethanolamine (MEA) and Ferric-Ethylenediaminetetraacetic acid (Fe<sup>3+</sup>/EDTA) [47].

Next, H<sub>2</sub>S removal from biogas by adsorption technique was based on two parallel adsorbent columns that operate under adsorption and regeneration mode concurrently and packed with iron oxide (Fe<sub>2</sub>O<sub>3</sub>), iron hydroxide (Fe (OH)<sub>3</sub>) or zinc oxide (ZnO). At the end of this process, sulphur binds as insoluble FeS or ZnS [47]. Additionally, the removal of H<sub>2</sub>S from biogas under the form of elemental sulfur could also be carried out using activated carbon that was impregnated with alkaline or oxide such as sodium carbonate (Na<sub>2</sub>CO<sub>3</sub>), potassium iodine (KI), sodium hydroxide (NaOH), potassium hydroxide (KOH), sodium bicarbonate (NaHCO<sub>3</sub>), and potassium permanganate (KMnO<sub>4</sub>) [47].

Desulphurization of biogas using membrane separation technique is similar to that of CO<sub>2</sub> removal process during biogas upgrading. The separation is based on the selective permeability property of the membranes, which allows the permeability of H<sub>2</sub>S while retaining the CH<sub>4</sub> on the other side of the membranes. However, the material of the membrane is crucial as it must withstand the corrosive nature of H<sub>2</sub>S, which is why polymeric membrane are usually chosen as the material [10].

Finally, H<sub>2</sub>S removal can be performed using BTF technique that can be performed using a column packed with materials with large surface such as pall rings or polyurethane foam. On the surface of the packing materials exist sulphur-oxidizing microorganisms (Thiomonas, Thiobacillus, Acidithiobacillus, Paracoccus, Halothiobacillus or Sulfurimonas) [10] that oxidized H<sub>2</sub>S into element sulfur or sulfate. The process operates by injecting raw biogas with O<sub>2</sub>, NO<sub>2</sub><sup>-</sup>, or NO<sub>3</sub><sup>-</sup> at the top of packed column. At the same time, water that serve as the nutrient for the microorganism is also injected at the top of the packed backed column using spray system. As the gases and water trickles down the packed column, the H<sub>2</sub>S was oxidized on the surface of the packing materials by the microorganism. With this technology, the H<sub>2</sub>S concentration can be reduced in the biogas stream along together with NH<sub>3</sub> [10].

## 2.3. Pressure Swing Adsorption (PSA)

In the context of this work, we are focusing on the biogas upgrading technique of PSA, or Pressure Swing Adsorption, which is a process that relies on the selective adsorption of at least one gaseous component onto an

adsorbent surface under elevated pressure. This adsorption occurs due to physical forces like van der Waals forces or electrostatic forces. In the PSA process, the strongly adsorbed constituents are retained in the column and composes the extract, while the effluent gas stream that contains the less interactive species composes the raffinate. The performances of PSA depend on various factors affecting the bed adsorption capacity and separation selectivity. Additionally, the regeneration capacity of the adsorbent material varying with pressure and temperature conditions also plays a crucial role in influencing the efficiency of the process.

A PSA unit operates in a cyclic mode, where high pressure steps lead to the adsorption of gas, while steps with pressure decrease causes gas release. Commercial PSA plants for biogas upgrading application feature four set of columns filled with adsorbents. These columns operate in parallel and in phase shift several steps, where the most conventional PSA cycle is known as Skarstrom cycle [48], The following describes the Skarstrom cycle applicable to a 4 column PSA unit in the case of biogas upgrading:

- **Adsorption (AD):** During this phase, biogas, from which hydrogen sulphide and water vapour have been removed, is introduced into one of the adsorbers. As the gas passes through the vessel, CO<sub>2</sub> is selectively adsorbed by the media, while methane exits at the top of the vessel. Before the adsorbent material becomes fully saturated, the raw biogas feed is redirected to another prepared vessel that has already been regenerated, ensuring continuous operation.
- **Blowdown (BD):** This step involves depressurizing the adsorber vessel to atmospheric pressure in countercurrent flow to that of feed gas. The decrease in pressure causes desorption of CO<sub>2</sub> from the adsorbent, and the CO<sub>2</sub>-rich gas is pumped out of the vessel.
- **Purge (P):** At the lowest column pressure, the purge step is initiated using upgraded biogas that flow in countercurrent direction to that of feed gas. This step ensures complete regeneration of the adsorbent bed, preparing it for the next cycle of adsorption.
- **Pressurization (PS):** Biogas is pressurized into an adsorption vessel (column) to a range of 4–8 bar [8]. Within the column, the adsorbent material selectively retains targeted compounds like CO<sub>2</sub>, while methane flows through and accumulates at the top of the column. The pressure inside the column gradually increases from the pressure of the purge step until reaching the operational pressure for adsorption

The sequence of Skarstrom cycle for each PSA unit is presented in Table 2-5 and the evolution of pressure in a PSA unit during each sequence is illustrated in Figure 2-12-a. In addition to that, Figure 2-12-b illustrate the flow of gas during each sequence. During this cyclic sequence, one of the columns is always engaged in adsorption while the other three are in different phases of regeneration to ensure continuous production. Additionally, a part of the raffinate produced during the adsorption phase is re-introduced into another column that is under the purge sequence.

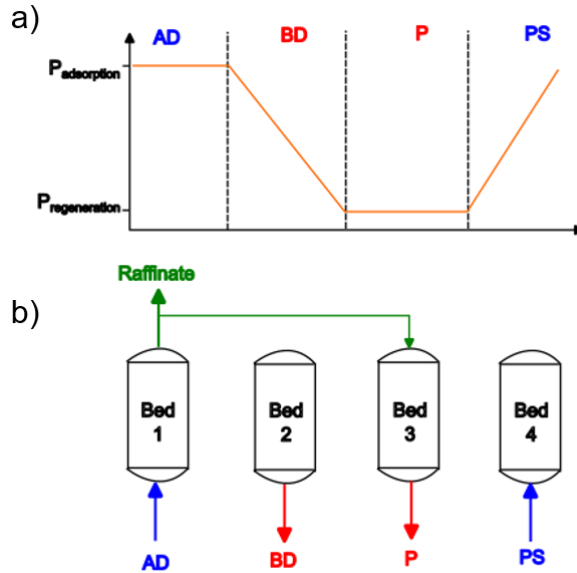


Figure 2-12: (a) Pressure profile for each step in Skarstrom cycle. (b) simplified schematic configuration of PSA units in the Skarstrom cycle.

Table 2-5: Sequences of PSA units in Skarstrom cycle.

Steps	1	2	3	4
Bed 1	AD	BD	P	PS
Bed 2	BD	P	PS	AD
Bed 3	P	PS	AD	BD
Bed 4	PS	AD	BD	P

Despite the maturity of Skarstrom cycle configuration in the PSA process, it is also known for its disadvantages. According to Ruthven [49], the PSA process is able to produce raffinate product under very pure form, but the extract product is generally discharged in an impure form as a byproduct. This evidently leads to the low recovery of raffinate gas component as a fraction of raffinate gas component will be discharged as the byproduct in the extract. In the context of  $\text{CO}_2/\text{CH}_4$  separation for biogas upgrading,  $\text{CH}_4$  as the raffinate product would be produced at high purity but  $\text{CH}_4$  recovery will be somewhat low as non negligible amount of  $\text{CH}_4$  would be lost in the extract product as off gas. To improve the  $\text{CH}_4$  recovery, two general approaches could be made. The first involves the optimization of the PSA cycle process by adding additional steps in the PSA cycle or number of adsorbent beds to further treat the  $\text{CH}_4$  content in extract product [49]. Further example of the optimization of PSA cycle for biogas upgrading is discussed in Chapter 4 of this work. The second approach would be to select an adsorbent with higher working capacity and better  $\text{CO}_2/\text{CH}_4$  selectivity [49].

The mechanism of adsorption in PSA onto adsorbent involves two main types of selectivity [49]: (1) equilibrium selectivity and (2) kinetic selectivity. The first refers to the preferential capture of the stronger adsorbing species by

the solid adsorbent when the process reaches operating conditions close to equilibrium. Meanwhile, the second relies on the separation driven by the differences in diffusional rates of constituent molecules through the adsorbent pores. Therefore, adsorbents used in PSA could also be categorized into two types: (1) kinetically selective adsorbents where the rate of CO<sub>2</sub> adsorption is faster than CH<sub>4</sub> and (2) equilibrium selective adsorbents where CO<sub>2</sub> adsorption capacity is higher than CH<sub>4</sub>. Examples of equilibrium selective adsorbent are activated carbon, zeolite, and silica gel, whereas carbon molecular sieves are an example of a kinetically selective adsorbent. Both CO<sub>2</sub>/CH<sub>4</sub> equilibrium selectivity,  $\alpha_{CO_2/CH_4}^{eq}$ , and kinetic selectivity,  $\alpha_{CO_2/CH_4}^{kin}$ , could be calculated by using the following equations [50]:

$$\alpha_{CO_2/CH_4}^{eq} = \frac{x_{CO_2}/x_{CH_4}}{y_{CO_2}/y_{CH_4}} \quad \text{Eq. 2-1}$$

$$\alpha_{CO_2/CH_4}^{kin} = \frac{K_{H,CO_2}}{K_{H,CH_4}} \sqrt{\frac{D_{CO_2}}{D_{CH_4}}} \quad \text{Eq. 2-2}$$

where  $\mathbf{x}$  is the molar fraction of the adsorbed phase,  $\mathbf{y}$  is the molar fraction of gas phase,  $\mathbf{K}_H$  (mol. kg<sup>-1</sup>. Pa<sup>-1</sup>) is the Henry coefficient and  $\mathbf{D}$  (m<sup>2</sup>. s<sup>-1</sup>) is the diffusivity of gas. Further explanation regarding  $K_H$  and  $D$  is available in Chapter 3 and Chapter 4 respectively.

Zeolites are inorganic crystalline materials which structure is composed of regular networks of alumina and silica tetrahedra (TO<sub>4</sub> – oxygen atoms bridge the tetrahedral atoms) [51]. This forms crystalline superlattices containing molecular-sized pores, formed between windows, into which gas molecules can penetrate. Zeolite exists naturally and can also be synthesized in the laboratory. It possesses regular pore sizes in the range of 0.3 – 1.5 nm [52] and specific surface area ranging between 3-925 m<sup>2</sup>/g [53] [54] [55]. The mechanism of gas separation of zeolites is based on dipole-quadrupole interactions between the gas molecules and the alkaline or alkaline-earth cations in the channel of the zeolite framework. One of the most commonly studied zeolites for CO<sub>2</sub>/CH<sub>4</sub> separation is zeolite 13X [56]. As an example, in the study by Chen et al. [57], Zeolite 13X was analyzed for adsorption isotherm for CO<sub>2</sub>/CH<sub>4</sub> at temperature of 298 K and 333 K and pressure range of 0-3.5 bar. The authors stated that the CO<sub>2</sub>/CH<sub>4</sub> equilibrium selectivity is in the range of 7.7-9.2 and 10-15.6 at 298K and 333K, respectively. Other type of zeolites that have a good CO<sub>2</sub>/CH<sub>4</sub> equilibrium selectivity are NaX, LiX, NaUSY, and CaX. [56] [58] [59]. Today, multiple methods for the synthesis of zeolites have been studied in literature such as hydrothermal synthesis (normal or elevated pressure) [60] [61], molten salt method [62], fusion method [63], alkali activation [64] [65], microwave-assisted synthesis [66] and synthesis by dialysis [67].

Activated carbon (AC) is a highly porous material that can be synthesized through chemical or physical activation processes. ACs have disordered and distributed broader range of pore sizes, ranging from 0.8–10 nm (micropores), 10–50 nm (mesopores) and 50–2000 nm (macropores) [68]. However, because of their fairly wide pore size distribution, activated carbons have rather low selectivities for the adsorption of molecules of different sizes. AC generally exhibits surface area ranging from 700 to 1800 m<sup>2</sup>. g<sup>-1</sup> [69] [70]. Thanks to their large porous surface area, high thermal stability and adsorption capacity as well as low production cost make it as a suitable adsorbent for CO<sub>2</sub>

capture [71] [72] [73] [74]. An example of the application of AC for CO<sub>2</sub>/CH<sub>4</sub> separation in biogas is a study by Peredo-Mancilla et al. [75], where activated carbon was used for the analysis of equimolar adsorption isotherm of CO<sub>2</sub>/CH<sub>4</sub> at 303 K on the pressure range of 0–3 MPa. The authors stated that the CO<sub>2</sub>/CH<sub>4</sub> equilibrium selectivity for AC is in the range of 1-6. The physical activation of the activated carbon first involves the heating of base material up to 900°C in the absence of oxygen and then followed by activation of carbon-enriched char at temperature up to 1000°C. Finally, the product is exposed to activating agents such as steam and oxygen for final pore formation [76]. Examples of common bases used for AC manufacturing are bituminous coal, lignite coal, and coconut shell [76] [77]. The chemical activation process for the production of activated carbon consists of a combination of carbonization and activation in a single step. The starting precursor was mixed with selected chemical activating agents under an inert atmosphere at the temperature of 400–800 °C [78]. Examples of chemical agents commonly used in chemical activation process of AC are ZnCl<sub>2</sub>, KOH, H<sub>3</sub>PO<sub>4</sub> and K<sub>2</sub>CO<sub>3</sub> [79] [80] [81] [82]. ACs produced from chemical activation need to undergo washing steps for the complete removal of impurities and chemical residues from carbon structure [83] [84].

Next, silica adsorbents are mesoporous materials with a pore diameter range of 2-50 nm and a large surface area (up to 2370 m<sup>2</sup>/g) [85] [86]. The highly adaptable structure and surface chemistry, as well as the low production cost, make it as a suitable adsorbent for CO<sub>2</sub> capture [86]. Typical silica adsorbents available commercially for CO<sub>2</sub> capture are Mobil Composition of Matter No. 41 (MCM-41) [87], Mobil Composition of Matter No. 48 (MCM-48) [88], Santa Barbara Amorphous No. 15 (SBA-15) [89] and Santa Barbara Amorphous No. 16 (SBA-16) [90]. The simplicity of the silica adsorbent synthesis process is one of its major advantages over other materials. Examples of available synthesis method available in literature are sol-gel processing [91], template assisted techniques [92], microwave assisted techniques [93], and chemical etching method [94].

Lastly, carbon molecular sieves (CMS) are a special group of activated carbon (AC). The CMS has an amorphous microporous structure and uniform micropore size distribution. Their uniform pore openings are similar in size to small molecules, usually between 3 and 7 Å [95] [56]. These properties allow the CMSs to provide selectivity for the separation of gas molecules with different molecular sizes [96] [97] [98]. The CMSs can be prepared from any carbonaceous material with low content of inorganic compounds such as lignocellulosic materials, coal and polymers by control pyrolysis or chemical vapor deposition methods [52] [99] [100] [101]. In the controlled pyrolysis process for CMS synthesis, the carbon precursor is pyrolyzed at a temperature of 600–1100 °C under different environment and the adsorption capacity is increased through creation of micropores. It is possible to mix the carbonized porous material with a chemical species followed by further pyrolyzation to induce a reduction in pore size by deposition of pyrolytic carbon at the pore entrance [102] [103] [104]. Meanwhile, the chemical vapor deposition (CVD) method involves the deposition of pyrolytic carbon at pore mouth to match the pore entrance with the adsorbate size. Pyrolytic carbon or pyrocarbon is obtained from thermal decomposition of volatile unsaturated hydrocarbons such as acetylene [105], benzene [106], methylpentane [107], cyclohexane [108] and methane [109].

The equilibrium and kinetic selectivity of some adsorbents commercially available for biogas upgrading application is presented in Table 2-6 for reference.



Table 2-6: Equilibrium and kinetic selectivity of adsorbents for CO<sub>2</sub> and CH<sub>4</sub> at 100 kPa [8].

Adsorbent	Absorbent name	Type	CO <sub>2</sub> /CH <sub>4</sub> equilibrium selectivity	CO <sub>2</sub> /CH <sub>4</sub> kinetic selectivity
Activated carbon (AC)	PCB, Calgon Corp.	Equilibrium	3.3	-
Zeolite 5A	5A (Sinopec)	Equilibrium	5.2	3.6
Zeolite 13X	13X (Sinopec)	Equilibrium	8.9	4.5
Carbon molecular sieves (CMS)	CORK-DC-0	Kinetic	4.8	8.9

## 2.4. Metal-organic framework (MOFs)

### 2.4.1. Introduction to MOFs structure and families

MOFs are two- or three-dimensional porous crystalline materials with well-defined structures and superior surface areas of 1000–10 000 m<sup>2</sup>. g<sup>-1</sup> [13]. MOF structure is made up of metal nodes such as transition metals, alkaline earth elements, p-block elements, actinides or mix metals [14], linked together with organic ligands, such as polycarboxylates, phosphonates, sulfonates, imidazoles, amines, pyridyl, phenolates [15]. Table 2-7 lists among the most commonly linkers used in MOF synthesis the ones of the carboxylate family. MOFs can be synthesized by various methods such as hydrothermal (solvothermal) [110] [111], electrochemical [112], mechanochemical [113] [114], microwave assisted synthesis [115], ultrasound assisted synthesis [116], spray-drying synthesis [117] [118] and by flow chemistry [119].

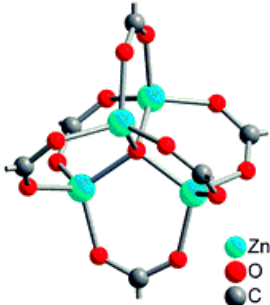
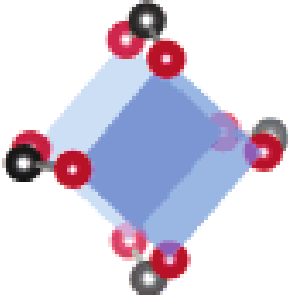
The large variety of MOF structures results from the possibility of designing the material frameworks by tuning the metal ions or the linkers adapting to the desired application. Therefore, to facilitate the synthesis and engineering of these versatile materials, Baerlocher *et al.* introduced a structural entity called Secondary Building Unit (SBU) [120], which refers to the one-dimensional chain of organic-inorganic structure of metal nodes and ligands. The interconnection among SBUs occurring through organic ligands results in the formation of an extended three-dimensional framework. By understanding and manipulating SBUs, researchers can determine and tailor the properties of MOFs to be synthesized. Table 2-8 lists some possible combinations of SBUs with organic linkers producing different families of MOFs.

Table 2-7: Different types of carboxylate ligands used in the synthesis of MOFs.

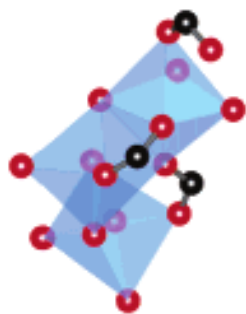
	Acid form		Base form (anion)
<b>H<sub>2</sub>BDC</b>	Benzene-1,4-dicarboxylic acid	<b>BDC</b>	1,4-benzenedicarboxylate
<b>H<sub>2</sub>BPDC</b>	4,4-biphenyldicarboxylic acid	<b>BPDC</b>	4,4-biphenyldicarboxylate
<b>H<sub>2</sub>NDC</b>	1,4-naphthalenedicarboxylic acid	<b>NDC</b>	1,4-naphthalenedicarboxylate

<b>H<sub>2</sub>DHBDC/</b> <b>H<sub>4</sub>DOBDC</b>	2,5-dihydroxy-1,4-benzene- dicarboxylic acid	<b>DHBDC/</b> <b>DOBDC</b>	2,5-dioxido-1,4-benzene- dicarboxylate
<b>H<sub>2</sub>PDC</b>	Pyridine-2,6-dicaboxylic acid	<b>HPDC</b>	Pyridine-2,6-dicarboxylate
<b>H<sub>3</sub>BTB</b>	1,3,5-tri (4carboxyphenyl) benzene	<b>BTB</b>	1,3,5-benzenetriyltribenzoate
<b>H<sub>3</sub>BTC</b>	Benzene-1,3,5-tricarboxylic acid	<b>BTC</b>	1,3,5-benzenetricarboxylate
<b>H<sub>3</sub>BTE</b>	1,3,5-triscarboxyphenylethynyl benzene	<b>BTE</b>	1,3,5-triscarboxyphenylethynyl
<b>H<sub>3</sub>BBC</b>	1,3,5-tris (4'-carboxy [1,1'-biphenyl]- 4-yl) benzene	<b>BBC</b>	,3,5-tris (4'-carboxy[1,1'-biphenyl]- 4-yl) benzoate

Table 2-8: Different MOF families produced from divers SBUs and linkers

SBU	Organic ligand	MOF's type	MOF's chemical formula	Ref
Octahedral Zn <sub>4</sub> O(CO <sub>2</sub> ) <sub>6</sub>	Linear BDC	MOF-5	Zn <sub>4</sub> O(BDC) <sub>3</sub>	[121]
	Triangular BTB	MOF-177	Zn <sub>4</sub> O(BTB) <sub>3</sub>	[122]
	Linear BDC-C <sub>2</sub> H <sub>4</sub>	IRMOF-6	Zn <sub>4</sub> O(C <sub>2</sub> H <sub>4</sub> BDC) <sub>3</sub>	[122]
Cubic Cu <sub>2</sub> (CO <sub>2</sub> ) <sub>4</sub>	Triangular BTC	HKUST-1	CU <sub>3</sub> BTC	[122]
				

$\{\text{Zn}_3[(\text{O})_3(\text{CO}_2)_3]\}_\infty$  helices



DHBDC

MOF-74

$\text{M}_2(\text{DOBDC})$

[122]

M= Mg, Zn, Co, Ni, Fe, Cu or Mn

#### 2.4.2. Potential for HKUST-1 as an adsorbent for CO<sub>2</sub>/CH<sub>4</sub> separation

Recently, MOFs have been gaining attention for their potential application in gas separation owing to their inherent properties, such as high specific surface area, large porosity and tunable pore size [14]. In the literature, MOFs have been extensively studied for their capability to separate CO<sub>2</sub> from CH<sub>4</sub>. For example, in a study by Loiseau *et al.* [11], CO<sub>2</sub> adsorption performance of MIL-96 synthesized through a solvothermal method was investigated. The authors found that at 30 °C and 10 bar, MIL-96 exhibits adsorption capacities of 4.4 mmol/g for CO<sub>2</sub> and 1.95 mmol/g for CH<sub>4</sub>, which demonstrates the preferential adsorption of CO<sub>2</sub> rather than CH<sub>4</sub>. In another study by Bourrelly *et al.* [12], MIL-53 (Al) was synthesized and its CO<sub>2</sub> and CH<sub>4</sub> adsorption capacities were investigated. MIL-53 (Al) exhibits CO<sub>2</sub> and CH<sub>4</sub> adsorption capacities of 3 mmol/g and 2 mmol/g respectively, at 5 bar and 303K. At this condition, the separation factor corresponding to the ratio of the adsorption capacities of the pure components, is around 1.5 and still indicates the preferential adsorption of CO<sub>2</sub>.

HKUST-1 (Hong Kong University of Science and Technology-1) refers to a metal-organic framework known as MOF-199 or Cu<sub>3</sub>(BTC)<sub>2</sub> and was first reported by Chui *et al.* [19]. The HKUST-1 composed of copper nodes linked with BTC as the linker. Figure 2-13 depicts a simplified scheme of the structural unit of HKUST-1, containing four carboxylate groups coordinated to two Cu<sup>2+</sup> ions to form a three-dimensional porous network with the chemical formula [Cu<sub>3</sub>(BTC)<sub>2</sub>(H<sub>2</sub>O)<sub>3</sub>]<sub>n</sub> [123]. Additionally, in a hydrated state, the HKUST-1 structure includes one water molecule unit coordinated to the two metal centers in an axial position. HKUST-1 adsorbent has been widely studied for CO<sub>2</sub>/CH<sub>4</sub> separation as it shows a good equilibrium selectivity [16, 17]. For example, in a study by Teo *et al.* [16], measurements of CH<sub>4</sub> and CO<sub>2</sub> adsorption isotherms at temperature condition of 130 K, 140 K, 180 K and 298 K and pressure range of 0-5 bar, shows that CO<sub>2</sub> is always preferentially adsorbed against CH<sub>4</sub>. This study also reveals what are the preferential adsorption sites for both gas constituents, located near the open metal sites for CO<sub>2</sub> and in the octahedral cages of the ligand for CH<sub>4</sub>. Besides, Hamon *et al.* [124] studied CO<sub>2</sub>/CH<sub>4</sub> separation by conducting breakthrough experiments at a pressure range of 1-5 MPa and at a temperature of 303 K by using adsorption column with a volume of 3.8x10<sup>-4</sup> m<sup>3</sup> and 2 g of powder HKUST-1 as the adsorbent. The authors measured the CO<sub>2</sub>/CH<sub>4</sub> equilibrium selectivities in the range between 4.8 to 11.5, depending on the composition amount of both gas constituents in the mixture (25% vol CO<sub>2</sub>/75% vol CH<sub>4</sub>, 50% vol CO<sub>2</sub>/50% vol CH<sub>4</sub> and 75% vol CO<sub>2</sub>/25% vol CH<sub>4</sub>).

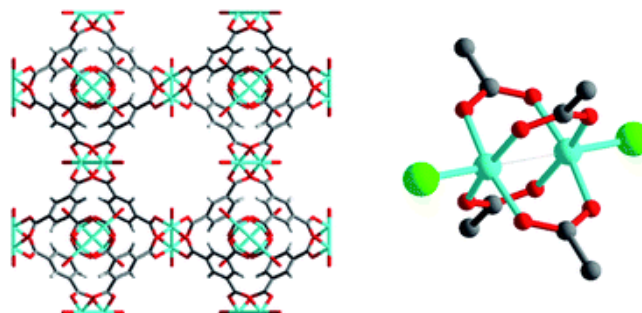


Figure 2-13: HKUST-1 cubic metal–organic framework structure (left), and its secondary building unit (SBU) (right). Grey—carbon; light grey—hydrogen; red—oxygen; cyan—copper. In the right-hand figure, the larger green spheres indicate the exchangeable axial positions of the SBU [125].

At low pressure, the CO<sub>2</sub> capture performance of HKUST-1 is mainly dictated by the interactions between the open metal sites and CO<sub>2</sub> molecules, whereas at high pressure, surface area of HKUST-1 has a significant impact of the adsorption capacity of CO<sub>2</sub>, as higher surface area results in a higher CO<sub>2</sub> adsorption capacity [123]. Figure 2-14 shows for the pressure conditions of 1 bar and 5 bar at 298 K, the comparison with literature data of CO<sub>2</sub> and CH<sub>4</sub> adsorption capacities of HKUST-1 with other MOFs, as well as with other conventional adsorbents, [124] [126] [12] [127] [128] [129] [130] [131] [132] [133] [134] [135] [136] [137]. It can be noted that CO<sub>2</sub> is always preferably adsorbed than CH<sub>4</sub> under the reported tested conditions. On one hand, HKUST-1 shows at both pressure conditions better CO<sub>2</sub> adsorption capacities than MOFs such as PCN-68 and MIL-101 (Cr), as well as than CMS. On the other hand, MOF-74 adsorbent family exhibits larger CO<sub>2</sub> adsorption capacities than HKUST-1 at both pressure conditions. Similarly, at 1 bar, the CO<sub>2</sub> adsorption capacity of zeolite 13X surpasses that of HKUST-1, though this trend is reversed at the higher pressure of 5 bar. Nevertheless, HKUST-1 is one of the few MOFs that are commercially available [18] making the procurement of large-scale amounts of material with consistent quality easier.

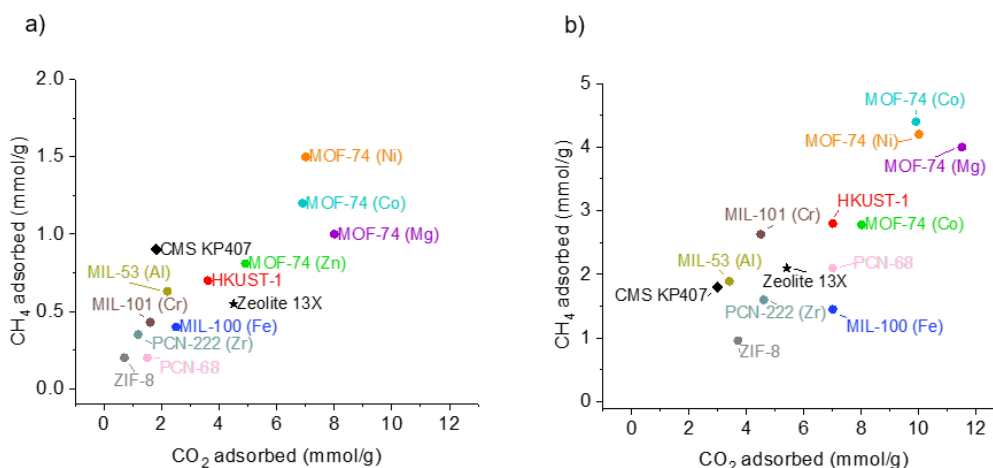


Figure 2-14: (a). Comparison of CO<sub>2</sub> and CH<sub>4</sub> adsorption capacities for different adsorbents at 298 K and 1 bar. (b) Comparison of CO<sub>2</sub> and CH<sub>4</sub> adsorption capacities for different adsorbents at 298 K and 5 bar.

Additionally, the screening of MOFs potential performance for CO<sub>2</sub>/CH<sub>4</sub> separation in the context of biogas upgrading can be carried out following equation (Eq. 2-3) as proposed by Wiersum et al. [138]:

$$API = \frac{(WC_{CO_2})^2 \cdot (\alpha_{CO_2/CH_4}^{eq/kin})^{0.5}}{\Delta H_{CO_2,ads}} \quad \text{Eq. 2-3}$$

where the *API* signify the “Adsorbent Performance Indicator” as proposed by Wiersum et al. to quantify the potential CO<sub>2</sub>/CH<sub>4</sub> separation performance of an adsorbent,  $WC_{CO_2}$  (cm<sup>3</sup> STP/cm<sup>3</sup> of adsorbent) is the working capacity of an adsorbent,  $\alpha_{CO_2/CH_4}^{eq/kin}$  is the selectivity (either equilibrium or kinetic) of an adsorbent and lastly  $\Delta H_{CO_2,ads}$  is the heat of adsorption of an adsorbent.

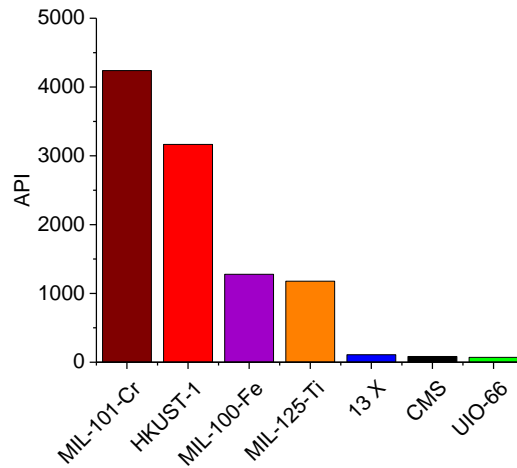


Figure 2-15 : Adsorbent Performance Indicator (API) of different adsorbent for equimolar CO<sub>2</sub>/CH<sub>4</sub> separation at 25 °C, 5 bar adsorption pressure and 1 bar regeneration pressure. Data taken from [138].

Figure 2-15 compares the different API values of adsorbents for CO<sub>2</sub>/CH<sub>4</sub> separation from biogas in the condition of equimolar mixture of CO<sub>2</sub> and CH<sub>4</sub>, 25 °C of biogas temperature, 5 bar adsorption pressure and 1 bar regeneration pressure. It is clear based on API value that HKUST-1 should be performing relatively better than conventional adsorbents such as zeolite 13X and CMS for biogas upgrading application at the stated operating condition. Therefore, based on all of the aforementioned reasons, we have chosen HKUST-1 as the MOF model for this study.

However, one of the main drawbacks for using HKUST-1 as an adsorbent for CO<sub>2</sub> capture from biogas is its sensitivity towards moisture, which may be still present at low concentrations in the biogas feed even after the drying step. HKUST-1 is known as a MOF that is sensitive to water as the Cu open-metal sites of HKUST-1 has a high affinity with water which results in the elongation of Cu-O bonds of HKUST-1 and thus leads to disintegration of HKUST-1 framework [20] [139]. Consequently, this leads to a drop in the CO<sub>2</sub> adsorption capacity of HKUST-1 as shown in the study by Alvarez *et al.* [140], where HKUST-1 exposed to water was shown to lose its CO<sub>2</sub> adsorption capacity at 303 K by 8% in comparison to dehydrated HKUST-1 (13 mg CO<sub>2</sub>/g HKUST-1).

## 2.5. Shaping technologies

For industrial application of MOF materials as adsorbents, one of the necessary conditions is the ability to process the shaping of powders in order to avoid clogging, gradual loss of the active materials and high-pressure losses throughout the adsorption column [141]. The shaping of MOF materials can be done either *in situ*, during MOF synthesis and crystal growth, or in a post-synthesis process [141]. In the *in situ* approach, the MOF crystals are synthesized simultaneously with a substrate immersed within the reaction mixture, and the MOF crystals in situ nucleate and grow on the surface of the substrate. Meanwhile, in post-synthesis approach, MOF crystals are pre-synthesized in a separate step, followed by compositing with the hybridizing agents and casting into various shapes. The choice of either the former or the latter approaches depends on the intended application and also on the stability of the intended MOF structure. Nonetheless, the main challenge of the shaping process is to ensure that the impact of the shaping process on MOFs intrinsic properties remains minimal while ensuring also that shaped materials demonstrate sufficient mechanical and chemical stability. In the following sub-section, various shaping technologies employed to engineer MOF powders for CO<sub>2</sub> capture application are reported. Furthermore, the impact of these shaping technologies on the MOFs properties, e.g. BET surface area and CO<sub>2</sub> adsorption capacities are discussed.

### 2.5.1. Post-synthesis shaping methods

#### a) Pressing/compression

MOF materials to be applied for CO<sub>2</sub> capture have been shaped by one of the most conventional powders shaping technologies, i.e. compression/pressing. This method involves pre-synthesized MOF crystals to be filled inside a mold and subjected to uniaxial compression to obtain a simple shape agglomerate (Figure 2-16) [141]. When MOFs are subjected to the high pressure from the compression, it undergoes inter-crystal fusion to form a macroscopic body that is mechanically strong enough to enable manual handling. However, the pressure applied during compression should be carefully selected to avoid the complete destruction of the crystal structure (amorphization) and therefore loss of intrinsic properties of MOFs [21]. This method could be carried out either without or with the addition of binding agent, where the binding agent facilitates bonding of individual particles by generating a link between them [21].

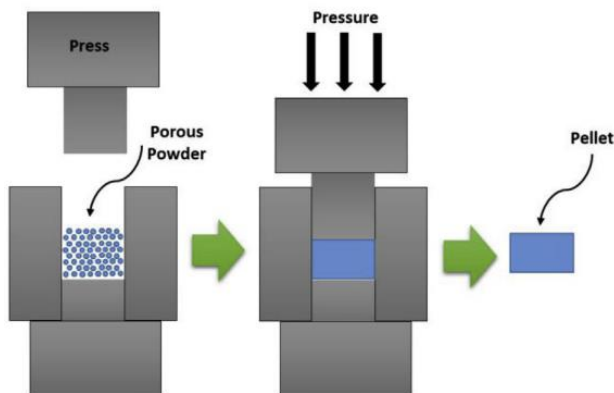


Figure 2-16: Schematic representation of the preparation procedure of MOF disk tablets by compression. Image reproduced from [142].

The shaping of ZIF-8 and MIL-53(Al) via mechanical compression without the usage of binding agent was reported by Ribeiro *et al.* [142]. MOFs pellets were obtained varying the compression pressure parameter at 62 MPa and at 125 MPa. At 62 MPa, shaped ZIF-8 material experiences both specific surface area and pore volume reduction as low as 7% relative to the pristine MOF powder, whereas compressed MIL-53(Al) particles suffer reduction of specific surface area and pore volume reduction by 46% and 36%, respectively. Meanwhile, at compression pressure of 62 MPa, both the specific surface area and pore volume of pelletized ZIF-8 recorded a reduction by 12 % relative to ZIF-8 pristine powder. In similar condition, pelletized MIL-53(Al) suffers a reduction of specific surface area and pore volume by 32% and 24% respectively. This study by Ribeiro *et al.* [142] demonstrate clearly that the application of compression method for MOFs shaping will inevitably lead to the loss of surface area and pore volume of materials, with the degree of severity depending on the type of MOFs used.

Apart from that, the shaping of MOF-801 powder into pellets via mechanical compression and addition of binding agents was reported by Taddei *et al.* [143], where three different binders were investigated: polyvinylalcohol (PVA), sucrose and polyvinylbutyral (PVB). The authors initially analyzed which binding agent results in a pelletized MOF-801 that possess highest mechanical strength by conduction a simple drop test. It was reported in this study that usage of PVB is the most preferred binder, as 5 wt% of PVB that underwent compression at 438 MPa at 15s was found to be sufficient to fabricate highly resilient MOF-801 pellets. The authors then determined the impact of different compression pressure (146 MPa, 292 MPa and 438 MPa) on the pelletized MOF-801 with 5 wt% of PVB binder. The authors concluded that with the presence of binding agent, the compression pressure did not have a major impact on the BET surface area of the pelletized MOF-801, as its reduction is only in the comparable range of 32-39% relative to the MOF-801 powder, whatever the compression pressure may be.

#### b) Wet granulation

Wet granulation is another available method to assemble MOF crystals into shape, in which binders with sticky surface are mechanically co-blended with the MOF crystals [141]. The wet granulation process that occurs in high-shear granulators can be divided into three main stages: (1) wetting and nucleation, (2) consolidation, (3) attrition and breakage, before finally an assembly of parent MOF powder into bigger agglomerates called granules was obtained (Figure 2-17-a) [144]. When the liquid binder is introduced to the powder mass, particles begin to aggregate and form clusters (nucleation). This binder functions as a bridge between clusters, creating granules. These granules then undergo compaction, resulting in solid particles (consolidation). Aggregation is a key process in granulation, leading to the formation of larger particles (agglomerates) from smaller ones. When subjected to shear forces, these larger agglomerates break down into smaller granules.

The most conventional granulator used to perform granulation is the mechanical granulator that works based on the mechanical forces such as shear (Figure 2-17-b) [145]. The shear wet granulator mainly consists of a mixing bowl, an impeller, and an auxiliary chopper. The impeller is used for powder mixing and promoting granule densification, while the function of the chopper is to break apart the wet lumps or promote the growth of smaller particles.

An example of MOF shaping using wet granulation method is a study by Valekar *et al.*, they have successfully shaped MIL-100(Fe), MIL-101(Cr), UiO-66(Zr), and UiO-66(Zr)\_NH<sub>2</sub> powders into spherical particles at atmospheric pressure and ambient temperature by using mesoporous  $\rho$ -alumina as a binder [146]. The resulting granulated MOF particles consist of up to 95 wt% of MOF powder loading. The material mechanical stability could be then improved by decreasing the MOF content and increasing the alumina content. A similar process was applied by Chanut *et al.* [131] to fabricate granules of UiO-66(Zr), UiO-66(Zr)\_NH<sub>2</sub>, MIL-100(Fe) and MIL-127(Fe) with a polyvinyl-based binding agent. The authors stated that the addition of binder did contribute to the blocking of pores in MOFs, resulting in a decrease of BET surface area of each granule in the range of 4-20% relative to their respective pristine MOF powder.

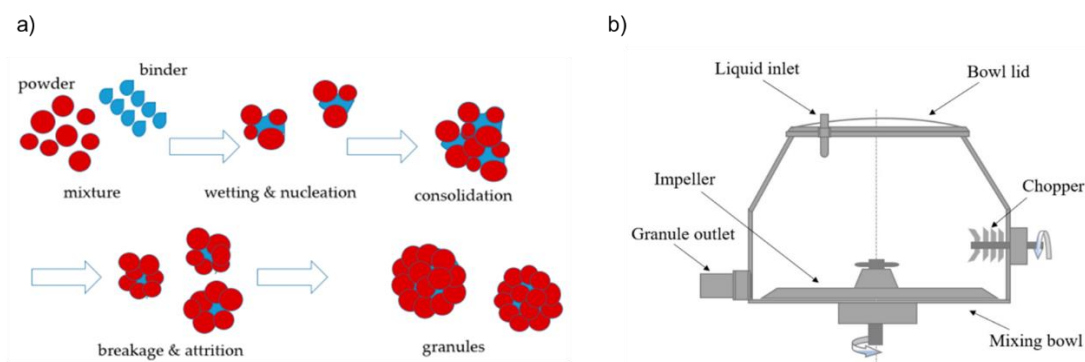


Figure 2-17: (a) Schematic representation of granulation method [144]. (b) Schematic diagram of shear wet granulator [145]

### c) Sol-gel

The term sol-gel is associated with chemical processes that firstly generate a sol, which is a colloidal suspension of submicron-sized particles in a solvent, followed by the formation of gel state, which is simply defined as a non-fluid 3D network that extends through a fluid phase [147]. Then, the gel was either dried slowly to form a dense ‘xerogel’ or the gel underwent supercritical drying to form aerogel (Figure 2-18). It has to be noted that this shaping method does not require the use of pressure to obtain large solid-state compact materials.

Another method for shaping MOFs without the usage of binder was reported in the studies by Madden *et al.* [148] and by Zhang *et al.* [149], where monoliths of HKUST-1, UiO-66, Ni(BDC) and Mn<sub>3</sub>(BTC)<sub>2</sub> were fabricated using a sol-gel preparation.. The shaping process then involves the preparation of solutions of MOFs precursors and their gelation taking place through stirring and centrifugation. This is followed by subsequent slow drying or CO<sub>2</sub> drying, resulting in the production of MOF xerogels and MOF aerogels, respectively. The monoliths obtained after the sol-gel method exhibit comparable CO<sub>2</sub> uptakes in comparison to pristine MOF powders, with no obvious degradation in their intrinsic properties. Their specific surface area was preserved with no pore blockage neither particle amorphization.



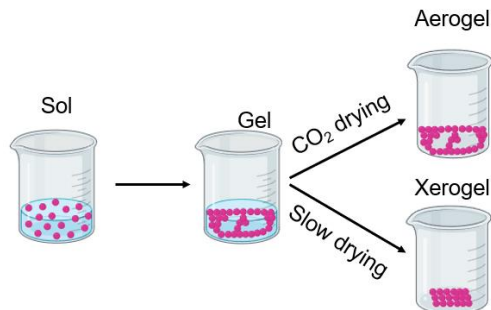


Figure 2-18: Schematic representation of the sol-gel method.

#### d) Extrusion

The application of an extrusion process was also reported to shape MOFs powder for CO<sub>2</sub> capture purpose. The principle behind shaping by extrusion is relatively straightforward (Figure 2-19): (1) MOFs were mixed with the binder and inserted into an extruder. (2) MOF-binder mixture paste was extruded out and cut into different desired lengths. (3) MOFs' extrudates were dried to eliminate any remaining solvents. Extruder may be divided into screw and piston types [21]. On one hand, a screw extruder allows continuous processing and might consist of one (single screw), two (twin screw) or multiple screws which operate in simultaneous and parallel rotations. On the other hand, piston extruders operate in batch mode that enables the extrusion of pastes with high viscosity and compaction.

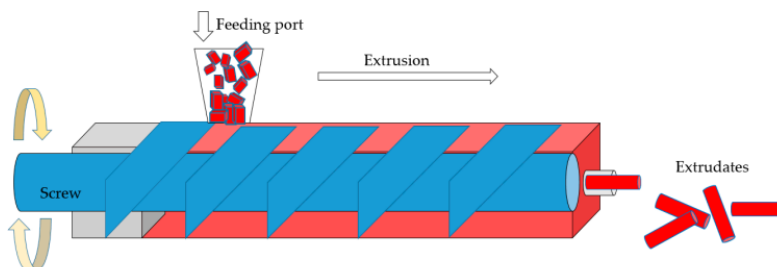


Figure 2-19: Schematic representation of the sol-gel method. Image taken from [144]

#### e) Additive manufacturing (3D printing)

Additive manufacturing (3D printing) is a relatively new technology for MOFs shaping and has been gaining attention as the process is easy and is able to produce geometrical complex designs at low cost. 3D printing is based on the same principle as conventional extrusion process, that is, it requires binder/plasticizer to form a MOF-binder paste which is then extruded through a printing nozzle and subsequently deposited on a substrate in a controllable layer-by-layer manner to form an object defined by the user. Four types of additive manufacturing techniques have been reported in literature [150] for the shaping of MOFs: (1) Fused Deposition Modelling (FDM), (2) Direct Ink Write (DIW), (3) Selective Laser Sintering (SLS) and (4) Digital Light Processing (DLP) (Figure 2-20).

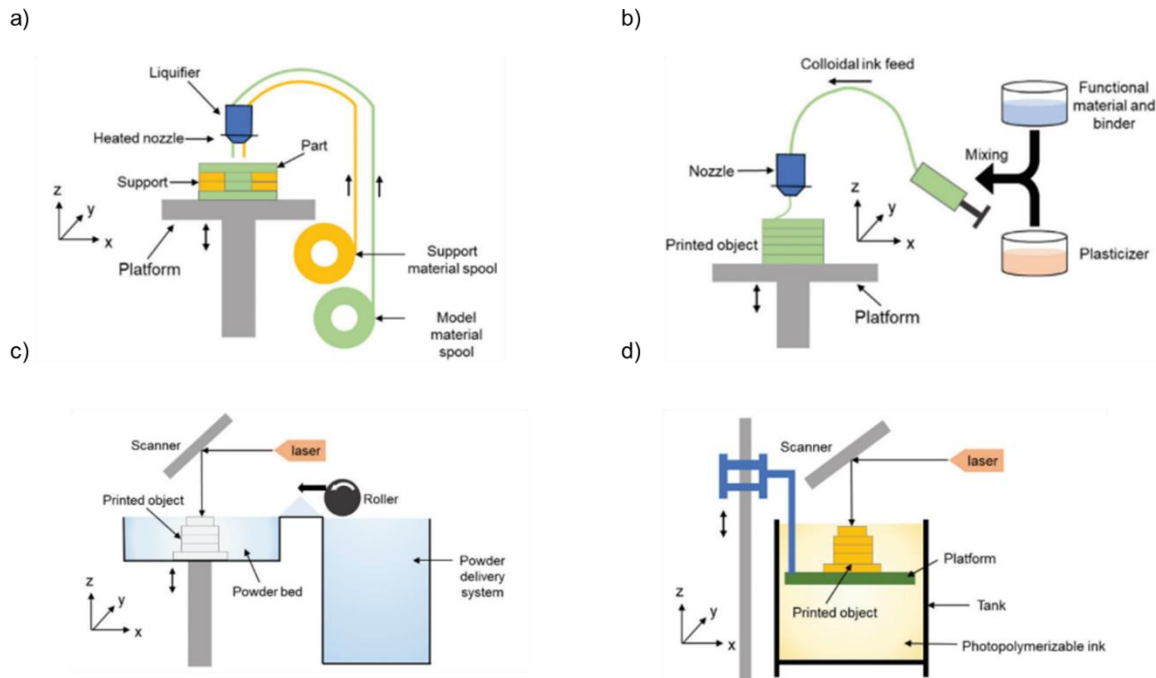


Figure 2-20: Schematic representation of additive manufacturing method for (a) FDM, (b)DIW, (c) SLS and (d)DLP. Image taken from [150].

Fused deposition modeling (FDM), also referred to as fused filament fabrication, is a process in which a thermoplastic polymer is heated above its glass-transition temperature ( $T_g$ ) and extruded through a nozzle (Figure 2-19-a). As the semi-molten polymer is deposited on the printer bed, it solidifies upon cooling, forming bonds between layers through chain diffusion, which results in a mechanically stable 3D printed object. In the context of MOFs shaping, a study by Evans et al. [151], demonstrates the shaping of ZIF-8 powder into a monolith via FDM. The ZIF-8-thermoplastic composite was heated up to  $1^\circ\text{C}$  above its melting point, so that it solidifies right after extrusion and subsequently welds to the previous layers. Zif-8 powder was incorporated homogeneously into both poly-lactic acid (PLA) and thermoplastic polyurethane (TPU) matrices, that act as the binder, and printed to produce ZIF-8 monoliths with MOF's loadings up to 50 wt%.

Next, the basic principle of Direct Ink Write (DIW) technique for additive manufacturing resembles the conventional extrusion process. The first step of DIW consist of the formation of a MOF-binder paste by suspending the parent powder in a liquid with dissolved binding agent and plasticizer. Thereafter, the paste is pushed through a thin printing nozzle and subsequently deposited on a substrate in a controllable, layer-by-layer manner. Finally, the 3D printed object is further subjected to a thermal treatment for the removal of solvent (Figure 2-19-b). Thakkar et al. [152] have reportedly shaped MOF-74(Ni) and UTSA-16(Co) monoliths using DIW technique that operates with layer-wise deposition of a slurry mixture containing MOF powder, bentonite clay (binding agent) and poly-vinyl alcohol, PVA (plasticizer). The resulting slurry mixture was printed in a layer-by-layer manner, followed by drying at 373 K. The 3D-printed MOF-74(Ni) and UTSA-16(Co) monoliths were fabricated with MOF loadings as high as 80 and 85 wt%, respectively.

Selective Laser Sintering (SLS) technique for additive manufacturing involves the melting of a thermoplastic material with a laser beam in the presence of the parent powder. The laser is traced over a cross-section of the printing object in the *xy* plane. Once a layer is sintered, the platform will be lowered by one-layer thickness, and a new layer of material is applied on the top by a roller on the printer and finally the 3D object is left to cool and solidify (Figure 2-19-c) [150]. An example of the application of SLS technique for the shaping of MOFs is the study by Lahtinen *et al.* [153], where 10 wt% of commercial HKUST-1 was mixed with Nylon-12 (N12) powder and printed at 443 K. The XRD analysis on the printed object confirms the presence of HKUST-1 particles and further CO<sub>2</sub> adsorption analysis reveals that the adsorption capacity of active HKUST-1 inside the 3D printed object is similar to that of bulk pristine HKUST-1 material.

Lastly, Digital Light Processing (DLP) technique consists of a light source of a specific wavelength (typically in the ultraviolet range), that is used to selectively cure the surface of a photopolymerizable liquid monomer, which contains small amounts of photoinitiators and additives (Figure 2-19-d). The light-activated reaction transforms the liquid monomer into solid resin, layer by layer, until the 3D structure is formed. An example of MOF shaping using DLP technique is a study by Halevi *et al.* [154], where 3D printed HKUST-1 structures were obtained. The authors mixed 10 wt% of HKUST-1 powder with a blend of 2-phenoxyethyl acrylate (PEA) and polyethylene glycol diacrylate (PGD) as the polymeric matrix, while Irgacure-819 and Irgacure-184 were applied as photoinitiators. The characterization of the 3D printed material reveals the preservation of HKUST-1 particles inside the 3D printed composite, showcasing the successful shaping of MOFs.

### 2.5.2. *In situ* shaping methods

#### a) Wet impregnation/coating

MOFs shaped composite adsorbents intended for CO<sub>2</sub> capture application have also been fabricated by addition of a binder via the wet impregnation/coating method. This method involves the usage of a porous monolith, which acts as a support of the adsorbing phase. The impregnation of MOF components onto the support is subsequently completed with the *in situ* growth of MOFs' crystallites (Figure 2-21). Such a shaping process was tested by Qian *et al.* [155]. In this study, HKUST-1 particles were crystallized onto the support material after by wet impregnation. The porous support was first soaked with the MOF precursor solution by immersion. This step was repeated multiple times to ensure an efficient penetration of the MOF precursors onto the support matrices. The *in situ* growth of HKUST-1 crystallites on the surface of the porous support was performed by heating the support at 363 K for 20 h. No deformation of the porous support monolith was observed after such a treatment and the presence of HKUST-1 particles was verified using XRD analysis. In another study by Rezaei *et al.* [156], the coating of MOF-74(Ni) and UTSA-16(Co) onto the surface of cordierite monolith, that acts as support, was successfully achieved via *in situ* dip coating (ISDC) and layer by layer (LBL) coating. ISDC technique involves the immersion of the support into the MOF precursor solution, which contains the linker and metal ions, prior to solvothermal reaction, resulting in the *in situ* growth of MOFs particles on the surface of the support. In the LBL coating technique, the support was first dipped in a solution containing the metal and organic linker alternately for several cycles to induce crystal growth. Then, the support was finally being totally submerged in MOF precursor solution, followed by a solvothermal reaction. The

resulting MOF-74(Ni) and UTSA-16(Co) monoliths were successfully fabricated with MOF loadings as high as 52 and 55 wt% respectively.

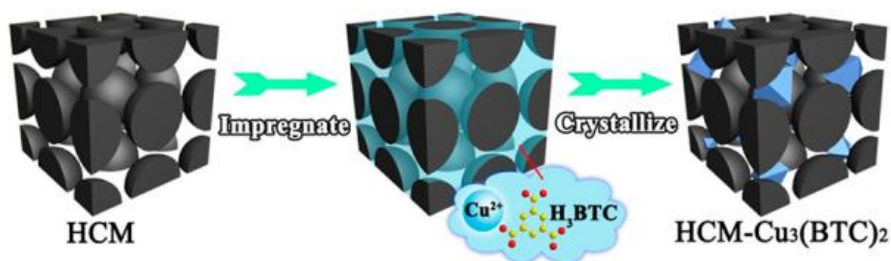


Figure 2-21: Schematic representation of the wet impregnation/coating method. Image taken from [155].

### 2.5.3. Impact of shaping methods on MOF's textural properties and CO<sub>2</sub> adsorption capacity

Ideally, the MOF shaping process should maintain the same characteristics and performances as its pristine powder. Nevertheless, numerous studies conducted so far show that shaping technologies may affect MOFs properties, especially when the process implies either pressurization [157, 158] or the use of a binder [159, 160]. The variations in the material specific surface area is one of the important indications for their performance as CO<sub>2</sub> adsorbents, as higher CO<sub>2</sub> adsorption capacities are reported with an increase in the surface area, so that a linear correlation could be established between them [161, 162]. The reductions in shaped MOF adsorbent specific surface area and CO<sub>2</sub> adsorption capacities (whichever data that is available), depending the applied shaping method mentioned in the previous sub-section, are reported in Table 2-9.

From the literature studies, it appears that shaping of MOFs via powder compression without usage of binder leads to a reduction in the MOF BET surface area and CO<sub>2</sub> adsorption capacities. This phenomenon could be observed in two separate studies by Ribeiro *et al.* [142] and by Chen *et al.* [163]. Ribeiro *et al.* conducted the shaping of ZIF-8 and MIL-53(Al) at the same process parameters (62 MPa and at 125 MPa). The authors observed different severity in BET surface area reduction for both MOFs, where pelletized ZIF-8 suffers reduction around 7-12% whereas that of pelletized MIL-53(Al) is around 32-46%, in comparison to their respective pristine material. Similarly, the reduction in CO<sub>2</sub> adsorption capacity of pelletized ZIF-8 is lower than that of pelletized MIL-53(Al), i.e. 5-7% vs 15-17%. The same impact of compression technique on BET surface area and subsequently CO<sub>2</sub> adsorption capacity was observed by Chen *et al.* [163], where compression Ni-MOF-74 without binder results in the decrease of BET surface area and CO<sub>2</sub> adsorption capacity by 10% and 36%, respectively. On another hand, compression with the usage of binder was carried out in study [143], where MOF-801 was shaped using a pressing process and polyvinyl butyral (PVB) as the binding agent. Pellets of MOF-801 were characterized by a reduction of up to 32-37% in their BET surface compared to pristine, depending on the pressure of compaction. The authors stated that binding agent contributes to the pores blockage, hence causing the observed severe reduction of BET surface area.

Next, MOFs shaping via granulation was conducted in a study [146], where MIL-101 (Cr) and UiO-66 (Zr) granules were synthesized using 5wt% of mesoporous  $\rho$ -alumina (MRA) as the binder. Interestingly, the granules obtained showed only 9-13 % of losses in the BET surface area and 7-8% of reduction in the CO<sub>2</sub> adsorption capacities

at 1 bar in comparison to pristine MOFs. The authors attributed these limited textural effects to the mesoporous nature of the binding agent. Similarly, MIL-100 (Fe) and MIL-127 (Fe) granules, which were prepared using 3 wt% of polyvinyl-based binder in study [131], exhibited small losses in BET surface area (5-10%), though their reduction of CO<sub>2</sub> adsorption capacity at 10 bar is non-negligible (18-20%). This study shows that even at a low loading of binder, pore blockage that leads to BET surface area reduction and CO<sub>2</sub> adsorption capacity would still occur.

The analysis of the effect of the sol-gel preparation on material BET surface area and CO<sub>2</sub> adsorption capacities appears a little complicated. On one hand, a study by Madden *et al.* [148] demonstrates that HKUST-1 and UIO-66 synthesized from sol-gel method exhibits lower BET surface area (19-21%) and CO<sub>2</sub> adsorption capacities (22-32%) than their respective pristine form. On the other hand, a study by Zhang *et al.* [149] demonstrated an increase in the BET surface area (71%) and CO<sub>2</sub> adsorption capacities (18%) after production of HKUST-1 aerogel. It is unclear why the findings of former studies are different from the latter, though it should be highlighted that shaped MOFs obtained from the study of Madden *et al.* were dried slowly to produce MOFs xerogels, whereas MOFs aerogels obtained from the study of Zhang *et al.* were dried by supercritical CO<sub>2</sub>.

Meanwhile, the shaping of MOFs via extrusion was carried in study by Hong *et al.* [164], where MIL-101 (Cr) extrudate, which used 40 wt% of bentonite clay as the binder, exhibits reduced BET surface area by 9%, and CO<sub>2</sub> adsorption capacities lowered by 45% compared to the pristine powder. Similarly, in another study by Rivera-Torrente *et al.* [165], aluminium fumarate extrudates, which included either 50 wt% of clays or SiO<sub>2</sub> as a binding agent, recorded a significant reduction in BET surface area (42-73%) and CO<sub>2</sub> adsorption capacities (50-67%). In both of these studies, the authors attributed these effects to the addition of different type binding agent as well as their high loading amount.

Table 2-9: BET surface area and CO<sub>2</sub> adsorption capacities reported for shaped MOF

Shaping method	MOF	Binder	Binder loading (wt%)	BET surface area (m <sup>2</sup> /g)			CO <sub>2</sub> adsorption capacity at 10 bar (mmol /g)			Adsorption Temperature (K)	Ref
				Powder	Shaped MOF	Reduction (%)	Powder	Shaped MOF	Reduction (%)		
Pressing	ZIF-8	-	-	1983	1736-1841	7-12	5.9	5.5-5.6	5-7	303	[142]
	MIL-53(Al)	-	-	796	432-538	32-46	4.1	3.4-3.5	15-17		
	Ni-MOF-74	-	-	820	733	10	11 <sup>a</sup>	7	36	298	[163]
	MOF-801	PVB	5	899	569-605	32-37	N/A	N/A	N/A	N/A	[143]
Granulation	MIL-101 (Cr)	ρ-alumina	5	4066	3685	9	2.9 <sup>b</sup>	2.7 <sup>b</sup>	7	298	[146]
	UiO-66 (Zr)			1050	911	13	1.2 <sup>b</sup>	1.1 <sup>b</sup>	8		
	MIL-100 (Fe)	PVA/PVB	3	2261	2043	5	8.3	6.5	22	303	[131]
	MIL-127 (Fe)			1181	1117	10	13.4	11	18		
Sol-gel	HKUST-1	-	-	307	834	71 <sup>c</sup>	5.1 <sup>b</sup>	6 <sup>b</sup>	18 <sup>c</sup>	273	[149]
	HKUST-1	-	-	1871	1512	19	6.2 <sup>b</sup>	4.2 <sup>b</sup>	32	298	[148]
	UiO-66	-	-	1288	1015	21	2.7 <sup>b</sup>	2.1 <sup>b</sup>	22		
Extrusion	MIL-101 (Cr)	Bentonite clay	40	202	183	9	1.1 <sup>b</sup>	0.6 <sup>b</sup>	45	298	[164]
	Aluminium Fumarate	Bentonite / montmorillonite	50	1034	595-274	42-74	6	3-2	50-67	303	[165]
		/ SiO <sub>2</sub>									
Additive manufacturing	MOF-74 (Ni)	Bentonite clay	15	1180	737	38	5.6	4.5	20	298	[152]
	UTSA-16 (Co)		10	727	568	22	3.5	2.9	17		
	ZIF-8	TPU/PVDF	60	1752	701	60	0.6 <sup>a, b</sup>	0.5 <sup>b</sup>	17	303	[151]

Wet impregnation/ Coating	HKUST-1	hierarchical porous carbon monolith	56-63	1448	270- 516	64-81	3.98 <sup>b</sup>	2.36- 2.75 <sup>b</sup>	31-41	298	[155]
	Ni-MOF-74 UTSA-16 (Co)	cordierite monolith	48 55	3398 746	652 223	81 70	6.5 <sup>b</sup> 4 <sup>b</sup>	1.7 <sup>b</sup> 1 <sup>b</sup>	74 75		[156]

<sup>a</sup> Value of CO<sub>2</sub> adsorption capacity of powder taken from [126]. <sup>b</sup> Value of CO<sub>2</sub> adsorption capacity measured at 1 bar. <sup>c</sup> Indicate the increase in value instead of reduction.

MOFs shaped via additive manufacturing were reported in studies by Thakkar *et al.* [152] and by Evans *et al.* [151]. In the former study, MOF-74 (Ni) and UTSA-16 (Co) materials were printed respectively using 15 wt% and 10 wt% of bentonite clay as binding agent and DIW as the printing technique. These 3D printed MOFs exhibited reduction in both BET surface area (22-38%) and CO<sub>2</sub> adsorption capacities (17-20%). Meanwhile, Evans *et al.* printed ZIF-8 using the FDM technique and a mixture of TPU/PVDR thermoplastic (60 wt%) as a binding agent. The 3D printed ZIF-8 suffers 60% reduction in BET surface area as well as 17% reduction in CO<sub>2</sub> adsorption capacity at 1 bar. The authors of both studies attributed the high loading amount of binder as the main cause of the observed effects, as the high content of binders further amplifies the risk of pore blockage.

Finally, the *in situ* shaping approach via wet impregnation/coating technique was employed by Qian *et al.* [155], where 37-44 wt% of HKUST-1 was grown on the surface of the hierarchical porous carbon monolith. The synthesized HKUST-1 monolith has lower BET surface area (64-81%) than powder HKUST-1, as well as lower CO<sub>2</sub> adsorption capacity (31-41%), as MOF active material only grown on the surface of support material. Similar pattern of reduced BET surface area and CO<sub>2</sub> adsorption capacity using wet impregnation/coating technique was also observed in the study by Rezaei *et al.* [156], where 48 wt% of Ni-MOF-74 and 55 wt% of UTSA-16(Co) was coated on the surface of cordierite monolith. The obtained MOFs monolith display a lower BET surface area (70-81%) and CO<sub>2</sub> adsorption capacity (74-75%) than powder MOFs as almost half of the monolith consist of the support material that does not adsorb well CO<sub>2</sub> and is non porous.

Overall, several key takeaways could be highlighted concerning bibliographical review on the shaping method of MOFs for CO<sub>2</sub> capture application. First, the use of pressure/compression technique for MOFs shaping is advantageous in terms of its simplicity and this shaping technique is able to produce shaped MOFs with good mechanical strength [141]. However, the high pressure exerted during this technique could lead to amorphization of crystals, leading to the decrease in BET surface area as well as CO<sub>2</sub> adsorption capacity. Furthermore, the severity of the impact is dependent on the type of MOFs used, thus, optimization of process parameters is needed for each MOFs. Second, the usage of binding agent for shaping of MOFs is advantageous in terms of yielding strong and hard monoliths under low pressure process (e.g. extrusion, granulation, additive manufacturing) [141]. Despite that, the addition of binder comes with the risk of pore blockage that will inevitably impact the BET surface area and CO<sub>2</sub> adsorption capacity of shaped MOFs, and the severity of this impact depends on the type of binder and its loading amount. Finally, the *in situ* approach of MOF shaping via wet impregnation/coating technique is advantageous as this technique is straightforward and could be applied concurrently during MOF synthesis [141]. However, the limitation of this approach is the support used for the coating, as it must be chemically resistance towards the chemical use for MOF synthesis. Furthermore, the porous nature of the support greatly influences the CO<sub>2</sub> adsorption capacity of shaped MOFs, as more active MOFs crystals could be grown on porous support than non-porous support.



## 2.6. Conclusion

The bibliographical review conducted in this chapter reveals the harm of GHG emission, especially CO<sub>2</sub> emission, into atmosphere as it contributes to climate change and if left unchecked, it would lead to irreversible impacts on natural systems such as the extinction of ~50% of tropical marine species, water scarcity for 4 billion people as well as concurrent heatwaves, droughts and flooding in global scale. One of the strategies to mitigate CO<sub>2</sub> emission is through the use of renewable energy that emits less carbon than fossil fuel. In the context of this study, biogas is the energy source of interest. The main contaminant in the biogas stream is CO<sub>2</sub>, which causes the calorific value of biogas to drop. The elimination of CO<sub>2</sub> from biogas, which is known as biogas upgrading, results in biomethane with a high purity of CH<sub>4</sub> that could be injected into a natural gas grid system.

Multiple biogas upgrading technologies are currently employed in industry such as absorption (chemical and physical), cryogenic distillation, membrane separation and PSA. PSA technology for biogas upgrading, which is the technology of interest in this study, works on the basis of selective adsorption of CO<sub>2</sub> over CH<sub>4</sub> by adsorbent bed. The performance of PSA CO<sub>2</sub>/CH<sub>4</sub> separation in biogas depends on two aspects; the first is the optimization of the PSA cycle configuration for CO<sub>2</sub>/CH<sub>4</sub> separation, where the most conventional configuration is known as Skarstrom cycle; the second aspect is the adsorbent's adsorption capacity and selectivity.

Conventional adsorbents used in PSA for biogas upgrading are zeolites, activated carbon, silica as well as carbon molecular sieve. Recently, a new candidate for adsorbent material for CO<sub>2</sub>/CH<sub>4</sub> separation has emerged, which is the Metal Organic Framework (MOF). MOFs are made up of metal ions linked together to form a porous network material capable of selectively adsorb gas molecules. HKUST-1 is one of the MOF often studied in literature for CO<sub>2</sub> capture, as it has a good CO<sub>2</sub>/CH<sub>4</sub> selectivity and high CO<sub>2</sub> adsorption capacity as well as one of the few MOFs available commercially. However, application of HKUST-1 or MOFs in general as the adsorbent for PSA is limited due to the synthesis of this material is often under powder form, which is not suitable for direct application in the PSA column.

The literature review on MOF shaping technology reveals that MOFs shaping technology can be done either in situ or post-synthesis. In situ shaping of MOFs consist of growing MOFs crystals on the surface of substrate, which is limited by the nature of the substrate and low loading of MOFs active material in the fabricated shaped MOFs. Another MOF shaping approach could be carried out after the synthesis of MOF powder, either using technique where MOF powder is compressed into agglomerate or using binding agent to produce shaped MOF. In this study, the approach of post-synthesis MOFs shaping techniques (extrusion and additive manufacturing), which uses binding agent, was adopted, as the knowledge of binding agent impact on MOF intrinsic properties is always crucial for this field and the shaping process itself is straightforward and does not require any specialized equipment.

This study is based on the potential of shaped HKUST-1 as an effective adsorbent for CO<sub>2</sub>/CH<sub>4</sub> separation using a widely developed PSA technology. The next chapter will discuss further on the methods carried out in this study to shape HKUST-1 as well as the analysis of the shaping impact on HKUST-1 properties.

# CHAPTER 3: Elaboration and Characterization of HKUST-1 composites

## 3.1. Introduction to thermoplastics

Thermoplastic is a type of polymer that becomes pliable or moldable when heated and solidifies upon cooling. Thermoplastics are composed of linear or branched macromolecules bonded by weak interactions forces (Van der Waals or hydrogen bonds) and could be either amorphous or semi crystalline [166] (Figure 3-1).

Thermoplastic present several advantages:

- Multiple cycles of heating and cooling can be repeated without severe damage, allowing reprocessing.
- Short processing time because of the absence of the chemical reaction of crosslinking.
- Processing is easy, because there is only a physical transformation.
- Absence of gases or water vapor if the material is correctly dried before processing.
- The wastes are partially recyclable.

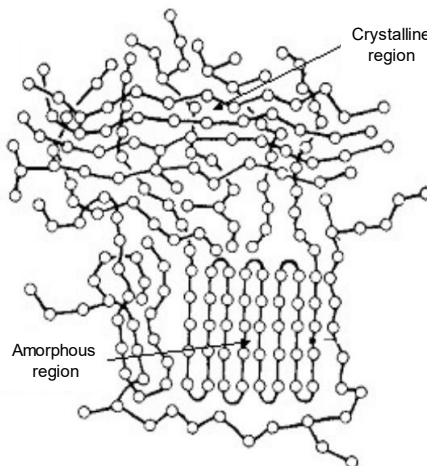


Figure 3-1: Schematic structure of a thermoplastic. Image reproduced from [167]

As the processing of thermoplastic is relatively easy, this makes it as an attractive choice as a binding agent as it will not complexify the shaping process. Today, as there are numerous thermoplastic materials available in the market, a simplified framework that allows the classification of these different thermoplastic materials, as proposed by the company Tangram Technology [168], which utilizes two criteria for the categorization of thermoplastics.

The first criterion to classify different thermoplastics materials is the crystallinity of the polymer. Amorphous polymers (those with no significant degree of crystallization) behave very different to semi-crystalline polymers (those with a significant degree of crystallization) [168], which helps to facilitate the segregation of different thermoplastic

polymers into their own respective category. The general properties of amorphous and crystalline polymers are summarized in Table 3-1:

Table 3-1 Comparison between properties of amorphous and semi-crystalline thermoplastic materials [168].

<b>Amorphous</b>	<b>Semi-crystalline</b>
Wide range of melting temperature	Distinct and sharp melting point
Low specific gravity	High specific gravity
Low tensile strength and tensile modulus	High tensile strength and tensile modulus
High ductility	Low ductility
Low creep resistance	High creep resistance
Usually transparent	Translucent or opaque
Low fatigue resistance	High fatigue resistance
Low chemical resistance	High chemical resistance
Suitable for structural applications	Suitable for structural applications

Another criterion that facilitates the distinction of different thermoplastic materials is to divide them into the relatively arbitrary grouping (e.g. ‘Commodity’ polymer, ‘Engineering’ polymer and ‘High-performance’ polymer), which takes into account the thermoplastic material’s performance and cost [168]. The performance considered is related to the mechanical and thermal properties of the material, whereas the cost is based on the worldwide production volume of the material, a large production volume signifying a cheaper cost of the material.

‘Commodity’ thermoplastics have the lowest performance among other two categories, though this does not necessarily signify that the thermoplastic materials in this group are not suitable for any particular application. Furthermore, thermoplastics in this category are generally cheaper as these bulk polymers make up the majority of the worldwide production volume of thermoplastics. Next, ‘Engineering’ thermoplastics have enhanced properties and are used for applications where the requirements for mechanical or thermal properties are stringent. These ‘Engineering’ thermoplastics are generally more expensive than ‘Commodity’ thermoplastics, and are also produced in less volume than the latter. Lastly, ‘High-performance’ thermoplastics have the highest performances in terms of mechanical and physical properties and are used in the most demanding applications. Due to this, they are generally very expensive and their worldwide production volume is the lowest among all three categories.

These two simple criteria (crystallinity and performance) allow the classification of most of the thermoplastic families as shown in Figure 3-2. A simple classification table, which is also dubbed as ‘*Periodic Table of Thermoplastics*’, has been created by Tangram Technology [168] as an attempt to provide a simple codification of the different thermoplastic types and structures. The first group of the classification table (amorphous polymers – commodity thermoplastics) includes several common thermoplastic families, such as vinyl chloride (PVC), styrene (PS) and cellulose (CA, CAB, CAP) [168]. These families of thermoplastics are inexpensive, easy to process and

exhibit a good moisture stability. However, their mechanical and thermal stability is relatively low. These thermoplastics are suitable to be used as packaging materials, piping materials, as well as cable insulation materials.

Next, the second group of the classification table (amorphous polymers – engineering thermoplastics) consists of thermoplastics families such as acrylics (PMMA) and polycarbonate (PC) [168]. These thermoplastics exhibit a moderate mechanical strength but low chemical resistance. Examples of application of these materials are optical lenses and headlamp sets, safety helmets and CD's.

Polysulphones/polysulphides (PES/PPS) and imides (PI) are among the thermoplastic families that could be classified in the third group [168]. They exhibit high mechanical and thermal resistance properties, as well as good resistance to chemical degradation. These thermoplastics are suitable to be used as components in chemical pumps, electric connectors, semiconductor wafer clamps, TV and automotive.

An example of thermoplastics family in the fourth group of the classification table (Semi-Crystalline polymers – commodity thermoplastics) is Polyolefins (PE, PP) [168]. This type of thermoplastics exhibits a good chemical and thermal resistance but its mechanical strength is moderate. Kitchen ware, food wrapping materials, toys and medical syringes are some of the examples for the application of this type of thermoplastics.

The fifth group (Semi-Crystalline polymers – engineering thermoplastics) includes thermoplastics families such as polyesters (PET) and polyamides (PA) [168]. These thermoplastics are tough and rigid with moderate chemical and thermal resistances. They are suitable to be used as kitchen utensils materials, drink bottles, gear wheels, as well as clothing fabrics.

Finally, an example of thermoplastics family in the sixth group (Semi-Crystalline polymers – high performance thermoplastics) is fluoropolymers (PTFE, FEP, PFA, CTFE, ECTFE, ETFE) [168]. This type of thermoplastics exhibits excellent chemical and thermal resistances, as well as excellent mechanical strength. Non-stick coatings, high and low temperature electrical and medical products, as well as other applications needing excellent dielectric strength, chemical, and temperature resistance are some of the examples for the application of this type of thermoplastics.

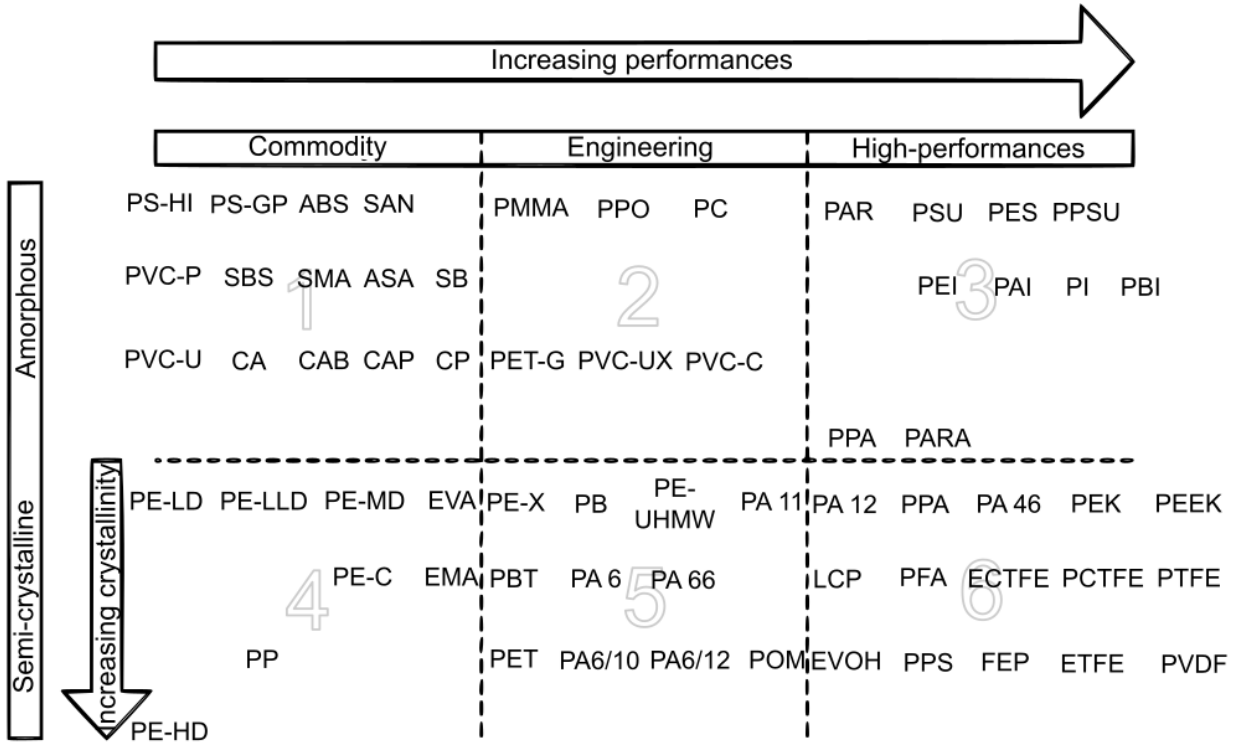


Figure 3-2: Periodic Table of Thermoplastics created by Tangram Technology [168].

This classification table, though it may seem vague and not well accurate, provides a general idea on what type of thermoplastic would be suitable to be chosen as binding agent in this work. For our application, the binding agent must have a strong mechanical strength so that the MOF/thermoplastic composite produced from the shaping process could retain its form when used inside an adsorption column. Furthermore, the chosen binder must also have a high thermal stability as to avoid its degradation during the exothermic adsorption process that usually results in local temperature increases in the adsorbent bed. Additionally, the cost of the thermoplastic to be chosen must be sufficiently low. Based on these criteria, the thermoplastic to be chosen in this work as the binding agent should belong to the 2<sup>nd</sup> or 5<sup>th</sup> group of the classification table.

### 3.2. Choice of the binder

In this work, two thermoplastics were chosen as the binding agent for the shaping of HKUST-1 powder: polylactic acid (PLA) and thermoplastic polyurethane (TPU), which can be categorized in 5<sup>th</sup> and 3<sup>rd</sup> group respectively [168] [169]. PLA belongs to the family of aliphatic polyesters which are considered biodegradable and compostable materials [170]. PLA can be either semi-crystalline or amorphous, depending on the synthesis process of the polymer [170]. Meanwhile, TPU belongs to the thermoplastic elastomers (TPE) family and can be considered as an amorphous polymer [171]. The general properties of these two thermoplastics are compared in Table 3-2.

Table 3-2: General properties of PLA and TPU

	PLA	TPU	Ref.

Tensile strength (MPa)	35.5-54.1	4.5-7.3	
Young modulus (MPa)	1476-1516	7-9	[172]
Elongation at break (%)	3.3-5.3	487.9-773.9	
Degradation temperature (K)	623	626-672	[173]

As PLA could be considered as a semi-crystalline thermoplastic, it possesses a higher tensile strength and tensile modulus than TPU that can be considered as amorphous. Conversely, TPU exhibits a rubbery property, with a higher elongation at break value in comparison to PLA. The degradation temperature of both thermoplastics is comparable, although the degradation temperature of PLA is fixed while it is set in a wider range for TPU.

A short description on the synthesis process of both PLA and TPU thermoplastics is presented below:

a) PLA

PLA was first discovered in the early 1800s by the French chemist Theophile-Jules Pelouze who produced low-molecular-weight PLA through the poly-condensation of lactic acid followed by a century later when Wallace Carothers synthesized PLA by heating lactide in vacuum [174]. The utilization of PLA is favored because it can be massively produced from agricultural source (lactic acid), avoiding the use of petrochemicals. PLA is synthesized through two well-known processes (Figure 3-3): direct polycondensation (DP) and ring-opening polymerization (ROP). It should be noted that polylactic acid and polylactide are the same substances, the difference in names is just an indication on which route has been taken to produce them.

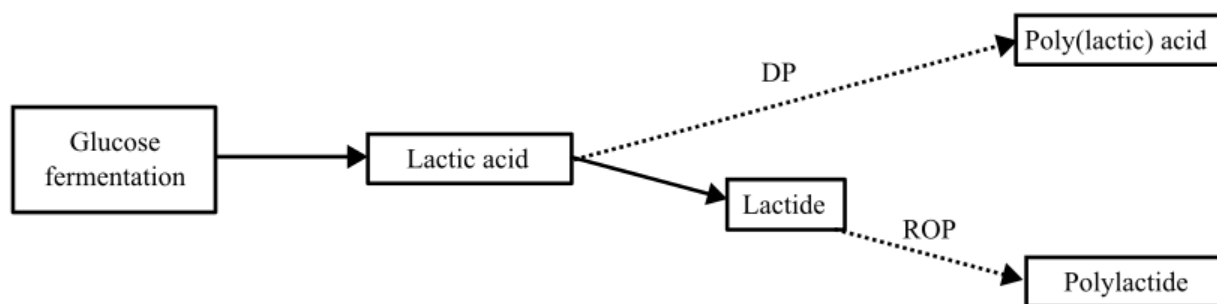


Figure 3-3: General routes of PLA production

Lactic acid, which is chemically known as 2-hydroxy-propionic acid, is the basic building block for the production of PLA. Most of the lactic acid produced globally is made using the fermentation process of carbohydrate. The sources can come from different types of starch and cellulosic materials, such as wheat and rice bran, corn cob, barley, wheat starch and corn starch [175]. Lactic acid produced from glucose fermentation can undergo DP process to produce PLA, but this process requires the usage of coupling agents. The purpose of the coupling agents is to increase the molecular weight of the lactic acid prepolymer ( $M_w = 1000-5000$  g/mol) which affects the mechanical properties of the subsequent PLA product [175]. Conversely, the usage of coupling agents is not required for the production of PLA via the ROP process, as the lactic acid prepolymer is transformed into an intermediate substance called lactide. The

anionic or cationic ring polymerization of lactide yields to the formation of polylactide (PLA). The ROP process remains the most widely used production method as this process has a higher yield and low toxicity impact [174].

PLA can easily be dissolved in chloroform, methylene chloride, dioxane, acetonitrile, 1,1,2-trichloroethane and dichloroacetic acid [175]. Additionally, PLA can also be dissolved in toluene, acetone, ethyl benzene and tetrahydrofuran when heated to boiling temperatures [175]. Generally, PLA is insoluble in water, alcohol and alkanes [175].

#### b) TPU

Polyurethanes (PUs) were first discovered by Bayer and coworkers in 1937, whereas thermoplastic polyurethanes (TPUs) were developed in the 1950s as a new type of PU, in Germany by Bayer-Fabfabriken and in the United States by B.F. Goodrich [176]. TPUs attract significant interest because they possess interesting properties, such as high flexibility, good mechanical strength and abrasion resistance, and transparency. TPUs are synthesized via the reaction of a polyol with a diisocyanate. Figure 3-4 illustrates the molecular morphology of TPUs, which generally consists of linear soft segments, SSs, and linear hard segments, HSs [176]. The HSs mainly consist of a rigid diisocyanate moieties and a chain extender moieties, whereas the SSs are typically made of long polyol chains (polyether, polyester, and polycarbonate). The diisocyanate component function in TPUs is twofold. First, it acts as a coupling agent between SSs–HSs–chain extender, whereas the second function of the diisocyanate is its structural contribution to TPU physical properties [177]. Meanwhile, the polyol components enable the formation of long, strong, linear TPU chains which make up the bulk of the derived TPUs (50-80 wt%) [177]. Therefore, the type of polyol components used for the synthesis of TPU exerts a considerable influence on the material's physical and chemical properties. Lastly, the chain-extender component, usually a glycol, has about the same size as the diisocyanate component. The main function of the chain-extender component is to react with some diisocyanate to produce urethane-rich hard segments that comprise regions of strong hydrogen bonding in the TPU polymer chains [177].

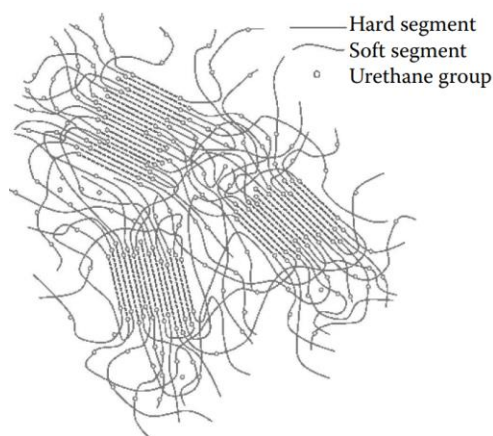


Figure 3-4: Illustration of structural morphology of TPU. Image reproduced from [176].

TPUs are typically synthesized either by one shot (OS) or two-shot (TS) process (Figure 3-5). In the OS method, the reaction components (polyols, isocyanates, and chain extenders) are simultaneously mixed and poured into a mold where the crosslinking reaction occurs. In order to increase the hardness and modulus of a TPU, it is possible to increase the quantity of isocyanates and chain extender, which will produce more longer hard segments [178]. The OS method yields to a narrower distribution of hard-segment lengths compared to the TS method. Meanwhile, the TS method, which is also known as “prepolymer method”, consists of two steps. The first step involves the preparation of prepolymer by reacting diisocyanate and long-chain diol to produce isocyanate-terminated linear chains (prepolymer). The second step involves the reaction of the prepolymer with chain extender, which is usually a short organic diol [178], to produce a high-molecular-weight TPU. The two-step synthesis procedure leads to high molecular weight transformable polymers ( $M_w = 100,000 \text{ g/mol}$ ) [178].

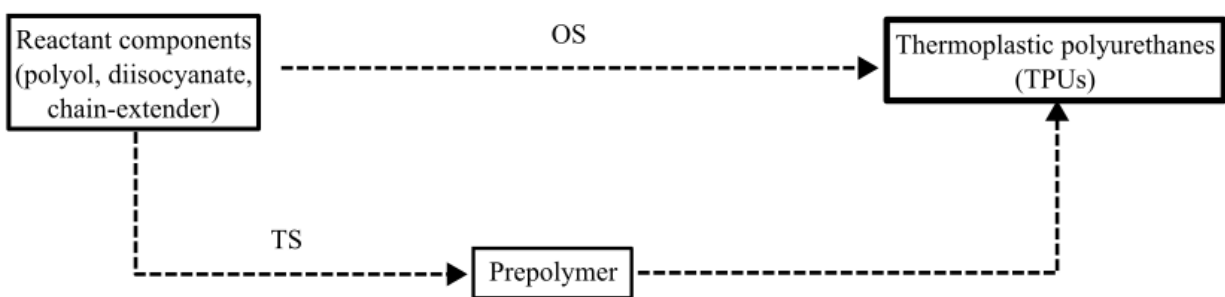


Figure 3-5: General routes of TPU production

It is difficult to generalize the solubility properties of TPUs in a chemical solution as they depend on the type of polyol (polyether, polyester and polycarbonate) used for their synthesis. Despite that, dipolar aprotic solvents such as Dimethylformamide (DMF), N-Methyl-2-pyrrolidone (NMP) or Dimethyl sulfoxide (DMSO) are usually able to dissolve TPUs [178].

### 3.3. Synthesis of HKUST-1 composites

#### 3.3.1. Materials

HKUST-1, also commercially known as Basolite@C300 (Basolite is a trademark of BASF SE), was supplied by Sigma Aldrich. The specific surface area, as specified by the supplier, was in the range of 1500–2100  $\text{m}^2/\text{g}$  and the bulk density was 0.35  $\text{g}/\text{cm}^3$ . The sieving conducted on 1g of HKUST-1 powder at 80 Hz for 20 mins reveals that the particles have a diameter less than 100  $\mu\text{m}$ . The binding agents used in this study were obtained from commercial PLA and TPU products, purchased respectively from JADI LIFE SOLUTIONS (Malaysia) and FormFutura (Netherlands). The melting temperature of the PLA and TPU is respectively in the temperature range of 473–503 K and 493–523 K, according to the suppliers. The powder materials were used as it is for the subsequent shaping process.



### 3.3.2. Shaping process of HKUST-1 by extrusion

Figure 3-6 illustrates the protocol developed for the HKUST-1 powder shaping process in this study, using either PLA or TPU as a binder. Briefly, the homogenous mixing of HKUST-1 with PLA or TPU was achieved by dissolving the binding agent in 1 ml of their respective solvent (chloroform for PLA and DMF for TPU) using a VWR Symphony ultrasonic bath at 328 K for 1 hour. Prior to their dissolution, the polymers were heated at 383 K to eliminate any possible water traces. Next, after addition of HKUST-1 powder, the solution was sonicated for another 30 mins in order to obtain a homogenous mixture of MOF/thermoplastic. The HKUST-1/thermoplastic suspension was then inserted into a 5mL DB syringe, followed by its extrusion to obtain HKUST-1 extrudates. At last, the synthesized extrudate were washed with methanol and subsequently heated overnight at 383 K under vacuum to remove the leftover solvent. The dried composites were then cut into small cylinders of about 1-2 mm in length.

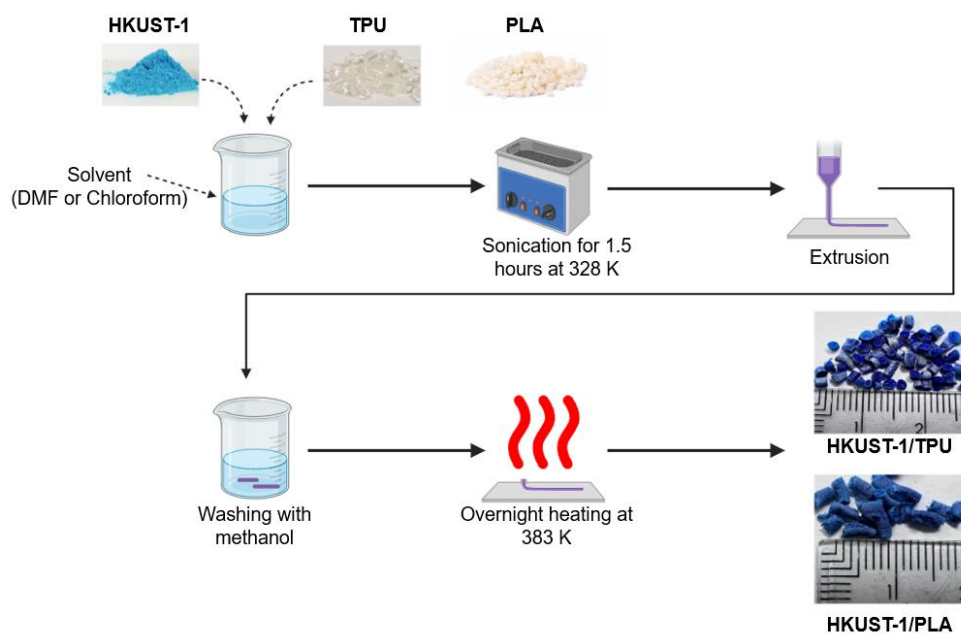


Figure 3-6: Schematic figure of the shaping process for HKUST-1/polymer composite by extrusion

The loading amount of PLA and HKUST-1 used for the synthesis of HKUST-1 extrudates in this study is available in Table 3-3. The PLA content was varied between 5 and 20 wt% during the synthesis of HKUST-1 extrudate, with the objective of finding the minimal binder loading required to elaborate an extrudate that able to retain its form after shaping. The criterion to judge whether an extrudate was able to retain its form was rather qualitative, that is, once the extrudate was dried, it was pickup by hand and rolled over the palm of the hand for several seconds. Any extrudate that shows sign of disintegration or deformation was then deemed as failure. The results obtained showed that a minimum of 10 wt% of PLA loading is needed to obtain a HKUST-1 composite capable to retain its shape after shaping. Therefore, in this work, this 10 wt% of binder loading has been chosen as the standard for the synthesis of HKUST-1 composites. The extrudates containing 10 wt% of PLA and TPU are denoted as **HKUST-1/PLA** and **HKUST-1/TPU**, respectively, and they were subsequently characterized in this work.

Table 3-3: Variation of PLA loading for the synthesis of HKUST-1 extrudate

<b>HKUST-1 mass (g)</b>	<b>PLA mass (g)</b>	<b>Binder loading (wt%)</b>	<b>Observation</b>
0.95	0.05	5	Non-extrudable paste obtained
0.90	0.10	10	Extrudate retained solid form
0.80	0.20	20	Extrudate retained solid form

### 3.3.3. Shaping of HKUST-1 by additive manufacturing

PLA and TPU are often used in additive manufacturing to elaborate 3D-printed shapes, owing to their relatively low melting temperature (PLA = 473–503 K and TPU = 493–523 K) and ability to solidify without alteration of their mechanical properties. Therefore, the shaping of HKUST-1 by additive manufacturing has also been tested in this study by using PLA and TPU. Fused Deposition Modeling (FDM) and Fused Granulate Fabrication (FGF) technologies were tested in this work. Note that only one type of thermoplastic was considered for each 3D printing strategy, due to the limited amount of HKUST-1 available. The first attempt to shape HKUST-1 powder (Basolite C300) via additive manufacturing was done using PLA as the thermoplastic material and FDM as the method. FDM is an extrusion-based additive manufacturing technology that uses the build input material in the form of thermoplastic filament. The filament is melted in the heating head and then extruded through the nozzle with consecutive re-solidification upon cooling in order to form the desired shape. The second attempt for shaping HKUST-1 via additive manufacturing was done by using Fused Granulate Fabrication (FGF) and TPU as the thermoplastic material. By analogy with FDM, FGF is also an extrusion-based additive manufacturing technology with the only difference that composite is charged in the heating head in form of the granulate/pellet. It should be noted that HKUST-1 shaping using FGF technology is in the early stage of development at the time of the manuscript writing and thus no qualitative or quantitative data related to the sample properties have been yet produced for this production route.

The detailed methodologies applied for HKUST-1 shaping via FDM and FGF technologies are described below:

#### a) HKSUT-1 shaping method by FDM

Figure 3-7 illustrates the protocol for the shaping process of HKUST-1 via FDM technology developed for this work. The shaping process includes three main steps: solvent casting, filament preparation and filament extrusion. The first step consists of dissolving PLA in a solvent (chloroform) using VWR Symphony ultrasonic bath at 328 K for 1 hour, followed by the addition of HKUST-1 to the solution and further sonication for another 30 minutes to ensure homogenous mixing. The mixture suspension is then cast onto a glass petri dish and left to dry overnight at 338 K to produce a film. The second step involves the fabrication of filament from the said film. The film was cut into small squares (0.1cm x 0.1cm) and inserted into a Wellzoom (China) desktop filament extruder (tip 1.75 mm) operating at 473 K. Finally, the obtained filament was inserted into a 3D pen (3DPEN-2) and extruded/printed layer by layer at a temperature of 473 K into a square shape composite with a dimension of 1cm x 1cm.

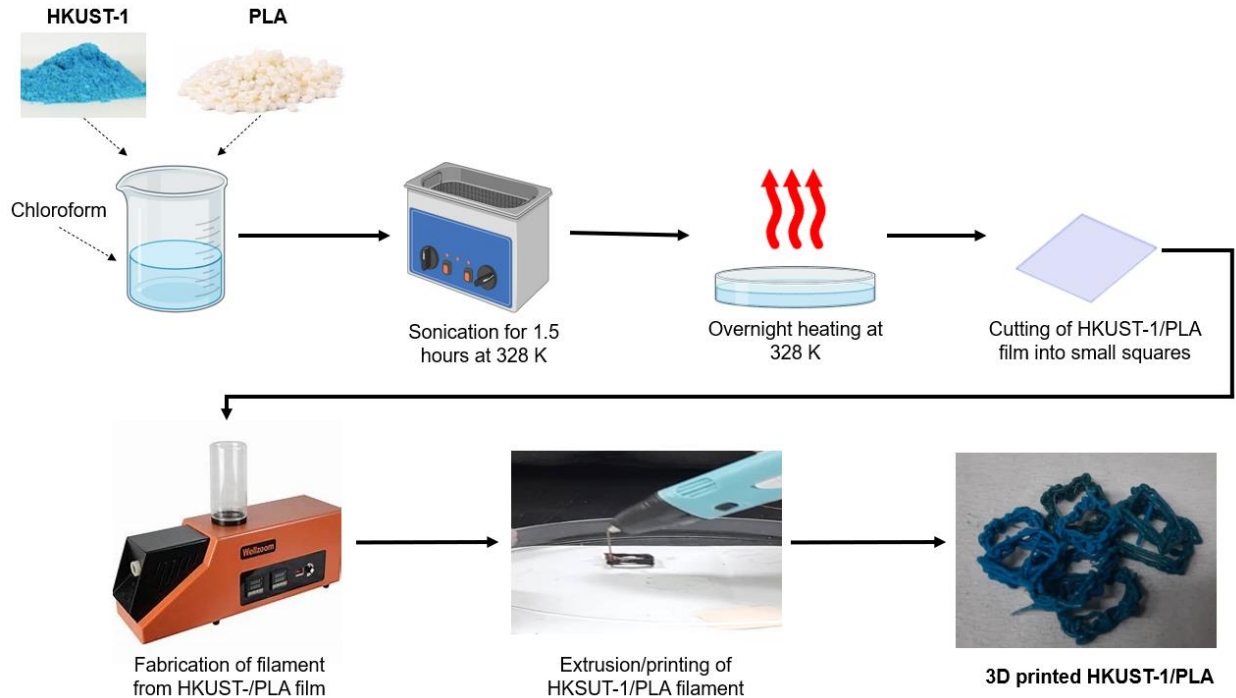


Figure 3-7 : Schematic figure for the shaping process of 3D printed HKUST-1/PLA by FDM.

Table 3-4 summarizes different PLA loadings that were tested for the fabrication of filaments and 3D printed composites. The filament used as input material for the 3D printed composite must possess sufficient strength so that it does not break during the printing step. The results obtained demonstrate that the minimal PLA loading of 70 wt% was needed to fabricate a 3D printed composite having a sufficient mechanical strength. This 3D printed composite with 70 wt% of PLA loading is henceforth denoted as **3D printed HKUST-1/PLA** and was subsequently characterized in this work.

Table 3-4: Variation of PLA loading for the fabrication of the filament and 3D printed composite

HKUST-1 mass (g)	PLA mass (g)	PLA loading (wt%)	Observation
1.5	1.5	50	Unable to produce filament/unable to print
1.2	1.8	60	Filament is fragile/3D printed object is fragile
0.9	2.1	70	Strong filament obtained/3D printed object retained solid form

b) HKSUT-1 shaping method by Fused Granulate Fabrication (FGF)

The process of HKUST-1 shaping by FGF technology is relatively straightforward in comparison to FDM. The input material employed for FGF is the HKUST-1/TPU extrudate (section 3.3.2, page 70) with a low TPU content, in order to minimize the degradation of MOF gas adsorption performances resulting from the presence of a binder. The choice of TPU is motivated by its high flexibility in comparison to PLA, thus facilitating the 3D printing process. Figure 3-8-a shows the 3D printer operating FGF technology that was used at the technical platform Compositic (France). It contains three main parts: motor, feed port and printer head. The motor controls the displacement of the moving parts (printing head and support) with respect to X, Y and Z axes during 3D printing. The HKUST-1/TPU extrudate is loaded into the feed port, which able to accommodate up to 50 cm<sup>3</sup> of the input material at a time. A rotating screw pushes the extrudate through a barrel towards the printer head, where the melting of thermoplastic takes place (493–523 K in case of TPU), followed by composite extrusion through the nozzle. After re-solidification, the designed 3D shape can be obtained. (Figure 3-8-b).

As previously mentioned, the shaping of HKUST-1 by FGF technology is still in the early stage of development, therefore there is yet any sample of 3D printed HKUST-1/TPU that was successfully obtained and characterized by quantitative analysis. Table 3-5 summarizes several attempts of the fabrication of 3D printed HKUST-1/TPU. The most recurrent problem occurring during the printing tests was the blockage of the printing nozzle (diameter = 1.4 mm), which could be attributed to the low amount of TPU in the molten plastic, contributing to a high viscosity. The most encouraging result obtained so far was the printing of HKUST-1/TPU with a thermoplastic binder loading of 40 % in mass (Figure 3-8-b). The extrusion through the printer nozzle was successful for this particular loading but problems could still be observed during the continuous printing process, where layers of the 3D printed HKUST-1/TPU parts did not adhere well to each other during the re-solidification. To solve this issue, further optimization of the 3D printing parameters (e.g. extrusion speed/deposit speed ratio, printing temperature, height of printer head, layer width) is being developed by the technical platform Compositic.

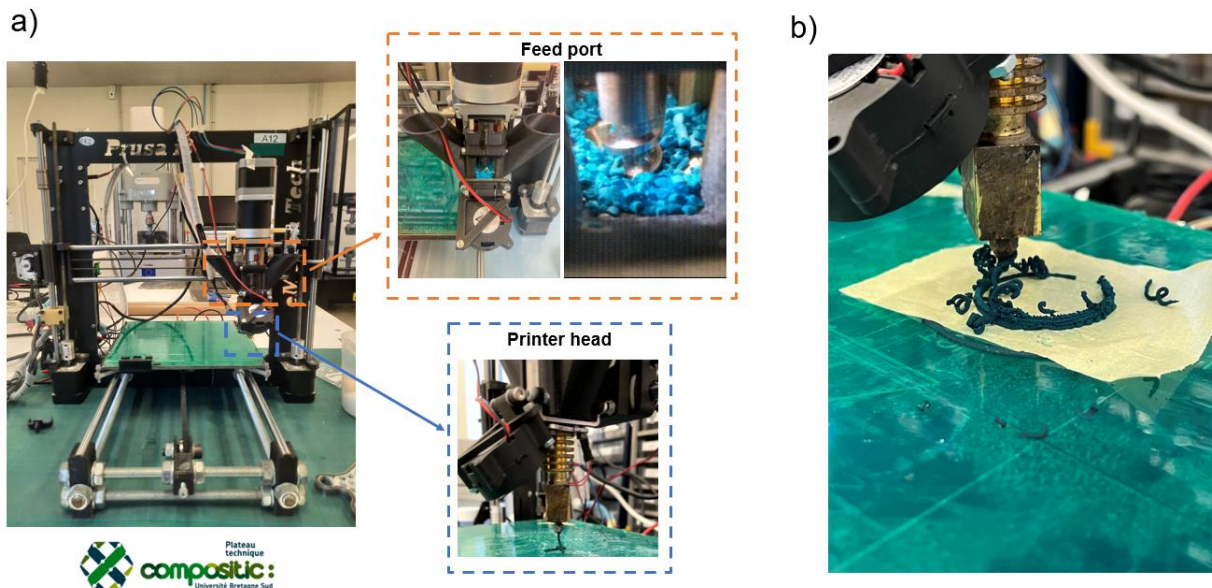


Figure 3-8: (a) FGF 3D printer used for the fabrication of 3D printed HKUST-1/TPU. (b) Printing of HKUST-1/TPU

Table 3-5: Summary of HKUST-1/TPU printing tests

Test	TPU loading (%)	Observation
1	10	
2	20	Obstruction in the nozzle during printing
3	25	
4	30	
5	35	
6	40	Extrusion of the material through printing nozzle was observed

### 3.4. Characterization methods

Apart from HKUST-1 powder (Basolite C300), three samples of HKUST-1 composites were subsequently characterized in this work, which are: HKUST-1/PLA, HKUST-1/TPU and 3D printed HKUST-1/PLA. The first two of the samples were synthesized from extrusion whereas the last sample was synthesized from additive manufacturing FDM method. In this section, the methods employed for the characterization of these materials are described.

#### 3.4.1. X-ray diffraction (XRD) analysis

The crystalline structure of the synthesized samples was analyzed using powder X-ray diffraction (PXRD). The patterns were recorded by using a Bruker AXS-D8 Advance Diffractometer (Massachusetts, U.S.) equipped with a copper anode ( $\lambda = 1.5406 \text{ \AA}$ ). Data were collected in the  $2\theta$  range from  $5$  to  $50^\circ$  with a step of  $0.02^\circ$  and a scan speed of  $1^\circ/\text{min}$ .

#### 3.4.2. Fourier transform infrared spectroscopy (FTIR) analysis

To perform local characterization of chemical bonds in composite materials, Fourier-transform infrared spectroscopy (FTIR) was employed. The spectra were acquired on Thermo Nicolet IS5 Spectrometer (Massachusetts, U.S.) in the Attenuated Total Reflection mode, allowing direct measurement of powder samples within 15 runs (scans) in a wavenumber range of  $5000\text{--}400 \text{ cm}^{-1}$ . Measurements were performed under ambient air on freshly outgassed samples (heated at  $383 \text{ K}$  under dynamic secondary vacuum for 24h). For every sample, the background scanning was performed to subtract signals of air impurities and specimen holder.

#### 3.4.3. Scanning electron microscopy (SEM) analysis

The morphology of the samples was observed from scanning electron microscopy (SEM) images acquired on JSM 7600F from JEOL (Japan) equipped with both backscattered electron (BSE) and secondary electron (SE) detectors. The samples were prepared using a standard specimen preparation technique, where the cast sample was deposited onto a conductive carbon double-sided adhesive tape on a stub. Coating of the sample was performed with a platinum sputter coater for 60 s. The sample was placed in a vacuum chamber before the imaging was done. Energy dispersive X-ray spectroscopy (EDXS) analysis was carried out to access the concentration distribution of different elements on the sample surfaces.

#### 3.4.4. Thermogravimetric analysis (TGA)

Thermogravimetric measurements were performed on a Setaram LabSys evo TGA-DTA instrument (Caluire, France). 5 mg of samples were heated in a platinum crucible from ambient temperature up to 800 °C with temperature ramp of 10 °C/min under flow of N<sub>2</sub> (20 ml/l) to homogenize heat transfer, protect the balance and avoid sample oxidation. In order to account for mass variation induced by factors other than sample weight loss, the TGA curve measured for an empty crucible was systematically subtracted from that of the sample.

#### 3.4.5. Attrition test analysis

The mechanical resistance of shaped MOFs against the frictional forces experienced in fluidized or packed beds, transportation, handling, and storage could be evaluated through the attrition test standard D4058–96 ASTM norm. In this work, a standard test similar to that employed by Khabzina et al. [179] was applied. Briefly, 0.2 g mass of material was introduced into a glass vial and was rolled at a frequency of 60 rotations per minute (rpm) for 30 min. Afterwards, the sample was passed through a 500 µm sieve to recover fine particles. Attrition percentage is calculated as follows:

$$\text{Attrition} = \frac{\text{initial mass} - \text{recovered mass above } 500 \text{ } \mu\text{m}}{\text{initial mass}} \times 100 \quad \text{Eq. 3-1}$$

#### 3.4.6. N<sub>2</sub>/CO<sub>2</sub> adsorption/desorption isotherm analysis

Textural properties of the materials were characterized by using N<sub>2</sub> adsorption/desorption isotherms at 77 K. The total porous volume was calculated from experimental N<sub>2</sub> adsorption data at p/p<sub>0</sub> = 0.98, whereas micropore volume was determined by applying the t-plot (Harkins-Jura) method on N<sub>2</sub> adsorption data. The isotherms were obtained using 3Flex manometric adsorption analyzer from Micromeritics (Unterschleißheim, Germany). The instrument is equipped with pressure transducers, allowing measurements in the domain of relative pressure (p/p<sub>0</sub>) ranging between 10<sup>-7</sup> and 1 with 0.15% precision of absolute pressure reading. The acquisition was performed in a fixed-dose mode until p/p<sub>0</sub> = 0.03 and then incrementing relative pressure. The aliquot was adjusted between 1.3 and 2 mmol N<sub>2</sub>/g. To reach the equilibrium conditions, the equilibration time for each isotherm point after aliquot injection was adjusted until pressure stabilization, but not exceeding 1h/point. Samples were degassed at 383 K under vacuum for at least 72 h using Smart VacPrep from Micromeritics. The volumes of cell non-occupied by sample were determined at ambient temperature and at 77 K by helium expansion. The apparent specific surface area was determined based on the linearized BET isotherm as follows [180]:

$$\frac{p/p_0}{q(1-p/p_0)} = \frac{1}{q_M C_{\text{BET}}} + \frac{C_{\text{BET}} - 1}{q_M C_{\text{BET}}} (p/p_0) \quad \text{Eq. 3-2}$$

where q is the specific amount adsorbed at the relative pressure p/p<sub>0</sub>, C<sub>BET</sub> is the constant parameter and q<sub>M</sub> is the specific monolayer capacity.

The pressure range considered for the BET calculations was adjusted in the domain between 10<sup>-7</sup> ≤ p/p<sub>0</sub> ≤ 10<sup>-2</sup> in the way to respect the four consistency criteria suggested by Rouquerol et al. [180]:

- the quantity  $C_{\text{BET}}$  should be positive (i.e., a negative intercept on the ordinate of the BET plot is the first indication that one is outside the appropriate range).
- application of the BET equation should be restricted to the range where the term  $q(1 - p/p_0)$  continuously increases with  $p/p_0$ .
- the  $p/p_0$  value corresponding to  $q_m$  should be within the selected BET range

The CO<sub>2</sub> adsorption isotherms at pressure less than 1 bar were measured using the 3Flex manometric adsorption analyzer from Micromeritics (Unterschleißheim, Germany) at IMT Atlantique. Ultrahigh purity CO<sub>2</sub> gas (>99.995 vol%) supplied by Air Liquide were used for this study. The instrument is capable of measuring equilibrium data in the domain of relative pressure  $P/P_0$  ( $P$  is the gas probe set pressure and  $P^0$  is the saturation pressure) ranging between  $10^{-7}$  and 1 bar with 0.15% precision of absolute pressure reading. The acquisition was performed in a fixed-dose mode, whereas the temperature of the materials in the sample cells was controlled by a water bath contained in a Dewar vessel, set to 298 K. Prior to measurements of gas equilibrium data, a mass of adsorbent of about 100 to 200 mg was placed in each sample cell and further outgassed under dynamic vacuum condition, at 383 K and for at least 12h. The dead volumes corresponding to the volumes non-occupied by the solid phase were determined from helium expansion measurements carried out at ambient and sample cell temperature, respectively.

#### 3.4.7. Water contact angle measurement

The water contact angle can be used as an indicator of a surface wettability. It is known that  $\theta < 90^\circ$  signifies that the sample is hydrophilic, if  $90^\circ < \theta < 120^\circ$ , the sample is hydrophobic and if  $\theta > 120^\circ$  the sample is super-hydrophobic. Water contact angle was measured using the sessile droplet method. A distilled water droplet was deposited from a syringe on the surface of the samples. An image of the water droplet was immediately taken by a high-speed digital microscope camera (Amscope MU1000), and the contact angle,  $\theta$ , between the droplet and the surface of the samples was determined using the ImageJ software with LB-ADSA plugin that uses Young-Laplace equation for the fitting of the droplet profile [181, 182]. Each test was repeated five times, and the reported results were the average of these five measurements.

#### 3.4.8. H<sub>2</sub>O adsorption isotherm and ageing under humid atmosphere analysis

The measurement of H<sub>2</sub>O adsorption isotherms was done using Micromeritics 3Flex manometric analyzer by analogy with N<sub>2</sub> physisorption. The experimental isotherm data were collected at 298 K from 0 to 2.1 kPa, which correspond to relative humidity (RH) of 0-60% at this temperature. Prior to each measurement, samples were degassed under dynamic vacuum at 393 K for 12 h, and the sample holder dead volume was measured using helium expansion.

Ageing of the samples under the effect of moisture was performed by exposing materials to the ambient air at 298 K in a room with controlled relative humidity (RH) of  $40 \pm 5\%$  for the duration up to 3 months. The stored samples were then characterized by measurements of N<sub>2</sub> and CO<sub>2</sub> adsorption isotherms at 77 and 298 K respectively up to 1 bar.

### 3.5. Results

#### 3.5.1. Materials structure verification

##### a) HKUST-1 composites synthesized from extrusion

The structural and composition analysis of the samples was performed by powder XRD. Figure 3-9 illustrates XRD peaks observed for HKUST-1/TPU, HKUST-1/PLA, pristine HKUST-1, TPU as well as PLA. Neat PLA exhibits strong characteristic peak at  $16.8^\circ$  due to diffraction from (110) and/or (200) planes. The less intense peaks at  $14.7^\circ$ ,  $19.1^\circ$  and  $22.4^\circ$  correspond to (010), (203), and (105) planes respectively [183, 184]. Meanwhile, pure TPU exhibits a characteristic broad peak around  $20^\circ$  due to the diffraction from (110) planes of the TPU soft segments [185, 186], subjected to a high degree of disorder. The XRD profiles for both neat PLA and TPU used in this work, suggest that the former is semi-crystalline whereas the latter is amorphous. HKUST-1 powder exhibits XRD peaks at  $6.7^\circ$ ,  $9.5^\circ$ ,  $11.6^\circ$  and  $13.4^\circ$  that can be assigned to the (200), (220), (222) and (400) crystal planes of HKUST-1 [187, 188].

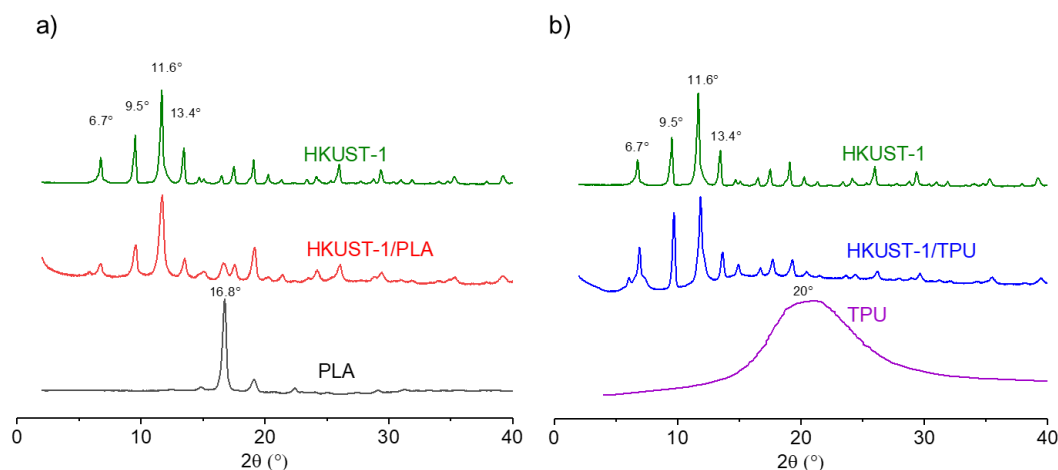


Figure 3-9: (a) XRD of HKUST-1, HKUST-1/PLA and PLA. (b) XRD of HKUST-1, HKUST-1/TPU and TPU.

The structural analysis of the HKUST-1/PLA system shows that HKUST-1 characteristic peaks are also present in the composite. In addition to that, characteristic diffraction peaks corresponding to the neat PLA can also be observed in the composite, specifically at  $16.8^\circ$ . At this position, the doublet peaks can be observed for pristine HKUST-1, where the intensity of the first peak of the doublet is smaller than the second. Interestingly, the intensity of the first and second peaks of this doublet becomes similar in the case of HKUST-1/PLA, which can be related to the main signal coming from PLA. Meanwhile, characteristic peaks associated with pristine HKUST-1 are also present in the XRD pattern of HKUST-1/TPU system. However, the presence of TPU is not easily distinguishable in HKUST-1/TPU composite, which is not surprising considering that TPU known as an amorphous polymer [171, 189, 190] thus the presence of its characteristic broaden peak is somewhat difficult to be identified in the XRD analysis signature of that composite.



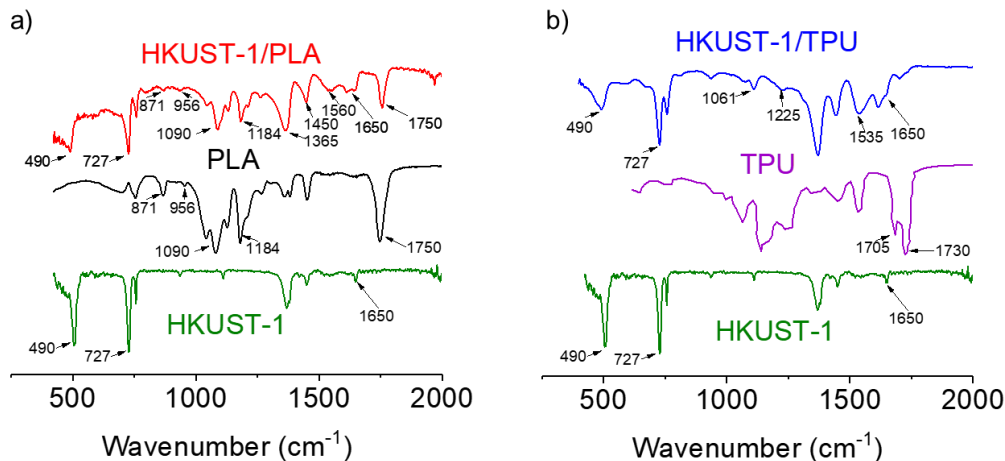


Figure 3-10: (a) FTIR of HKUST-1, neat PLA and HKUST-1/PLA extrudate. (b) FTIR of HKUST-1, neat TPU and HKUST-1/TPU extrudate

Analysis of FTIR spectra enables to further analyze the composition of the HKUST-1/thermoplastic composites. Figure 3-10-a shows the FTIR spectra of HKUST-1/PLA extrudate, pristine HKUST-1 and PLA. PLA is made up of lactic acid, which is rich in carbon chain containing C=O groups. The band at 1750 cm<sup>-1</sup> can be assigned to the presence of carbonyl groups for both the PLA and the extrudate samples. In addition, both HKUST-1/PLA extrudate and PLA spectra exhibit peaks at 1184 cm<sup>-1</sup> and 1090 cm<sup>-1</sup>, originating from the symmetric and antisymmetric stretching vibrations of C-O groups. Next, peaks with small intensity at 956 cm<sup>-1</sup> and 871 cm<sup>-1</sup>, observable in FTIR spectra for both materials, correspond respectively to the in plane bending vibrations (rocking vibration) of CH<sub>3</sub> and vibration of (C-COO) groups [191]. Furthermore, HKUST-1/PLA spectrum also exhibits bands similar to the ones observed for pristine HKUST-1. Both spectra of HKUST-1 powder and HKUST-1/PLA extrudate exhibit characteristic asymmetric vibrations of carboxylate groups at 1500-1700 cm<sup>-1</sup> and symmetric vibrations at 1300-1500 cm<sup>-1</sup> [113]. The peak at 1650 cm<sup>-1</sup> is assigned to the C=O stretching vibration of deprotonated benzene tricarboxylic acid [192], whereas the bands at 490 cm<sup>-1</sup> and 727 cm<sup>-1</sup> correspond to the copper-oxygen bond (Cu-O) and aromatic C-H bending of benzene rings [193, 194].

Figure 3-10-b compares the FTIR spectra between HKUST-1, TPU and HKUST-1/TPU materials. Several characteristic bands of TPU could be observed on the spectrum of HKUST-1/TPU: polyurethane C-N bond stretching at 1535 cm<sup>-1</sup>; stretching vibrations of non-hydrogen bonded C-(C=O)-O- (ester group) at 1225 cm<sup>-1</sup>; stretching vibration of hydrogen bonded C-(C=O)-O- at 1061 cm<sup>-1</sup>. However, the characteristic peaks at 1730 and 1705 cm<sup>-1</sup>, which correspond to C=O stretching, does not properly appear in the spectrum of HKUST-1/TPU composite [195, 196]. In addition to that, similar characteristic HKUST-1 peaks, which were already explained in the previous paragraph, could also be observed in the HKUST-1/TPU spectrum.

To summarize, both XRD and FTIR analysis point out the presence of HKUST-1 and PLA in the HKUST-1/PLA composite. However, the signature of TPU cannot be distinguished from XRD analysis of the HKUST-1/TPU sample, which may be due to the amorphous structure of the thermoplastic. FTIR analysis shows some characteristic peaks of

TPU in the HKUST-1/TPU composite, while peaks corresponding to the pristine HKUST-1 remains visible in the HKUST-1/TPU.

b) HKUST-1 composites synthesized from additive manufacturing

Evidence of incorporation of HKUST-1 and PLA in 3D printed HKUST-1/PLA fabricated through FDM technology, was investigated through XRD analysis. Figure 3-11-a shows the comparison of XRD patterns between 3D printed HKUST-1/PLA, extruded HKUST-1/PLA, pristine PLA and pristine HKUST-1. Once again, the presence of HKUST-1 inside the 3D printed HKUST-1/PLA structure is evidenced by the presence of its characteristic peaks. Interestingly, the characteristic peak of PLA at 16.8 ° is clearly distinguishable in the XRD pattern of 3D printed HKUST-1/PLA. This is attributed to the high loading of PLA (70 % in mass) present in the 3D printed material.

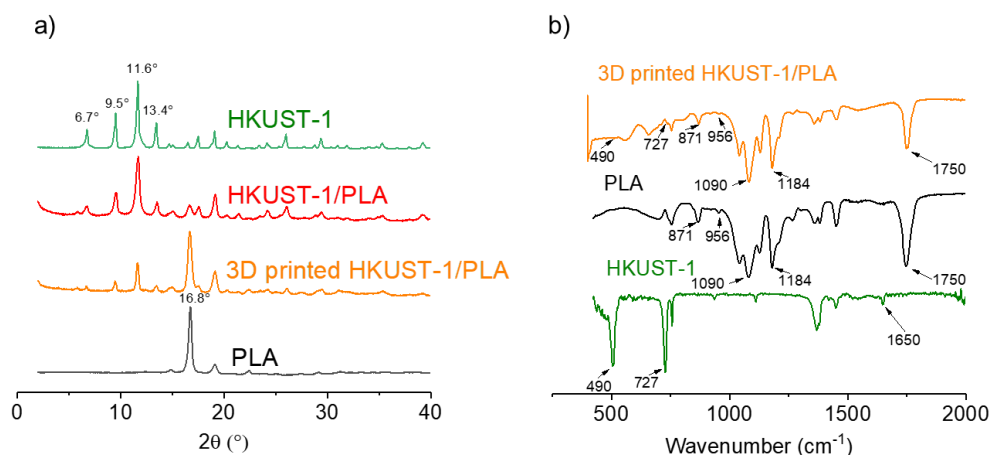


Figure 3-11: (a) XRD of PLA, HKUST-1, HKUST-1/PLA and 3D printed HKUST-1/PLA. (b) FTIR of HKUST-1, neat PLA and 3D printed HKUST-1/PLA.

Figure 3-11-b shows the FTIR spectra of 3D printed HKUST-1/PLA, pristine HKUST-1 and PLA. It can be observed that all characteristic peaks of PLA are clearly distinguishable in 3D printed HKUST-1/PLA spectrum. Characteristic peaks of HKUST-1 at 490 cm<sup>-1</sup> and 727 cm<sup>-1</sup>, corresponding to the copper-oxygen bond (Cu-O) and aromatic C-H bending of benzene rings, are barely visible in 3D printed HKUST-1/PLA IR spectrum.

To conclude, the combined XRD and FTIR analysis on 3D printed HKUST-1/PLA reveals that both PLA and HKUST-1 components are present in the composite material, which verifies the successful shaping of HKUST-1 adsorbent via additive manufacturing using FDM technology.

### 3.5.2. Morphology of samples

a) Extruded HKUST-1 composites

Scanning electron microscopy (SEM) imaging was used to characterize the surface morphology of adsorbent materials. Figure 3-12 compares the morphology observed between HKUST-1/TPU, HKUST-1/PLA and pristine HKUST-1. Most of pristine HKUST-1 particles exhibit an octahedron shape, which is the reported morphology of Basolite C300 [197]. A minor fraction of large crystallites of irregular shape probably signifies the presence of defects

induced by the synthesis route. An interesting observation that can be highlighted for both composites is the arrangement of polymer binders and HKUST-1 crystallites within the composites. In HKUST-1/TPU composite, MOF crystallites are held together by a fibrous network of TPU polymer, whereas in HKUST-1/PLA material, crystallites are surrounded by continuous PLA matrix. In both composites, particles of HKUST-1 are not totally encapsulated by their respective polymeric binder after shaping, thus remaining accessible for gas adsorption. This can be attributed to the low loading amount of thermoplastic binder, which reduces the likelihood of particle encapsulation.

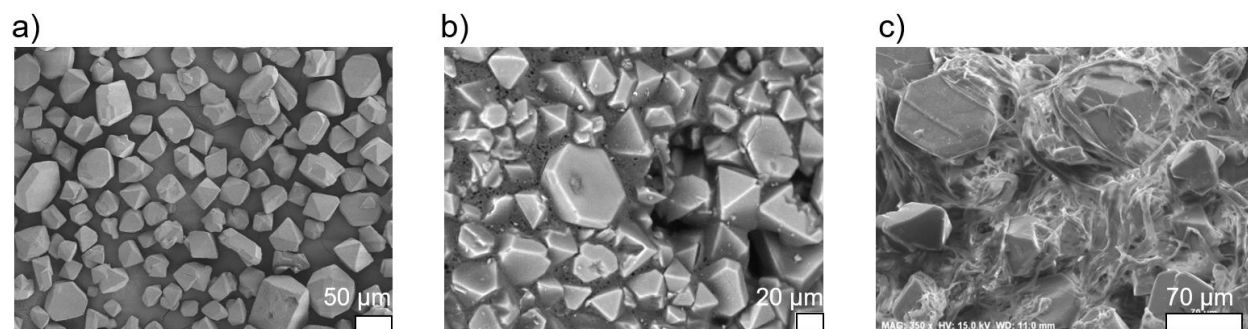


Figure 3-12: SEM image of (a) HKUST-1. (b) HKUST-1/PLA. (c) HKUST-1/TPU.

The Energy-dispersive X-ray spectroscopy (EDS) analysis was conducted on both composites to investigate elements present in the systems. Chemical cartography of the surface was performed in order to characterize the distribution of C and Cu elements between MOF and polymer. Figure 3-13-a and 2-13-c display elemental mapping for HKUST-1/PLA and HKUST-1/TPU, respectively. The mapping reveals a uniform distribution of C element (represented by blue color) over the surface of composites as it is present in both MOF particles and binders. However, Cu element (represented by red color) has a more heterogenous distribution, as it is only present in HKUST-1 particles. By combining the mapping of Cu and C elements together, it can be observed that there is a clear separation between the Cu element in HKUST-1 and C element in the polymeric binder in both composites. This observation indicates the absence of HKUST-1 alteration with following Cu transfer in polymer phase upon composite formation. It should be noted here that the greyish section in the elemental mapping corresponds to the area where EDS analysis is unable to detect the elements due to shadowing.

EDS spectra of HKUST-1/PLA and HKUST-1/TPU are presented in Figure 3-13-b and 2-13-d, respectively. Qualitatively, the peaks corresponding to the expected main elements in the composites (C, O and Cu) were identified. C and O elements are present in both HKUST-1 and polymeric binder, whereas Cu element is only present in HKUST-1. In addition, the platinum (Pt) element detected in the EDS analysis correspond to the coating that was done on the sample prior to the analysis. It should be noted that the difference of an element's relative content in HKUST-1/TPU and HKUST-1/PLA are not exploited as the samples used for the analysis were not flat, which renders the quantitative analysis of EDS unreliable. Nevertheless, peaks for EDS spectra measured for HKUST-1 composites were similar to that of powder HKUST-1 reported in other studies [198, 199] (Figure 3-13-e), albeit with different intensity. Nevertheless, this confirms the preservation of HKUST-1 particles upon composite formation.

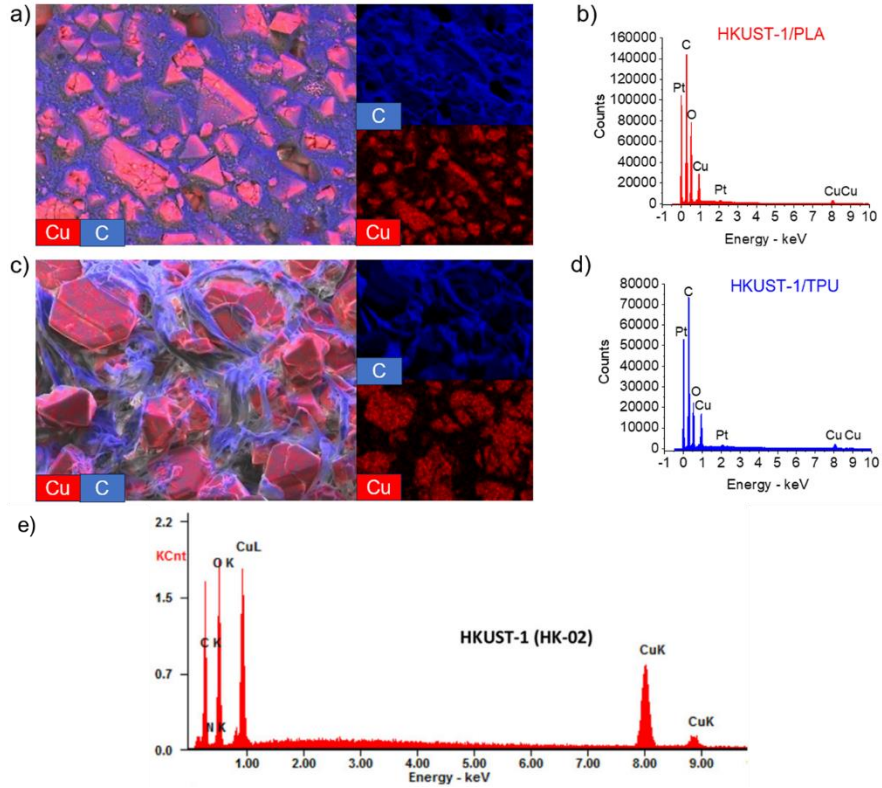


Figure 3-13: (a) EDS mapping for HKUST-1/PLA. (b) EDS spectra for HKUST-1/PLA. (c) EDS mapping for HKUST-1/TPU. (d) EDS spectra for HKUST-1/TPU (e) EDS spectra for HKUST-1 powder from study [198].

b) HKSUT-1 composites synthesized from additive manufacturing

Surface morphology of 3D printed HKUST-1/PLA is shown in Figure 3-14. A much lower number of MOF particles are exposed on the surface and most of them feature an irregular shape, different from octahedrons like for the pristine material. The observed cleavage of MOF crystallites in smaller fragments is likely due to the high stress applied onto the particles during the synthesis process (fabrication of filament and/or 3D printing of filament). The encapsulation of MOF crystallites in PLA limits the accessibility of gas towards the particles, thus degrading adsorption performances of the materials (discussed below).

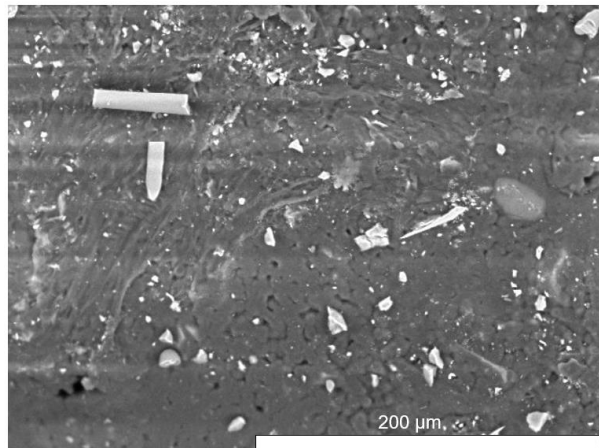


Figure 3-14: SEM image of 3D printed HKUST-1/PLA.

### 3.5.3. Thermal properties of materials

#### a) Extruded HKUST-1 composites

In a study by Domán et al. [200], thermal decomposition of HKUST-1 has been well described. In an inert atmosphere, the degradation of HKUST-1 could be observed at several temperature ranges. Generally, the first mass loss in HKUST-1 occurred at a temperature range of 373–423 K, and is attributed to the evaporation of water entrapped inside of microporous porous network. The next mass loss (very small quantity) usually occurred at 433–523 K region, which leads to the release of organic vapor originated from esters, carbon dioxide and water vapor. The last mass loss occurred in the region 553–583 K, which results in a release of a large amount of volatiles due to the degradation of the organic BTC ligand (approximately 1.7 ratio of linker-to-metal weight loss). The solid residue remaining after 583 K mainly consists of CuO and Cu<sub>2</sub>O as a minor constituent. The presence of the latter signifies a partial reduction of Cu(II) by organic species during heating.

Thermal degradation of PLA has also been well described [174]. The decomposition temperature of PLA is normally in the range of 503–533 K. The mechanism of the thermal decomposition for PLA starts with hydrolytic degradation by water traces followed by lactide reformation, oxidative main-chain scission and inter- or intramolecular transesterification reaction. During the decomposition process of PLA several gaseous products are formed. Among the major species determined by FTIR analysis [201], figure volatile aldehyde, carbon dioxide and carbonyl complexes. Traces of water could also be produced during the degradation of PLA due to fragmentation of lactide oligomer

The degradation of TPU polymer has been extensively studied in literature. In 1972, Wooley studied the thermal decomposition in nitrogen atmosphere of polyurethane made up of polyethers and polyesters [202]. It was shown that the decomposition behavior of both polyurethane types has a similar pathway. Wooley proposed that polyurethane degradation starts at the temperature range of 473–573 K, where a complete loss of diisocyanate unit occurred and leads to the formation of a nitrogen-free polyol residue. At the immediate temperature range (573–1073 K), polyol residue continues to decompose, forming complex products which probably consist of hydrocarbons and oxygenated

species. Finally, at high temperature (1073-1273 K), the residue decomposes into nitrogen-containing products of low molecular weight (mainly hydrogen cyanide, acetonitrile, acrylonitrile, pyridine and benzonitrile). A similar study was conducted by Herrera et al. [203], regarding the thermal decomposition under nitrogen flow of TPUs made up from different polyol (polyethers and polyesters) and 4,4'-diphenylmethane diisocyanate (MDI). Both TPUs exhibit two distinct peaks on their respective TA-curves at temperature range of 623-758 K, as well as mass losses above 1023 K. Carbon dioxide was found to be the most abundant product during the first step of degradation in nitrogen, indicating the scission of the urethane bond. In addition to that, the TPU synthesized with polyethers losses around 85% of its initial mass, while the polyester-based TPU mass losses attain 90%. This deviation is attributed to the difference in the oxygen-content of the used polyols. For the second degradation stage in nitrogen, a much more complex mixture of product originated from polyol-segment was observed.

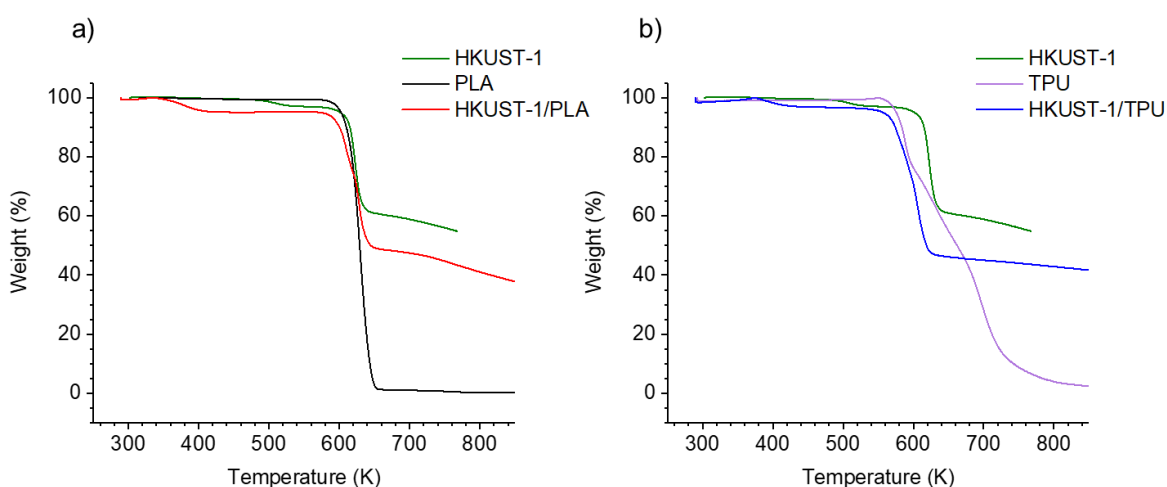


Figure 3-15: TGA profile for TPU, PLA, HKUST-1 and its composites.

The TGA profiles for pristine HKUST-1, its composites, as well as for neat PLA and TPU are shown in Figure 3-15. The first weight loss of the pristine HKUST-1 used in this study occurs at 373 K, followed by gradual mass loss in the range 433–523 K and ends with a sharp mass loss at 613 K. This TGA profile is similar to the one previously reported in the study by Domán et al. [200]. Thermal degradation of neat PLA starts at a slightly higher temperature than the one reported in literature [174] (593 vs. 533 K). Meanwhile, the profile of the TPU thermal degradation starting at 553 K, is perfectly in line with that for polyurethane reported in [202]. TGA curve for TPU exhibits two distinct peaks in the ranges 553-613 K (decomposition of polyol groups in soft segments) and 663–733 K (decomposition of urethane bonds in hard segments) [204, 205].

The thermal degradation of HKUST-1/TPU and HKUST-1/PLA proceeded in two steps; a first mass loss occurred between 350 K–410 K, which corresponds to a 3% and 5% weight loss for HKUST-1/TPU and HKUST-1/PLA, respectively. This initial mass loss was associated with the evaporation of leftover solvent molecules (chloroform, DMF or methanol) that remain trapped inside the pores. The second mass loss started around 560 K and 590 K for HKUST-1/TPU and HKUST-1/PLA, respectively, which can be attributed to the start of the framework and polymeric binder degradation. Moreover, the decomposition behavior of both hard and soft segments of TPU is

no longer distinguishable in the HKUST-1/TPU composite. It can be observed that both HKUST-1/TPU and HKUST-1/PLA composites display a lower degradation temperature than pristine HKUST-1 and their respective pure polymeric binders. This can be attributed to the presence of metal in MOF particles that may act as a catalyst for polymer degradation, as concluded in several other studies [206, 183, 151].

b) HKUST-1 composite synthesized from additive manufacturing

The TGA profile of a 3D printed HKUST-1/PLA together with that for pristine HKUST-1 and neat PLA, are shown in Figure 3-16. As expected, a similar pattern of thermal evolution can be observed as for extruded HKUST1/PLA. It involves two steps of weight loss: at around 323-573 K, attributed to the evaporation of guest solvent molecules that remain trapped inside the pores, and a second weight loss at 584 K, attributed to the collapse of the framework as well as degradation of PLA. This result shows that degradation pattern of HKUST-1/PLA composite produced either through extrusion or additive manufacturing have similar thermal degradation behaviors. Therefore, it can be concluded that different binder loading content in a composite does not have a significant impact on the final material's thermal stability.

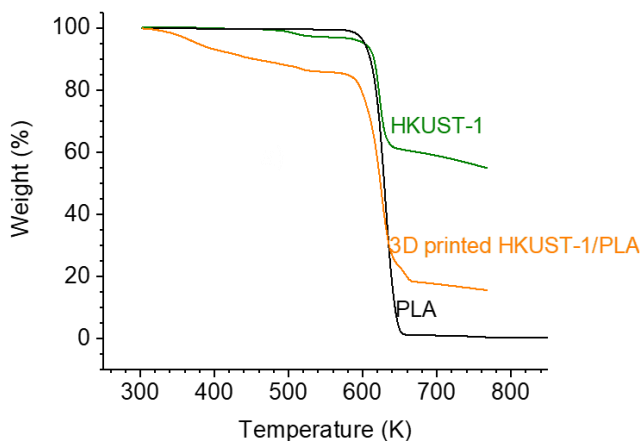


Figure 3-16: TGA profiles for pristine HKUST-1, PLA and 3D printed HKUST-1//PLA.

#### 3.5.4. Mechanical resistance

In the existing literature, multiple mechanical properties of granulated porous solids and MOFs were used to evaluate and quantify their mechanical properties such as elastic moduli and tensile strength [207, 208, 209], hardness [210] and attrition/abrasion strength [211, 179]. However, in spite of the growing trend towards reporting the mechanical properties of shaped MOFs, these are usually not compared to industrial standards for their proposed applications [207].

In this work, an attrition strength is considered as an indicator of mechanical resistance of HKUST-1 composites, because adsorbents with a high attrition value could lead to bed clogging or an increase in pressure drop inside the adsorption column. The attrition test was conducted by referring to the test of D4058–96 ASTM norm [212], where

solid samples are rotated for a fixed number of revolutions in a cylindrical drum. Fines produced by attrition and abrasion in the test are determined by sieving through a standard sieve.

Table 3-6 compares the attrition values measured for the HKUST-1/TPU and HKUST-1/PLA along with commercial adsorbents and MOF extrudates from other studies. It could be observed that HKUST-1/TPU is only slightly lower in attrition value in comparison to HKUST-1/PLA (0.4% vs 0.5%), but both samples possess a comparable mechanical resistance attrition with other commercial adsorbents, as reported in [207]. In addition to that, 3D printed HKUST-1/PLA does not exhibit any mass loss due to attrition after the test, which can be explained by a high loading of PLA increasing its mechanical stability. Considering that the materials used in developing the D4058–96 ASTM standard method exhibited attrition less than 7 % [212], which is higher than that of HKUST-1/PLA, HKUST-1/TPU and 3D printed HKUST-1.PLA, it is reasonable to conclude that all synthesized HKUST-1 composites have a good resistance to attrition.

Table 3-6: Attrition percentage of HKUST-1/TPU, HKUST-1/PLA, 3D printed HKUST-1/PLA, conventional zeolite adsorbents and MOF extrudates.

Sample	Attrition loss (% wt)	Reference
HKUST-1/TPU	0.4	This study
HKUST-1/PLA	0.5	
3D printed HKUST-1/PLA	0	
Zeolite 3A	$\leq 0.2$	[207]
4A	$\leq 0.2$	
5A	$\leq 0.2$	
13X	$\leq 0.2$	
AC-Norit RZN <sub>1</sub>	0.2	[179]
UiO-66 extrudate	1.4	

### 3.5.5. Textural properties

#### a) Extruded HKUST-1 composites

The specific surface areas of samples were determined using the BET model applied to nitrogen adsorption isotherms measured at 77 K. In the first step, the N<sub>2</sub> adsorption isotherms of pure TPU and pure PLA were measured to verify whether the binding agent used for the shaping is porous or not. Figure 3-17 shows that both polymeric binders adsorbed negligible amounts of N<sub>2</sub>, thus signifying a non-porous character of both materials.



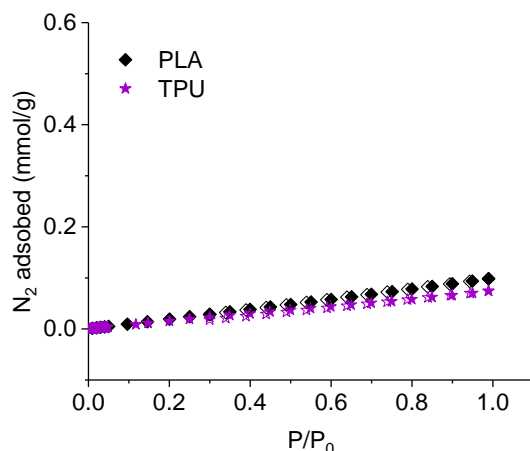


Figure 3-17:  $N_2$  adsorption isotherms for TPU and PLA. Filled and unfilled symbols signify adsorption and desorption branches respectively

As a next step,  $N_2$  adsorption isotherms of HKUST-1 powder and its composites obtained by extrusion were investigated. Figure 3-18 shows the adsorption isotherms in both linear and logarithmic scales. All isotherms feature a shape I type relevant of microporous solids [213]. The  $N_2$  adsorption capacities of HKUST-1/TPU and HKUST-1/PLA are slightly larger than that of pristine HKUST-1, which signifies that HKUST-1 particles in both composites remain accessible for gas diffusion, as evidenced by SEM imaging at micron scale. In addition to that, it can be seen that nitrogen filling at pressure range  $p/p_0 < 10^{-4}$  is different for both composites when compared to pristine HKUST-1. This indicates some changes related to the accessibility of the primary adsorption sites located in the microporous domain after shaping.

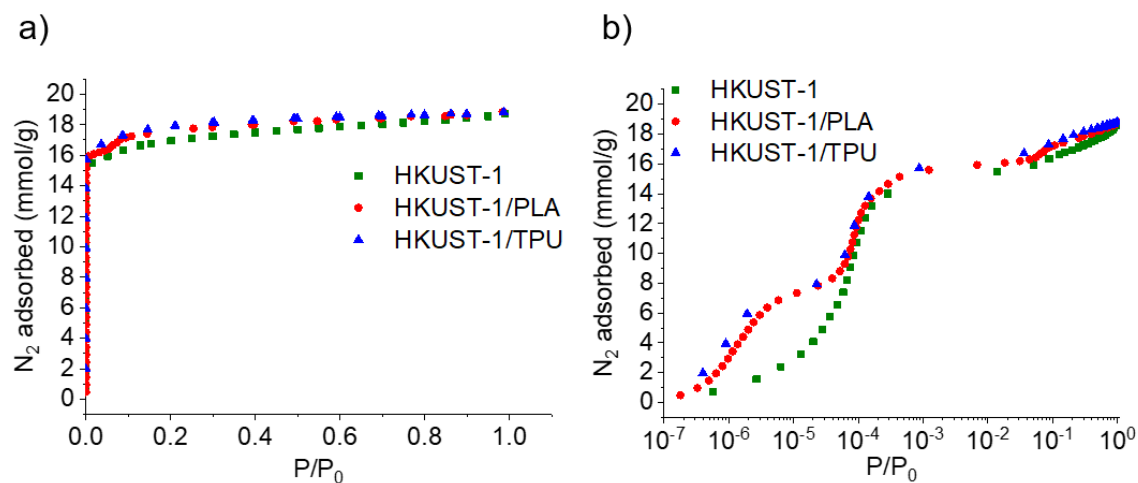


Figure 3-18:  $N_2$  adsorption isotherm plots for HKUST-1/TPU, HKUST-1/PLA and HKUST-1 in (a) linear scale and in (b) log scale

Table 3-7: BET Surface areas, pore volumes of HKUST-1, HKUST-1/TPU and HKUST-1/PLA

Sample	S <sub>BET</sub> (m <sup>2</sup> /g)	Micropore volume (cm <sup>3</sup> /g)	Total pore volume (cm <sup>3</sup> /g)
HKUST-1	1500 ± 4	0.46	0.65
HKUST-1/TPU	1557 ± 28	0.50	0.65
HKUST-1/PLA	1528 ± 17	0.54	0.65

Table 3-7 summarizes the BET surface areas and the pore volume data derived from the 77K-N<sub>2</sub> adsorption isotherms for HKUST-1/TPU, HKUST-1/PLA and pristine HKUST-1. The micropore volumes and BET surface areas of both HKUST-1/TPU and HKUST-1/PLA are slightly larger than that of pristine HKUST-1. This result is surprising because, as reported by numerous studies [214, 215, 216], the introduction of non-porous binder required for the shaping usually degrades textural and gas adsorption properties of porous materials. Most probably, the observed trend can be explained by the effect of “washing” of pristine HKUST-1 with the solvents (DMF or Chloroform, Methanol) during the shaping process. To verify that immersion in solvents influences the porosity and BET surface area of HKUST-1, pristine MOF powder was washed in methanol, DMF and chloroform respectively, for three times (hereafter will be referred as “methanol washed HKUST-1”, “DMF washed HKUST-1” and “Chloroform washed HKUST-1”), and then subsequently characterised by N<sub>2</sub> adsorption at 77 K (Figure 3-19 and Table 3-8). As expected, when pristine HKUST-1 is rinsed with these solvents, an increase in the BET surface area of the pristine adsorbent is observed. This indicates the presence of some residual reactant(s) in micropores of the MOF material directly received from the manufacturer.

As both HKUST-1/PLA and HKUST-1/TPU have a commonality of being washed with methanol at the end of their respective synthesis process, their BET surface area are compared with that of methanol-washed HKUST-1. It could be observed a difference of 22% and 20% for HKUST-1/PLA and HKUST-1/TPU respectively, in comparison to methanol-washed HKUST-1. These deviations are larger than 10% which is the expected minimal reduction in the surface areas of the composites considering the 10% mass loading of non-porous binder introduced in their synthesis. Therefore, it is likely that partial micropore blockage does occur in the composites due to the shaping process.

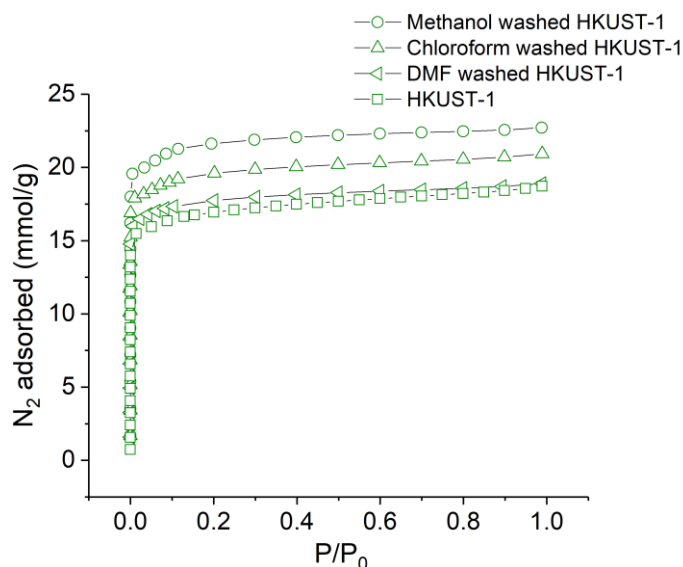


Figure 3-19: N<sub>2</sub> adsorption isotherms of HKUST-1 and solvent-washed HKUST-1.

Table 3-8: BET Surface area, pore volume of HKUST-1 and the respective solvent-washed HKUST-1.

Sample	S <sub>BET</sub> (m <sup>2</sup> /g)	<i>t</i> -plot Micropore volume (cm <sup>3</sup> /g)	Total pore volume (cm <sup>3</sup> /g)
Pristine HKUST-1	1500 ± 4	0.46	0.65
DMF washed HKUST-1	1616 ± 45	0.46	0.65
Chloroform washed HKUST-1	1762 ± 20	0.51	0.72
Methanol washed HKUST-1	1956 ± 47	0.60	0.79

b) HKUST-1 composite synthesized from additive manufacturing

Figure 3-20-a shows the N<sub>2</sub> adsorption isotherms of HKUST-1, PLA and 3D printed HKUST-1/PLA. Their BET surface areas and pore volumes are summarized in Table 3-9. It can be observed that 3D printed HKUST-1/PLA suffers significant reductions in N<sub>2</sub> adsorption capacity, BET surface area, and pore volume in comparison to the pristine HKUST-1. This finding is coherent with the results of SEM imaging, which revealed that MOF particles in the 3D printed composite are encapsulated by PLA, thus limiting their exposure to gas phase. Furthermore a severe degradation of CO<sub>2</sub> adsorption capacities of the 3D printed material in comparison to pristine HKUST-1 (Figure 3-20-b), demonstrate that 3D printed HKUST-1/PLA could not be considered for CO<sub>2</sub>/CH<sub>4</sub> separation as the high loading

amount of the binder causes pore blockages. It was then decided to stop further analysis of this material due to this discouraging finding.

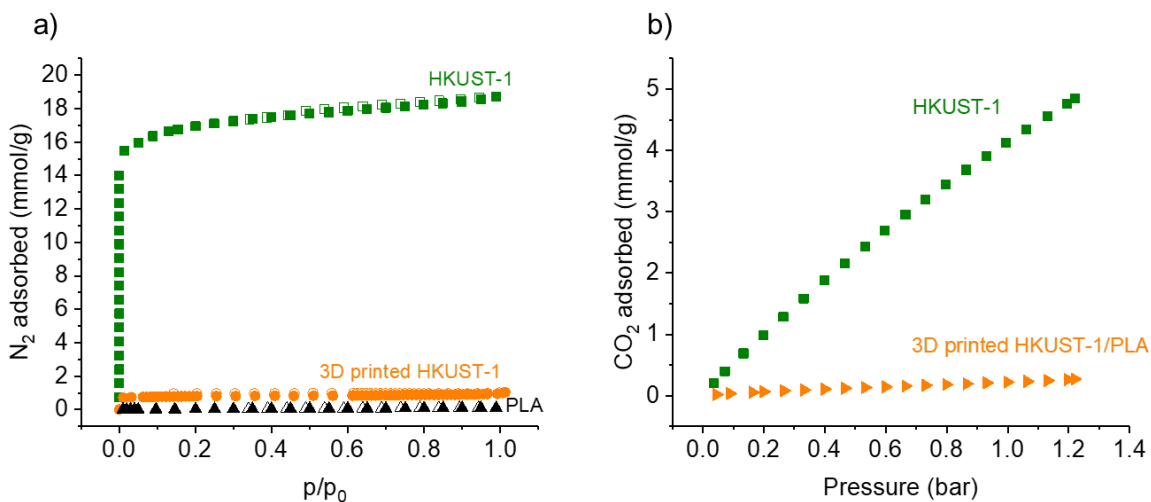


Figure 3-20: (a) N<sub>2</sub> adsorption isotherms of HKUST-1, PLA and 3D printed HKUST-1/PLA. (b) CO<sub>2</sub> adsorption isotherms of HKUST-1 and 3D printed HKUST-1/PLA

Table 3-9: BET Surface area, pore volume of HKUST-1, PLA and 3D printed HKUST-1/PLA.

Sample	S <sub>BET</sub> (m <sup>2</sup> /g)	Micropore volume (cm <sup>3</sup> /g)	Total pore volume (cm <sup>3</sup> /g)
HKUST-1	1500	0.46	0.65
PLA	3	0	0
3D printed HKUST-1/PLA	70	0	0

### 3.5.6. Ageing analysis and hydrophilicity

#### a) Ageing of materials

HKUST-1 is known to be sensitive to water as its open-metal sites have a high affinity to H<sub>2</sub>O molecules, resulting in the formation of Cu-O bonds and disintegration of HKUST-1 framework [20] [139]. Figure 3-21 displays the H<sub>2</sub>O adsorption isotherms for HKUST-1-TPU, HKUST-1-PLA and pristine HKUST-1 at 298 K. As expected, pristine HKUST-1 is able to adsorb a larger quantity of water in comparison to the extruded composites when the relative humidity (RH) increases. Furthermore, the accessible pores of pristine HKUST-1 start to be completely filled with water at P/P<sub>0</sub> ≈ 0.17. Meanwhile, the presence of either TPU or PLA in the composite has an effect on lowering the quantity of adsorbed water molecules as the relative pressure increases. It is possible that the polymeric binder partially hinders the access of water molecules to certain open metal-sites in HKUST-1. Interestingly, it can be noticed that the accessible pores in HKUST-1-PLA start to be filled with water at a similar relative pressure than pristine HKUST-1, while this is not the case for HKUST-1-TPU, as completion of adsorption only comes at higher relative pressure P/P<sub>0</sub> ≈ 0.27. This can be explained by the hydrophobic nature of TPU, reducing the interaction intensity of the adsorbent

composite with water. Pristine HKUST-1 powder in this work demonstrates H<sub>2</sub>O adsorption capacity of 32 mmol/g at saturation and temperature of 298 K, which were considered high as traditional adsorbent such as commercial silica exhibited H<sub>2</sub>O adsorption capacity of 25 mmol/g at similar temperature [217].

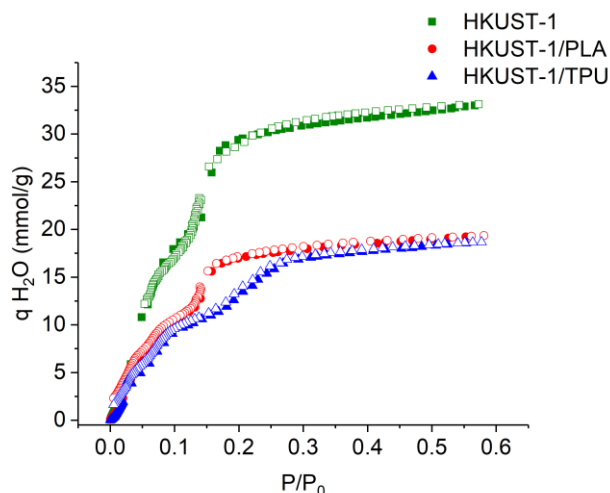


Figure 3-21: H<sub>2</sub>O adsorption-desorption isotherm plots for HKUST-1-TPU, HKUST-1-PLA and HKUST-1 at 298 K.

In addition, samples have been subjected to multiple cycles of H<sub>2</sub>O adsorption isotherm acquisition at 298 K. This analysis allows the observation of HKUST-1 adsorption performance degradation after the exposure to water vapor upon multiple cycles of adsorption-desorption. The desorption step is similar to the adsorption procedure, that is, the acquisition of desorption points was performed by decreasing the relative pressure until  $p/p_0 = 0.03$  followed by fixed-dose mode until  $p/p_0 = 0.01$ . The aliquot was adjusted between 1.3 and 2 mmol H<sub>2</sub>O/g. To reach the equilibrium conditions, the equilibration time for each isotherm point after aliquot injection was adjusted until pressure stabilization, but not exceeding 1h/point.

Figure 3-22 shows the evolution of the H<sub>2</sub>O adsorption capacities for HKUST-1 and its composites during 5 continuous H<sub>2</sub>O adsorption-desorption cycles. The most notable observation is the fast degradation of H<sub>2</sub>O loading by pristine HKUST-1 upon cycling, related to the alteration of open metal sites when exposed to water molecules. Meanwhile, the H<sub>2</sub>O adsorption capacity for HKUST-1/PLA is only slightly reduced under the same conditions, which indicates that PLA presence in the composite slows down material's degradation. Finally, HKUST-1/TPU displays a consistent H<sub>2</sub>O uptake after each cycle, which indicates no significant degradation of the material, most probably due to the higher hydrophobicity of TPU in comparison to PLA.

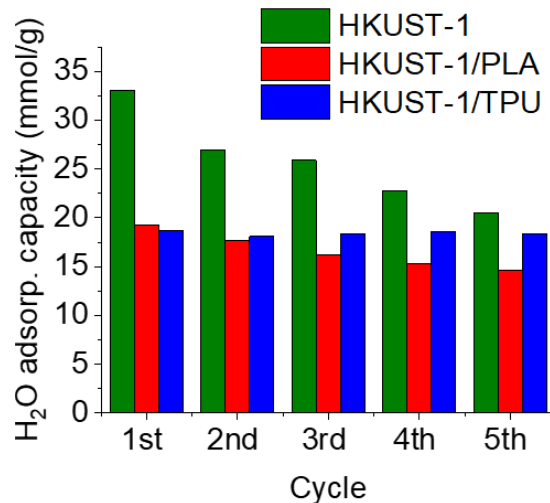


Figure 3-22: Variation of H<sub>2</sub>O adsorption capacity for HKUST-1, HKUST-1-PLA and HKUST-1-TPU after multiple cycles of adsorption equilibrium.

To further evaluate the stability of MOF composites exposed to moisture, samples were stored in a humid environment (RH = 40 ± 5% and controlled temperature of 298 K) for the duration of 3 months and several re-characterizations of the samples (N<sub>2</sub> and CO<sub>2</sub> adsorption isotherm analysis) were performed during this period on a monthly basis. Considering the H<sub>2</sub>O isotherm data previously obtained for HKUST-1 and its composites, the tested air RH was sufficiently high to ensure a complete micropore filling with water from the atmosphere. Figure 3-23-a presents the variation of the BET surface areas for HKUST-1-TPU, HKUST-1-PLA and pristine HKUST-1 after 3 months of storage in humid environment. As expected, pristine HKUST-1 shows a degradation of its BET surface area after 3 months of storage in the humid environment. Meanwhile, HKUST-1-PLA has a similar degradation pattern as pristine HKUST-1 during the 1<sup>st</sup> month of storage, but the texture seems to stabilize after 1 month. Interestingly, HKUST-1-TPU exhibits a less sensitivity to degradation under humid exposure than HKUST-1-PLA during the 1<sup>st</sup> month, which moreover seems to be halted after 1 month of storage. We hypothesized that TPU being more hydrophobic than PLA, it contributes to a slower degradation of HKUST-1 in the composite. Additionally, both polymeric binders may have hindered access towards the MOF open metal sites, which are the preferential adsorption sites for water molecules, and that can also explain the stabilization of the degradation for both composites after 1 month of storage. Additionally, similar patterns of degradation in the CO<sub>2</sub> adsorption capacities of the different samples measured at 298 K and 1 bar can be observed (Figure 3-23-b).

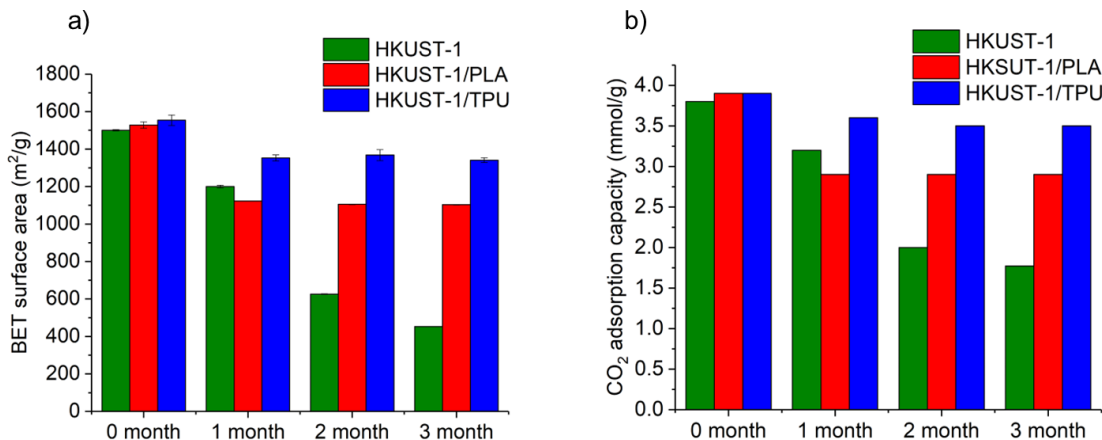


Figure 3-23: Variations of (a) BET surface areas and (b) CO<sub>2</sub> adsorption capacities for HKUST-1, HKUST-1-PLA and HKUST-1-TPU extrudates stored in humid condition for 3 months.

#### b) Characterization of hydrophobicity of thermoplastics

A surface is considered hydrophobic when its static water contact angle,  $\theta_{\text{water}}$  is  $>90^\circ$  and assumed as hydrophilic when  $\theta_{\text{water}}$  is  $<90^\circ$  [218]. In literature, TPU is known to be more hydrophobic than PLA [219, 220] and we have subsequently verified this by conducting surface wettability tests on the surface of both thermoplastic (Figure 3-24). The average water contact angle for TPU and PLA are presented in Table 3-10. It can be deduced that TPU is more hydrophobic than PLA, based on water contact angle value of each polymer. Therefore, the presence of a more hydrophobic TPU as a binding agent in comparison to PLA is the reason for improvement of moisture stability of HKUST-1 composite observed in this work. This finding corroborates those reported in other studies [221, 222, 223], relating the presence of a hydrophobic polymer with increasing moisture stability of a MOF's composite.



Figure 3-24: Image of water drop onto the surface of PLA (left) and TPU (right).

Table 3-10: Average value of water contact angle on the surface of TPU and PLA.

Polymer	Average contact angle ( $^\circ$ )
PLA	66.9
TPU	90.3

### 3.6. Conclusion

In this chapter, three shaping processes of HKUST-1 powder using two different thermoplastic binding agents were investigated. The first shaping process involves the extrusion of HKUST-1 with 10 wt% of binding agent, either TPU or PLA. The second shaping process involves the printing of HKUST-1 by additive manufacturing using FDM technology. This method was only tested using PLA as the binding agent and requires the fabrication of HKUST-1/PLA filament, which in turn requires a high loading amount in mass (70%), followed by printing of the filament. The third shaping process of HKUST-1 involves additive manufacturing using the FGF printing technology. The FGF was applied to manufacture HKUST-1/TPU composites starting from the extruded material as prepared in the first shaping process. As the shaping process by FGF technology is still in the early stage of tests, there is no suitable example of composite that could be used for subsequent analysis. Composites synthesized from the first and second shaping processes were then characterized to verify the preservation of HKUST-1 crystallites in the composites. XRD and FTIR analysis results show that HKUST-1 particles are present in composites without subsequent alteration. In addition to that, SEM imaging reveals that the external surface of the HKUST-1 particles in composites elaborated by extrusion are not fully covered by the polymeric matrix and remain accessible to gas, whereas SEM images of 3D printed HKUST-1/PLA show a significant encapsulation of MOF crystallites by PLA, being at the origin of a limited gas access to the MOF's porous network. Apart from that, all composites synthesized either by extrusion or by additive manufacturing (FDM) process have sufficient mechanical stability to be employed as adsorbents inside fixed-bed columns in a gas treatment unit. Nitrogen adsorption isotherms reveal that both HKUST-1 composites synthesized via extrusion have a higher BET surface area than the pristine form ( $1500 \text{ m}^2/\text{g}$ ), which is attributed to the effect of washing of the samples with methanol at the end of the shaping process that helps to remove any subsequent impurities remaining in the pores. However, it should be noted that both HKUST-1/PLA and HKUST-1/TPU exhibit a lower BET surface area (22% and 20% respectively) in comparison to methanol-washed HKUST-1, which is an indication of partial pore blockage occurring inside the composites. Meanwhile, the nitrogen adsorption isotherm of 3D printed HKUST-1/PLA reveals a significant reduction in the BET surface area ( $70 \text{ m}^2/\text{g}$ ) after shaping. This is due to the presence of a high amount of non-porous PLA polymer in the sample, which leads to the encapsulation of HKUST-1 particles and hence prevent them from being accessible to gas. Based on the obtained results, it is clear that only HKUST-1 composites synthesized by extrusion present a potential to be used as an adsorbent for  $\text{CO}_2/\text{CH}_4$  separation, whereas 3D printed HKUST-1/PLA exhibiting a poor porosity cannot be considered as a good adsorbent candidate. Finally, the effect of hydrophobicity between TPU and PLA was quantitatively investigated, and it was verified that the former is more hydrophobic than the latter. It was so revealed that the use of a more hydrophobic thermoplastic as a binding agent helps improving the moisture stability of HKUST-1 based composites, as their degradation rate was reduced in presence of moisture. As only HKUST-1 composites synthesized via extrusion results in encouraging results, only HKUST-1/PLA and HKUST-1/TPU as well as pristine HKUST-1 are further analyzed for  $\text{CO}_2/\text{CH}_4$  adsorption analysis in next chapter.



# CHAPTER 4: Adsorption performance of materials

This chapter focusses on the analysis of CO<sub>2</sub>/CH<sub>4</sub> adsorption for HKUST-1 composites synthesized via extrusion as well as pristine HKUST-1. For that, the first section will be focusing on the presentation of thermodynamics aspect of an adsorption phenomenon. Several theoretical models that could be utilized to describe the adsorption equilibria of pure gases will be explained together with the principles of adsorption enthalpy calculations. Additionally, the formalism of Ideal Adsorbed Solution Theory (IAST) to describe the co-adsorption isotherms for multi-component gas mixtures will also be introduced. Next, the second section of this chapter explains experimental techniques adopted for the measurements of pure gas adsorption isotherms under different pressure and temperature conditions. Finally, the last section will be revolving around the results of experimental pure gas adsorption isotherms of the synthesized composites, their respective adsorption heats values as well as the prediction of CO<sub>2</sub>/CH<sub>4</sub> co-adsorption isotherms, CO<sub>2</sub> working adsorption capacity and selectivity for each material as to assess the potential performance of the synthesized materials when being applied as an adsorbent for CO<sub>2</sub>/CH<sub>4</sub> separation in PSA process.

## 4.1. Modelling of adsorption thermodynamics

### 4.1.1. Generality

Adsorption is a phenomenon of molecules or ions transfer from a fluid (liquid or gas) to an exposed solid surface or a porous space. This process depends on the existence of a force field of a surface, which reduces the potential energy of an adsorbed phase below that of the ambient bulk phase. The inverse phenomenon from that leads to the desorption of gas molecules. The gas molecules that were adsorbed by solid is called adsorbate, whereas the solid where the adsorption took place is called adsorbent.

Adsorption can be classified into two main types, depending on the nature of interaction forces at the surface:

- Physical Adsorption (Physisorption): This type of adsorption results from weak dispersion-repulsion interactions (van der Waals forces) and other supplementary electrostatic contributions (polarization, field-dipole and field gradient-quadrupole interactions) between the adsorbate and the adsorbent surface. Physisorption typically occurs at relatively low temperatures and is reversible.
- Chemical Adsorption (Chemisorption): The forces involved in chemisorption involve a substantial degree of electron transfer/sharing, which leads to the formation of chemical bonds between the adsorbate and the adsorbent surface, such as covalent bonds or ionic bonds. This type of adsorption can occur at temperature significantly higher than room temperature and can be irreversible.

The physisorption is reversible, with low enthalpy (typically ranging from 10 to 40 kJ.mol<sup>-1</sup>) [224] and the adsorption could be either monolayer, multilayer or take place in the whole adsorption volume (usually micropore volume). Meanwhile, the chemisorption is usually irreversible, with high enthalpy (typically ranging from 20 to 400

$\text{kJ}\cdot\text{mol}^{-1}$ ) [224] and limited to monolayer adsorption. In this work, we restrict in what follows to physisorption phenomena, as MOF can be classified as physical adsorbents.

The description regarding adsorbent properties and different types of adsorbents typically employed in industry has already been explained previously in chapter 1 (cf. Section 2.3, page 42) and thus will not be re-elaborate here. However, it would be beneficial to reiterate here the three different classifications of pores for an adsorbent: (1) micropores are narrower than 2 nm with subdivision in ultra ( $<0.7$  nm) and super (0.7-2 nm) micropores, (2) mesopores - pore diameter between 2 and 50 nm, (3) macropores - diameter above 50 nm.

The shape of physical adsorption isotherm is a good qualitative indicator in identifying the textural characteristics of an adsorbent. In addition to that, the adsorption isotherm graph is also often used to describe the equilibrium adsorption of a pure gas. According to IUPAC classification [225], the majority of adsorption isotherm could be classified into six types, as described in Figure 4-1.

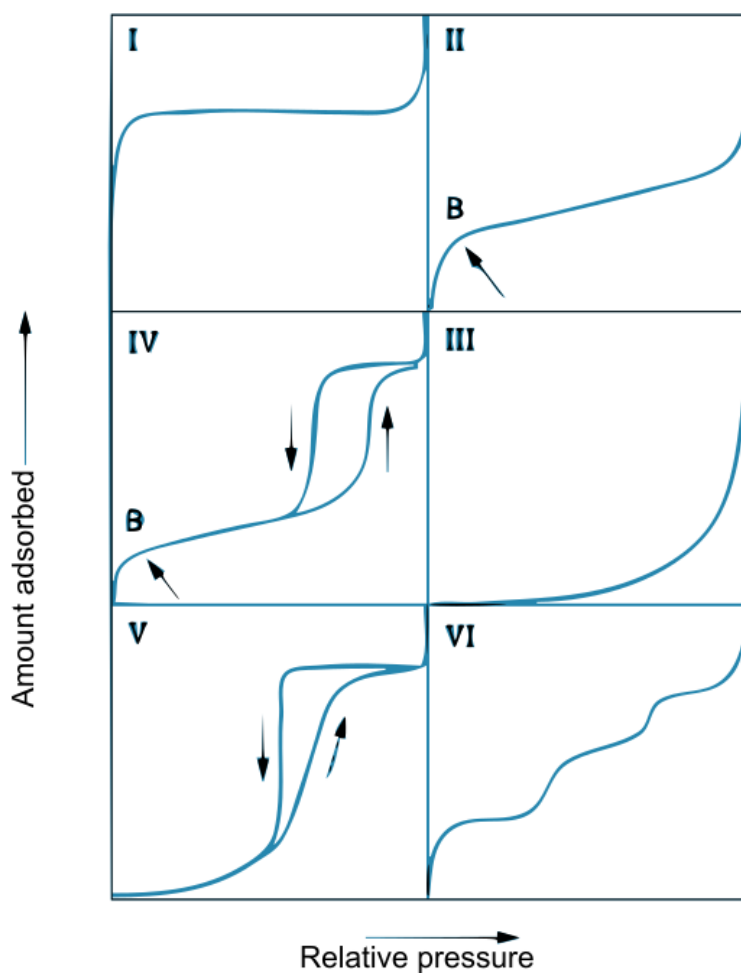


Figure 4-1: Different type of physical adsorption isotherm

### *Type I*

This type of isotherm is characterized by the constant existence of a horizontal plateau, which represents saturation of the adsorbent, even as the relative pressure increases. This type of isotherm is usually obtained for microporous adsorbent, where the filling of the micropores occurred at very low relative pressure.

### *Type II*

This type of isotherm is characterized by the progressive increment of adsorbed quantity with relative pressure and it is usually obtained for non-porous adsorbent or macroporous adsorbent. This type of adsorbent also indicates a multilayer adsorption. Point B, which is situated at the starting point of the quasi-linear region of the adsorption graph, corresponds to a statistical monolayer completion on the adsorbent surface and beginning of multilayer formation.

### *Type III*

This type of isotherm corresponds to the case where the interactions between adsorbate-adsorbent are weaker than intermolecular interactions in the adsorbed phase. In other words, the adsorbate molecules initially at low pressure becomes hard to be adsorbed, but once sufficient adsorbate molecules have been loaded on the surface, further uptake tends to facilitate thanks to the growth of “islands” of the adsorbed phase induced by intermolecular interactions.

### *Type IV*

This type of isotherm exhibits the same shape as isotherm type II in the region of low relative pressure. At a higher relative pressure, this type of isotherm exhibits a characteristic hysteresis due to capillary condensation occurring in the mesopores of an adsorbent.

### *Type V*

This type of isotherm is usually obtained from microporous materials with low adsorbate-adsorbent interactions. The shape of this type of isotherm is similar to that of type II and III in the low relative pressure region. At higher relative pressure, the capillary condensation in the mesopores occurred, as indicated by the apparition of hysteresis.

### *Type VI*

This type of isotherm is usually observed in the case of an adsorption on an energetically homogenous solid surface. Each step of the horizontal line that appears in the shape of the isotherm as relative pressure increases, correspond to formation of adsorption layers on the solid surface.

Depending on the structure of the adsorbent used, any type of physical adsorption isotherm shown above would be obtained. For MOFs, the typical adsorption isotherm shapes are of type I, IV or V [226] [227]. It should be highlighted that all these isotherm types are typical for fluids under subcritical conditions, i.e. when all the described phenomena taking place due to intermolecular interactions. However, the shape of adsorption isotherm for supercritical fluids (e.g. CO<sub>2</sub>, CH<sub>4</sub>) might be different from that of IUPAC classification [228].

Apart from the qualitative information that could be obtained from these adsorption isotherms on the textural properties of an adsorbent, some quantitative information, such as monolayer adsorption capacity or pore volume, could also be acquired. For that reason, numerous adsorption models have been developed to describe either for pure gas or multi-component gas adsorption isotherm, which will be introduced in the following sections.

#### 4.1.2. Adsorption models for pure gas

The adsorption models employed to describe adsorption isotherm for pure gas are not only useful in carrying the quantitative analysis of experimental isotherms, it is also necessary parameters for the establishment of adsorption models for multi-component gas and the simulation of adsorption process. In this section, we will present some adsorption models developed in the literature that were based on Gibbs isotherms, multilayer adsorption models, and empirical models.

##### a) Adsorption models based on Gibbs isotherm

Gibbs isotherm serves as a basis for numerous developments of adsorption models. Gibbs isotherm was based on the thermodynamics of gas and adsorbed phase. Gibbs has demonstrated that at the equilibrium condition, the chemical potential of both phases are equal [229]. Consequently, an equation known as the general equation of Gibbs isotherms has been established and could be expressed as:

$$v_g dP = \frac{d\pi}{\Gamma} \quad \text{Eq. 4-1}$$

where  $v_g$  correspond to the molar volume ( $\text{m}^3 \cdot \text{mol}^{-1}$ ) of gas phase,  $P$  is the pressure of gas phase (Pa),  $\pi$  is the spreading pressure of adsorbed phase (Pa.m) and  $\Gamma$  is the surface concentration of adsorbed phase ( $\text{mol} \cdot \text{m}^{-2}$ ). Spreading pressure of the adsorbed phase plays the same role as pressure in bulk gas phase [229].

##### ❖ Henry's law

Henry's law, which was first developed in 1803 [230], could be considered as the simplest adsorption isotherm model. The model was developed with the following hypotheses:

1. The adsorbed molecules form a monolayer on the solid surface.
2. The surface of adsorbent is energetically equivalent.
3. The adsorbed molecules are energetically isolated from one another, thus, there are no interactions between them.
4. Each adsorption site could only accommodate a single molecule.
5. Gas phase is considered ideal.
6. Adsorbed phase behaves similarly to gas phase.

As the adsorbed phase behaves similar to the gas phase, which is considered ideal, thus the equation of state for adsorbed phase could be expressed as:

$$\pi A = nRT \quad \text{Eq. 4-2}$$

where  $\mathbf{A}$  is the surface of adsorbent ( $\text{m}^2$ ),  $\mathbf{R}$  is the molar gas constant ( $\text{J} \cdot \text{mol}^{-1} \cdot \text{K}^{-1}$ ),  $\mathbf{T}$  is the temperature ( $\text{K}$ ) and  $\mathbf{n}$  is the quantity of adsorbed phase ( $\text{mol}$ ). Eq 3-2 can be further expressed in terms of surface concentration of adsorbed phase  $\Gamma$ :

$$\frac{\pi}{RT} = \frac{n}{A} = \Gamma \quad \text{Eq. 4-3}$$

Meanwhile, for the gas phase, the ideal gas law could be expressed as:

$$\frac{RT}{P} = v_g \quad \text{Eq. 4-4}$$

By combining both Eq. 4-4 and Eq. 4-3 with the general equation of Gibbs isotherm (Eq. 4-1), following expression is obtained:

$$\frac{dP}{P} = \frac{d\Gamma}{\Gamma} \quad \text{Eq. 4-5}$$

Eq. 4-5 reveals a linear relationship between the pressure of the gas phases with the surface concentration of the adsorbed phase. By expressing the amount of adsorbed phase per mass of adsorbent,  $\mathbf{q}$  ( $\text{mol} \cdot \text{kg}^{-1}$ ), instead of surface concentration,  $\Gamma$ , Eq. 4-5 can be re-written as:

$$q = \frac{dq}{dP} P = K_H P \quad \text{Eq. 4-6}$$

Eq. 4-6 is known as Henri's law, which demonstrates the proportionality of the amount of gas adsorbed with the pressure of the gas phase. The proportionality factor is called Henry's law coefficient,  $\mathbf{K}_H$  ( $\text{mol} \cdot \text{kg}^{-1} \cdot \text{Pa}^{-1}$ ).

The Henry isotherm model only offers an appropriate fit of the adsorbate adsorption at low pressure and thus unsuitable to be used in this study, as the adsorption isotherm measurements are done at a pressure higher than ambient allowing to reach high surface coverage / high degree of micropore filling with adsorbed phase, enabling significant intermolecular interactions.

#### ❖ Langmuir isotherm

Langmuir isotherm model is a two-parameter model that is easy to use and often provides a good approximation of experimental isotherms. It was developed based on a kinetics principle where the adsorption and desorption rates are equal, and the adsorption equilibrium will be defined as a state of dynamic equilibrium [229, 231]. The assumptions of this mathematical model are [232]:

1. Adsorption occurs in a single layer
2. The surface of adsorbent is energetically equivalent.
3. The adsorbed molecules are energetically isolated from one another., thus, there are no interactions between them.
4. Each adsorption site could only accommodate a single molecule.
5. Gas phase is considered ideal

Langmuir adsorption isotherm was originally developed in 1916 to describe gas–solid-phase adsorption onto activated carbon [233]. The Langmuir isotherm equation is given by:

$$q = q_m \cdot \frac{K_L \cdot P}{1 + (K_L \cdot P)} \quad \text{Eq. 4-7}$$

where  $q_m$  is the maximum adsorption capacity (mol. kg<sup>-1</sup>) and  $K_L$  (Pa<sup>-1</sup>) is the Langmuir coefficient representing the theoretical affinity parameter of the adsorption site-adsorbate. In addition, the linearized form of the Langmuir model, which can be used for data fitting, is given by:

$$\frac{1}{q} = \frac{1}{q_m} + \frac{1}{q_m(K_L \cdot P)} \quad \text{Eq. 4-8}$$

The Langmuir model describes adsorption isotherms of the type I with saturation at infinite pressure and is consistent with Henry's model at low pressures. An example on the application of this model to describe an adsorption isotherm is the work by Zito et al. [234], where Langmuir model was used to fit various experimental adsorption isotherms of pure gas (H<sub>2</sub>, CH<sub>4</sub>, CO<sub>2</sub>, CO and H<sub>2</sub>O) on Faujasite NaX and NaY zeolites, at analysis temperature ranging from 100 to 500 K and analysis pressure up to 5 bar. All experimental adsorption isotherms in this work display a type I isotherm shape, where a horizontal plateau could be observed after certain equilibrium pressure indicating saturation adsorption capacity of the adsorbent. It was observed that the Langmuir model fit well the experimental adsorption isotherms of each pure gas with a value of  $R^2 > 0.99$ .

In another work by Saha, D. and Deng, S. [235], CO adsorption on MOF-5 and MOF-177 was carried out at analysis temperature of 195 K, 237 K and 298 K as well as analysis pressure up to 1 bar. The obtained experimental adsorption isotherms was successfully described by Langmuir isotherm at the mentioned analysis condition.

#### b) Multilayer adsorption model

##### ❖ Brunauer–Emmett–Teller (BET)

Brunauer–Emmett–Teller (BET) model is a theoretical equation developed in 1938 [236] and it was an extended from the classical Langmuir adsorption isotherm with modification from monolayer to ideal multilayer adsorption. This model made use of the same assumptions as those in the Langmuir model, that is, for each layer, the surface is energetically homogenous and there is no interaction among adsorbed molecules. In addition to that, it assumes the formation of multiple layers of adsorbed molecules due to condensation phenomena starting from the second layer. As the adsorbed molecules on a layer is considered becoming the adsorption site for new molecules of the next layer,

it is theoretically possible to form an infinite number of layers,  $N$ , during adsorption of pure gas, where BET model could be expressed as:

$$\frac{q}{q_m} = \left( \frac{C_{\text{BET}} \cdot \frac{P}{P_0}}{1 - \frac{P}{P_0}} \right) \left( \frac{1 - \left[ (N+1) \cdot \left( \frac{P}{P_0} \right)^N \right] + \left[ N \cdot \left( \frac{P}{P_0} \right)^{N+1} \right]}{1 + \left[ (C_{\text{BET}} - 1) \cdot \frac{P}{P_0} \right] - \left[ C_{\text{BET}} \cdot \left( \frac{P}{P_0} \right)^{N+1} \right]} \right) \quad \text{Eq. 4-9}$$

where  $C_{\text{BET}}$  corresponds to BET constant that relates the adsorption energy of the first layer,  $E_1$ , to the liquefaction energy of the adsorbate,  $E_l$ , which could be expressed as:

$$C_{\text{BET}} = e^{\left( \frac{E_1 - E_l}{RT} \right)} \quad \text{Eq. 4-10}$$

Eq. 4-9 could be further simplified, as demonstrated in [237], where for a known value of  $C_{\text{BET}}$ , the graph of  $q/q_m = f(P/P_0, N)$  superposes with each other for whatever number of adsorption layer,  $N$ , at relative pressure less than 0.35. It could be said that, for a range of relative pressure  $P/P_0 < 0.35$  (commonly employed for specific surface area measurements), the BET model can be re-written as:

$$\frac{q}{q_m} = \frac{C_{\text{BET}} \cdot \frac{P}{P_0}}{\left[ 1 + (C_{\text{BET}} - 1) \left( \frac{P}{P_0} \right) \right] \left[ 1 - \left( \frac{P}{P_0} \right) \right]} \quad \text{Eq. 4-11}$$

where the linearized form for Eq. 4-11, as previously introduced in chapter 2, could be obtained:

$$\frac{P/P_0}{q(1 - P/P_0)} = \frac{1}{q_M C_{\text{BET}}} + \frac{C_{\text{BET}} - 1}{q_M C_{\text{BET}}} (P/P_0) \quad \text{Eq. 3-2}$$

It should be noted here that  $q_M$  signifies the monolayer saturation capacity, BET model is suitable to describe gas-adsorbent system in which results in the obtention of adsorption isotherm of type II or type III (non-porous solid), that generally involve the use of  $N_2$  as the pure gas at 77 K for the determination of the adsorbent's specific surface area [238]. However, when BET model is applied for microporous solid, there is a risk of micropore filling that takes places in the pores rather than mono or multilayer coverage, which could lead to the overestimation of specific surface area [239]. Thus, the choice of pressure range that respects the consistency criteria by Rouquerol *et al.* [180] (cf. section 3.4.6, page 75) is crucial in obtaining results comparable between different works.

### c) Empirical adsorption models

As there are diverse adsorbent materials with complex structure available today, it is inevitable that assumptions of models previously presented are unable to be respected, which leads to incompatibility of the adsorption models with experimental adsorption isotherms. For that purpose, multiple empirical models have been developed throughout

the years to describe gas-solid adsorption equilibria by various porous solids. Here, we summarize the most common models applied to describe physisorption by MOFs.

❖ Freundlich model

Freundlich model was originally developed in 1906 [240] and it is the earliest known empirical equation describing the non-ideal and reversible adsorption process, not restricted to the formation of an adsorbed monolayer. This model is able to account for multilayer adsorption, considering a non-uniform distribution of interaction intensities over a heterogeneous surface [232]. This adsorption isotherm equation is given by:

$$q = K_F \cdot P^{\frac{1}{n}} \quad \text{Eq. 4-12}$$

where  $K_F$  (mol. kg<sup>-1</sup>. Pa<sup>-1/n</sup>) is the Freundlich coefficient related to the adsorption capacity and  $n$  is the Freundlich constant representing the heterogeneity of the adsorbent surface. Freundlich model could also be written under a linear form as follows:

$$\log q = \log K_F + \frac{1}{n} \log P \quad \text{Eq. 4-13}$$

The value for  $1/n$  is generally less than 1 ( $0 < 1/n < 1$ ). When  $1/n$  has the value of 0, it signifies that the adsorption is constant and thus independent of pressure, whereas when  $1/n$  has the value of 1, it signifies that adsorption is directly proportional to pressure thus the adsorbent will never become saturated.

However, this Freundlich isotherm model has some theoretical limitations, restricting its experimental validity: it does not fit the Henry's law in the low-pressure range and does not predict any finite adsorption capacity at saturation pressure [231]. An infinite surface coverage in the high-pressure range is thus mathematically predicted, but this has no physical sense.

❖ Langmuir–Freundlich (or Sips) model

The Langmuir–Freundlich (or Sips) isotherm model was developed in 1948 [241], with the consideration of the surface heterogeneity of an adsorbent, which is contrary to that of the Langmuir model. Additionally, the Langmuir–Freundlich isotherm reaches a finite surface saturation limit at sufficiently high pressures, opposite to the Freundlich model. Sips isotherm model is given by:

$$q = q_m \cdot \frac{(K_S \cdot P)^{1/n}}{1 + (K_S \cdot P)^{1/n}} \quad \text{Eq. 4-14}$$

where  $K_S$  (mol. kg<sup>-1</sup>. Pa<sup>-1</sup>) is the Sips coefficient representing the theoretical affinity parameter of adsorption site-adsorbate and  $n$  is the Sips constant representing the surface heterogeneity parameter.



In general, Sips model works better than Freundlich model in describing the high-pressure range of an adsorption isotherm as it takes into consideration the saturation capacity of an adsorbent with a heterogenous surface. However, Sips model possess the same disadvantage as Freundlich model where it does not follow Henry's law when pressure is low [232]. Both the advantage and limitation of this model need to be taken into account before applying it to describe an experimental adsorption isotherm. As an example, Gargiulo et al. [242] have studied the CO<sub>2</sub> adsorption on mesoporous silica SBA-15 functionalized with polyethylenimine, at analysis temperature ranging between 298 K – 348 K and analysis pressure up to 1 bar. The experimental isotherm obtained in the study shows that at low pressure, the amount of CO<sub>2</sub> adsorbed is not proportional to the equilibrium pressure and as the equilibrium pressure approaches 1 bar, a horizontal plateau signifying the saturation with CO<sub>2</sub> could be observed. Sips model was successfully used to describe the experimental adsorption isotherm and the value of *n* obtained is greater than unity, demonstrating a certain degree of heterogeneity of the studied material.

#### ❖ Toth model

Toth isotherm model is another empirical equation developed in 1971 [243] to describe an adsorption with sub-monolayer coverage, supposing an asymmetrical quasi-Gaussian energy distribution, with most of the sites having an adsorption energy lower than the peak (maximum) or mean value [231]. It is expressed as follows:

$$q = q_m \cdot \frac{K_T \cdot P}{[1 + (K_T \cdot P)^n]^{1/n}} \quad \text{Eq. 4-15}$$

where **K<sub>T</sub>** (mol. kg<sup>-1</sup>. Pa<sup>-1/n</sup>) is the Toth coefficient representing the theoretical affinity of adsorption site-adsorbate and **n** is the Toth constant representing the surface heterogeneity parameter.

This model reduces to the Langmuir isotherm equation when *n* equals to 1 [229]. In addition to that, at low pressure, this model follows Henry's law [244]. Therefore, the Toth model is suitable to describe an adsorption isotherm where the amount of gas adsorbed at low pressure is proportional to the equilibrium pressure and there is a finite saturation capacity at higher pressure region. An example of the application of this model was demonstrated in the work of Wang et al. [245], where CH<sub>4</sub> adsorption on granulated AC was investigated at an analysis temperature range of 283 K – 328 K and analysis pressure up to 50 bar. The obtained experimental adsorption isotherm shows that, at low pressure, the quantity of CH<sub>4</sub> adsorbed is proportional to the equilibrium pressure and at higher pressure, the apparition of horizontal plateau starts to be observed. Authors confirm that Toth model was able to perfectly fit the experimental adsorption isotherm of the study.

#### ❖ Dual-site Langmuir model

The dual-site Langmuir model was developed to model an adsorbent surface with energetic heterogeneities, supposing two different types of adsorption sites [246]. As this model was derived from the Langmuir model, it retains the same assumptions, with the exception that each type of adsorption sites acts independently so that the dual-site Langmuir model results from the sum of the single Langmuir isotherm models applied to for the two types of sites [246]. It is expressed as follows:

$$q = q_{m,1} \cdot \frac{K_{DL,1} \cdot P}{1 + (K_{DL,1} \cdot P)} + q_{m,2} \cdot \frac{K_{DL,2} \cdot P}{1 + (K_{DL,2} \cdot P)} \quad \text{Eq. 4-16}$$

where  $q_{m,1}$  and  $q_{m,2}$  ( $\text{mol} \cdot \text{kg}^{-1}$ ) are the theoretical saturation capacity of gas per unit mass of adsorbent of site 1 and 2 respectively,  $K_{DL,1}$  and  $K_{DL,2}$  ( $\text{Pa}^{-1}$ ) are the Dual-site Langmuir coefficients representing the theoretical affinity parameter of adsorption site 1-adsorbate and site 2-adsorbate, respectively.

Since this model is based on a single Langmuir isotherm model, it also exhibits an asymptotic property at low pressures and there exist a finite limit at high concentration (pressure). A successful implementation of this model for particular pure gas adsorption isotherm signifies the existence of dual adsorption sites inside an adsorbent towards a particular adsorbate. Such is the case for the study of Chowdhury et al. [247], where adsorption of  $\text{CO}_2$  and  $\text{CH}_4$  along with  $\text{C}_3\text{H}_8$ ,  $\text{SF}_6$ , and Ar on MIL-101, were measured at three temperatures 283, 319, and 351 K and analysis pressure up to 10 bar. Authors highlighted that all pure gas adsorption isotherms were successfully modeled by the dual site Langmuir model, where the adsorption capacity of both sites differs significantly, demonstrating the heterogeneity of MIL-101 materials.

#### ❖ Dubinin–Radushkevitch (DR) model

The Dubinin–Radushkevich model is another empirical isotherm, which was specifically developed in 1947 [248, 229] for modeling of subcritical vapor adsorption onto the micropore solids, obeying a pore-filling mechanism. This model applied the potential theory developed by Polanyi [249], which assumes a heterogeneous “adsorption space” within which a molecule from the bulk phase loses an amount of potential energy and this potential increases with closer proximity to the solid surface. When the potential energy of a system is sufficient to bring the vapor to the saturation pressure, condensation occurs, leading to the liquefaction of the vapor. This condensation, together with the usually much smaller effects of concentration in the remainder of the adsorption space, accounts for physical adsorption.

Polanyi has described this adsorption potential,  $\epsilon_{\text{ads}}$ , as:

$$\epsilon_{\text{ads}} = RT \ln \left( \frac{P_0}{P} \right) \quad \text{Eq. 4-17}$$

where  $\epsilon_{\text{ads}}$  ( $\text{J} \cdot \text{mol}^{-1}$ ) is the adsorption potential. According to Polanyi [249], the quantity of adsorbed phase could therefore be expressed in the function of adsorption potential:

$$q = f(\epsilon_{\text{ads}}) \quad \text{Eq. 4-18}$$

The function  $f$  in Eq. 4-18 has not been defined theoretically and Dubinin and Radushkevich proposed their empirical equation [248, 229]:

$$q = q_m \cdot e^{\left(-\frac{1}{(\beta E_0)^2}(\epsilon_{ads})^2\right)} = q_m \cdot e^{\left(-\frac{1}{(\beta E_0)^2}\left(RT \ln \frac{P}{P_0}\right)^2\right)} \quad \text{Eq. 4-19}$$

where  $E_0$  ( $\text{kJ}\cdot\text{mol}^{-1}$ ) is the characteristic energy of adsorption towards a reference adsorbate and  $\beta$  is the similarity constant. Polanyi proposed [249] that the value of  $\beta$  for different adsorbates could be deduced from a reference adsorbate, often benzene:

$$\frac{\epsilon_{ads}}{\beta} = \frac{\epsilon_{ref}}{\beta_{ref}} \quad \text{Eq. 4-20}$$

where  $\beta_{ref} = 1$  for benzene and benzene potential curve is the  $\epsilon_{ref}$ .

DR equation is widely used to describe the adsorption isotherm of sub-critical vapors in microporous solids and is useful for the determination of the microporous volume and apparent surface area of this type of solids [250]. The model fits the data at high pressures and in the intermediate range of pressure as well, but does not predict the Henry's law at low pressures [232].

#### 4.1.3. Heat of adsorption

The heat of adsorption is an indicator of the strength of interaction between an adsorbate and a solid adsorbent. Heat of adsorption represents the difference in the enthalpy of the system prior to and after the adsorption process [251]. The heats of adsorption of components of a gas mixture are key thermodynamic variables for the design of practical gas separation processes such as pressure swing and thermal swing adsorption [252, 253]. Knowledge of heat of adsorption helps to determine the extents of temperature changes within the adsorbent bed during adsorption and desorption steps of the separation process. These temperature changes ultimately govern the performance of the separation process as desorption is favored at high temperature, whereas adsorption is favored at low temperature.

In addition, the heat of adsorption may also provide information about the mechanism of the adsorption process, either physisorption or chemisorption. In a physisorption process, the heat of adsorption is normally lower than 40  $\text{kJ/mol}$ , while in a chemisorption, it is significantly higher [224]. However, it should be noted that these limits are approximate and should be considered with caution in any theoretical analysis.

Two experimental procedures are commonly applied to assess the heat of adsorption: (i) calorimetric method (usually called direct method), which directly measures the heat released during the adsorption process and (ii) method of isosters (indirect method) deducing the adsorption heat from the quantitative relationship established at different equilibrium pressure and temperature data determined for a constant amount of the adsorbed substance [253].

#### ❖ Direct method

Direct calorimetric measurement of heats of adsorption,  $\Delta H$ , for pure gases or multicomponent gas systems is a convenient and accurate method [252]. The principle behind this method involves the measurement of heat flow profile followed by the integration of the obtained signal. It frequently operates in a fixed aliquot mode and can be coupled

with manometric set-up for simultaneous measurement of adsorption equilibria and associated adsorption heats. There are basically numerous types of calorimeters that are sensitive enough to directly measure the heat of adsorption of gas molecules such as but not limited to; (i) isoperibol (constant temperature) calorimeters, (ii) adiabatic calorimeters, and (iii) heat-flow calorimeters [254]. Nowadays, most modern calorimeters are of the heat-flow type, such as Tian-Calvet type heat flux microcalorimeter [252, 254].

❖ Indirect method

The determination of heat of adsorption via the indirect method may be preferred to the calorimetric method because of its ease of use [255].

This method determines the isosteric heat of adsorption from experimental isotherm data measured at different temperatures, assuming this quantity to be independent of temperature and pressure [229]. It may, however, vary with adsorption loading. Isosteric heat of adsorption,  $Q_{ST}$ , can be calculated from Van't Hoff thermodynamic equation which is assimilated to Clausius–Clapeyron-type relation (Eq. 4-21) at a given amount of adsorption loading [229]. By integrating Eq. 4-21, the linear function of  $\ln P$  versus  $1/T$  is obtained (Eq. 4-22).

$$Q_{ST} = -R \cdot \left( \frac{\partial \ln P}{\partial \frac{1}{T}} \right)_q \quad \text{Eq. 4-21}$$

$$\ln P = \frac{Q_{ST}}{R} \left( \frac{1}{T} \right) + C \quad \text{Eq. 4-22}$$

where,  $Q_{st}$  ( $\text{kJ} \cdot \text{mol}^{-1}$ ) and  $C$  is a constant.

Figure 4-2 illustrates the values of  $Q_{ST}$  determined from  $\text{CO}_2$  adsorption isotherms at 298 K, 308 K and 323 K onto 13X [137], which were subsequently fitted using three different isotherm models; Dual-site Langmuir-Freundlich (DLF), Sips and Freundlich. Figure 4-2-a compares the goodness of fit of the three isotherm models. DLF (solid lines) fits the isotherm data the best, followed by the Sips model (dashed lines) and the Freundlich model (dotted lines) respectively. The  $\text{CO}_2$  heat of adsorption data,  $Q_{ST}$ , derived from these different models are reported in Figure 4-2-b. The significances of the fitting goodness of the isotherm model are well enlightened, because the profile of adsorption heat in the function of the adsorbed amount is highly sensitive to the choice of the isotherm model.

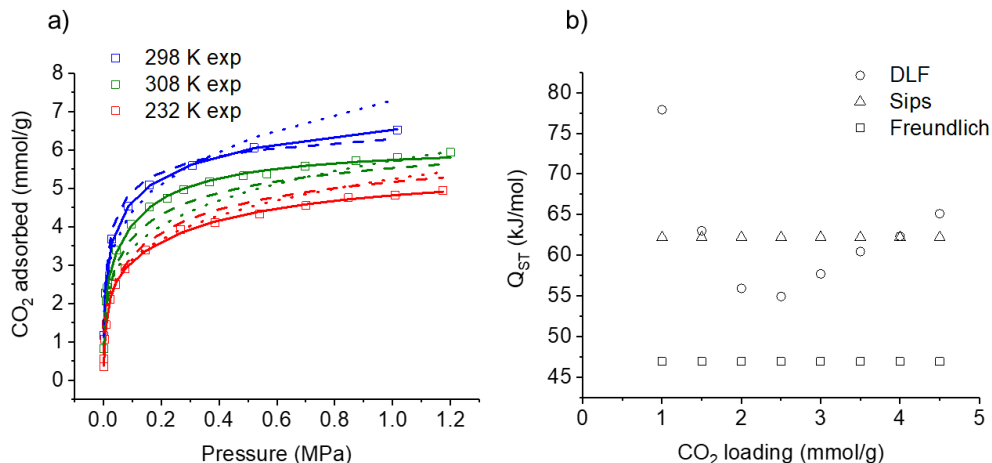


Figure 4-2: (a) CO<sub>2</sub> adsorption isotherm on 13X at 298 K, 308 K and 323 K with DLF fitting (solid line), Sips fitting (dashed line) and Freundlich fitting (dotted line). (b) Q<sub>ST</sub> values in function of CO<sub>2</sub> loading amount determined from DLF, Sips and Freundlich model.

Figure 4-3 shows the difference in the CO<sub>2</sub> heats of adsorption values, obtained from either direct or indirect methods for different adsorbents, at different loadings [256] [257] [258] [259] [260]. It can be observed that although the isosteric heat of adsorption Q<sub>ST</sub> and calorimetric heat of adsorption ΔH are generally in good agreement, with some deviations could be observed, around 30%. A comprehensive review by Du *et al.* [255] reports CO<sub>2</sub> heat of adsorption data obtained for HKUST-1 (Table 4-1) from different studies using either direct or indirect approaches. It should be noted that, even when using similar approaches for the determination of Q<sub>ST</sub>, slight variations still occur.

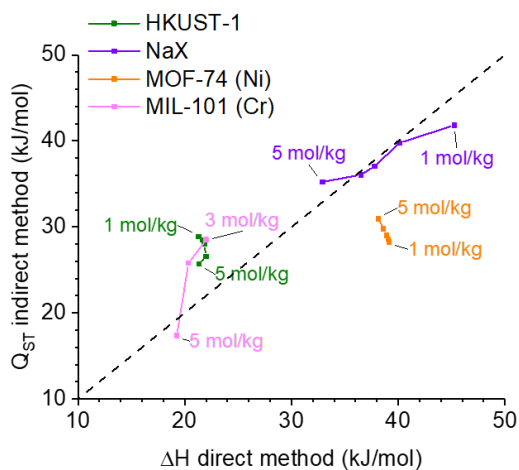


Figure 4-3: Comparison between isosteric heat of adsorption Q<sub>ST</sub>, and calorimetric heat heats of adsorption, ΔH, for a different quantity of CO<sub>2</sub> adsorbed.

Table 4-1: CO<sub>2</sub> heat of adsorption of HKUST-1 determine via direct and indirect approach.

Approach	Heat of adsorption (kJ/mol)	Description	Ref.
Calorimetric	30	Differential thermal analysis	[261]

	21.4 – 24.5	Calvet calorimeter	[256]
Isosteric	24.1 – 34.4	Without using fitting equation	[257]
	25.7 – 29.2	Pade fitting equation	[262]
	26.1 – 27.0	-	[263]

#### 4.1.4. Adsorption models for gas mixture

Industrial adsorption processes generally involve a mixture of several adsorbates interacting with each other. For these systems, it is important to know not only the adsorption isotherms of the pure substances but also the co-adsorption equilibria for mixtures, in order to make accurate predictions of process performances. Carrying out experimental measurement of adsorption isotherm for a gas mixture is generally more complicated than that of pure gas, which is why it is more interesting to develop co-adsorption models capable of predicting mixture behavior based on knowledge of pure substance isotherms. In this section, we will present a frequently used model for predicting the adsorption of gas mixture; Ideal Adsorbed Solution Theory (IAST).

##### a) Ideal Adsorbed Solution Theory (IAST)

Ideal adsorption solution theory was developed by Myers and Prausnitz [264] to provide a solid theoretical foundation in predicting multi-component adsorption isotherm from single pure component adsorption isotherm data. IAST works on the assumption that the adsorbed phase and gas phase forms an ideal mixture. This leads to an expression analogous to Raoult's law for the adsorbed phase as follows [246]:

$$y_i \cdot P = x_i \cdot P_i^0(\pi) \quad \text{Eq. 4-23}$$

where  $y_i$  and  $x_i$  are the molar fraction of gas component  $i$  in the gas and adsorbed phase respectively,  $P$  (Pa) is the pressure of gas mixture,  $P_i^0(\pi)$  is the hypothetical pressure of the pure component that gives the same spreading pressure on the surface

Next, to describe the thermodynamic equations for the adsorbed phase, three major assumptions were made [264]:

1. The adsorbent is assumed to be thermodynamically inert, i.e. the change in a thermodynamic property of the adsorbent, such as internal energy, during an adsorption process at constant temperature is assumed to be negligible compared with the change in the same property for the adsorbing gas.
2. Each adsorbed species has access to the same area of the adsorbent surface.
3. The Gibbs definition of adsorption applies to the adsorbed phase, i.e. Gibbs dividing surface equation defines an adsorbed phase accounting for the amount of adsorbate condensed in the pores in excess and the amount of gaseous adsorptive occupying the intra-particle voids.

With these assumptions, the basic thermodynamic equations for the adsorbed phase emerged in a form perfectly analogous to the familiar thermodynamic equations for a real fluid could be expressed as [246]:

$$A d\pi_i = \sum q_i^0 d\mu_i \quad \text{Eq. 4-24}$$

where  $A$  ( $\text{m}^2 \cdot \text{kg}^{-1}$ ) is the adsorption specific surface area,  $\pi_i$  (Pa. m) is the spreading pressure of component  $i$  in the pure gas system,  $\mu_i$  is the chemical potential of component  $i$  and  $q_i^0$  ( $\text{mol} \cdot \text{kg}^{-1}$ ) is the quantity of component  $i$  adsorbed when in equilibrium with the gas phase in the pure gas system. The integration of Eq. 4-24 leads to the following expression [246]:

$$\frac{\pi_i A}{RT} = \int_0^{P_i^0} \frac{q_i^0(P)}{P} dP \quad \text{Eq. 4-25}$$

Eq. 4-25 describe the thermodynamic equation of adsorbed phase in the pure gas system, expressed in function of the quantity of component  $i$  adsorbed in pure gas system,  $q_i^0$ , and the reference pressure of component  $i$  in pure gas system that has the same thermodynamic state as in the gas mixture system,  $P_i^0$ . It should be noted here that the expression of  $q_i^0$  depends on the chosen model to describe pure gas adsorption isotherm (cf. section 4.1.2, page 97).

In a gas mixture system, equilibrium is attained when the reduced spreading pressure ( $\pi_i A / (RT)$ ) has the same value for each component in the system. Assuming a binary component gas mixture, Eq 3-25 could be expressed as [246]:

$$\frac{\pi_1 A}{RT} = \frac{\pi_2 A}{RT} = \int_0^{P_1^0} \frac{q_1^0(P)}{P} dP = \int_0^{P_2^0} \frac{q_2^0(P)}{P} dP \quad \text{Eq. 4-26}$$

Using the above equations, the composition of the adsorbed phase  $x_i$  and the reference pressures  $P_i^0$ , (Eq. 4-23), can be determined, usually by numerical resolution. Since the solution of the adsorbed phase in the gas mixture system is ideal, the total quantity of the adsorbed phase is the sum of the adsorbed quantities of the various constituents [246]:

$$\frac{1}{q_t} = \sum_{i=1} \frac{x_i}{q_i^0(P_i^0)} \quad \text{Eq. 4-27}$$

where  $q_t$  ( $\text{mol} \cdot \text{kg}^{-1}$ ) is the total quantity of component  $i$  adsorbed in the mixture gas system. As the value of  $q_t$  and  $x_i$  for each component in the gas mixture system are identified, it is possible to predict the co-adsorption capacity of the component in the gas mixture system,  $q_i$  ( $\text{mol} \cdot \text{kg}^{-1}$ ), expressed as follows [246]:

$$q_i = x_i \cdot q_t \quad \text{Eq. 4-28}$$

Finally, the IAST- equilibrium selectivity,  $\alpha_{i/j}^{IAST}$ , was derived from the distribution of the molar fractions of the components in both the gas and adsorbed phases at equilibrium conditions, as expressed in Eq. 4-29 [246]:

$$\alpha_{i/j}^{IAST} = \frac{x_i^{IAST}/x_j^{IAST}}{y_i/y_j} \quad \text{Eq. 4-29}$$

It should be noted that the non-ideality of the adsorbed phase can be modeled by introducing vapor-liquid equilibrium theories for non-ideal solutions (activity coefficients, etc.). This is the basis of Real Adsorbed Solution Theory (RAS) though we will not explain it in further detail in this work.

## 4.2. Experimental methods

### 4.2.1. Manometric measurement

#### a) General approach

Measurements of pure gas adsorption isotherms in this study were done via the manometric method. This technique measures the amount of gas removed from the gas phase in a static mode by determining the pressure drop  $\Delta P$  in a fixed volume [265]. General configuration of manometric equipment is shown in Figure 4-4. The equipment generally consists of two main compartments: a reservoir and a sample cell.

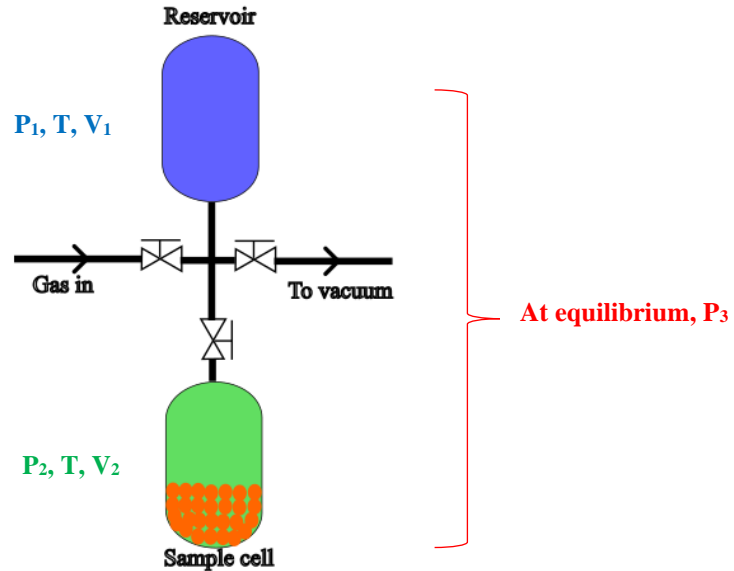


Figure 4-4: General configuration of manometric apparatus where the sample cell temperature equals to the reservoir temperature

The determination of gas removed from the gas phase in manometric experiments is based on the application of non-ideal gas law as presented in Eq. 4-30. If  $V$  and  $T$  are known, the measurement of  $P$  at equilibrium allows the determination of the number of moles of gas present in the bulk phase.



$$P \cdot V = n \cdot Z \cdot R \cdot T \quad \text{Eq. 4-30}$$

where  $P$  (Pa) is gas pressure,  $V$  ( $\text{m}^3$ ) is the gas volume,  $n$  is the number of moles in the gas phase,  $Z$  is the gas compressibility factor ( $Z=1$  for an ideal gas),  $R$  ( $\text{J} \cdot \text{mol}^{-1} \cdot \text{K}^{-1}$ ) is the gas constant and  $T$  (K) is the temperature).

Prior to measurement of equilibrium data, the adsorbent samples in the sample cell were degassed at 383 K for 12 h under dynamic vacuum condition. Following cell, both sample cell and reservoir were connected together by opening the separating valve and they are both held under vacuum to remove any trace of residual gases in the equipment. Then, the separating valve was closed, the reservoir was pressurized with the tested gas up to an initial pressure  $P_1$ , whereas the sample cell is kept under vacuum (denoted  $P_2$  in a general case). In order to dose the amount of gas introduced into the sample cell, the separating valve between the reservoir and the sample cell is re-opened and the new equilibrium pressure  $P_3$  is determined in both vessels after equilibration delay, determined from the rate of gas pressure variation. By applying a mass balance on the system, the number of moles adsorbed in excess per unit of mass of the adsorbent sample can be determined. The mass balance equation is expressed according to Eq. 4-30 [50]:

$$\Delta n = \frac{P_1 \cdot V_1}{Z_{P_1,T} \cdot R \cdot T} - \frac{P_3 \cdot (V_1 + V_2)}{Z_{P_3,T} \cdot R \cdot T} \quad \text{Eq. 4-31}$$

where  $\Delta n$  (mol) is the number of moles adsorbed,  $Z_{P_1,T}$  and  $Z_{P_3,T}$  are the gas compressibility factors,  $P_1$  and  $P_3$  are respectively the pressure in the reservoir before dosing and the equilibrium pressure in both the reservoir and sample cell,  $V_1$  is the volume of the reservoir and  $V_2$  is the dead volume in the sample cell which include inter and intra porosity of adsorbent.

Once the first equilibrium data point is determined, the reservoir is re-pressurized to a new initial pressure, whilst the pressure in the sample cell is kept to the previous equilibrium pressure by closing the separating valve. After introducing a new gas dose into the sample cell by re-opening the separating valve, a new equilibration pressure is attained in both vessels, which allows the determination of the new isotherm point. Therefore, Eq. 4-32 can be further generalized to determine the number of moles adsorbed in excess at any instantaneous point  $m$  of an isotherm:

$$n_{\text{ads},m} = \sum_{m=1}^m \left[ \underbrace{\frac{P_{1,m} \cdot V_1}{Z_{P_{1,m},T} \cdot R \cdot T}}_{\text{Moles in } V_1 \text{ before dosing}} + \underbrace{\frac{P_{2,m} \cdot V_2}{Z_{P_{2,m},T} \cdot R \cdot T}}_{\text{Moles in } V_2 \text{ before dosing}} - \underbrace{\frac{P_{3,m} \cdot (V_1 + V_2)}{Z_{P_{3,m},T} \cdot R \cdot T}}_{\text{Moles in } V_1 + V_2 \text{ at equilibrium}} \right] \quad \text{Eq. 4-32}$$

It should be noted that  $P_{3,m} = P_{2,m-1}$  and that the value of the compressibility factor  $Z$  can be assumed as 1 for the acquisition of equilibrium data at pressure and temperature close to ambient as most gases behave as ideal under these conditions. The non-ideality of the gas needs to be accounted for the acquisition of data at elevated pressure. In this study, the well-developed NIST REFPROP database, derived from a variety of thermodynamic state equations, which provides a large panel properties of different fluids, was used for the determination of the compressibility factor [266].

The determination of dead volume in the sample cell,  $V_2$ , can be done either through indirect or direct method. The former approach consists of deducing the volume non occupied by adsorbent by determining the skeletal density of the adsorbent via ex-situ Helium pycnometry analysis [267] whereas the direct determination of dead volume,  $V_2$ , involves the usage of an *in situ* Helium gas expansion approach. In this study, we have adopted the direct approach to determine the value of  $V_2$ . Supposing He to be a non-adsorbing gas ( $n_{ads,m} = 0$ ) dosing sample cell with He aliquots allows to deduce  $V_2$ , Eq 3-32.

b) Influence of temperature on manometric measurement

Up to this point, the configuration of a manometric equipment was described in the condition where the temperature of analysis in the sample cell is assumed to be equal to temperature of the reservoir,  $T$ . However, this condition is not necessarily true as the measurement of isotherm may be conducted at temperature that differs significantly from those in the reservoir. This situation will result in temperature inhomogeneities along the system which need to be accounted for when determining the dead volume in the sample cell,  $V_2$ . Figure 4-5 describes the configuration of the manometric apparatus when a single gas component is adsorbed with a gradient temperature between the reservoir  $T_1$ , and the sample cell  $T_2$ . In this configuration, the term apparent “up” dead volume  $V_u$ , and “down” dead volume  $V_d$ , are introduced to separate two regions in the sample cell  $V_2$ , which are at different temperature.  $V_u$  is the upper region in the sample cell at the temperature of the reservoir  $T_1$ , while  $V_D$  is the lower region in the sample cell at the analysis temperature  $T_2$ .

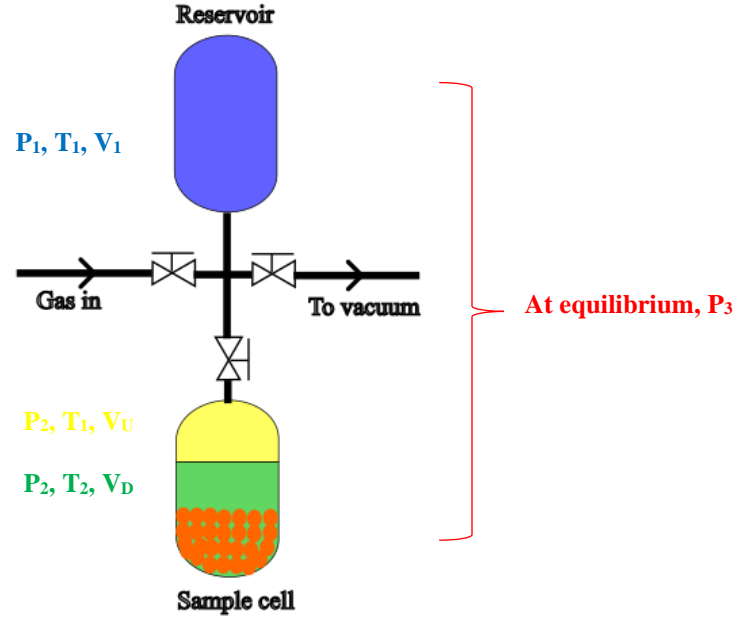


Figure 4-5: Configuration of the manometric system taking into consideration the gradient of temperature between the sample cell and the gas reservoir

Knowing that  $V_2 = V_u + V_D$  in the condition where analysis temperature in the sample cell,  $T_2$  differs from reservoir temperature,  $T_1$ , then Eq. 4-32 becomes:

$$n_{\text{ads},m} = \sum_{m=1}^m \left[ \frac{P_{1,m} \cdot V_1}{Z_{P_{1,m}T_1} \cdot R \cdot T_1} + \frac{P_{2,m} \cdot V_U}{Z_{P_{2,m}T_2} \cdot R \cdot T_2} + \frac{P_{2,m} \cdot V_D}{Z_{P_{2,m}T_2} \cdot R \cdot T_2} - \frac{P_{3,m} \cdot V_1}{Z_{P_{3,m}T_1} \cdot R \cdot T_1} - \frac{P_{3,m} \cdot V_U}{Z_{P_{3,m}T_1} \cdot R \cdot T_1} - \frac{P_{3,m} \cdot V_D}{Z_{P_{3,m}T_2} \cdot R \cdot T_2} \right] \quad \text{Eq. 4-33}$$

The determination of temperature depended dead volume  $V_U$  and  $V_D$  are obtained from helium expansion experiments. This experiment starts with the assumption that there is no adsorption of helium by the adsorbent and the sample cell was initially void of gas ( $P_2 = 0$ ). Furthermore, the reservoir was initially filled with helium at pressure  $P_1$  and both the sample cell and the reservoir achieved equilibrium pressure of  $P_3$  when dosing was done. When the analysis temperature for the helium expansion experiment is similar to the reservoir temperature,  $T_1$ , the gas mass conservation in the system can be written as:

$$\frac{P_1 \cdot V_1}{R \cdot T_1} = \frac{P_3 (V_1 + V_{2,T_1})}{R \cdot T_1} \quad \text{Eq. 4-34}$$

When the analysis temperature inside the sample cell differs from the reservoir,  $T_2 \neq T_1$ , then  $V_2 = V_{2,T_2} = V_U + V_D$ . In this condition, the gas mass conservation in the system can be written as:

$$\frac{P_1 \cdot V_1}{R \cdot T_1} = \frac{P_3 \cdot V_1}{R \cdot T_1} + \frac{P_3 \cdot V_U}{R \cdot T_1} + \frac{P_3 \cdot V_D}{R \cdot T_2}$$

$$\frac{P_1 \cdot V_1}{R \cdot T_1} = \frac{P_3 \cdot (V_1 + V_U)}{R \cdot T_1} + \frac{P_3 \cdot V_D}{R \cdot T_2} \quad \text{Eq. 4-35}$$

By combining Eq. 4-34 with Eq. 4-35, either  $V_D$  or  $V_U$  can be determined from helium expansion measurement at two controlled temperatures  $T_1$  and  $T_2$  respectively:

$$\begin{aligned} \frac{P_3 \cdot (V_1 + V_{2,T_1})}{R \cdot T_1} &= \frac{P_3 \cdot (V_1 + V_U)}{R \cdot T_1} + \frac{P_3 \cdot V_D}{R \cdot T_2} \\ \frac{V_{2,T_1} - V_U}{T_1} &= \frac{V_D}{T_2} \end{aligned} \quad \text{Eq. 4-36}$$

As  $V_2 = V_{2,T_2} = V_U + V_D$ , Eq. 4-36 can be further simplified into:

$$V_D = \frac{V_{2,T_1} - V_{2,T_2}}{\left(\frac{T_1}{T_2} - 1\right)} \quad \text{Eq. 4-37}$$

When  $V_D$  was determined from the helium-calibrated values of  $V_{2,T_1}$  and  $V_{2,T_2}$ ,  $V_U$  can then be calculated. Once  $V_D$  and  $V_U$  are determined, Eq. 4-33 can be used to determine the amount of gas adsorbed at any isotherm point.

### c) Influence of high pressure on manometric measurement

In general, adsorption refers to the increase in the Eq.y of a gas (or fluid) near a solid surface. Figure 4-6-a shows the density profile of a gas near the surface for the case of single-component adsorption [268]. Three regions can be identified in the figure, from left to right: (1) the density is zero in the solid region, (2) the interfacial region where there are presence of adsorbed molecules (black circles) and unabsorbed molecules (white circles, and the density is substantially higher because of the potential field of the solid, (3) gas region where the density decays to the bulk gas density at some far away distance from the surface [269]. The interface region poses some uncertainty when the calculation of the total gas adsorbed wanted to be carried out, as there is ambiguity concerning the choice of lower boundary limit of the interface region that depends on the type of gas.

According to Gibbs, the boundary of the interfacial region between adsorbed and gas phases [270], can be defined by a so called Gibbs Dividing Surface (GDS) located somewhere within the interfacial region, as illustrated in Figure 4-6-b. The gas region with volume  $V^g$  has a homogeneous density,  $\rho^g$  (mol.  $m^3$ ), up to the dividing surface, whereas the adsorbed phase region with volume  $V^a$  and density  $\rho(z)$ . At the surface of adsorbent, the adsorbed molecules are supposedly under condensed liquid-like form has a higher density than gas phase (area of “a” in Figure 4-6-b) whereas the unabsorbed molecules located further than the adsorbent surface have a similar density to bulk gas phase (area of “b” in Figure 4-6-b).

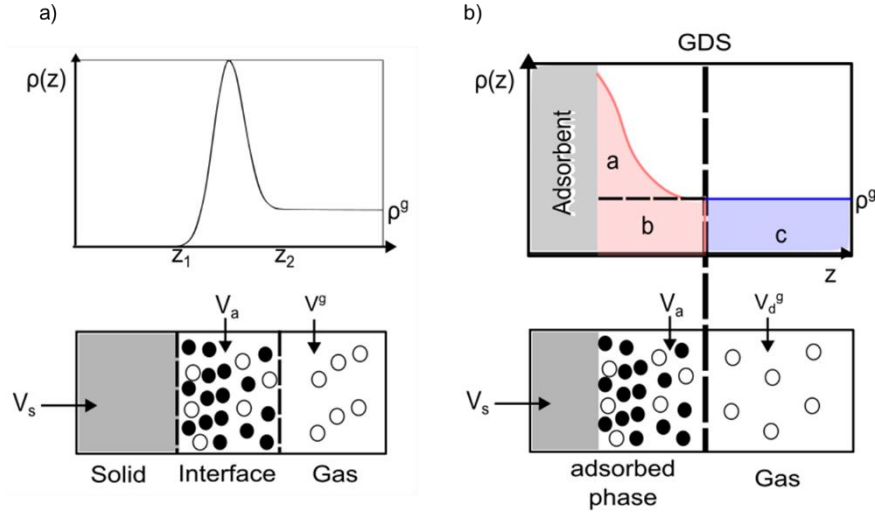


Figure 4-6: (a) Profile of gas density at standard gas-solid interface (b) Profile of gas density with introduction of GDS.

The measured adsorbed quantities in manometric experiments (and other volume-basis measurement techniques) can be related to net, absolute and excess adsorption concepts (Figure 4-7) [271]. What separates these concepts between each other is the location of GDS.

In absolute adsorption, the GDS is drawn around the adsorbent solid particle, which comprises the porous solid and the micropore volume. In this case, the volume of adsorbed phase,  $V^a$ , and the volume of gas phase region,  $V^g$ , are expressed as follows:

$$V^a = V^s + V_{pore} = V_{abs}^a \quad \text{Eq. 4-38}$$

$$V^g = V_{cell} - V^s - V_{pore} = V_{abs}^g \quad \text{Eq. 4-39}$$

Where the suffix “abs” signifies the absolute adsorption condition,  $V^s$  is the inaccessible solid volume and  $V_{cell}$  is the volume of the sample cell.

Meanwhile, in excess adsorption, the GDS is drawn through the pores to consider only the inaccessible solid phase volume. Therefore, the volume of adsorbed phase,  $V^a$ , and the volume of gas phase region,  $V^g$ , are expressed as follows:

$$V^a = V^s = V_{ex}^a \quad \text{Eq. 4-40}$$

$$V^g = V_{cell} - V^s + V_{pore} = V_{ex}^g \quad \text{Eq. 4-41}$$

Where the suffix “ex” signifies the excess adsorption condition.

Lastly, in net adsorption, the GDS is defined to make the volume adsorbed phase region,  $V^a$ , to be zero, whereas the volume of gas phase region,  $V_{net}^g$ , is the volume of sample cell, as expressed as follows:

$$V^a = 0 = V_{net}^a \quad \text{Eq. 4-42}$$

$$V^g = V_{cell} = V_{ex}^g \quad \text{Eq. 4-43}$$

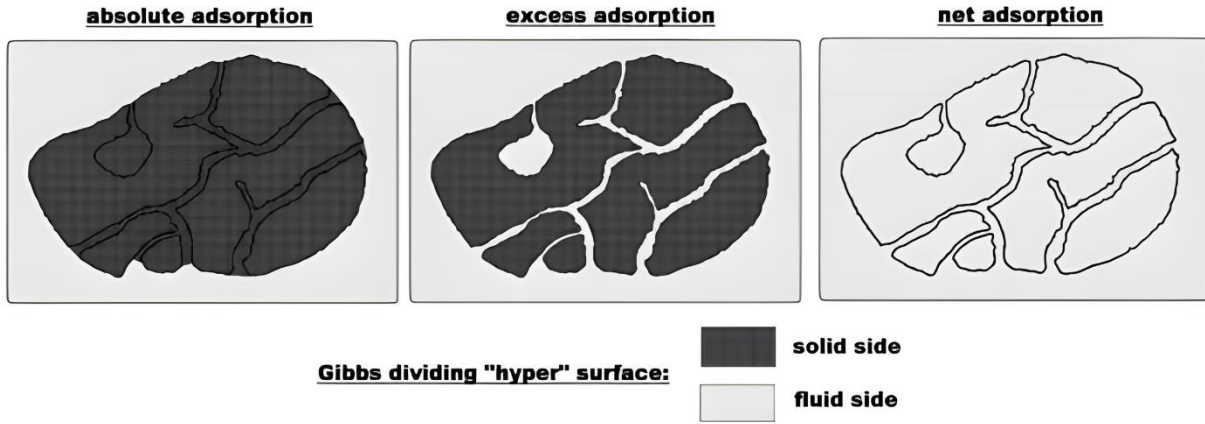


Figure 4-7: Illustration of Gibbs hyper-surface definitions by absolute, excess, and net adsorption. Dark shaded regions are not accessible by fluid molecules [271]

As previously described, the manometric measurement conducted in this study involves the use of Helium as probe molecules to determine the dead volume of the adsorption system. In other words, the volume of gas phase region defined during the manometric measurement is equivalent to the condition where GDS is drawn on the surface of the solid, which results in the volume of adsorbed phase region  $V^a$  and gas region  $V^g$  expressed as Eq. 4-39 and Eq.3-40 respectively. Consequently, the amount of adsorbed gas at measured at each equilibrium pressure as expressed in Eq. 4-32 corresponds to excess adsorbed quantity,  $n_{ex}$

At elevated pressure conditions, the density of uncondensed gas molecules near the solid surface,  $\rho^g$ , approaches or may even surpass that of condensed adsorbed phase (Figure 4-6-b). making measured excess adsorbed quantity,  $n_{ex}$ , zero or negative. Therefore, for the adsorption measurements at high pressure range, it is recommended to convert the measured excess adsorbed quantity  $n_{ex}$ , into absolute adsorbed quantity,  $n_{abs}$ . The value of  $n_{abs}$  can be computed using the following expression [271]:

$$n_{abs} = n_{ex} + \rho_g V_{pore} \quad \text{Eq. 4-44}$$

Figure 4-8 illustrates the evolution of  $n_{ex}$  and  $n_{abs}$  as the adsorption pressure increases. At low pressure, the value of  $n_{ex}$  is very similar to  $n_{abs}$  as there are not much of uncondensed gas molecules near the surface of adsorbent. However, at point C, the value of  $n_{ex}$  starts to stagnant and decreases as higher pressure, due to the increases the gas density resulting in the presence of more and more uncondensed molecules near the adsorbent surface. In this work, the chosen analysis pressure is not sufficiently high and it was verified that the fraction of uncondensed molecules near the adsorbent surface could be omitted. Therefore, the measured excess adsorbed capacity,  $n_{ex}$  is similar to the absolute adsorbed quantity,  $n_{abs}$ , in the tested analysis condition ( $n_{abs} \approx n_{ex}$ ).

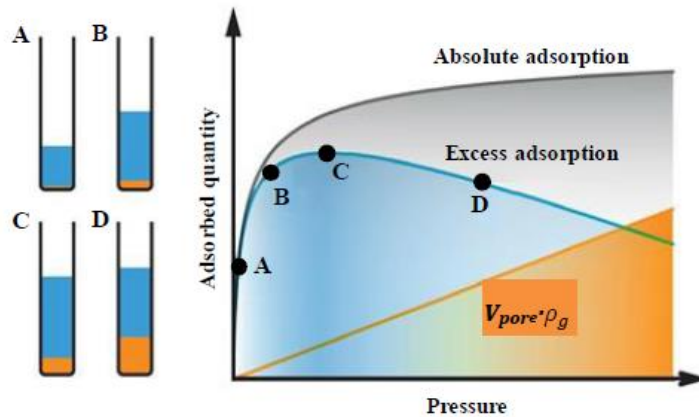


Figure 4-8 : A schematic representation of the difference between excess and absolute adsorption capacities as a function of pressure at constant temperature [272].

d) Materials and protocol for manometric measurement

The adsorption isotherms at pressure less than 1 bar were measured using the 3Flex manometric adsorption analyzer from Micromeritics (Unterschleißheim, Germany) at IMT Atlantique (Figure 4-9-a). Ultrahigh purity CO<sub>2</sub> and CH<sub>4</sub> gases (>99.995 vol%) supplied by Air Liquide were used for this study. The instrument is capable of measuring equilibrium data in the domain of relative pressure  $P/P^0$  ( $P$  is the gas probe set pressure and  $P^0$  is the saturation pressure) ranging between  $10^{-7}$  and 1 bar with 0.15% precision of absolute pressure reading. The acquisition was performed in a fixed-dose mode, whereas the temperature of the materials in the sample cells was controlled by a water bath contained in a Dewar vessel, set to 273 K, 298 K and 323 K respectively. Prior to measurements of gas equilibrium data, a mass of adsorbent of about 100 to 200 mg was placed in each sample cell and further outgassed under dynamic vacuum condition, at 383 K and for at least 12h. The dead volumes corresponding to the volumes non-occupied by the solid phase were determined from helium expansion measurements carried out at ambient and sample cell temperature, respectively.

Next, the adsorption isotherms at pressure higher than 1 bar were measured the using PCT-Pro manometric equipment from SETARAM (Caluire, France) at IMT Atlantique (Figure 4-9-b), in the range of pressure from 1 bar up to 10 bar. Ultrahigh purity CO<sub>2</sub> and CH<sub>4</sub> gases (>99.995 vol%) supplied by Air Liquide were used to carry out the experiments. The adsorption equilibrium data were measured by varying the increment of pressure between the reservoir and sample cell ( $\Delta P = P_1 - P_2$ ) before dosage: i.e.  $\Delta P = 0.5$  bar for equilibrium pressure  $P_3 \leq 3$ bar, and  $\Delta P = 1$  bar for  $P_3 > 3$  bar. The isotherms were determined at three different temperatures; 273 K, 298 K and 323 K. The sample holder made up of stainless steel with a cylindrical shape has a volume of 40 cm<sup>3</sup>. The temperature inside the sample cell is controlled thanks to a heating jacket, an isolation coating and a thermocouple when heating above room temperature. A water bath in a Dewar vessel was used for chilling below room temperature. The whole manometric system (pipelines, reservoirs and sample cell) was first evacuated using a vacuum pump and purged using a gas probe. 2 g of material was placed inside the sample holder and cylindrical stainless-steel spacers were used to fill in the remaining volume inside it. Prior to the equilibrium data measurement, the sample was outgassed *in situ* under dynamic vacuum conditions, at 283 K for at least 12h. Next, the sample holder dead volume was determined from

helium expansion experiments maintaining the sample cell temperature equals to the reservoir temperature (301 K) or set to the analysis temperature.

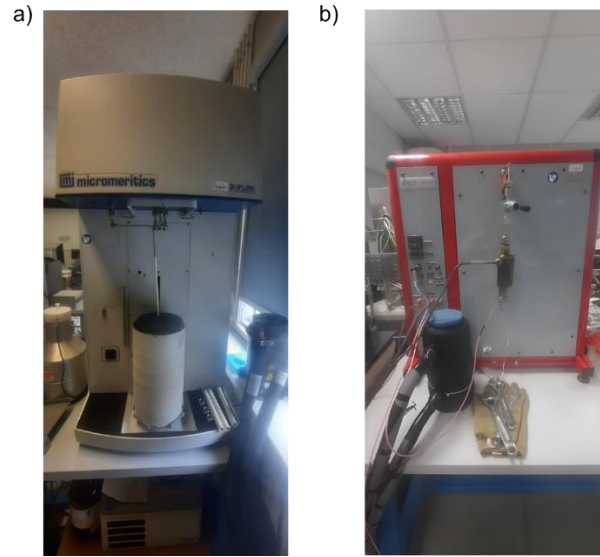


Figure 4-9: (a) Micromeritics 3Flex used in this work for adsorption isotherm measurement at pressure up to 1 bar. (b) SETARAM PCT-PRO used in this work for adsorption isotherm measurement at pressure up to 10 bar.

#### 4.2.2. Fitting of adsorption model for pure gas isotherm

In this work, the fitting of adsorption models, which previously introduced in section 4.1.2, page 97, with experimental CO<sub>2</sub> and CH<sub>4</sub> adsorption isotherms data was carried out using following adsorption models:

1. Henry's law
2. Langmuir
3. Freundlich
4. Sips
5. Toth
6. Dual-site Langmuir

As the raw adsorption data collection was done at different temperature (273 K, 293 K and 323 K), the influenced of temperature needs to be taken into account to ensure that the tested adsorption model above fits well the experimental results at any given temperature. As an example, the temperature dependent Henry's coefficient,  $K_H$ , is expressed as:

$$K_H = k_1 e^{k_2 \left( \frac{1}{T} - \frac{1}{T_{ref}} \right)} \quad \text{Eq. 4-45}$$

where  $k_1$  (Pa<sup>-1</sup>) and  $k_2$  (K) is respectively the pre-exponential and exponential constant for temperature dependence of  $K_H$ , whereas  $T$  and  $T_{ref}$  is respectively the analysis temperature and reference temperature. It should be noted that Eq. 4-45 could also be used to expressed the Langmuir coefficient ( $K_L$ ), Freundlich coefficient ( $K_F$ ), Sips coefficient ( $K_{LF}$ )



and Toth coefficient ( $K_T$ ) in function of temperature. Meanwhile, for DSL model that have two coefficients, which corresponds to two adsorption sites, their temperature dependent expression are as follows:

$$K_{DL,1} = k_{a,1} e^{k_{b,1} \left( \frac{1}{T} - \frac{1}{T_{ref}} \right)} \quad \text{Eq. 4-46}$$

$$K_{DL,2} = k_{a,2} e^{k_{b,2} \left( \frac{1}{T} - \frac{1}{T_{ref}} \right)} \quad \text{Eq. 4-47}$$

where  $k_{a,1}$  ( $\text{Pa}^{-1}$ ) and  $k_{a,2}$  ( $\text{Pa}^{-1}$ ) is respectively the pre-exponential constant for adsorption site 1 and site 2, whereas and exponential constant for temperature dependence of  $K_H$ , whereas  $k_{b,1}$  ( $\text{K}^{-1}$ ) and  $k_{b,2}$  ( $\text{K}^{-1}$ ) is respectively exponential constant for adsorption site 1 and site 2.

As previously explained, an adsorption model could be said to describe well an adsorption isotherm when the predicted values of the former are similar or closely resemble to that of the latter at any analysis conditions. To achieve this, the parameters of each adsorption model need to be estimated and optimized. Additionally, the optimized parameters must physically make senses, which is achieved by considering a constraint for each adsorption model parameter (e.g.  $q_s$ ,  $K_H$ ,  $n$ ) that must have a positive value  $> 0$ .

The optimization of parameters for each tested adsorption model was carried out using Least Square Method (LSM). The main idea of LSM is to reduce the error between the predicted value of a model and raw data by finding the optimal parameters of linear/non-linear regression. The optimal parameters were obtained by minimizing the residual sum of squares (RSS), expressed as:

$$\text{RSS} = \sum_{i=1}^n (q_{\text{exp}} - q_{\text{model}})_i^2 \quad \text{Eq. 4-48}$$

where  $q_{\text{exp}}$  ( $\text{mol. kg}^{-1}$ ) is the measured adsorption capacity value whereas  $q_{\text{model}}$  ( $\text{mol. kg}^{-1}$ ) is the predicted value from an adsorption model. The estimation and optimization of the adsorption model parameters can be done either analytically or numerically.

➤ Analytical solution

Assuming linearized Langmuir model are used to fit the raw adsorption data, then  $q_{\text{model}}$  could be expressed as:

$$q_{\text{model}} = \frac{1}{q_s (K_L \cdot P)} + \frac{1}{q_s}$$

$$q_{\text{model}} = b_0 \frac{1}{P} + b_1 \quad \text{Eq. 4-49}$$

where  $b_0 = 1/(q_s \cdot K_L)$  and  $b_1 = 1/q_s$ . Adsorbed amount thus becomes function of two variables:  $b_0$  and  $b_1$ .

When RSS function is minimal, the partial derivatives with the respect of each variable = 0:

$$RSS = \sum_{i=1}^n (q_{exp} - q_{model})_i^2 = \sum_{i=1}^n \left( q_{exp} - b_0 \frac{1}{P} + b_1 \right)_i^2 \rightarrow \min$$

$$\left\{ \begin{array}{l} \frac{\partial RSS}{\partial b_1} = -2 \cdot \sum_{i=1}^n \left( q_{exp} - b_0 \frac{1}{P} + b_1 \right) \cdot \frac{1}{P} = 0 \\ \frac{\partial RSS}{\partial b_0} = -2 \cdot \sum_{i=1}^n \left( q_{exp} - b_0 \frac{1}{P} + b_1 \right) = 0 \end{array} \right.$$

By solving differential equations for simple linear regression, we obtained:

$$\left\{ \begin{array}{l} b_0 \sum_{i=1}^n \left( \frac{1}{P} \right)^2 + b_1 \sum_{i=1}^n \left( \frac{1}{P} \right) = \sum_{i=1}^n \left( \frac{1}{P} \right) \cdot q_{exp} \\ b_0 \sum_{i=1}^n \left( \frac{1}{P_i} \right) + b_1 \cdot n = \sum_{i=1}^n q_{exp} \end{array} \right. \quad \begin{array}{l} \text{Eq. 4-50} \\ \text{Eq. 4-51} \end{array}$$

Solving the sum of two linear equations, the values of  $b_0$  and  $b_1$  can be calculated and thus the saturation capacity,  $q_s$ , and equilibrium Langmuir constant,  $K_L$ , can be deduced correspondingly. The analytical solution for LSM could be applied to any of the previously mentioned isotherm model either in linearized or non-linearized form. In this work, we did not adopt the linear approach, as it is too time consuming with different adsorption models that wanted to be tested. Instead, we have carried out the optimization using numerical approach.

#### ➤ Numerical solution

The numerical approach to minimize the RSS is a much easier and faster than analytical approach. In this approach, the estimations and optimizations of adsorption model parameters are implemented using algorithms and are executed on computers. Four concepts are essential in optimization of parameters in the numerical approach:

1. Decision variables
2. Objective function
3. Constraint
4. Linearity

A decision variable is the input parameters chosen in a problem represented by a model. In this work, the parameters of an adsorption model are chosen as the decision variables. As an example, the decision variables in this work for Langmuir model are  $k_1$ ,  $k_2$ , and  $q_s$ . The decision variables are the value that will be estimated iteratively in numerical approach.

An objective function is a mathematical formula that calculates the result the decision maker uses to determine how well their choices work out. The objective function in this work is the RSS and we seek to minimize it.

A constraint is a restriction or requirement that decision variables must meet. In this work, the constraint for all decision variables is that they must not have a negative value.

Linearity refers to the mathematical form of the objective function and constraints, which determine which algorithm that can be used for the iterative calculation of decision variable values and objective function. In this work, all the tested adsorption models are used in their non-linear form.

The algorithm used in this to find the optimal values of the decision variables is the Generalized Reduced Gradient (GRG) nonlinear algorithm. It takes the initial values of the decision variables (value defined randomly by decision maker) as its initial solution and considers small changes in those variables until the minimization of objective function.

In this work, the numerical approach for the optimization of an adsorption model parameters was carried out using “solver” tools in Excel.

Finally, to quantify the goodness of fitting of equilibrium experimental data with isotherm model after LSM, another error function called coefficient of determination,  $R^2$ , (Eq 3-52) was computed in this study. The goodness of fit of an isotherm model is justified by maximizing  $R^2$  approaching 1 and minimizing RSS approaching 0.  $R^2$  is defined as follows [232].

$$R^2 = 1 - \frac{\left( q_{\text{exp}} - q_{\text{model}} \right)^2}{\sum \left( q_{\text{exp}} - \overline{q_{\text{exp}}} \right)^2} \quad \text{Eq. 4-52}$$

Where  $\overline{q_{\text{model}}}$  (mol. kg<sup>-1</sup>) is the mean value of  $q_{\text{model}}$ .

#### 4.2.3. Computation of adsorption heat

When the most suitable adsorption model was chosen to describe the adsorption isotherms of pure gas at any analysis condition, the calculation of isosteric heat of adsorption  $Q_{ST}$  could be carried out. Figure 4-10 helps to illustrate the method to determine  $Q_{ST}$  from a pure gas adsorption isotherm model at different temperature values. First, for each adsorbed amount of equilibrium loading  $q$ , we determined is the value of equilibrium pressure  $P_i$  at each temperature level  $T_i$ . Next, the plot  $\ln P$  vs.  $1/T$  for each  $q_{\text{eq}}$  is built (isoster), and according to Eq. 4-22, the  $Q_{st}$  can be determined from the slope of the line. It should be highlighted that for a large range of systems, isosters are linear in  $\ln P$  vs.  $1/T$  coordinates [257, 258, 273] By repeating above steps for different value of equilibrium loading, the graph of  $Q_{ST}$  in function of  $q$  could be traced for a particular gas.

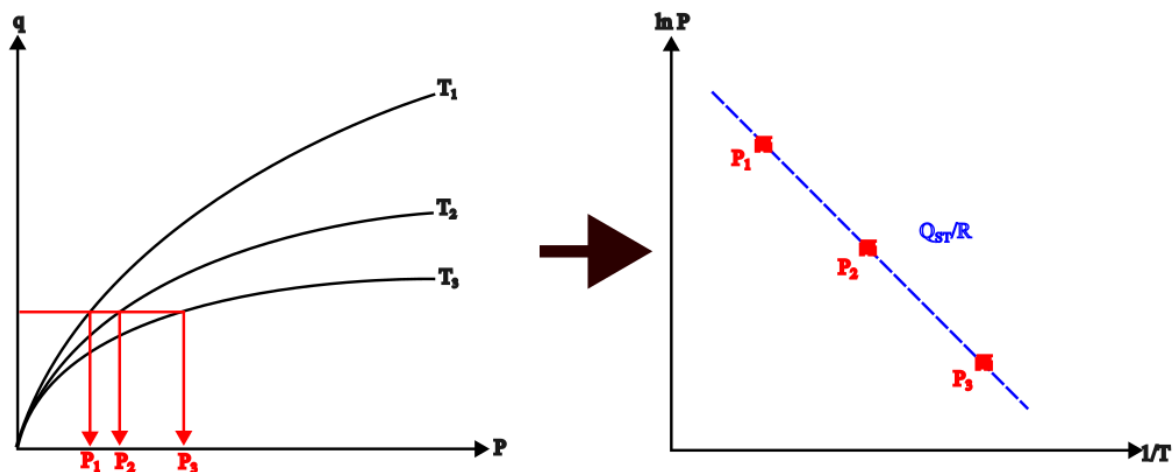


Figure 4-10: The method of calculation of isosteric heat of adsorption using Clausius–Clapeyron approach

#### 4.2.4. Method for predicting co-adsorption isotherm using IAST model

After the appropriate adsorption model was chosen to describe the pure gas adsorption isotherm, the prediction of co-adsorption isotherm for gas mixture using IAST could be carried out. The IAST calculation procedure can be executed in multiple ways, such as using Visual Basic for Applications (VBA) in Excel, Math Lab or other available software such as pyIAST [246] and IAST++ [274]. For this study, we have opted to use IAST++ software [274] to predict the co-adsorption isotherms of CO<sub>2</sub> and CH<sub>4</sub> in a mixture representative of a biogas. Figure 4-11 summarizes the workflow of the IAST calculation procedure in IAST++, assuming: (i) an equimolar binary mixture of species A and B ( $y_A = y_B = 0.5$ ), and (ii) both adsorption isotherms of each pure component described by the Langmuir model (cf. Eq. 4-7, page 99).

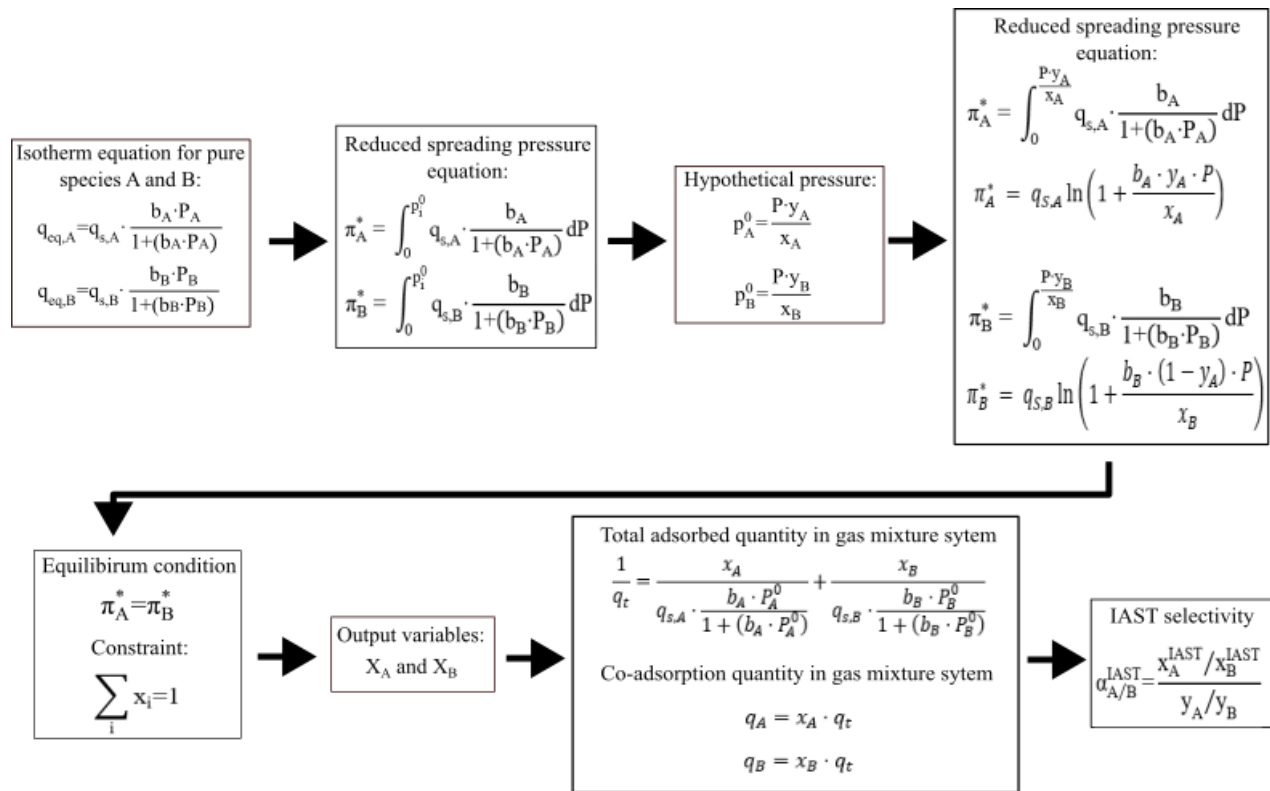


Figure 4-11 : Workflow of IAST calculation assuming Langmuir isotherm model was used to describe pure gas adsorption isotherm.

The first step involves the choice of pure gas adsorption model for each gas species and introduces them in Eq. 4-25. The upper limit of integration of Eq. 4-25 is  $P_1^0$ , which could be expressed in terms of adsorbed phase molar fraction  $x_i$ , using Eq. 4-23. Next, at equilibrium condition for a gas mixture, the reduced spreading pressure (Eq. 4-25) is similar for each gas component and as the sum of adsorbed phase molar fraction is equal to 1, the value of  $x_i$  for each gas mixture could be computed. Then, the known value of  $x_i$  allows the determination of  $P_1^0$  (Eq. 4-25), total adsorbed quantity  $q_t$  (Eq. 4-27) and the co-adsorption capacity of the component in the gas mixture system  $q_i$  (Eq. 4-28). Finally, the selectivity of both gas species is deduced from Eq. 4-29.

### 4.3. Results

#### 4.3.1. CO<sub>2</sub> and CH<sub>4</sub> adsorption isotherms

Figure 4-12 and Figure 4-13 presents the CO<sub>2</sub> and CH<sub>4</sub> isotherms measured at 298 K for pristine HKUST-1 material and its composites with PLA and TPU thermoplastics. The reported isotherms describe the equilibrium mass adsorption capacities (molar quantity adsorbed by 1g of adsorbent) as a function of pressure for each pure component.

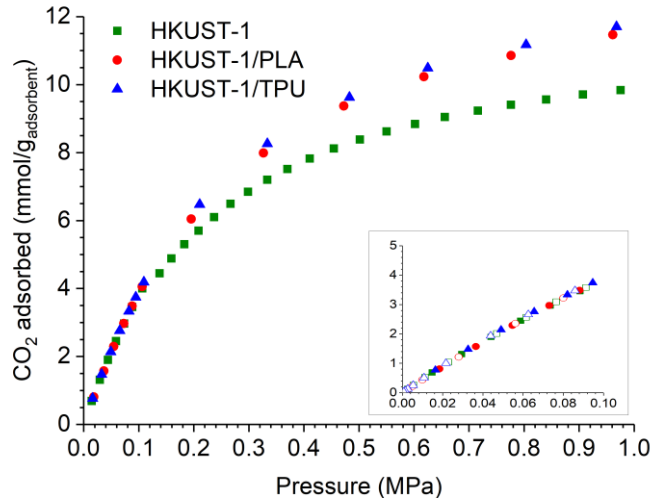


Figure 4-12 : CO<sub>2</sub> adsorption isotherms on HKUST-1 (green square), HKUST-1/PLA (red circle), and HKUST-1/TPU (blue triangle), up to 10 bar at 298 K. Graph in inset represent CO<sub>2</sub> adsorption/desorption isotherm up to 1 bar where solid and open symbols represent the adsorption and desorption of CO<sub>2</sub>, respectively.

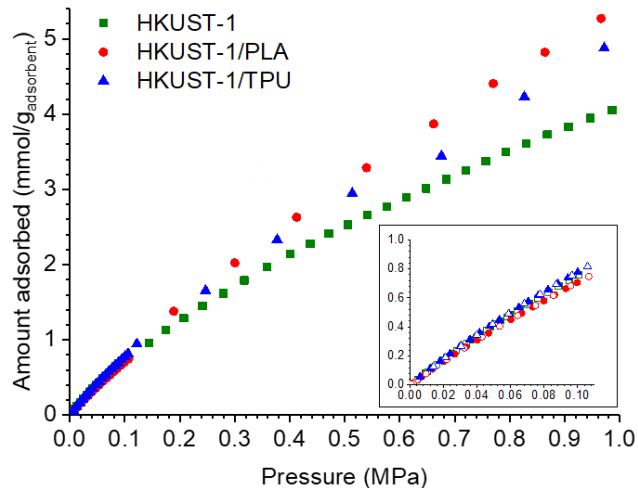


Figure 4-13: CH<sub>4</sub> adsorption isotherms on HKUST-1 (green square), HKUST-1/PLA (red circle), and HKUST-1/TPU (blue triangle), up to 10 bar at 298 K. Graph in inset represent CH<sub>4</sub> adsorption/desorption isotherm up to 1 bar where solid and open symbols represent the adsorption and desorption of CH<sub>4</sub>, respectively.

In Figure 4.12, pristine HKUST-1 (Basolite C300) is shown to reach a CO<sub>2</sub> adsorption capacity of 3.7 mmol/g and 9.8 mmol/g at 1 and 10 bar, respectively. These values are within the range of data reported in the literature (3.5 – 4 mmol/g at 1 bar and 8.5 – 11 mmol/g at 10 bar) for the same adsorbent material [275, 276, 277]. Moreover, the CO<sub>2</sub> adsorption capacities in the low pressure range (<1 bar) are proportional to the equilibrium pressure, which is in accordance with the Henry's law. In this region, the adsorption and desorption isotherms coincide so that adsorption is fully reversible. When the equilibrium pressure is higher than 1 bar, the CO<sub>2</sub> adsorption isotherm on HKUST-1 is still increasing but no longer appears to be linear with the equilibrium pressure. At 10 bar, the saturation of the material appears close to be completed as the curve tend to a plateau.

Meanwhile, the CO<sub>2</sub> adsorption isotherms for both HKUST-1/PLA and HKUST-1/TPU composites are shown to be similar to that of HKUST-1 in the low-pressure region, up to 1 bar. At higher pressure, between 2 to 10 bar, the CO<sub>2</sub> adsorption capacities of both HKUST-1/PLA and HKUST-1/TPU exhibit adsorption capacities up to 18% higher than those measured on pristine HKUST-1. This increase in the composite adsorption capacities could be related with the larger BET surface areas and micropore volumes of the composites as pointed out in the previous chapter.

Figure 4-13 shows that the CH<sub>4</sub> adsorption capacities on pristine HKUST-1 are 0.8 mmol/g and 4.1 mmol/g, at 1 bar and 10 bar, respectively. As observed previously with CO<sub>2</sub>. Both HKUST-1/PLA and HKUST-1/TPU composites exhibit a CH<sub>4</sub> adsorption capacity increase up to 30% in comparison to HKUST-1, in the equilibrium pressure range higher than 1 bar. The higher BET surface areas and pore volumes of the composites explain such an increase. For all the materials, CH<sub>4</sub> adsorption isotherms are almost linear in the whole equilibrium pressure range. The saturation of the materials appears then far to be reached, and no trend towards the apparition of a plateau at 10 bar can be observed. The CH<sub>4</sub> uptake capacities are found significantly below those of CO<sub>2</sub>, around 2 ties lower. This result is indicative of the better affinity of CO<sub>2</sub> for HKUST-1 surface, and preferential adsorption of CO<sub>2</sub> over CH<sub>4</sub> is corroborated in other studies [275, 276, 277].

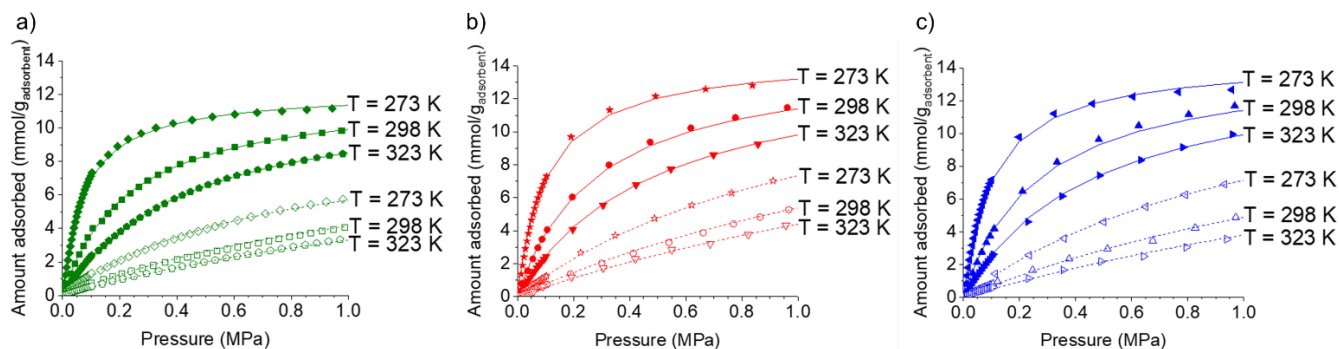


Figure 4-14 : Adsorption isotherms of CH<sub>4</sub> (open symbols) and CO<sub>2</sub> (solid symbols) at different temperatures for (a) HKUST-1, (b) HKUST-1/PLA, and (c) HKUST-1/TPU. The lines represent DSL model fitting.

The CO<sub>2</sub> and CH<sub>4</sub> adsorption isotherms at different temperature are presented in Figure 4-14 for HKUST-1, HKUST-1/PLA and HKUST-1/TPU respectively. Unsurprisingly, it can be observed that an increase in temperature results in a decrease in both CO<sub>2</sub> and CH<sub>4</sub> adsorption capacities. The modelling of the experimental adsorption

isotherm data at all temperatures for each material was done considering different isotherm equations, as described previously. The predictive ability of each isotherm model, as well as their parameters, are presented in Table 4-2.

The predictive ability of the temperature-dependent isotherm models was evaluated through two criteria; the coefficient of determination,  $R^2$  and the sum squares errors, RSS. It can be observed that both Freundlich and Henry isotherm models are unsuitable to describe temperature dependent CO<sub>2</sub> and CH<sub>4</sub> isotherms for any material. This is explained because of the inconsistency of these models and the absence of any predicted saturation plateau at high pressure. Additionally, even if the Langmuir model is not satisfactory to describe well the CO<sub>2</sub> and CH<sub>4</sub> isotherms, the introduction of the saturation capacity term contributes to improving the experimental data fitting, as specified by the values of  $R^2$  and RSS, in comparison to the Henry and Freundlich model.

The model retained to fit the best the CO<sub>2</sub> and CH<sub>4</sub> isotherms data for all the materials is the Dual-Site Langmuir model for which we observe a good prediction of the experimental isotherm data at all temperature and for all the materials, with the value of  $R^2 = 0.99$  and  $RSS = 0.8 - 1.20$ . The comparison between the predicted and experimental isotherm data obtained by using the Dual-Site Langmuir model is graphically illustrated in previous Figure 4-14. The parameter adjustment of the dual-site Langmuir model on the experimental isotherms representative of CO<sub>2</sub> adsorption up to 10 bar, reveals that the monolayer saturation capacity of adsorption sites 1,  $q_{s1}$ , is higher than the monolayer saturation capacity of adsorption sites 2,  $q_{s2}$ . Because it is known that CO<sub>2</sub> adsorbs preferentially onto adsorption sites near the open metal sites of the HKUST-1 crystalline structure [278, 16] (Figure 4-15-a), it is likely that  $q_{s1}$  corresponds to those adsorption sites, whereas  $q_{s2}$  describes the monolayer saturation capacity near the ligand. The dual-site Langmuir model was also successfully applied to the CH<sub>4</sub> isotherms on HKUST-1. Similarly, the adjusted value of  $q_{s1}$  was found superior to  $q_{s2}$ . The adsorption of CH<sub>4</sub> on HKUST-1 surface crystal predominantly occurs in the octahedral cages of the ligand, whereas adsorption near the metal sites would be lower due to its reduced accessibility [16, 279] (Figure 4-15-b). Therefore,  $q_{s1}$  most likely represents the monolayer CH<sub>4</sub> saturation capacity near the ligand, whereas  $q_{s2}$  describes the capacity of CH<sub>4</sub> for the adsorption sites near the open metal sites of HKSUT-1. The dual-site Langmuir also reveals that both composites exhibit higher monolayer saturation capacities when compared to pristine HKUST-1.



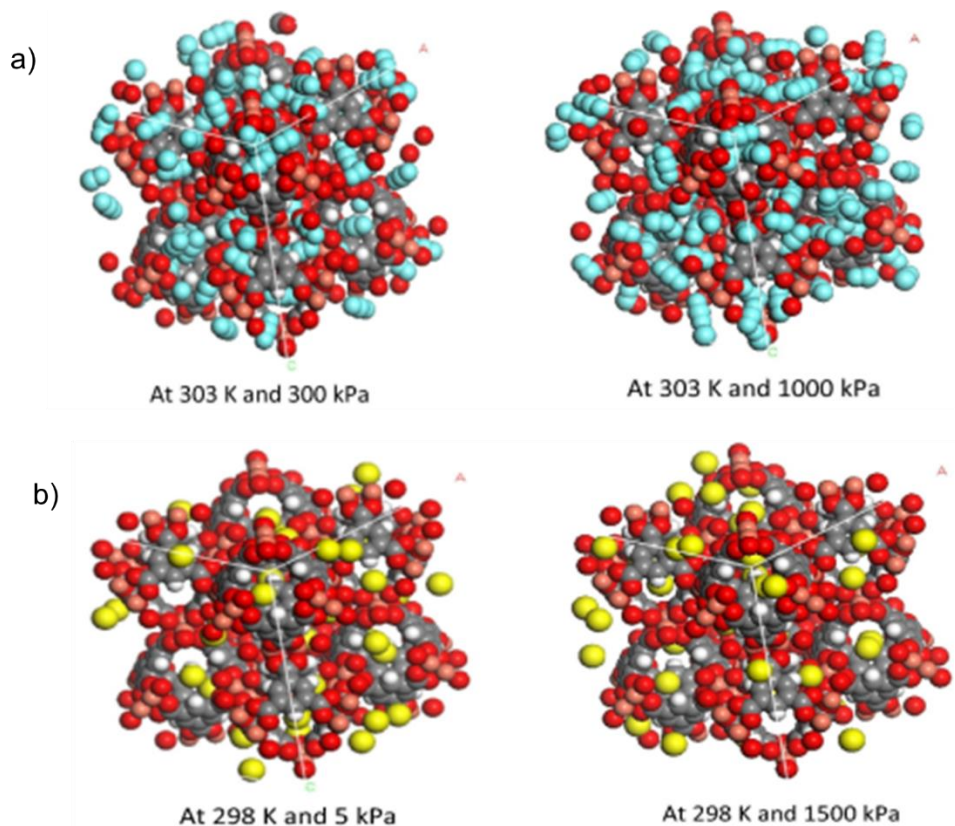


Figure 4-15 : Molecule structure for (a) CO<sub>2</sub> adsorption and (b) CH<sub>4</sub> adsorption on HKUST-1 at different pressure and temperature. The light blue atoms represent CO<sub>2</sub> molecules and the yellow atoms represent CH<sub>4</sub> molecules that are adsorbed onto the structure. The open metal sites are represented by gray atoms whereas the red atoms represent the ligands. The image is reproduced from [16]

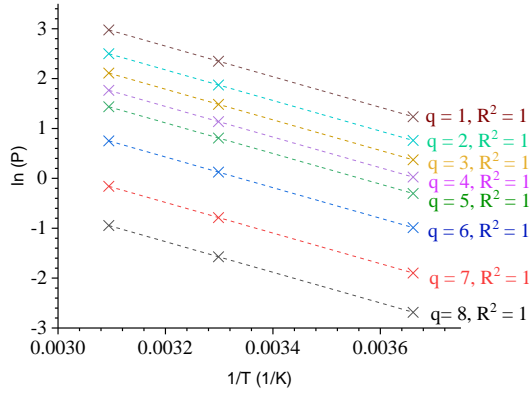
The results of fitting of CO<sub>2</sub> and CH<sub>4</sub> isotherms using Toth and Sips models are also recapitulated in Table 4-2. It should be highlighted here that based on their  $R^2$  values, both these models describe the equilibrium data as well dual-site Langmuir model, especially in the high pressures range. Nevertheless, the dual-site Langmuir model was chosen to represent the whole sets of CO<sub>2</sub> and CH<sub>4</sub> isotherms of the materials due to the relevance of the model accounting for two different types of adsorption sites as already suggested in several other studies [278, 16, 279]. Isothermic heats of adsorption.

#### 4.3.2. Isotheric heat of adsorption

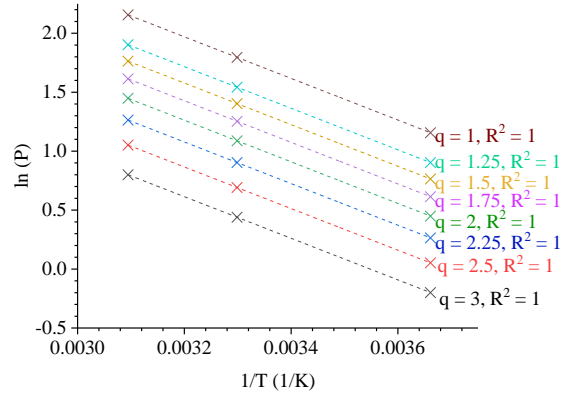
The effect of temperature on equilibrium adsorption uptakes for all samples were previously presented in Figure 4-14 for both CO<sub>2</sub> and CH<sub>4</sub> gases. The adsorption capacity of the gases in all samples decreases with the increasing temperature demonstrating the mechanism of physical adsorption (exothermic). The level of binding strength in the adsorbate-adsorbent interaction of a MOF material can be quantified by the isosteric enthalpy of adsorption,  $Q_{ST}$ . The  $Q_{ST}$  values were calculated for the range of CO<sub>2</sub> loading of 1–10 mmol·g<sup>-1</sup> and CH<sub>4</sub> loading of 1-3 mmol·g<sup>-1</sup>. As previously mentioned, the determination of  $Q_{ST}$  is done using the linear regression of equilibrium data, thus to ensure the accuracy of the calculation, the coefficient of determination  $R^2$  for each loading must be sufficiently high. Figure 4-16 shows the Arrhenius plots used to deduce the CO<sub>2</sub> and CH<sub>4</sub> isosteric heat of adsorption at different loading for all the materials. Thanks to the fitting goodness of the isotherms with the dual-site Langmuir model, the linear regression of equilibrium data for all the samples is accurate with the value of  $R^2$  equal to 1. The results are then presented in Figure 4-17 for different adsorbed amounts.

The values of isosteric adsorption heats of CO<sub>2</sub> (25 kJ/mol) and CH<sub>4</sub> (15 kJ/mol) on the pristine HKUST-1 are comparable to the ones reported in other studies (CO<sub>2</sub>: 20 – 26 kJ/mol and CH<sub>4</sub>: 15 – 17 kJ/mol) [280, 281, 16]. For all samples, the difference between the isosteric heat values for CO<sub>2</sub> and CH<sub>4</sub> is significant and in line with the difference in molecule affinities observed from the isotherm measurements. In the range of tested pressure, the values of  $Q_{ST}$  for both gases also remain constant even as the adsorption coverage keeps on increasing. When comparing the CO<sub>2</sub> isosteric heats of adsorption between pristine HKUST-1 and the composites, the latter appear lower by at least 10% which can be considered as advantageous for the separation process as this should imply lower regeneration temperature. It is possible that after shaping the pristine HKUST-1 with the respective polymers, lower energy adsorption sites in the MOF structure become more easily accessible by both gases, hence reducing the heat of adsorption.

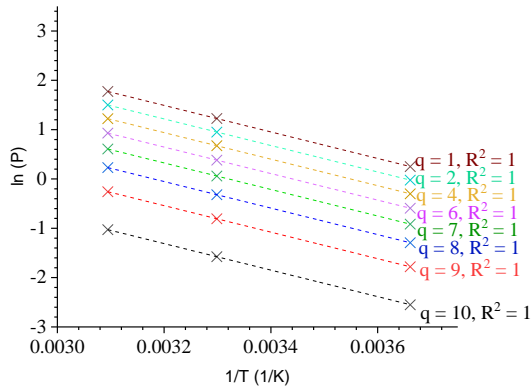
(a-i)



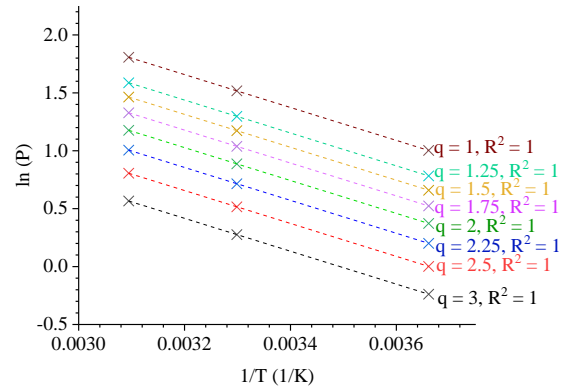
(a-ii)



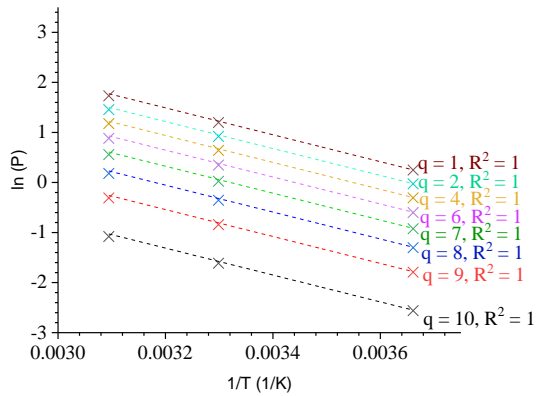
(b-i)



(b-ii)



(c-i)



(c-ii)

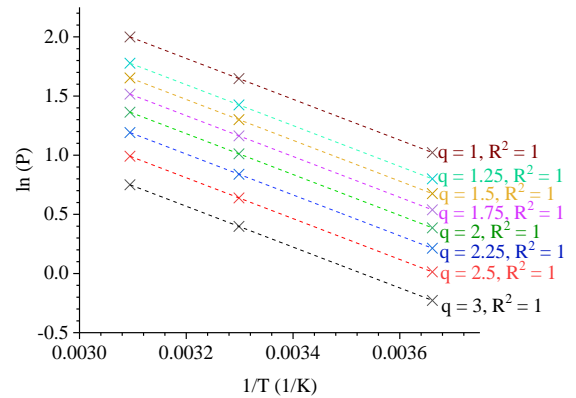


Figure 4-16 : Arrhenius plot for the calculation of CO<sub>2</sub> and CH<sub>4</sub> isosteric heat of adsorption for HKUST-1 (a-i and b-ii), HKUST-1/PLA (b-i and b-ii) and HKUST-1/TPU (c-i and c-ii) with the coefficient of determination, R<sup>2</sup>, for each amount adsorbed, q, in mmol·g<sup>-1</sup>

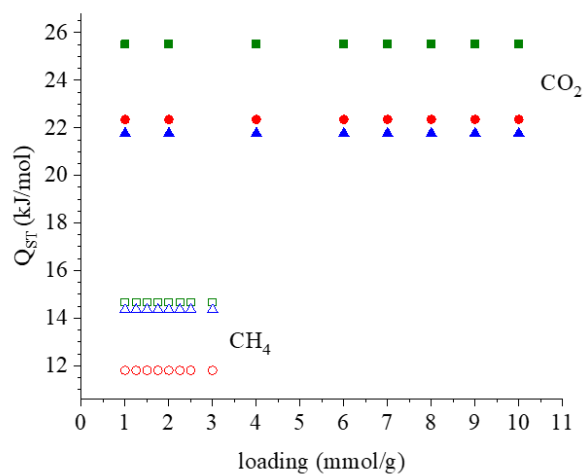


Figure 4-17: Isosteric heat of adsorption for HKUST-1 (green square), HKUST-1/PLA (red circle) and HKUST-1/TPU (blue triangle). Solid and open symbols represent CO<sub>2</sub> and CH<sub>4</sub> respectively.

#### 4.3.3. CO<sub>2</sub>/CH<sub>4</sub> adsorption selectivity

By using the dual-site Langmuir isotherm model for the fitting of CO<sub>2</sub> and CH<sub>4</sub> equilibrium data, the co-adsorption isotherms for equimolar mixture of CO<sub>2</sub>/CH<sub>4</sub> [282], were predicted for all the materials using IAST. Figure 4-17 describes the predicted co-adsorption isotherms of pristine HKUST-1 and the composites for an equimolar mixture of CO<sub>2</sub>/CH<sub>4</sub> at 298K. For comparison purpose, the prediction of the co-adsorption isotherm onto zeolite 13X (isotherm data obtained from [137] using IAST has also been included in Fig 4-18 as this material is cited in literature as a referent adsorbent for CO<sub>2</sub>/CH<sub>4</sub> separation. It can be observed that CO<sub>2</sub> is more preferably adsorbed than CH<sub>4</sub> on all investigated adsorbent materials. In the pressure range lower than 2 bar, pristine HKUST-1 and the composites have comparable CO<sub>2</sub> and CH<sub>4</sub> co-adsorption capacities, whereas at higher pressure, the composites demonstrate larger adsorption capacities than pristine HKUST-1.

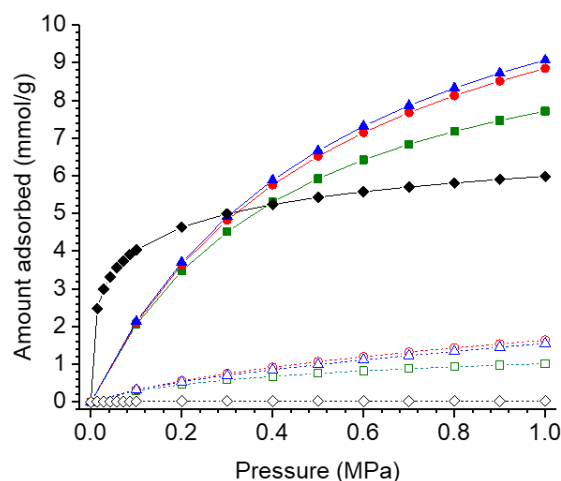


Figure 4-18 : IAST-predicted co-adsorption isotherms for equimolar CO<sub>2</sub>/CH<sub>4</sub> mixtures on HKUST-1 powder (green square), HKUST-1/PLA (red circle), HKUST-1/TPU (blue triangle) and 13X (black diamond) at 298 K as a function of total bulk pressure. Solid and open symbols represent CO<sub>2</sub> and CH<sub>4</sub> adsorption, respectively.

When comparing performances of composites with benchmark zeolite 13X, it can be noted that the latter has a higher CO<sub>2</sub> adsorption capacity when the operating pressure is lower than 3 bar. Above that pressure, the composites have better CO<sub>2</sub> adsorption capacities. However, the benchmark zeolite 13X is characterized with a significantly lower CH<sub>4</sub> adsorption capacity in the pressure range up to 10 bar. Working capacity of an adsorbent, which is defined by the difference between the adsorbed quantities at production and purge pressure is an important characteristic for choosing an adsorbent in PSA. As an example, when considering a production pressure for biogas upgrading at 8 bar [17] and a purge pressure at 1 bar. We can observe that the CO<sub>2</sub> working capacities of HKUST-1/PLA composite (6.3 mmol/g) and HKUST-1/TPU composite (6.1 mmol/g) are significantly higher than with the adsorbent 13X (1.8 mmol/g) which demonstrates the applicability of the composites for biogas upgrading.

Figure 4-19 presents the variations in the IAST-predicted selectivities of equimolar CO<sub>2</sub> and CH<sub>4</sub> mixtures on pristine HKUST-1 and the composites in the pressure range up to 10 bar, at 298 K. Interestingly, it can be observed that the CO<sub>2</sub>/CH<sub>4</sub> selectivities for the composites slightly diminish as the bulk pressure increases, whereas the selectivity of pristine HKUST-1 does not vary so much with increasing pressure. Nevertheless, the difference of the selectivities between pristine HKUST-1 and the composites are not substantial and they could be said to be comparable to each other. The predicted IAST CO<sub>2</sub>/CH<sub>4</sub> selectivity of pristine HKUST-1 in this work was compared with that obtained from experimental results of equimolar CO<sub>2</sub>/CH<sub>4</sub> separation by Hamon *et al.* [124]. The authors reported that in the range of 1-10 bar and 303 K, the measured CO<sub>2</sub>/CH<sub>4</sub> selectivity of HKUST-1 powder is in the range of 6-9, which are comparable with the predicted results in this work.

Meanwhile, when comparing IAST selectivities between MOF extrudates and benchmark zeolite 13X, it can be observed that the value of the latter is significantly higher than the former. Such a difference in the material selectivities may be related to the more competitive CO<sub>2</sub> rather than CH<sub>4</sub> adsorption onto the zeolite 13X, due to CO<sub>2</sub> quadrupole

moment, resulting in a strong interaction with the  $\text{Na}^+$  cations on the adsorbent surfaces of 13X while  $\text{CH}_4$  has no dipole or quadrupole moment resulting in a lesser interaction [283].

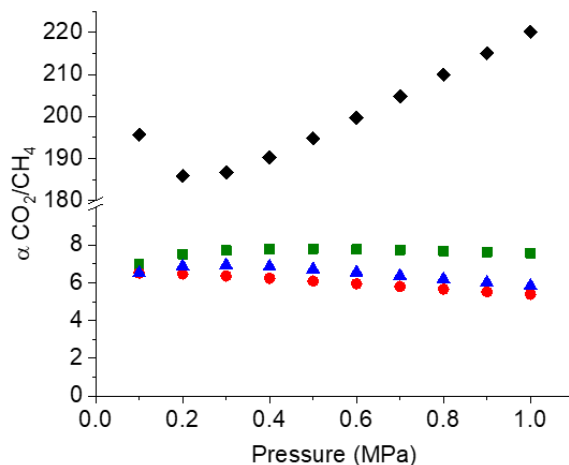


Figure 4-19 : IAST-predicted selectivities toward  $\text{CO}_2$  and  $\text{CH}_4$  for equimolar  $\text{CO}_2/\text{CH}_4$  mixtures on HKUST-1 (green square), HKUST-1/PLA (red circle), HKUST-1/TPU (blue triangle) and 13X (black diamond) at 298K as a function of total bulk pressure.

Finally, Figure 4-20 demonstrates the effect of temperature on the selectivity of HKUST-1 and its composites. It could be observed that an increase in temperature decreases the  $\text{CO}_2/\text{CH}_4$  selectivity for all materials while the materials are more selective toward  $\text{CO}_2$  than  $\text{CH}_4$  at lower temperature. Additionally, the prediction by IAST shows that the selectivity for composites generally starts to decrease gradually when the equilibrium pressure surpasses 4 bar. This could be related to the shape of  $\text{CO}_2$  adsorption isotherms for the composites, where increment of  $\text{CO}_2$  adsorption capacity starts to show signs of slowing down from this equilibrium pressure, contrary to  $\text{CH}_4$  where the adsorption capacities continue to increase proportionally with equilibrium pressure up until 10 bar.

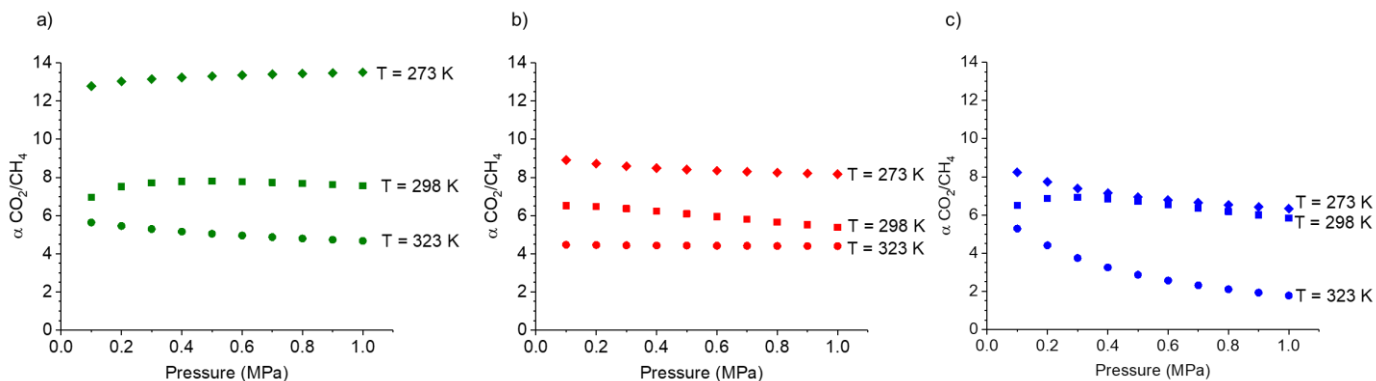


Figure 4-20: IAST-predicted selectivities toward  $\text{CO}_2$  and  $\text{CH}_4$  for equimolar  $\text{CO}_2/\text{CH}_4$  mixtures on (a) HKUST-1 (b) HKUST-1/PLA and (c) HKUST-1/TPU at different temperatures.

Table 4-2 : Fitted parameters of different models for CO<sub>2</sub> and CH<sub>4</sub> adsorption isotherms of HKUST-1, HKUST-1/PLA and HKUST-1/TPU up to 10 bar at 273 K, 298 K and 323 K.

Isotherm model	Fitted parameters	HKUST-1						HKUST-1/PLA						HKUST-1/TPU					
		CO <sub>2</sub>			CH <sub>4</sub>			CO <sub>2</sub>			CH <sub>4</sub>			CO <sub>2</sub>			CH <sub>4</sub>		
		273 K	298 K	323 K	273 K	298 K	323 K	273 K	298 K	323 K	273 K	298 K	323 K	273 K	298 K	323 K	273 K	298 K	323 K
Henry's law	R <sup>2</sup>	0.508	0.295	0.773	0.909	0.965	0.980	0.075	0.646	0.856	0.956	0.992	0.990	0.087	0.625	0.860	0.902	0.979	0.983
	RSS	914.34			22.54			542.96			8.40			545.34			4.97		
	k <sub>1</sub> (bar <sup>-1</sup> )	4.54			3.58			3.93			2.81			4.45			4.38		
	k <sub>2</sub> (K <sup>-1</sup> )	721.51			1138.86			609.94			879.18			659.64			1177.78		
Langmuir	R <sup>2</sup>	0.935	0.970	0.991	0.981	0.991	0.995	0.998	0.998	0.999	0.999	0.999	0.998	0.998	0.997	0.999	0.999	0.996	0.996
	RSS	38.39			4.73			1.21			0.25			1.73			0.35		
	q <sub>m</sub> (mol/kg)	14.61			16.07			14.61			16.07			14.49			15.30		
	k <sub>1</sub> (bar <sup>-1</sup> )	56.67			0.57			48.14			0.67			44.24			1.10		
	k <sub>2</sub> (bar <sup>-1</sup> )	2899.26			1504.48			2685.58			1418.62			2614.56			1724.16		
Freundlich	R <sup>2</sup>	0.867	0.944	0.913	0.995	0.998	0.993	0.895	0.945	0.908	0.993	0.996	0.996	0.894	0.947	0.905	0.990	0.998	0.996
	RSS	104.05			1.57			76.18			1.72			76.03			0.60		
	k <sub>1</sub> (bar <sup>-1</sup> )	20.57			6.05			19.49			4.82			19.41			7.45		
	k <sub>2</sub> (K <sup>-1</sup> )	879.50			1086.37			842.02			930.07			838.14			1212.75		
	n	2.66			1.44			2.37			1.28			2.34			1.30		
Sips	R <sup>2</sup>	0.999	0.999	0.999	0.999	0.999	0.998	0.999	0.999	0.999	0.999	0.999	0.998	0.999	0.999	0.999	0.999	0.998	0.999
	RSS	0.94			0.32			0.50			0.24			0.75			0.16		
	q <sub>m</sub> (mol/kg)	11.97			14.05			14.14			15.77			13.83			22		

	$k_1$ (bar <sup>-1</sup> )	123.74			0.82			53			0.72			50.21			0.55		
	$k_2$ (bar <sup>-1</sup> )	3072.52			1707.75			2691.14			1425.31			2618.12			1706.04		
	n	0.96			1.15			0.93			0.99			0.91			1.11		
Toth	R <sup>2</sup>	0.999	0.999	0.999	0.999	0.999	0.998	0.999	0.999	0.999	0.999	0.999	0.998	0.999	0.999	0.999	0.999	0.998	0.998
	RSS	0.89			0.36			0.41			0.24			0.53			0.19		
	q <sub>m</sub> (mol/kg)	11.87			22.26			13.88			14.57			13.49			42.49		
	$k_1$ (bar <sup>-1</sup> )	112.77			1.02			46.19			0.74			42.72			0.50		
	$k_2$ (bar <sup>-1</sup> )	3076.66			1711.04			2707.98			1428.1			2640.49			1706.33		
	n	1.09			0.56			1.18			1.09			1.23			0.55		
Dual-Site Langmuir	R <sup>2</sup>	0.998	0.999	0.999	0.998	0.997	0.998	0.998	0.998	0.999	0.999	0.999	0.998	0.998	0.997	0.999	0.999	0.996	0.996
	RSS	1.24			0.80			1.21			0.25			1.73			0.35		
	q <sub>m1</sub> (mol/kg)	12.23			9.81			14.61			16.07			14.50			15.30		
	q <sub>m2</sub> (mol/kg)	2.09			2.09			2.09			2.09			2.09			2.09		
	k <sub>1,a</sub> (bar <sup>-1</sup> )	116.76			1.83			48.14			0.67			44.23			1.10		
	k <sub>1,b</sub> (K <sup>-1</sup> )	3066.95			1762.24			2685.58			1418.62			2614.42			1724.25		
	k <sub>2,ba</sub> (bar <sup>-1</sup> )	60.29			60.28			60.29			60.28			60.29			60.28		
	k <sub>2,b</sub> (K <sup>-1</sup> )	1404.2			36328.4			14404.1			36328.42			14404.5			36328.42		



#### 4.4. Conclusion

Adsorption equilibria of CO<sub>2</sub> along with CH<sub>4</sub> were examined for the pristine HKUST-1 and its composites, HKUST-1/PLA and HKUST-1/TPU. The equilibrium data for both gases were collected using manometric equipment in the pressure range up to 10 bar and temperature 273 K, 298 K and 323 K. In the pressure range below 1 bar and at the temperature of 298K, all the investigated adsorbents have similar CO<sub>2</sub> and CH<sub>4</sub> adsorption capacities, following a linear trend with pressure according to the Henry's law. However, in the high pressure range (between 2 to 10 bar), the CO<sub>2</sub> adsorption capacities of both HKUST-1/PLA and HKUST-1/TPU are increased up to 18% compared to pristine HKUST-1. Such an increase was attributed to the larger BET surface areas and micropore volumes of the composites compared with pristine HKUST-1. Similar observations are made regarding the adsorption of CH<sub>4</sub>. In comparison to pristine HKUST-1, both HKUST-1/PLA and HKUST-1/TPU have a gradual increment in the CH<sub>4</sub> adsorption capacity up to 30% as the equilibrium pressure is increased above 1 bar.

The dual-site Langmuir isotherm model was found to accurately describe the experimental equilibrium data of CO<sub>2</sub> and CH<sub>4</sub>. Temperature was found to strongly impact adsorption performances of materials, as a higher temperature results gas adsorption depression. Additionally, the isosteric heat of adsorption of HKUST-1 composites are slightly lower than its pristine material, which would reduce the energy required to regenerate the adsorbent. To establish the separation performances of the composites and pristine HKUST-1, the co-adsorption isotherms were derived from the IAST, considering the case of equimolar gas mixture representative of biogas composition. The predicted co-adsorption isotherms show that CO<sub>2</sub> is always more favorably adsorbed than CH<sub>4</sub> onto all the materials, which is a good indication of their suitability as an adsorbent for CO<sub>2</sub>/CH<sub>4</sub> gas separation. The composites exhibit higher CO<sub>2</sub> and CH<sub>4</sub> adsorption capacities than pristine HKUST-1 but the equilibrium selectivities of both composites were slightly reduced above pressure of 1 bar compared to the pristine HKUST-1 because of larger amounts of co-adsorbed CH<sub>4</sub> at this pressure range. The predicted separation performances of the composites according to the IAST were compared with the reference zeolite 13X. Under the same operational process conditions ( $P_{\text{ads}} = 8$  bar,  $P_{\text{purge}} = 1$  bar and  $T = 298\text{K}$ ), the CO<sub>2</sub> working capacities of HKUST-1/PLA composite (6.3 mmol/g) and HKUST-1/TPU composite (6.1 mmol/g) are significantly higher than the one derived for the zeolite 13X (1.8 mmol/g). However, zeolite 13X has a significantly higher CO<sub>2</sub>/CH<sub>4</sub> selectivity than both the two composites, as it adsorbs far less CH<sub>4</sub>. Nevertheless, the results obtained in this section demonstrate the interest to further the potential of use of explore the shaped HKUST-1 composites as adsorbents in PSA for CO<sub>2</sub>/CH<sub>4</sub> gas separation from biogas. In order to objectively evaluate CO<sub>2</sub>/CH<sub>4</sub> separation performances, it is important to go beyond the analysis and comparison of adsorption selectivities by performing simulation and optimization of the whole PSA process operating HKUST-1 composite adsorbent material.

# CHAPTER 5: Simulation and optimization of PSA process for biogas upgrading

In this chapter, two separate cases were simulated using simulation software, gPROMS: (1) Model validation. (2) PSA cycle for CO<sub>2</sub>/CH<sub>4</sub> separation in the context of biogas upgrading. The objective for the 1<sup>st</sup> case is to verify that gPROMS is able to reliably reproduce the experimental and simulation results reported by Asadi *et al.* [17]. Meanwhile, the objective of the 2<sup>nd</sup> case is to estimate the performance of the synthesized HKUST-1 composites for biogas upgrading process, which are biomethane purity, recovery of biomethane, productivity of PSA cycle and energy consumption per cycle as a function of operation conditions.

It should be noted that in the 2<sup>nd</sup> case of the simulation, several important context/hypotheses have been taken to simplify the overall process. First, the simplified composition of a pre-treated raw biogas, that is CO<sub>2</sub> and CH<sub>4</sub> in equimolar ratio without minor impurities (H<sub>2</sub>S, N<sub>2</sub>) and moisture, was considered. Second, the simulation was only done only using one of the HKUST-1 composites as an adsorbent (HKUST-1/PLA), as both of them have similar gas adsorption capacities. Finally, as the information concerning the kinetic adsorption properties of synthesized HKUST-1 composites was not analyzed in this study, we have opted to use the kinetics data available in literature, as reported by Asadi *et al.* [17] for commercial HKUST-1 material. In that study, the slope of the CO<sub>2</sub> breakthrough profile for commercial HKUST-1 adsorbent is very steep, indicating fast mass transfer/adsorption kinetics resulting in a quasi-instantaneous equilibration of adsorbent materials and a quasi-complete saturation of adsorbent bed after breakthrough.

All of these assumptions help to complete the mathematical model for the biogas upgrading simulation, thus allowing to acquire a better understanding of the impact of operational parameters on CO<sub>2</sub>/CH<sub>4</sub> separation. The obtained simulation results provide a good starting point in estimating the efficiency of the HKUST-1 composite, though it is undeniable that experimental breakthrough analysis and kinetic characterization of the composite would improve the accuracy of the simulation results.

This section will first start with the presentation of recent developments of the PSA process cycle configuration for biogas upgrading and available kinetics models to describe the mass transfer. Then, the simulation methodology in this work is shown and finally the results of both simulation cases are presented.

## 5.1. Different configurations of PSA/VPSA cycle for biogas upgrading

The typical biogas composition from industrial biogas plants (in terms of CO<sub>2</sub> and CH<sub>4</sub> content) depends on the type of raw material used [284]: (i) household or industrial waste (CO<sub>2</sub> = 20-35% vol and CH<sub>4</sub> = 65-75% vol), (ii) sludge from wastewater treatment plant (CO<sub>2</sub> = 20-55% vol and CH<sub>4</sub> = 45-75% vol) or (iii) agricultural waste (CO<sub>2</sub> = 25-30% vol and CH<sub>4</sub> = 40-55% vol). For the biogas upgrading within this range of composition via PSA/VPSA process, the CO<sub>2</sub> capture performance is influenced by the choice of adsorbent and the cycle configuration. In this

section, a short review of the PSA/VPSA configurations for biogas upgrading applications reported in literature will be presented. Table 5-1 shows the comparison of different configurations of adsorption cycle and their respective biogas upgrading performances.

Table 5-1: Comparison of the operational parameters and CO<sub>2</sub>/CH<sub>4</sub> separation performance of a different configuration of PSA/VPSA process for biogas upgrading

PSA/VPSA configuration	Adsorbent	Separation mechanism	Operational parameters				Separation performances			Ref.
			P <sub>ads</sub> /P <sub>regen</sub> (bar)	CO <sub>2</sub> /CH <sub>4</sub> composition (% vol)	Biogas flowrate (Nm <sup>3</sup> /h)	Biogas velocity (Nm/s)	CH <sub>4</sub> purity (%)	CH <sub>4</sub> recovery (%)	CH <sub>4</sub> productivity (kg <sub>CH<sub>4</sub></sub> ·m <sup>-3</sup> ·h <sup>-1</sup> )	
Skarstrom cycle	CMS	Kinetics	5.8/0.1	45/55	500	1.4	98	90	-	[285]
Dual-stage (V)PSA	CMS	Kinetics	70 <sup>a</sup> /2 <sup>a</sup> 5 <sup>b</sup> /0.5 <sup>b</sup>	10/90	80-100	1.1 – 2.3 x 10 <sup>-3</sup>	98	99	56	[286]
VPSA + N <sub>2</sub> purging	Zeolite 13X	Equilibrium	4/0.08	40/60	2-12	0.1 – 0.6	99	93	-	[287]
Dual-stage VPSA	Zeolite 5A	Equilibrium	6/0.2	40/60	100	0.2 – 0.4	97	99	-	[288]
VPSA + off gas recycling	CMS	Kinetics	8/0.5	40/60	396-971	0.1 – 0.2	97	80-95	80-160	[289]

<sup>a</sup>First stage. <sup>b</sup>Second stage.

Biogas upgrading using the Skarstrom cycle, which is the most conventional cycle configuration, is able to produce biomethane with high CH<sub>4</sub> purity, but the inconvenient is the non-negligible amount of CH<sub>4</sub> lost during the process. Therefore, multiple configurations derived from the Skarstrom cycle have been introduced in the literature to increase CH<sub>4</sub> recovery (cf. Table 5-1). The dual-stage VPSA process contributes to a higher methane recovery than the single stage VPSA process. It should be highlighted here that biogas upgrading simulation for studies listed in Table 5-1 involves both laboratory scale and industrial scale, with biogas flowrate ranging from 2 up to 1000 Nm<sup>3</sup>/h. The principle behind each configuration is given in Table 5-1 as well as their respective advantages and limitations, discussed presented in the following sections.

#### 5.1.1. Skarstrom cycle

Detailed explanation regarding the concept of Skarstrom cycle configuration has been previously given in section 2.3, page 42, thus it will not be further described here. An example on the application of this type of configuration is a study by Barbera et al. [285], where the simulation of biogas upgrading with CO<sub>2</sub> and CH<sub>4</sub> volumetric composition of 45% and 55% respectively, was done using operational pressure and flow rate listed in Table 5-1 at 308 K. In addition to that, the simulation used CMS as adsorbent media and the raw biogas was assumed to have undergone a pretreatment process prior to adsorption, leaving only CO<sub>2</sub> and CH<sub>4</sub> as the gas constituents. The authors employed six interconnected columns (Figure 5-1), with three coupled adsorption/desorption pairs working in parallel and each adsorption column treats 1/3 of the inlet biogas flowrate. Each adsorption column underwent simple Skarstrom cycle: co-current pressurization using the biogas feed, co-current adsorption step, a counter current blowdown step and finally a counter current purge using the product stream. The results of simulation for this section reveal that

biomethane obtained as upstream product has purity of 98% and total CH<sub>4</sub> recovery of 85%, whereas the off gas obtained during blowdown and purge step has a CO<sub>2</sub> purity of 89.7% and CO<sub>2</sub> recovery of 99%. The loss of CH<sub>4</sub> is mainly attributed to the purge step that uses a fraction of CH<sub>4</sub>-rich product to push downward CO<sub>2</sub> that was accumulated at the top of an adsorption column. Authors stated that by lowering adsorption pressure and increasing adsorption time, it is possible to increase CH<sub>4</sub> recovery but at the expense of biomethane purity. Additionally, authors reported that the specific energy consumption for the Skarstrom to be on the order of 0.27 kWh.Nm<sup>3</sup>CH<sub>4</sub>.

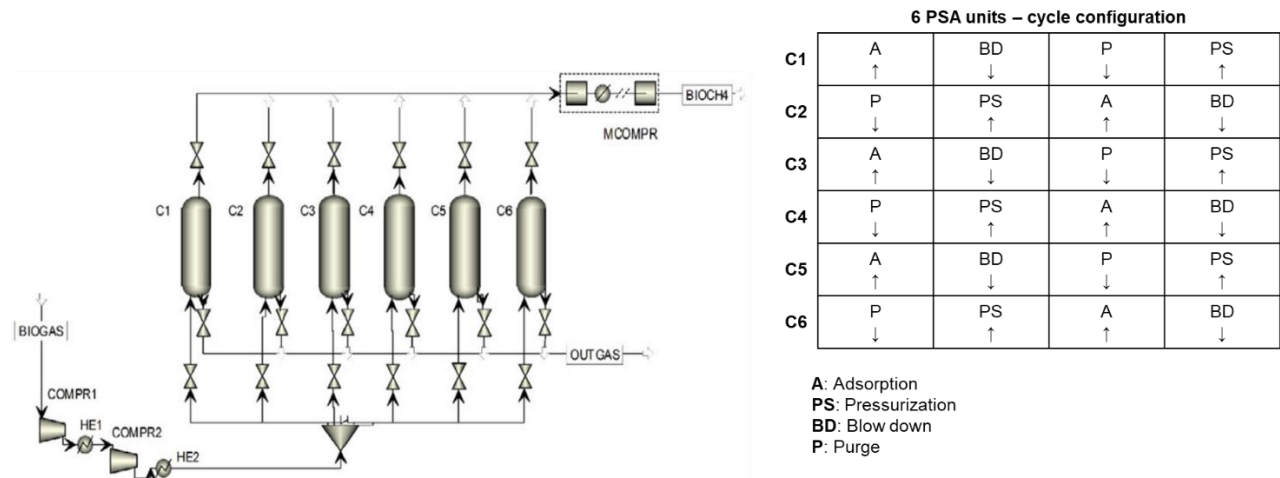


Figure 5-1: Process Flow Diagram of a Skarstrom cycle configuration [285]

### 5.1.2. Dual-stage (V)PSA process configuration

The concept of dual-stage (V)PSA process resembles that of distillation process, which consist of one rectifying section for purification of the light component and one stripping section for the purification of the most adsorbed gas (Figure. 4-2). In the context of biogas upgrading, the light component obtained in the rectifying section is biomethane (CH<sub>4</sub>) whereas the gas obtained in the stripping section is CO<sub>2</sub>. This type of configuration allows to obtain each gas constituent at high purity, either as a product or off gas.

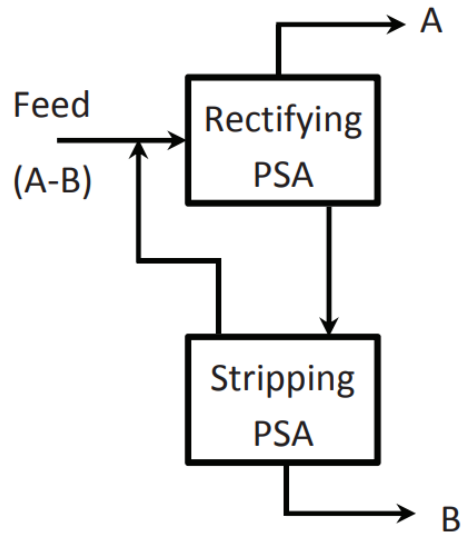


Figure 5-2: Dual-stage PSA scheme used to obtain purified streams of methane and carbon dioxide [286].

As raw biogas enters the first separation stage, the less adsorbed  $\text{CH}_4$  will be obtained at high purity at the top of the column, though a certain quantity of  $\text{CH}_4$  will be inevitably co-adsorbed with  $\text{CO}_2$  in the adsorbent media. As the adsorbent undergoes regeneration process, the off gas contains a large amount of desorbed  $\text{CO}_2$  as well as non-negligible amount of  $\text{CH}_4$ , which will inevitably lead to low  $\text{CH}_4$  recovery for the biogas upgrading process. This is where the stripping section plays an important role. The  $\text{CO}_2$  rich off-gas from “rectifying section” is sent to the “stripping section”, where  $\text{CO}_2$  will be retained by adsorbent media and the less adsorbed  $\text{CH}_4$  will be recycled back to the feed stream of the rectifying section. This step contributes to a higher  $\text{CH}_4$  recovery for the biogas upgrading process and consequently a higher purity of  $\text{CO}_2$  in the off-gas stream.

In a study by Grande and Blom [286], dual-stage (V)PSA configuration was simulated for natural gas upgrading with  $\text{CO}_2$  and  $\text{CH}_4$  volume composition of 10% and 90%, respectively, using operational parameters previously listed in Table 5-1. It should be noted here that the lowest pressure applied in the rectifying section never reaches vacuum condition, making it a PSA process. The simulation was done by assuming that the gas was pre-treated prior to the PSA process and CMS was used as adsorbent media. The simulation of the first rectifying section was made using 6 columns within 10 different steps (Figure 5-3). The results of the initial simulation for this section reveal the  $\text{CH}_4$  purity obtention of 98% with a total  $\text{CH}_4$  recovery of 85% (Table 5-2). The 2% contamination with  $\text{CO}_2$  in the product stream is attributed to the transfer of some desorbed  $\text{CO}_2$  from the saturated adsorbent media towards another regenerated column during the pressure equalization steps, whereas the loss of 15% in  $\text{CH}_4$  recovery is attributed to the recycling of  $\text{CH}_4$  during the purge and pressurization steps. Additionally, the simulation reveals that the  $\text{CO}_2$  purity of the streams taken from the blowdown and purge steps is merely 39%. This is caused by the low effective utilization of adsorbent media (40% of its total adsorption capacity) as the adsorbent is not completely regenerated due to the thermal and mass transfer effects in the column.

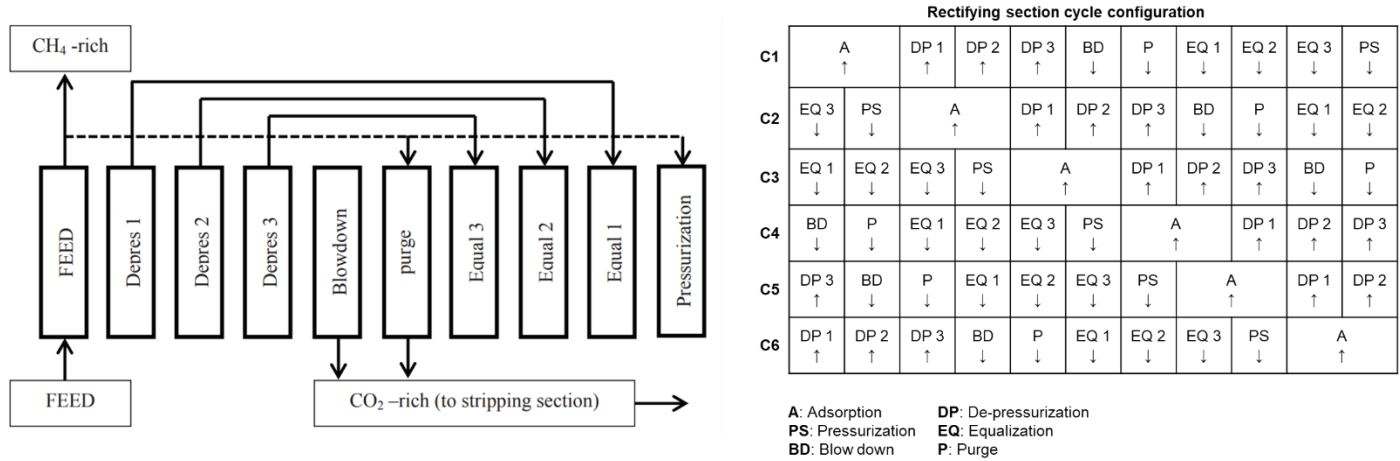


Figure 5-3: Scheme of the cycle steps employed in the rectifying section of the PSA unit by Grande and Blom [286].

The simulation was then continued for the “stripping section” using the CO<sub>2</sub> stream obtained from the simulation of rectifying section and the operational parameters listed in Table 5-1. This section was simulated using three columns with 5 different steps (Figure 5-4) and vacuum condition was used for the regeneration of the adsorbent. The results obtained reveal that 94% of the CH<sub>4</sub> entering the “stripping section” were able to be recovered as a top product with the CH<sub>4</sub> purity of 90% (Table 5-2) and be recycled back the feed gas stream of the rectifying section. In addition, a relatively high purity of CO<sub>2</sub> stream (91%) is able to be obtained during blowdown. By integrating the results of the simulation of both sections, Grande and Blom demonstrated that dual-stage (V)PSA configuration is able to obtain CH<sub>4</sub> recovery higher than 99% and overall CH<sub>4</sub> purity of 98%. Meanwhile, if the simulation was conducted without stripping, its CH<sub>4</sub> purity and recovery would be 98% and 85%. It should also be noted that the productivity of the overall process is around 50% lower than the one obtained in PSA units for biogas upgrading, due to the existence of the stripping section, which inevitable prolong the overall adsorption cycle time.

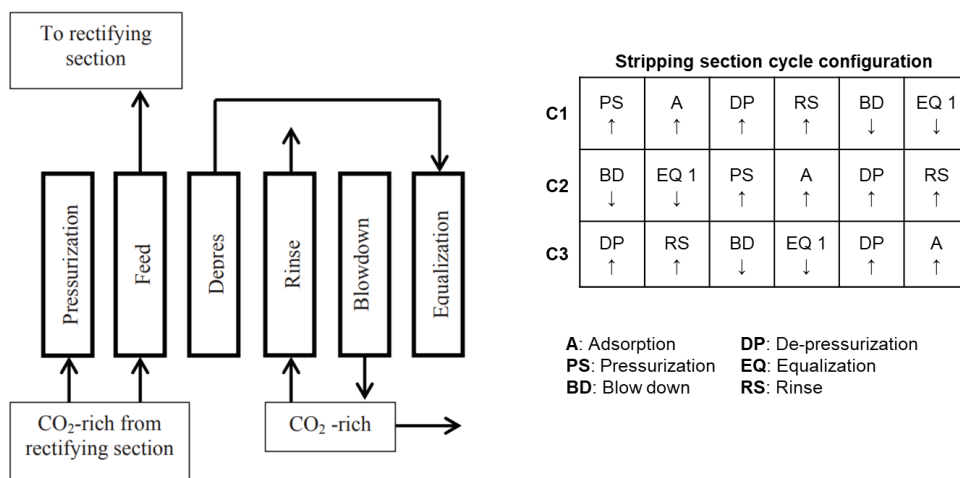


Figure 5-4: Scheme of the cycle steps employed in the stripping section of the PSA unit by Grande and Blom [286].

Table 5-2: Separation performance for single-stage and dual-stage PSA unit by Grande and Blom [286]

	Dual-stage PSA	Single-stage PSA
CH <sub>4</sub> purity (%)	98	98
CH <sub>4</sub> recovery (%)	99	85

An example of dual-stage VPSA configuration for biogas upgrading application is the study by Augelletti et al. [288], where the binary CH<sub>4</sub> and CO<sub>2</sub> mixture separation with a volumetric composition of respectively 60% and 40% was performed. In contrast to [286] where the separation of CO<sub>2</sub>/CH<sub>4</sub> on CMS is operated under kinetic control, the study of Augelletti et al. uses Zeolite 5A as the adsorbent media in both rectifying and stripping sections, operating the separation under equilibrium conditions. Additionally, vacuum regeneration of the columns is employed in both sections (operational parameters are listed in Table 5-1). As the operational pressure used in this study is lower than that of Grande and Blom [286], Augelletti et al. were able to apply the same dual-stage VPSA configuration by using only eight columns in total, where four interconnected columns were used for each rectifying and stripping section. These columns underwent 6 steps for a complete biogas upgrading cycle (Figure 5-5), which are: (i) Feed (FE), (ii) equalization of pressure (EQ1 & EQ2), (iii) blowdown (BD), (iv) purge (PU) and (v) pressurization (PR). EQ 1 involves connecting a column initially at low pressure with another column that has a higher pressure, until both columns reach a new intermediate pressure, whereas EQ 2 is the inverse of EQ 1. The simulation of the rectifying section reveals that biomethane obtained as product has a purity of 98.8% with a methane recovery of 83.9%, whereas CO<sub>2</sub> purity in the stream taken from BD and PU steps is around 78.5%. Next, the simulation of said CO<sub>2</sub> stream in the stripping section results in the obtention of 99.1% in CO<sub>2</sub> purity for the off gas, whereas the product stream, which was eventually recycled back to the feed of rectifying section, consist of 17.8% and 82.2% in CO<sub>2</sub> and CH<sub>4</sub> purity, respectively. Overall, the application of dual-stage VPSA configuration for biogas upgrading as simulated by Augelletti et al., demonstrates the viability of the obtention of high purity biomethane with total CH<sub>4</sub> recovery greater than 99%.

Bed 1	FE		EQ2	BD		PU		EQ1	PR	
Bed 2	EQ1	PR		FE		EQ2	BD		PU	
Bed 3	PU		EQ1	PR		FE		EQ2	BD	
Bed 4	EQ2	BD		PU		EQ1	PR		FE	

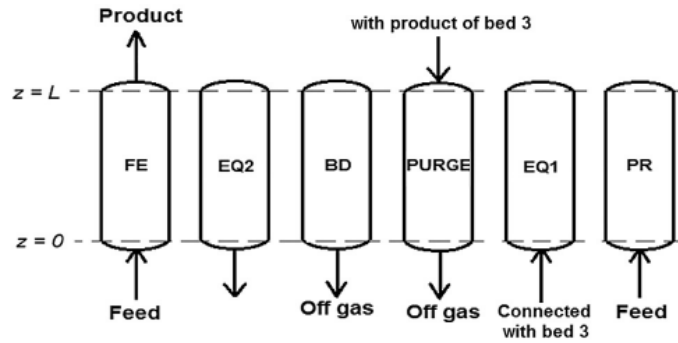


Figure 5-5: Scheme of the cycle steps employed in both the rectifying and stripping section of the VPSA unit by Augletti et al. [288].

### 5.1.3. VPSA with N<sub>2</sub> purging

Khunpolgrang et al. [287] have studied the effect of adding N<sub>2</sub> purging step in the VPSA process for biogas upgrading. VPSA unit containing four interconnected columns (Figure 5-6) operating 13X zeolite as an adsorbent was fed with the mixture of 40% CO<sub>2</sub> and 60% CH<sub>4</sub>, simulating the pre-treated biogas. Operational parameters used for the simulation are listed in Table 5-1. Each column underwent 9 steps within the cycle: (i) Pressurization (P) from atmospheric pressure to the adsorption pressure, (ii) Adsorption (A): continuous feed of the column with CH<sub>4</sub>/CO<sub>2</sub> mixture, (iii) Equalization pressure drop 1 (ED1) between adsorption column and intermediate tank, (iv) Equalization pressure drop 2 (ED2): the equalization of residual pressure in an adsorption column with a second adsorption column, which had just been evacuated, (v) Blowdown (BD): to decrease the residual pressure in an adsorption column to atmospheric pressure, (vi) Purge (PG): feed of the column with N<sub>2</sub> flow to flush the column at the pressure of adsorption (A) under countercurrent regime (with the respect to feed), (vii) evacuation (EV) through the feed end by vacuum pump, (viii) Equalization pressure rise 2 (ER2)–re-pressurization of a freshly regenerated column 1 with the gas from another adsorption column. (ix) Equalization pressure rise 1 (ER1): further increase of pressure in column 1 (after ER1) by the transfer of gas from an intermediate tank.



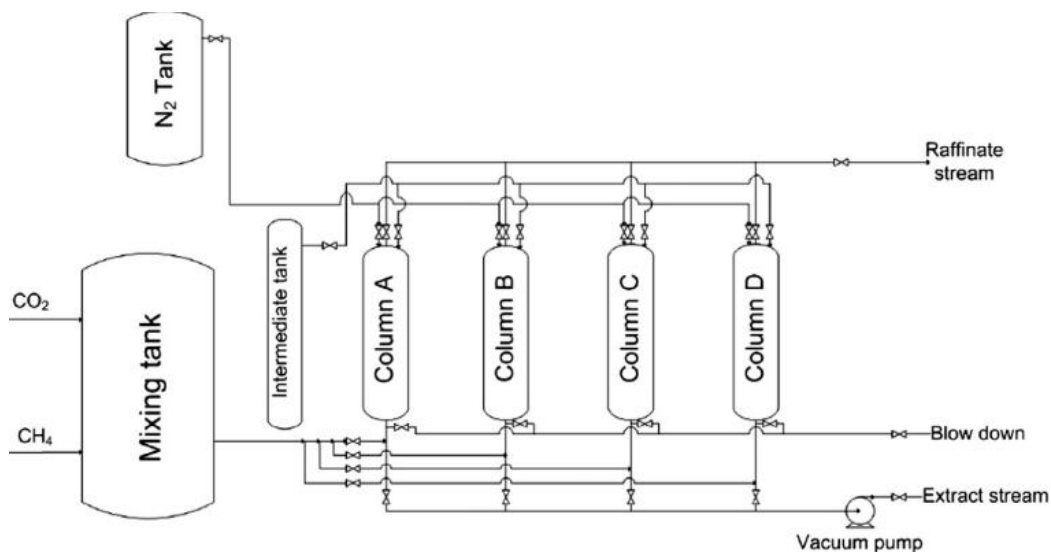


Figure 5-6: A simplified diagram of the pilot-scale four-column VPSA process with N<sub>2</sub> purging [287]

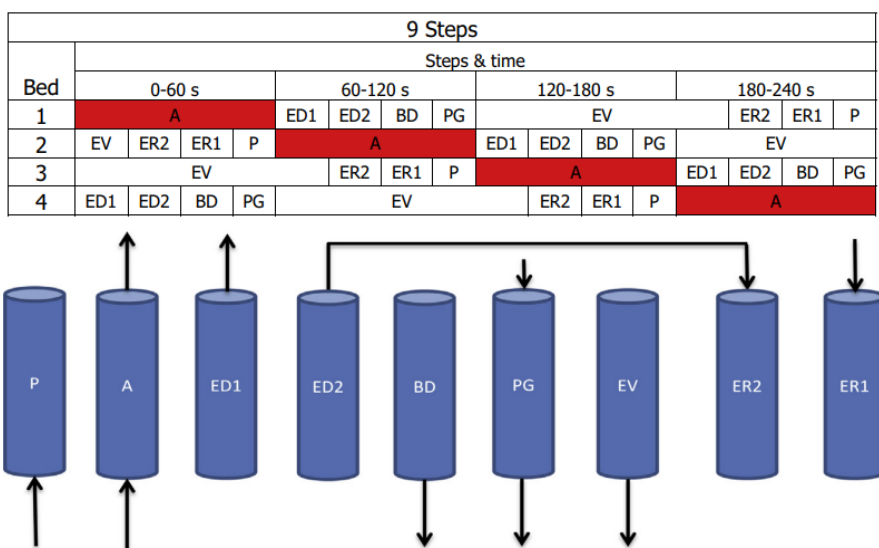


Figure 5-7: Scheme of the cycle steps for the VPSA process with N<sub>2</sub> purging [287].

Authors stated that the simulation of this VPSA process configuration results in the obtention of biomethane purity of more than 99% and a methane recovery of 93%. In comparison, they simulated another simulation for the VPSA process of biogas upgrading but without the N<sub>2</sub> purging step. It was revealed that the absence of N<sub>2</sub> purging contributes to a decrease of biomethane purity by 9% and a decrease of methane recovery by 10%. However, the energy consumption of the VPSA configuration with N<sub>2</sub> purging was found to be increased around 70% compared with VPSA configuration without purging, i.e. from 0.136 to 0.232 kW h/m<sup>3</sup> of CH<sub>4</sub>, due to the extra energy required to pressurize N<sub>2</sub> from atmospheric pressure to adsorption pressure.

#### 5.1.4. VPSA with off gas recycling

In a study by Choukhi et al. [289], a new configuration of VPSA process for biogas upgrading was simulated for a mixture of CO<sub>2</sub> and CH<sub>4</sub> with a volumetric composition of 40% and 60%, respectively. CMS was chosen as the adsorbent media for the simulation and its operational parameters are listed in Table 5-1. The main feature of the VPSA configuration proposed by Choukhi et al. revolves around the recycling of off gas, which is obtained during purging and blowdown stages, to increase the purity and recovery of CH<sub>4</sub>. The simulation of biogas upgrading using this type of VPSA configuration by Choukhi et al. consists of 5 columns with 15 steps. The sequence of the cycle steps for a single bed is shown in Figure 5-8.

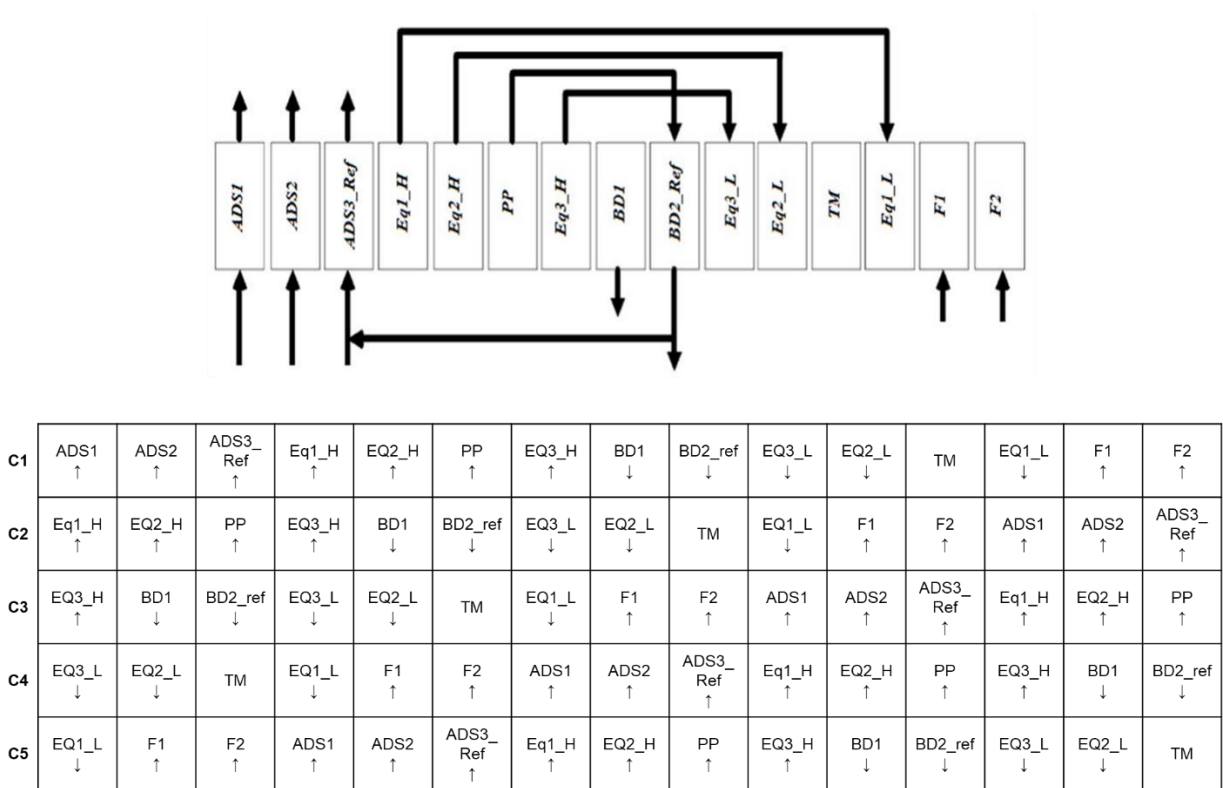


Figure 5-8: Cycle representation based on a single bed sequence of 15 steps [289].

These 15 steps can be categorized into 5 phases, which are:

#### I. Production phase:

- Adsorption steps (ADS1; ADS2).
- Adsorption reflux step (ADS3\_Ref): recycling of a fraction of the off-gas (rich in CO<sub>2</sub>) obtained during blowdown back to the bottom of the column.

#### II. Depressurization phase:

- Two equalization depressurization steps (Eq1\_H & Eq2\_H): partial pressurization of two columns with a high-pressure gas present in a column at the end of the production phase.

- Purge provides step (PP) wherein a column that just underwent Eq2\_H is further depressurized and connected to another column undergoing the blowdown step. The gas stream from the former column allows to push the impurities in the latter.

### III. Regeneration phase:

- One equalization depressurization step (Eq3\_H) wherein the gas at the intermediate pressure present in a column is used to pressurize partially another column, which just underwent blowdown step and is under atmospheric pressure, to a higher-pressure condition.
- One blowdown step (BD1).
- One blowdown with reflux step (BD2\_Ref), wherein the regeneration is completed by evacuating a column using a vacuum pump, with some gas stream originated from PP step entered from the top of the column to push away impurities inside the column. Additionally, a fraction of the desorbed gas exiting from the bottom of the column is recycled as feed stream of another column, which is in the ADS3\_Ref step.

### IV. Low pressurization phase:

- Two equalization pressurization steps (Eq3\_L, Eq2\_L) wherein a column initially at atmospheric pressure is pressurized with the gas extracted from two different columns, which are in Eq3\_H and Eq2\_H steps, respectively.
- A time-out step (T-M) in which a column is isolated by closing all the valves. During this step, the column waits for the other columns to finish their respective steps.

### V. High pressurization phase:

- An equalization pressurization step (Eq1\_L), wherein a column is partially pressurized with the high-pressure gas extracted from another column that underwent Eq1\_H step.
- Two Pressurization steps (F1, F2).

Authors stated that the simulation of this process configuration results, but without recycling of off gas, in the obtention of biomethane purity of 97% and CH<sub>4</sub> recovery of 80% using 3.5 m<sup>3</sup> of adsorbent inside an adsorption column. The initial analysis of the simulation reveals that the 20% of the CH<sub>4</sub> was lost during the purge steps and blowdown steps. Therefore, a series of simulations with different recycle ratio values for the off gas were conducted to evaluate the impact of the recycling. Results indicate when the off gas was not recycled, the CH<sub>4</sub> recovery of the simulation is 80 % with productivity of 80 kg<sub>CH<sub>4</sub></sub>.m<sup>-3</sup>.h<sup>-1</sup>, whereas when 80 % of the off gas was recycled, the CH<sub>4</sub> recovery increases to 95% with productivity of 160 kg<sub>CH<sub>4</sub></sub>.m<sup>-3</sup>.h<sup>-1</sup>. There is a clear trade-off between CH<sub>4</sub> recovery and the productivity of biogas upgrading as the recycled gas substitutes the feed flow rate.

## 5.2. Adsorption kinetics

### 5.2.1. Principle of diffusion

A proper understanding of adsorption kinetics in PSA process could be achieved by analyzing the mechanism of mass transfer in macropores and micropores of an adsorbent. For a porous adsorbent, the diffusion of adsorbate inside a

porous space involves different transfer mechanisms. The molecules of adsorbate must first travel through the external film barrier enveloping an adsorbent particle, followed by diffusion inside the pores of the adsorbent (macropores and micropores). Different mechanisms of mass transfer inside an adsorbent particle are summarized in Figure 5-9-a. As the bulk gas comes into contact with an adsorbent particle, (i) gas molecules diffuse inside the film (or boundary layer) surrounding the external surface of the solid particle, followed by (ii) diffusion inside macropores and mesopores and finally (iii) diffusion inside micropores. Figure 5-9-b illustrates the typical concentration profile of adsorbate from the bulk phase until the interior of an adsorbent particle at the start of adsorption. The adsorbate in the bulk phase has a concentration of  $C_g$ . As the capacity of the fluid film is small compared with that of the adsorbent particle, it could be assumed that there is very little accumulation of adsorbate within the film. Consequently, there exist a concentration gradient between the bulk phase and the film. The adsorbate concentration continues to decrease close to its minimum value as adsorbate approaches the center of the adsorbent particle.

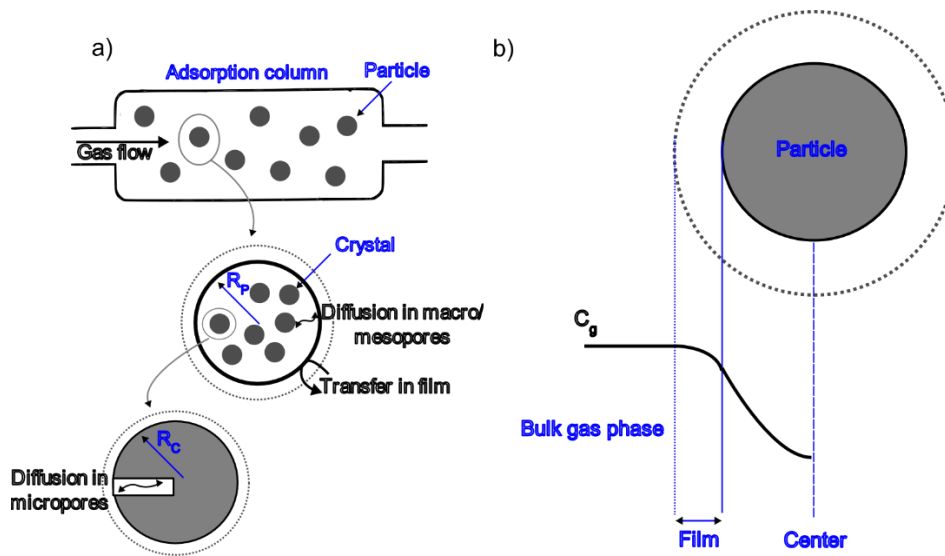


Figure 5-9: (a) Schema of mass transfers from bulk gas phase to the adsorbent solid surface. (b) Concentration profile of gas component in bulk phase, film layer and inside adsorbent particle at the start of adsorption.

a) External film diffusion

External film diffusion involves the transfer of gas molecule in the film (or boundary layer) surrounding the external surface of the solid particle. This arises because the surface of an adsorbent or catalyst particle is always be surrounded by a laminar boundary layer through which transport can occur only by molecular diffusion [290]. The thickness of this layer is related to hydrodynamic gas flow conditions, whereby it decreases with increasing superficial velocity of a highly turbulent regime.

External resistance is generally correlated in terms of film mass transfer coefficient,  $k_{fi}$  ( $m \cdot s^{-1}$ ), which could be estimated from the correlation proposed by Wakao et al. [291].

$$\frac{2k_f R_p}{D_m} = 2 + 1.1 Sc^{1/3} Re^{0.6} \quad \text{Eq. 5-1}$$

where  $R_p$  ( $m \cdot s^{-1}$ ) corresponds to the radius of adsorbent particle and  $D_m$  ( $m^2 \cdot s^{-1}$ ) corresponds to the molecular diffusivity of constituent  $i$  in bulk gas phase.

$Sc$  and  $Re$  are Schmidt and Reynold numbers, respectively and they are both dimensionless. Reynold number allows to empirically estimate whether a flow regime (laminar or turbulent) whereas Schmidt number represents the ratio between momentum diffusivity and mass diffusivity. Both of them are expressed as follows:

$$Sc = \frac{\mu}{\rho_g D_m} \quad \text{Eq. 5-2}$$

$$Re = \frac{\rho_g u d_p}{\mu} \quad \text{Eq. 5-3}$$

where  $u$  superficial velocity of gas ( $m \cdot s^{-1}$ ), it is calculated by dividing volumetric flowrate,  $Q$  ( $m^3 \cdot s^{-1}$ ), with cross sectional area of bed,  $A_{bed}$  ( $m^2$ );  $\rho_g$  density of gas ( $kg \cdot m^{-3}$ );  $d_p$  diameter of adsorbent particle ( $m$ );  $\mu$  dynamic viscosity of gas ( $Pa \cdot s$ ).

b) Mesopore and macropore diffusion

The mechanism of diffusion depends on the ratio of molecular kinetic diameter and pore width. Within the macropore range, transfer occurs mainly by molecular diffusion mechanism, as the collisions between diffusion molecules occur more frequently than the collision between diffusing molecules and pore walls [290]. Meanwhile, within the mesopore range, Knudsen diffusion is generally more dominant, but there may also be a significant contribution from Poiseuille diffusion.

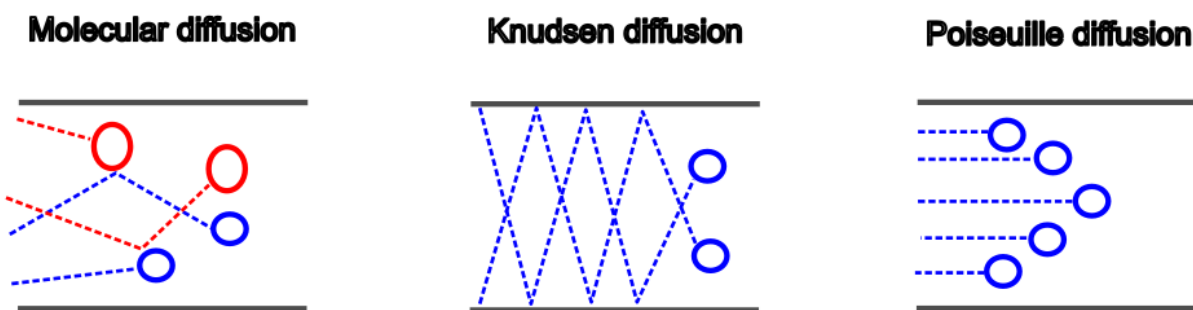


Figure 5-10: Representation of a different mechanism for internal diffusion.

❖ Molecular diffusion

Molecular diffusion occurs when two or more different molecular species of diffusing gas collided [290] (Figure 5-10). This phenomenon tends to become more predominant when the mean free path of gas molecules is shorter than pore diameter (Figure 5-10). The relative frequency of the intermolecular collisions and molecule-wall collisions are

determined from the ratio of the pore diameter ( $d_{\text{pore}}$ ) to the mean free path ( $\lambda$ ). In the case of binary gas mixture of species A and B, the molecular diffusivity,  $\mathbf{D}_m$  ( $\text{m}^2 \cdot \text{s}^{-1}$ ), can be expressed as Eq. 5-4 [292]:

$$D_m = \frac{0.0018583 \cdot T^{1.5} \cdot \varepsilon_{AB}}{\rho_g \cdot \sigma_{AB}^2 \cdot \Omega_D} \left( \frac{1}{M_A} + \frac{1}{M_B} \right)^{0.5} \quad \text{Eq. 5-4}$$

where  $\sigma_{AB}$  ( $\text{\AA}$ ) is a characteristic diameter of molecules, frequently referred as collision diameter between molecules;  $\varepsilon_{AB}$  (K) is the maximum energy attraction between molecules A and B;  $\mathbf{M}_A$  and  $\mathbf{M}_B$  ( $\text{mol} \cdot \text{kg}^{-1}$ ) is molecular weight of gas component A and B;  $k_b$  is Boltzmann constant ( $\text{m}^2 \cdot \text{kg} \cdot \text{s}^{-2} \cdot \text{K}^{-1}$ ).

$\sigma_{AB}$  can be further expressed as follows:

$$\begin{aligned} \sigma_{AB} &= 0.5 \cdot \sigma_A + 0.5 \cdot \sigma_B \\ \varepsilon_{AB} &= \sqrt{\varepsilon_A \varepsilon_B} \end{aligned} \quad \text{Eq. 5-5}$$

where  $\sigma_A$  and  $\sigma_B$  ( $\text{\AA}$ ) are the kinetic diameter of gas component A and B.

#### ❖ Knudsen diffusion

In small pores or at low pressure condition, the mean free path,  $\lambda$ , could become comparable with or even greater than pore diameter,  $d_{\text{pore}}$ . Consequently, the collision between pore walls and diffusing molecules is no longer negligible (Figure 5-10). In Knudsen diffusion, the rate at which momentum is transferred to the pore walls greatly exceeds the transfer of momentum between diffusing molecules, so that the latter can be neglected [290]. The value of Knudsen diffusivity of a constituent,  $\mathbf{D}_k$  ( $\text{m}^2 \cdot \text{s}^{-1}$ ), could be estimated from the following equation [290]:

$$D_k = 97 R_{\text{pore}} \left( \sqrt{\frac{T}{M}} \right) \quad \text{Eq. 5-6}$$

where  $\mathbf{R}_{\text{pore}}$  (m) corresponds to the radius of the pore. The Knudsen diffusivity varies only weakly with temperature and it is independent of pressure, as this mechanism does not depend on intermolecular collisions. Additionally, the diffusivity is dependent on molecular weight, which is the same as case as molecular diffusion.

When transitioning from molecular diffusion to Knudsen, meaning when the mean free path is comparable with the pore diameter, the effect of both molecular and Knudsen diffusion is significant. Therefore, the approximation of the transport diffusivity of both mechanisms,  $\mathbf{D}_{k-m}$  ( $\text{m}^2 \cdot \text{s}^{-1}$ ), can be done using the following equation [290];

$$\frac{1}{D_{k-m}} = \frac{1}{D_k} + \frac{1}{D_m} \quad \text{Eq. 5-7}$$

❖ Poiseuille diffusion

Poiseuille (or viscous or streamline) flow describes a steady laminar flow of incompressible and Newtonian fluid (Figure 5-10), which resulted from the difference in total pressure between the ends of a pore capillary [290]. This mechanism could be significant during the pressurization of the PSA column. The diffusivity by Poiseuille,  $D_{i,v}$  ( $m^2 \cdot s^{-1}$ ), could be estimated from the following equation [290]:

$$D_v = \frac{PR_{pore}^2}{8\mu} \quad \text{Eq. 5-8}$$

c) Micropore diffusion

Diffusion in micropores is dominated by interactions between the diffusing molecules and the pore wall. Diffusion within micropores is known as configurational diffusion, surface diffusion, or simply micropore diffusion, but these terms are essentially synonymous. The mechanism of surface diffusion is based on the motion of adsorbed phase jumping from one adsorption site to another vacant site (Figure 5-11). The effect of surface diffusion is important when the physically adsorbed molecules are mobile and the concentration of the adsorbed phase is high. Surface diffusion is an activated process that follows Arrhenius law and can be expressed as Eq. 5-6 [293]:

$$D_s = D_{s0} e^{\left(\frac{-E_{a,s}}{RT}\right)} \quad \text{Eq. 5-9}$$

where  $D_s$  ( $m^2 \cdot s^{-1}$ ) the surface diffusivity;  $D_{s0}$  ( $m^2 \cdot s^{-1}$ ) is the surface diffusivity at zero adsorption coverage for a reference temperature and;  $E_{a,s}$  ( $J \cdot mol^{-1}$ ) is the activation energy related to surface diffusion.

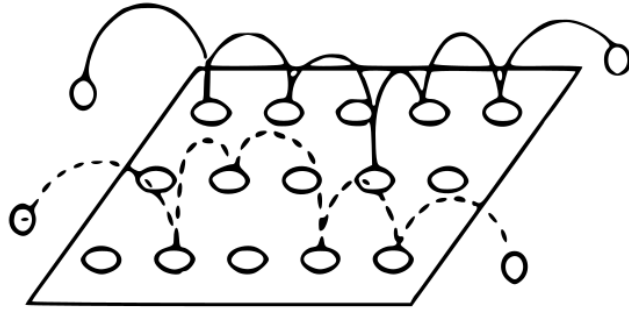


Figure 5-11: Representation of the mechanism for surface diffusion

The internal diffusional resistance in mesopores/macropores and micropores region can be combined together by considering the combination of diffusional resistances in terms of the equivalent resistance circuit (Figure 5-12). The Knudsen and molecular resistances are positioned in series while being parallel to surface resistance and Poiseuille resistance, respectively. The total diffusivity for internal diffusion,  $D_{tot}$  ( $m^2 \cdot s^{-1}$ ), could be expressed as:

$$D_{tot} = \frac{\varepsilon_p}{\tau} \left[ \left( \frac{1}{D_{i,k}} + \frac{1}{D_{i,m}} \right)^{-1} + D_{i,v} + D_{i,s} \right] \quad \text{Eq. 5-10}$$

where  $\tau$  is the tortuosity factor of an adsorbent and  $\varepsilon_p$  is the porosity of an adsorbent particle (intraparticle void volume only).

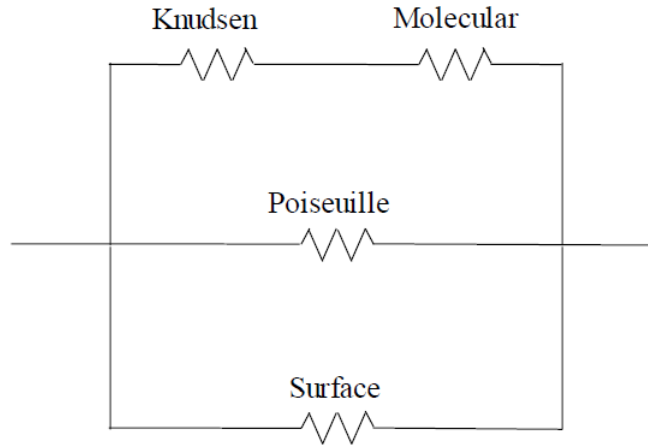


Figure 5-12: Combination of internal diffusional resistance according to a resistor network model [290].

### 5.2.2. Kinetics model

Kinetics model is used to represent the mass transfer mechanism inside the particles of adsorbents. Multiple kinetics model with varying degree of complexity have been developed and reported in literature. In this section, we will briefly present some of these kinetics' models.

#### a) Fick's model

In the period 1850–1855, Thomas Graham and Adolf Fick verified the proportionality between the diffusive flux and concentration gradient. Fick's first law of diffusion was then formulated [290] (Eq. 5-11):

$$J = -D \cdot \frac{\partial C}{\partial z} \quad \text{Eq. 5-11}$$

where  $J$  ( $\text{mol} \cdot \text{m}^2 \cdot \text{s}^{-1}$ ) is the diffusive flux,  $D$  is Fickian diffusivity ( $\text{m}^2 \cdot \text{s}^{-1}$ ),  $C$  ( $\text{mol} \cdot \text{m}^{-3}$ ) the species concentration in fluid phase and  $z$  (m) is the distance coordinate in the space.

Consequently, Fick has demonstrated from material balance that the diffusion of a species in a parallel-sided duct with a constant diffusivity could be expressed as Eq. 5-12:

$$\frac{\partial C}{\partial t} = -\frac{\partial J}{\partial z}$$



$$\frac{\partial C}{\partial t} = \frac{\partial \left( D \cdot \frac{\partial C}{\partial z} \right)}{\partial z} = D \cdot \frac{\partial^2 C}{\partial z^2} \quad \text{Eq. 5-12}$$

It is a mass conservation equation commonly known as Fick's second law of "non-stationary" diffusion [290] in which both spatial ( $\partial z$ ) and temporal ( $\partial t$ ) variations of species concentration are defined.

b) Gradient of chemical potential

Kinetics model based on chemical potential was developed by Barrer in 1971 [294] with the aim of describing the mass transfer of adsorbate inside an adsorbent particle. Fick's first law of diffusion has established that the driving force of diffusion is the gradient of concentration,  $\partial C$ , which could be related to the gradient of chemical potential,  $\partial \mu$ , defined by the change in chemical energy in a system per mole of molecules at constant temperature and pressure [290]. Hence, if the diffusive flux is considered as a flow driven by the gradient of chemical potential, then the flow must be opposed by frictional forces [290]. The steady-state energy balance for a differential element can be expressed as following [290]:

$$\frac{\partial \mu}{\partial z} = -f u \quad \text{Eq. 5-13}$$

where  $\mu$  ( $\text{J} \cdot \text{mol}^{-1}$ ) is the chemical potential of the adsorbate,  $u$  ( $\text{m} \cdot \text{s}^{-1}$ ) is the gas flow velocity and  $f$  ( $\text{kg} \cdot \text{m} \cdot \text{s}^{-1} \cdot \text{mol}^{-1}$ ) is the coefficient of molecular friction with its surrounding when the molecules are moving.

To relate the gradient of chemical potential to the concentration in adsorbed phase, the equilibrium gas phase must be considered as an ideal gas system in which the activity of the adsorbate,  $a$ , is identified by its partial pressure,  $P$ , as shown in Eq. 5-14 [290]:

$$\mu = \mu^0 + R \cdot T \cdot \ln a = \mu^0 + R \cdot T \cdot \ln P \quad \text{Eq. 5-14}$$

where  $\mu^0$  is the standard chemical potential for pure phase,  $R$  is the gas constant ( $R=8.314 \text{ J} \cdot \text{mol}^{-1} \cdot \text{K}^{-1}$ ) and  $T$  (K) is the temperature.

Therefore, the differential element  $\partial \mu / \partial z$  presented in Eq. 5-13 could also be expressed as follows:

$$\frac{\partial \mu}{\partial z} = R \cdot T \cdot \frac{\partial \ln P}{\partial z} \quad \text{Eq. 5-15}$$

Eq. 5-15 can then be substituted into Eq. 5-13:

$$u = -\frac{R \cdot T}{f} \cdot \frac{\partial \ln P}{\partial z} \quad \text{Eq. 5-16}$$

The expression of diffusive flux in adsorbed phase,  $\mathbf{J}$  (mol.m<sup>-2</sup>. s<sup>-1</sup>) can also be defined as the product of  $u$  (m.s<sup>-1</sup>) gas concentration,  $C$  (mol. m<sup>-3</sup>) [290] :

$$\begin{aligned} J &= u \cdot C \\ J &= -\frac{R \cdot T}{f} \cdot \frac{\partial \ln P}{\partial z} \cdot C \\ J \cdot \frac{1}{C} &= -\frac{R \cdot T}{f} \cdot \frac{\partial \ln P}{\partial z} \\ J \cdot \frac{\partial \ln C}{\partial C} &= -\frac{R \cdot T}{f} \cdot \frac{\partial \ln P}{\partial z} \\ J &= -\frac{R \cdot T}{f} \cdot \frac{\partial \ln P}{\partial \ln C} \cdot \frac{\partial C}{\partial z} \end{aligned} \quad \text{Eq. 5-17}$$

The diffusive flux expressed in Eq. 5-17 could be compared with that defined by Fick's first law (cf. Eq. 5-11, page 149). Hence, at a given temperature, Fickian diffusivity,  $D$ , could be expressed as:

$$D = -\frac{R \cdot T}{f} \cdot \left( \frac{\partial \ln P}{\partial \ln C} \right)_T = D_0 \cdot \left( \frac{\partial \ln P}{\partial \ln C} \right)_T \quad \text{Eq. 5-18}$$

where  $D_0$  (m<sup>2</sup>.s<sup>-1</sup>) is the Fickian diffusivity in adsorbed phase at nearly zero adsorption coverage (corrected diffusivity) [290] and  $\partial \ln P / \partial \ln C$  is the thermodynamic corrective factor which follows adsorption coverage, known as Darken corrective factor.

Kärger *et al.* have stated that in a microporous adsorbent, there is no clear distinction between molecules on the surface and molecules in the gas phase in the central region of the pore [290]. Therefore, it is more convenient to consider only adsorbed phase concentration,  $q$  (mol.m<sup>-3</sup>), instead of gas phase concentration  $C$ . Therefore, assuming an ideal vapor phase, the Eq. 5-17 and Eq. 5-18 can be re-written as:

$$J = -\frac{R \cdot T}{f} \cdot \frac{\partial \ln P}{\partial \ln q} \cdot \frac{\partial q}{\partial z} \quad \text{Eq. 5-19}$$

$$D = -\frac{R \cdot T}{f} \cdot \left( \frac{\partial \ln P}{\partial \ln q} \right)_T = D_0 \cdot \left( \frac{\partial \ln P}{\partial \ln q} \right)_T \quad \text{Eq. 5-20}$$

If the isotherm of a system is linear following Henry's law, which is usually the case for diluted system or low-pressure region, the Darken corrective factor  $\partial \ln P / \partial \ln q \approx 1$  and thus  $D \approx D_0$  [290]. However, if the adsorption occurs beyond Henry's law region, then the Fickian diffusivity is dependent on  $D_0$  coefficient and Darken corrective factor, determined by isotherm shape (e.g. Langmuir, Freundlich, Toth, etc..).

As an example, assuming Langmuir model (cf. Eq. 4-7, page 99) was used to describe the pure gas isotherm, the fractional adsorption loading,  $\theta$ , can be written as:

$$\theta = \frac{q}{q_m} = \frac{K_L P}{1 + (K_L P)} \quad \text{Eq. 5-21}$$

As an example, the Darken corrective factor for Langmuir isotherm can be expressed as Eq. 5-22 [290]:

$$\begin{aligned} \left( \frac{\partial \ln P}{\partial \ln q} \right)_T &= \frac{1}{1 - \theta} \\ \left( \frac{\partial \ln P}{\partial \ln q} \right)_T &= \frac{1}{1 - \frac{K_L P}{1 + (K_L P)}} \end{aligned} \quad \text{Eq. 5-22}$$

#### c) Linear Driving Force (LDF) model

As explained previously, the diffusion of gas molecules involves different transfer mechanisms, which are the diffusion in external film, internal macro/mesopores diffusion and micropores diffusion. The LDF model, which originally proposed by Glueckauf and Coates [295], assumed that all the possible mass transfer resistances related to each transfer mechanism could be simplified into a single global mass transfer coefficient,  $\mathbf{K}_{LDF}$ . According to this model, the uptake rate of a species into adsorbent particles is proportional to the linear difference between the average adsorbate concentration at present conditions,  $\mathbf{q}$ , and the adsorbate concentration in equilibrium with the bulk phase of that species at the outer surface of the particle,  $\mathbf{q}_{eq}|_c$ , and is given by [295]:

$$\frac{\partial q}{\partial t} = K_{LDF} \left( q_{eq}|_c - q(t) \right) \quad \text{Eq. 5-23}$$

where  $\mathbf{q}_{eq}|_c$  (mol. m<sup>-3</sup>) corresponds to adsorbed quantity in equilibrium with bulk phase concentration C and  $\mathbf{K}_{LDF}$  (s<sup>-1</sup>) is the global LDF mass transfer coefficient.

#### d) Biporous Linear Driving Force (bi-LDF) model

Another model that is available inside simulation tool gPROMS is the Bi-LDF model. Bi-LDF model is a variant of LDF model, where instead of grouping all possible mass transfer resistance into a single mass transfer coefficient, Bi-LDF takes into account each of the mass transfer resistance in the film, macro/mesopore and micropores region separately. This model describes the rate of adsorption of a single adsorbate component into an adsorbent particle by:

$$\frac{\partial q}{\partial t} = a_p k_f (C - C_s) \quad \text{Eq. 5-24}$$

where  $\mathbf{a}_p$  is the specific area of adsorbent (m<sup>2</sup>.m<sup>-3</sup>);  $\mathbf{k}_f$  (m. s<sup>-1</sup>) is the external film mass transfer resistance (cf. Eq. 5-1, page 145);  $\mathbf{C}_s$  is the concentration of a gas component at the adsorbent pellet surface (mol.m<sup>-3</sup>).

The value of  $C_s$  is dependent on the macro/mesopores and micropores mass transfer resistance, and could be further expressed as:

$$C_s = \left[ \frac{\varepsilon_p}{k_{mac-mes}} \cdot \frac{\partial C_{pore}}{\partial t} + \frac{k_{micro}}{k_{mac-mes}} \cdot \left( q_{eq}|_{C_{pore}} - q(t) \right) \right] + C_{pore}(t) \quad \text{Eq. 5-25}$$

where  $C_{pore}$  (mol. m<sup>-3</sup>) is the concentration of gas in the pores of adsorbent;  $q_{eq}|_{C_{pore}}$  (mol. m<sup>-3</sup>) is the adsorbed quantity in equilibrium with gas phase concentration in the pores;  $k_{micro}$  (s<sup>-1</sup>) is the LDF coefficient for mass transfer through micropores;  $k_{mac-mes}$  (s<sup>-1</sup>) is the LDF coefficient for mass transfer through macro/mesopores. The terms  $k_{micro}$  and  $k_{mac-mes}$  could be estimated as follows:

$$k_{mac-mes} = \frac{15D_{i,k-m}}{r_p^2} \quad \text{Eq. 5-26}$$

$$k_{micro} = \frac{15D_s}{r_c^2} \quad \text{Eq. 5-27}$$

where  $r_p$  and  $r_c$  (m) correspond to the adsorbent particle radius and crystal radius, respectively. By injecting Eq. 5-25 into 4-24, the rate of adsorption of a single adsorbate component into an adsorbent particle by the bi-LDF model could be re-written as:

$$\frac{\partial q}{\partial t} = a_p k_f \left( C(t) - \left[ \frac{\varepsilon_p}{k_{mac-mes}} \cdot \frac{\partial C_{pore}}{\partial t} + \frac{k_{micro}}{k_{mac-mes}} \cdot \left( q_{eq}|_{C_{pore}} - q(t) \right) \right] - C_{pore}(t) \right) \quad \text{Eq. 5-28}$$

In this work, we are unable to determine the adsorption kinetics parameters for our materials. Therefore, we have opted to acquire the relevant adsorption kinetics parameters for HKUST-1 from the literature instead. For that, we have referred to the study by Asadi et al. [17], where CO<sub>2</sub>/CH<sub>4</sub> breakthrough analysis of commercial Cu-BTC/HKUST-1 procured from by the same supplier in our study, was conducted at 308 K and 1 bar. The authors successfully implemented bi-LDF model with appropriate kinetic parameters to describe the breakthrough of CO<sub>2</sub>/CH<sub>4</sub>. Thus, for this work, we implemented the same bi-LDF model with the same adsorption kinetics parameters as reported by Asadi et al. [17].

### 5.3. Simulation methodology

#### 5.3.1. Column dynamic (mass, energy and momentum balances)

##### a) General assumptions

As previously mentioned, two cases of simulation were conducted in this study. Following main assumptions are taken for both cases:

- The system is considered one dimensional, which only involves axial configuration. No mass, heat or velocity variations in the radial direction.
- The adsorbent is assumed to be perfectly homogeneous. All the beads of an adsorbent are considered being identical (cylindrical pellet).
- The porosities are constant, and the solids are perfectly rigid.
- Gases are considered ideal gases, and the gaseous mixture is supposed to be ideal.
- The mass transfer rate is represented by a bilinear driving force (bi-LDF) model.
- The dispersion coefficient of each gas constituent in the gas mixture is considered the same.

Additionally, for the 1st case of simulation, it was assumed that there is an exchange of energy with the environment, whereas for the 2<sup>nd</sup> case external heat exchange is neglected.

#### b) Mass conservation equations

The mass balance for each component inside a column is described through equation 4-29. This expression takes into account the axial dispersion in the column, the gas convection, the accumulation in the bulk gas phase and the accumulation in the adsorbed phase.

$$\underbrace{\varepsilon_{tot} \frac{\partial C}{\partial t}}_{\text{Accumulation in gas phase}} = \underbrace{-\frac{\partial(uC)}{\partial z}}_{\text{Convection}} + \underbrace{\varepsilon_{bed} \frac{\partial}{\partial z} \left( D_L \frac{\partial C}{\partial z} \right)}_{\text{Axial dispersion}} - \underbrace{\frac{\partial q}{\partial t}}_{\text{Accumulation in adsorbed phase}} \quad \text{Eq. 5-29}$$

where  $D_L$  is the axial dispersion coefficient ( $m^2 \cdot s^{-1}$ );  $y$  is the gas molar fraction,  $\rho_{bed}$  ( $kg \cdot m^{-3}$ ) is the bed density,  $\varepsilon_{tot}$  is the total inter- and intra- particle void ( $\varepsilon_{tot} = \varepsilon_{bed} + [1 - \varepsilon_{bed}] \varepsilon_p$ ) and  $q$  is concentration of adsorbed phase ( $mol \cdot m^{-3}$ ).

As bi-LDF was chosen as the model to describe the mass transfer, Eq. 5-28 is used to express the accumulation in the adsorbed phase in Eq. 5-29:

$$\frac{\partial q}{\partial t} = a_p k_f \left( C(t) - \left[ \frac{\varepsilon_p}{k_{mac-mes}} \cdot \frac{\partial C_{pore}}{\partial t} + \frac{k_{micro}}{k_{mac-mes}} \cdot \left( q_{eq|_{C_{pore}}} - q(t) \right) \right] - C_{pore}(t) \right) \quad \text{Eq. 5-28}$$

Additionally, the gas phase dispersion in the axial flow direction,  $D_L$ , can be either specified or calculated based on molecular diffusivities,  $D_m$  (Eq. 5-1). When calculated, the correlation by Wakao [291] may be used as expressed in Eq. 5-30:

$$\frac{\varepsilon_{bed} D_L}{D_m} = 20 + 0.5 \cdot Sc_i \cdot Re \quad \text{Eq. 5-30}$$

#### c) Energy conservation equations

The continuity equation for energy transport of gas phase throughout the bed in axial direction is given in Eq.4-31.

$$\sum_{i=1}^N (\Delta H_i) \frac{\partial q_i}{\partial t} = \varepsilon_{bed} \frac{\partial}{\partial z} \left( D_L \frac{\partial H_f}{\partial z} \right) - \frac{\partial (u H_f)}{\partial z} + \frac{\partial}{\partial z} \left( \lambda_{eff} \cdot \frac{\partial T}{\partial z} \right) - \frac{4}{d_{bed}} h_{f-w} (T - T_w) \quad \text{Eq. 5-31}$$

Energy in      Axial      Convection      Conduction      Energy exchange  
adsorbed phase      dispersion                     fluid-wall

where  $\Delta H_i$  is the heat of adsorption of gas component  $i$  ( $\text{J} \cdot \text{mol}^{-1}$ );  $H_f$  is the bulk gas phase specific enthalpy ( $\text{J} \cdot \text{mol}^{-1}$ );  $\lambda_{eff}$  is the effective thermal conductivity ( $\text{W} \cdot \text{m}^{-1} \cdot \text{K}^{-1}$ ),  $h_{f-w}$  is the heat transfer coefficient between gas phase and wall ( $\text{W} \cdot \text{m}^{-2} \cdot \text{s}^{-1}$ ),  $T_w$  is the temperature of wall (K) and  $d_{bed}$  is the diameter of the wall (m).

The effective thermal conductivity of the adsorbent-adsorbate system may be estimated from Specchia correlation [296], as given by the following equation:

$$\lambda_{eff} = \varepsilon_{bed} \lambda_g + (1 - \varepsilon_{bed}) \frac{1}{\frac{0.22 \varepsilon_{bed}^2}{\lambda_g} + \frac{2}{3} \lambda_p} \quad \text{Eq. 5-32}$$

where  $\lambda_g$  is the thermal conductivity of gas mixture ( $\text{W} \cdot \text{m}^{-1} \cdot \text{K}^{-1}$ ) and  $\lambda_p$  is the thermal conductivity of adsorbent particle ( $\text{W} \cdot \text{m}^{-1} \cdot \text{K}^{-1}$ ).

In the condition where heat exchange with environment is not neglected, the energy balance at the bed wall must be taken into account in Eq. 5-31 and is given by the following equation:

$$\rho_w C_{p,w} \frac{\partial T_w}{\partial t} = \frac{\partial}{\partial z} \left( \lambda_w \frac{\partial T_w}{\partial z} \right) + h_{f-w} \frac{d_{bed}}{\left( \frac{d_{bed}}{2} + l_w \right)^2 - \left( \frac{d_{bed}}{2} \right)^2} (T - T_w) + h_{w-ext} \frac{(d_{bed} + 2l_w)}{\left( \frac{d_{bed}}{2} + l_w \right)^2 - \left( \frac{d_{bed}}{2} \right)^2} (T_{ext} - T_w) \quad \text{Eq. 5-33}$$

where  $\rho_w$  ( $\text{kg} \cdot \text{m}^{-3}$ ) is the mass density of wall material;  $C_{p,w}$  ( $\text{J} \cdot \text{kg}^{-1} \cdot \text{K}^{-1}$ ) is the specific heat capacity of the wall material;  $\lambda_w$  ( $\text{W} \cdot \text{m}^{-1} \cdot \text{K}^{-1}$ ) is the thermal conductivity of the wall material;  $T_{ext}$  (K) is the temperature of the environment;  $l_w$  (m) is the thickness of the wall;  $h_{w-ext}$  ( $\text{W} \cdot \text{m}^{-2} \cdot \text{K}^{-1}$ ) is the heat transfer coefficient from the wall to the environment.

#### d) Momentum conservation equations

We have considered that pressure loss throughout the column is expressed through Ergun's law:

$$-\frac{\partial P}{\partial z} - 150\mu \frac{(1 - \varepsilon_{bed})^2}{\varepsilon_{bed}^3 d_p^2} - \frac{1.75(1 - \varepsilon_{bed})\rho^g u^2}{\varepsilon_{bed}^3 d_p} = 0 \quad \text{Eq. 5-34}$$

e) Boundary conditions

To solve the system of partial differential equations detailed above, the boundary conditions are needed. The flow direction of the gas inside the column is from the feed at  $z = 0$  to the product side of the bed,  $z = L$ . The boundary condition is summarized in Table 5-3.

Table 5-3: Boundary conditions for each conservation equation

	Z = 0	Z = L
Mass conservation equation	$\frac{\dot{n}^{in} y^{in}}{A_{bed}} = uC - \varepsilon_{bed} D_L \frac{\partial C}{\partial z}$	$\varepsilon_{bed} D_L \frac{\partial C}{\partial z} = 0$
Energy conservation equation	$\frac{\dot{n}^{in} H_f^{in}}{A_{bed}} = uH_f - \varepsilon_{bed} D_L \frac{\partial H_f}{\partial z} - \frac{1}{1000} \lambda_{eff} \frac{\partial T}{\partial z}$	$\frac{\partial T}{\partial z} = 0$
Momentum conservation equation	$P = P^{in}$	-

where  $\dot{n}^{in}$  is the molar flow rate at the entrance of bed (mol. s<sup>-1</sup>);  $y^{in}$  is the molar fraction at the entrance of the bed;  $A_{bed}$  is the bed cross-sectional area (m<sup>2</sup>),  $H_f^{in}$  is the mass specific enthalpy at the entrance of the adsorption section of the bed on the feed side (J. mol<sup>-1</sup>);  $P^{in}$  the pressure at the feed entrance of the adsorption bed (Pa).

### 5.3.2. Single column design

a) Case 1: Model validation

As previously mentioned, the objective of the simulation for case 1 is to verify the reliability of the simulation tool gPROMS. This is done by replicating the experimental CO<sub>2</sub>/CH<sub>4</sub> breakthrough results, reported by Asadi et al. [17], with our own simulation. Therefore, it is important to re-use the same parameters as reported by Asadi et al. in the simulation of case 1

Figure 5-13 presents the simplified version of an adsorption column used for our simulation of the case 1. The feed gas, which consists of CO<sub>2</sub>/CH<sub>4</sub> mixture as well as He as carrier gas, enters the adsorption column from the bottom with its flow rate being controlled by valve VA opening. As the gas mixture passes through the adsorbent bed, the less adsorbed component leaves the column through the valve VB at the top. Once breakthrough has been achieved, the regeneration of the bed is started by changing the feed gas stream to pure He, closing of the valve VB and opening of the valve VA. Additionally, Table 5-4 lists the parameters related to the column design. It should be highlighted, that unless it is stated otherwise, all the listed parameters in this section are taken from Asadi et al. [17]

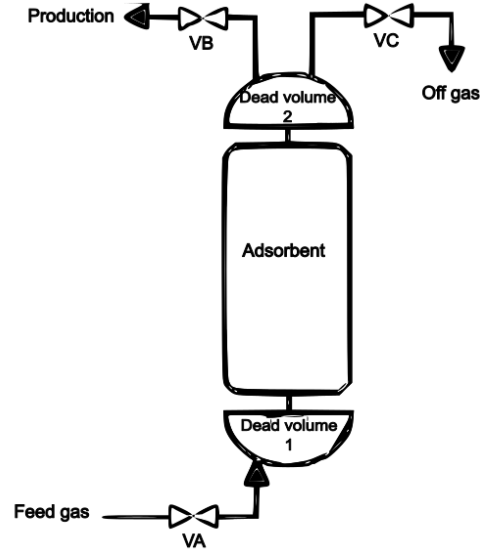


Figure 5-13: Simplified scheme of an adsorption column used for the CO<sub>2</sub>/CH<sub>4</sub> breakthrough simulation [17].

Table 5-4: Column design parameters and adsorbent properties for CO<sub>2</sub>/CH<sub>4</sub> breakthrough simulation [17].

Bed length (m)	0.305
Adsorbent volume (m <sup>3</sup> )	0.103 x 10 <sup>-3</sup>
Dead volume 1 (m <sup>3</sup> )	N/A
Dead volume 2 (m <sup>3</sup> )	N/A
Adsorbent layer	Single
Adsorbent	Cu-BTC/ HKUST-1
Adsorbent shape	Cylindrical
$d_p$ (mm)	3
$\rho_p$ (kg. m <sup>-3</sup> )	958
$C_{p,p}$ (kJ.kg <sup>-1</sup> .K <sup>-1</sup> )	0.7 <sup>a</sup>
$\Lambda_p$ (W.m <sup>-1</sup> .K <sup>-1</sup> )	1.5 <sup>b</sup>
$\epsilon_{bed}$	0.4
Adsorption pressure (bar)	1.1
Regeneration pressure (bar)	1
Column's initial temperature (K)	308
CO <sub>2</sub> /CH <sub>4</sub> /He initial molar fraction	0/0/1

<sup>a</sup> Value taken from [297]. <sup>b</sup> Value taken from [298].

b) Case 2: PSA cycle for CO<sub>2</sub>/CH<sub>4</sub> separation in the context of biogas upgrading



Figure 5-14 represents the simplified version of an adsorption column used for our PSA simulation with indication of gas stream flow directions. The feed gas consists of CO<sub>2</sub>/CH<sub>4</sub> mixture entering the column from the bottom through the valve V1 also used for the control of flow rate. The less adsorbed component (CH<sub>4</sub>) is collected as the product at the outlet of valve V3 and a fraction of it is also be used as purge gas for another column by opening valve V4. Finally, the depressurization and purging inside the column are done at counter-current flow and the off gas is channeled out from the bottom of the column by opening V2 valve.

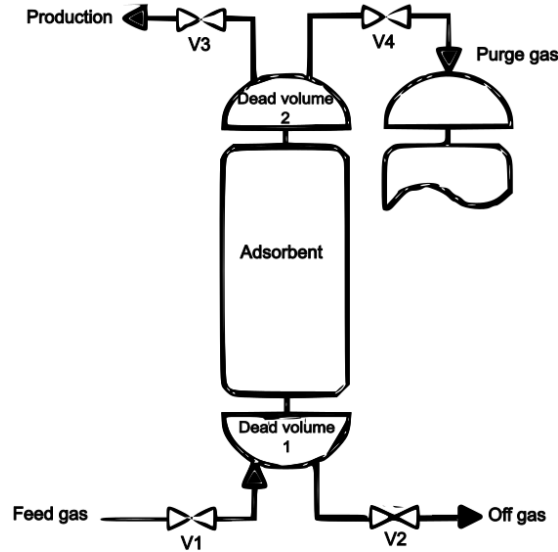


Figure 5-14: Simplified scheme of an adsorption column used for PSA simulation

The parameters for the design of the column are listed in Table 5-4. The dead/void volume 1 and 2 at the feed and product section of the column ensure a good distribution of gas upon entering and leaving the adsorption bed. Column design parameters used in this simulation (e.g. bed length, adsorbent volume, dead volume) were based on the study of Chouikhi et al. [289], where the industrial scale adsorption column was designed and simulated for biomethane production. The adsorbent chosen for the simulation of 2<sup>nd</sup> case is HKUST-1/PLA, with its respective physical properties. Next, in order to achieve the highest working CO<sub>2</sub> adsorption capacity, the adsorption pressure was set at 4 bar during the feed stage. Beyond this pressure level, as the predicted by IAST modeling, material's CO<sub>2</sub>/CH<sub>4</sub> adsorption selectivity starts to decrease (cf. Figure 4-19, page 131). Lastly, the regeneration pressure is set at 1 bar since we wanted to simulate the PSA process without using vacuum regeneration.

Table 5-5: Column design parameters and adsorbent properties for PSA simulation

Bed length (m)	2.4
Adsorbent volume (m <sup>3</sup> )	3.6
Dead volume 1 (m <sup>3</sup> )	0.1
Dead volume 2 (m <sup>3</sup> )	0.1
Adsorbent layer	Single
Adsorbent	HKUST-1/PLA

Adsorbent shape	Cylindrical
$d_p$ (mm)	2
$\rho_p$ (kg. m <sup>-3</sup> )	990
$C_{pp}$ (kJ.kg <sup>-1</sup> .K <sup>-1</sup> )	0.7 <sup>a</sup>
$\Lambda_p$ (W.m <sup>-1</sup> .K <sup>-1</sup> )	1.5 <sup>b</sup>
$\varepsilon_{bed}$	0.3
Adsorption pressure (bar)	4
Desorption/purge pressure (bar)	1

<sup>a</sup> Value taken from [297]. <sup>b</sup> Value taken from [298].

### 5.3.3. Cycle configuration

#### a) Case 1: Model validation

The CO<sub>2</sub>/CH<sub>4</sub> breakthrough experiment conducted by Asadi et al. [17] was simulated using a general PROcess Modelling System (gPROMS) environment (PSE Enterprise, UK), and numerically solved Finite Volume (FV) discretization scheme with 200 intervals. The simulation of the breakthrough process was carried out using an adsorption column initially filled with pure He at the pressure of 1.1 bar. The overall simulated breakthrough experiment steps are presented in Figure 5-15:

- **Adsorption (A):** Mixture of CO<sub>2</sub>, CH<sub>4</sub> and He with the molar fraction of 0.83, 0.04 and 0.13, respectively, enters the adsorption column from the feed section at the bottom of the column. The He gas acts as a carrier gas and together with less adsorbed major component CH<sub>4</sub> it leaves the product section at the top of the column. The adsorption step ends when the CO<sub>2</sub> concentration at the outlet is similar to that of the inlet.
- **Regeneration (R):** After a complete utilization of the dynamic CO<sub>2</sub> working adsorption capacity, the regeneration of the bed is started by flashing pure He from the feed section of the column. The adsorbed gas in the adsorbent media is then desorbed and pushed upwards by the carrier gas. The off gas (rich in CO<sub>2</sub>) then leaves the column at the top section. The regeneration step ends when only He is detected in the off gas stream.

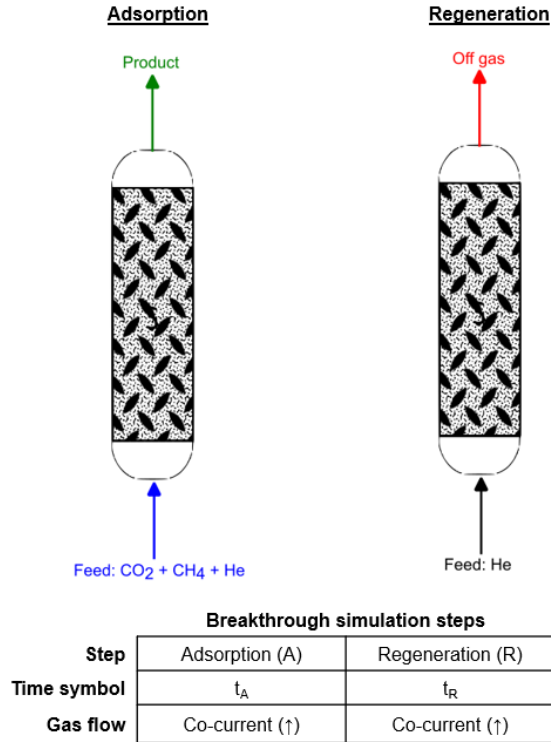


Figure 5-15: Descriptive scheme of steps applied for the simulation of CO<sub>2</sub>/CH<sub>4</sub> breakthrough conducted by Asadi et al. [17].

b) Case 2: PSA cycle for CO<sub>2</sub>/CH<sub>4</sub> separation in the context of biogas upgrading

The evaluate CO<sub>2</sub>/CH<sub>4</sub> separation performances of HKUST-1/polymer composite materials elaborated in this study, the simulation of PSA involving HKUST-1/PLA composite as the adsorbent media was carried out. The system of partial differential equations describing mass and heat transfer within PSA unit was solved in gPROMS using FV discretization scheme with 200 elementary volumes. Additionally, the simulation was executed until Cyclic Steady-State (CSS) is detected before the maximum number of simulation cycle is reached (1000 cycles). For the simulation of the 2<sup>nd</sup> case, two cycle configurations were tested: (i) Skarstrom cycle and (ii) Skarstrom + Pressure Equalisation (PE) cycle.

❖ Skarstrom cycle configuration

The biogas upgrading simulation using Skarstom cycle configuration was carried out using 2 PSA units instead of 4. This is to minimize the time required to carry out a complete simulation until CSS. Figure 5-16 illustrates the Skarstrom cycle process steps simulated for the two PSA units. The PSA units undergo 4 steps in total, which are Adsorption (A), Blowdown (BD), Purge (P) and Pressurization (PS), as previously described in section 2.3, page 42. The time for each 4 steps is denoted as  $t_A$ ,  $t_{BD}$ ,  $t_P$  and  $t_{PS}$ .

Concerning PSA cyclic time, the adsorption time,  $t_A$ , is synchronized with the purging time,  $t_P$ , as a fraction of biomethane produced during the former step is used for the latter as purging gas. Additionally, the blowdown time,  $t_{BD}$ , and the pressurization time,  $t_{PS}$ , are set to be similar.

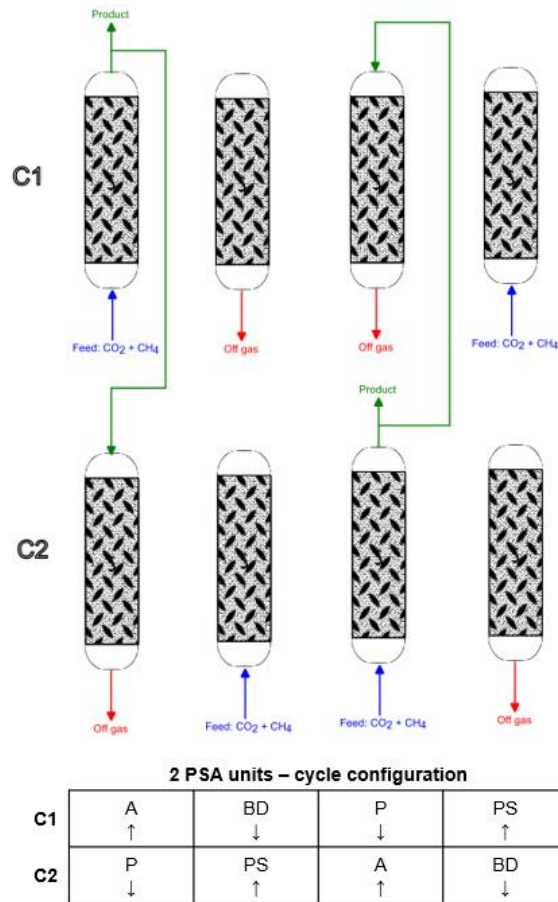


Figure 5-16: Descriptive scheme of Skarstrom cycle applied to the simulation of CO<sub>2</sub>/CH<sub>4</sub> separation using HKUST-1/PLA as adsorbent media. The arrows signify the flow of the gas stream.

Initial conditions inside the column prior to the start of simulation are listed in Table 5-6. Both of the PSA units are initially considered being filled with pure CH<sub>4</sub>. Temperature inside both PSA units is initially similar to that of the temperature of feed gas (298 K). Finally, the initial pressure inside Column 1 was set to 4 bar as at the beginning of the cycle this column would have just undergone pressurization step, whereas Column 2 was set to 1 bar, as would have been expected after the blowdown step.

Table 5-6: Initial conditions of Skarstrom PSA cycle for biogas upgrading

Column 1 initial pressure (bar)	4
Column 2 initial pressure (bar)	1
Column 1 initial temperature (K)	298
Column 2 initial temperature (K)	298
CO <sub>2</sub> /CH <sub>4</sub> initial molar fraction	0/1

❖ Skarstrom + Pressure Equalization cycle

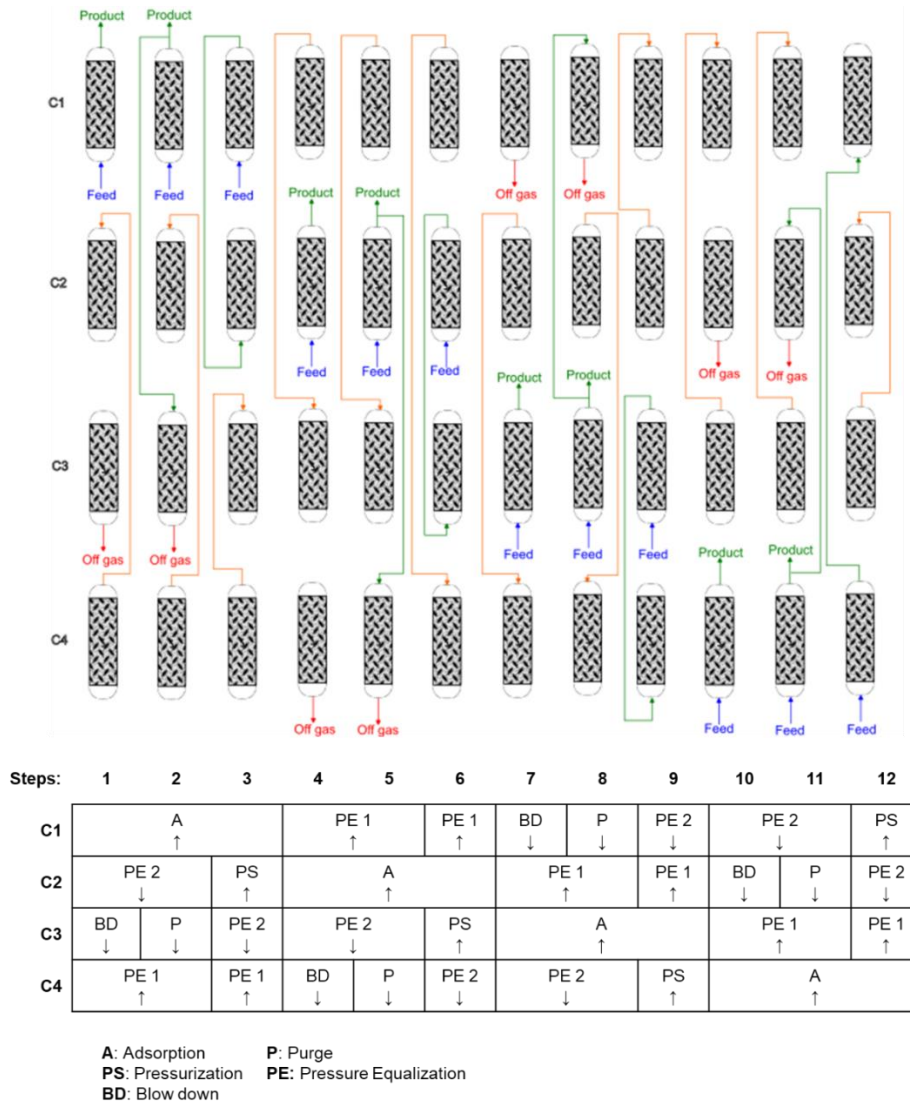


Figure 5-17: Descriptive scheme of Skarstrom + Pressure Equalization cycle applied to the simulation of CO<sub>2</sub>/CH<sub>4</sub> separation using HKUST-1/PLA as adsorbent media. The arrows signify the flow of the gas stream.

Figure 5-17 illustrates the configuration of Skarstrom cycle with Pressure Equalization step that was simulated with four interconnected columns. The newly added **Pressure Equalization (PE)** involves the connection of two PSA columns at different pressure, until the pressure in both of them stabilizes and reaches a new intermediate value. The PE step can be categorized into two phases: PE 1 and PE 2. PE 1 starts when a PSA column, which just underwent adsorption step and is still under a high-pressure, is connected to another column that has a lower pressure condition after purge step. This results in the desorbed gas in the high-pressure PSA unit to flow in co-current direction towards the other connected PSA column. Conversely, PE 2 starts when a PSA column, which just underwent purge step and is at low pressure condition, is connected to another PSA column that has a higher pressure. This results in the desorbed gas from the other high pressure PSA unit to enter the lower pressure PSA unit in the counter-current direction.

Table 5-7: Column's initial condition parameters for Skarstrom + PE configuration

Column 1 initial pressure (bar)	4
Column 2 initial pressure (bar)	2
Column 3 initial pressure (bar)	2
Column 4 initial pressure (bar)	4
Column 1 initial temperature (K)	298
Column 2 initial temperature (K)	298
Column 3 initial temperature (K)	298
Column 4 initial temperature (K)	298
CO <sub>2</sub> /CH <sub>4</sub> initial molar fraction	0/1

Initial conditions inside the columns at the beginning of simulation are listed in Table 5-7. All the columns are initially considered being filled with CH<sub>4</sub>. Temperature inside both columns is initially similar to that of the temperature of feed gas, which is 298 K. Furthermore, the initial pressure inside Column 1 and Column 4 were set to 4 bar as they would have just undergone pressurization and adsorption, respectively, prior to the start of the cycle. Meanwhile, Column 2 and Column 3 were set to be initially at 2 bar as both columns would have just undergone PE prior to the beginning of the cycle.

#### 5.3.4. Operational/Isotherms/Mass and heat transfer parameters

##### a) Case 1: Model validation

Table 5-8 summarizes operational/isotherms/mass and heat transfer parameters used for this simulation. Specifications of the feed gas stream, breakthrough steps time, parameters of heat transfer and mass transfer are similar to those reported by Asadi et al. [17]. Meanwhile, the parameters for CO<sub>2</sub> and CH<sub>4</sub> isotherm models (Langmuir) were determined from isotherm data, as reported by Asadi et al. [17] (cf. Eq. 4-7, page 99).

Table 5-8: Operational/Isotherms/Mass and heat transfer parameters applied for the simulation of CO<sub>2</sub>/CH<sub>4</sub> breakthrough reported by Asadi et al. [17]

	CO <sub>2</sub>	0.83
CO <sub>2</sub> /CH <sub>4</sub> /He feed molar fraction	CH <sub>4</sub>	0.04
	He	0.13
		13.4 x 10 <sup>-6</sup>
Feed volumetric flow rate (m <sup>3</sup> .s <sup>-1</sup> )		
Feed gas temperature (K)		308
Feed pressure (bar)		1.1
Adsorption time, t <sub>A</sub> (s)		3000
Regeneration time, t <sub>R</sub> (s)		1500
Isotherm model		Langmuir-IAST
Monolayer saturation capacity, q <sub>s,i</sub> (mol/kg)	CO <sub>2</sub>	13.70

	CH <sub>4</sub>	8.14
Pre-exponential constant $b_{1,i}$ (bar <sup>-1</sup> )	CO <sub>2</sub>	46.72
	CH <sub>4</sub>	2.54
Exponential constant $b_{2,i}$ (K <sup>-1</sup> )	CO <sub>2</sub>	2719.50
	CH <sub>4</sub>	1815.76
$\Delta H_{i,ads}$ (kJ.mol <sup>-1</sup> )	CO <sub>2</sub>	22.8
	CH <sub>4</sub>	15.1
Heat transfer coefficient between bulk gas and adsorbent, $h_{f-ads}$ (W.m <sup>-1</sup> .K <sup>-1</sup> )		65.3
Heat transfer coefficient between bulk gas and wall, $h_{f-w}$ (W.m <sup>-1</sup> .K <sup>-1</sup> )		25
Heat transfer coefficient between wall and environment, $h_{w-ext}$ (W.m <sup>-1</sup> .K <sup>-1</sup> )		20
Dispersion coefficient, $D_L \times 10^4$ (m <sup>2</sup> .s <sup>-1</sup> )		3.10
Macro/mesopore diffusivity, $D_{k-m} \times 10^5$ (m <sup>2</sup> .s <sup>-1</sup> )	CO <sub>2</sub>	1.88
	CH <sub>4</sub>	1.92
	He	2.08
Micropore diffusivity, $D_s$ (m <sup>2</sup> .s <sup>-1</sup> )	CO <sub>2</sub>	0.0174
	CH <sub>4</sub>	0.0059

b) Case 2: PSA cycle for CO<sub>2</sub>/CH<sub>4</sub> separation in the context of biogas upgrading

Table 5-9 summarizes operational/isotherms/mass and heat transfer parameters used for the simulation of 2<sup>nd</sup> case. The parameters of isotherm model are taken from the results presented in chapter 3 for HKUST-1/PLA adsorbent whereas the mass and heat transfer parameters previously used in the simulation of case 1, as we have not measured them for HKUST-1/polymer composites synthesized in the frame of this work.

Next, the pressure of the feed gas was set to be similar to the pressure of adsorption, which is 4 bar, though it should be noted that pressure of biogas obtained by anaerobic digestion could vary from atmospheric pressure up to more than 10 bar [299, 300], depending on the process parameters applied. For the PSA simulation performed in this section, it was assumed that the CO<sub>2</sub>/CH<sub>4</sub> mixture used as feed gas was initially at 1 bar before being compressed to feed pressure.

Finally, it should be noted that the duration of either Skarstrom cycle or its modified with PE steps version is not detailed here, being variable parameter which is constantly adjusted to obtain the best PSA performances.

Table 5-9: Operational/Isotherms/Mass and heat transfer applied for the PSA simulation of CO<sub>2</sub>/CH<sub>4</sub> separation using HKUST-1/PLA.

CO <sub>2</sub> /CH <sub>4</sub> /He feed molar fraction	CO <sub>2</sub>	0.5
	CH <sub>4</sub>	0.5
Feed mass flow rate (kg. s <sup>-1</sup> )		0.074

Feed gas temperature (K)		298
Feed pressure (bar)		4
Isotherm model		Dual site Langmuir-IAST
Adsorbent saturation capacity for site 1, $q_{s1,i}$ (mol/kg)	CO <sub>2</sub>	14.61
	CH <sub>4</sub>	16.07
Adsorbent saturation capacity for site 2, $q_{s2,i}$ (mol/kg)	CO <sub>2</sub>	2.09
	CH <sub>4</sub>	2.09
Pre-exponential constant for site 1 $b_{1a,i}$ (bar <sup>-1</sup> )	CO <sub>2</sub>	48.14
	CH <sub>4</sub>	0.67
Pre-exponential constant for site 2 $b_{2a,i}$ (bar <sup>-1</sup> )	CO <sub>2</sub>	60.29
	CH <sub>4</sub>	60.28
Exponential constant $b_{1b,i}$ (K <sup>-1</sup> )	CO <sub>2</sub>	2685.58
	CH <sub>4</sub>	1418.62
Exponential constant $b_{2b,i}$ (K <sup>-1</sup> )	CO <sub>2</sub>	14404.1
	CH <sub>4</sub>	36328.4
$\Delta H_{i,ads}$ (kJ.mol <sup>-1</sup> )	CO <sub>2</sub>	22.3
	CH <sub>4</sub>	11.8
Heat transfer coefficient between bulk gas and wall, $h_{f-w}$ (W.m <sup>-1</sup> .K <sup>-1</sup> )		25
Macro/mesopore diffusivity, $D_{i,k-m} \times 10^5$ (m <sup>2</sup> .s <sup>-1</sup> )	CO <sub>2</sub>	1.88
	CH <sub>4</sub>	1.92
Micropore diffusivity, $D_{i,s}$ (m <sup>2</sup> .s <sup>-1</sup> )	CO <sub>2</sub>	0.0174
	CH <sub>4</sub>	0.0059

### 5.3.5. Simulation performance criteria

#### a) Case 1: Model validation

To verify that the process simulation software gPROMS is a reliable tool to solve differential equations describing mass and heat transfer processes in the adsorption column, we directly compared simulation results and experimental CO<sub>2</sub>/CH<sub>4</sub> breakthrough data reported by Asadi et al. [17]. As a first step, we focused on CO<sub>2</sub> breakthrough time, denoted as  $t_{b, CO_2}$ , which is the time when CO<sub>2</sub> gas is detected at the outlet of the column due to the consumption of the adsorption media CO<sub>2</sub> working capacity. Next, the bed saturation time, denoted as  $t_{sat, CO_2}$ , which is the time when the concentration of CO<sub>2</sub> gas constituent at the outlet of the column becomes equal to that of the column inlet. Additionally, the maximum/minimum temperature values of the bed throughout the breakthrough analysis are also compared with experimental values to determine the accuracy of the simulation. These temperatures are measured at different positions of the bed, which are 0.01 m, 0.12 m and 0.23 m from the bed inlet section for the total bed height of 0.305 m, and they are denoted as  $T_{bot}$ ,  $T_{mid}$  and  $T_{top}$  respectively. The overall goodness of fit of temperature and



outlet CO<sub>2</sub> concentration profiles with experimental results is also taken into consideration when determining gPROMS reliability.

b) Case 2: PSA cycle for CO<sub>2</sub>/CH<sub>4</sub> separation in the context of biogas upgrading

Two main PSA process performance indicators were defined: CH<sub>4</sub> purity, which corresponds to the averaged methane content in the outlet product (Eq. 5-35), and CH<sub>4</sub> recovery, which is the ratio between the quantity of CH<sub>4</sub> produced during the production phase and the quantity of CH<sub>4</sub> (Eq. 5-36) used as feed during the adsorption and pressurization steps. The simulation was carried out with the objective of achieving biomethane purity > 97%, which is the recommended purity for the injection of biomethane into French gas pipeline grid [301].

$$CH_4 \text{ purity (\%)} = \frac{CH_4 \text{ product quantity}}{CH_4 \text{ product quantity} + CO_2 \text{ product quantity}} \quad \text{Eq. 5-35}$$

$$CH_4 \text{ recovery (\%)} = \frac{CH_4 \text{ product quantity}}{CH_4 \text{ feed quantity}} \quad \text{Eq. 5-36}$$

CH<sub>4</sub> productivity (Eq. 5-37), which is the amount of CH<sub>4</sub> produced per unit of volume of adsorbent for the total duration of cycle time, is another PSA performance indicator, determining the scale of a PSA unit.

$$CH_4 \text{ productivity } \left( \frac{kg}{h \cdot m^3} \right) = \frac{CH_4 \text{ produced by a PSA unit}}{\text{Adsorbent volume} * \text{total cycle time}} \quad \text{Eq. 5-37}$$

The specific energy consumption, being mainly due to: (1) compression of feed gas, (2) vacuum regeneration of adsorbent and (3) recycling of gas streams, allows evaluating the economic performance of a PSA units. For the simulation carried out in this work, the feed gas mixture, which represents cleaned biogas, is assumed to be produced from anaerobic digestion and to be initially at 1 bar [300] before being compressed to feed pressure. The specific energy consumption is expressed as follows [289]:

$$\text{Specific energy } \left( \frac{kWh}{Nm^3 \text{ methane}} \right) = \frac{\text{total cycle time} * \left( \frac{Y}{Y-1} \right) RT \frac{\dot{n}}{\delta} \left[ \left( \frac{P^{out}}{P^{in}} \right)^{\frac{Y-1}{Y}} - 1 \right]}{\text{total CH}_4 \text{ produced}} \quad \text{Eq. 5-38}$$

where  $Y = c_p/c_v$  is the ratio of specific heat (assumed to be equal to 1.4);  $\delta$  the mechanical efficiency of the compressor (assumed to be 80%);  $\dot{n}$  the molar flow rate (mol. s<sup>-1</sup>);  $P^{out}$  and  $P^{in}$  the pressure of gas exiting and entering the compressor, respectively.

## 5.4. Simulation results

### 5.4.1. Case 1: Model validation

The experimental results reported by Asadi et al. [17] were compared with the results of the simulation to verify the reliability gPROMS solver used in this work. Figure 5-18 shows the CO<sub>2</sub> breakthrough and temperature profile of the simulation and their comparison with literature values. A simplified scheme of the column showing the localization of thermocouples is also presented in the figure. Additionally, Table 5-10 summarizes the simulated results for CO<sub>2</sub> breakthrough and saturation time, as well as temperatures at different axial position of adsorbent bed for a gas mixture of 83% CO<sub>2</sub>, 4% CH<sub>4</sub> and 13% He.

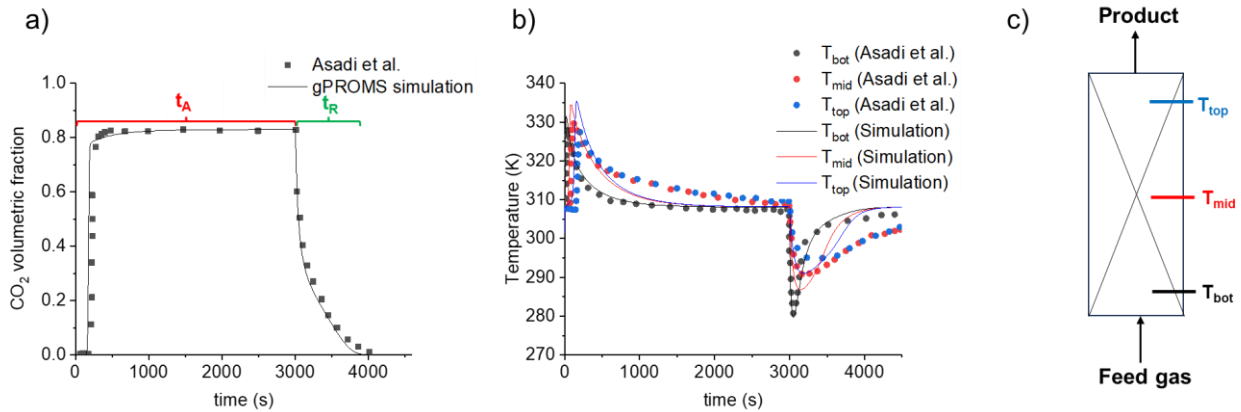


Figure 5-18: (a) CO<sub>2</sub> breakthrough profile (b) Temperature profile along adsorbent bed. (c) Simplified scheme of the column showing the position of each thermocouple.  $t_A$  and  $t_R$  signifies adsorption time and regeneration time.

Table 5-10: Comparison between simulation results and experimental values of CO<sub>2</sub>/CH<sub>4</sub> breakthrough analysis reported by Asadi et al. [17]

	$t_{b, CO_2}$ (s)	$t_{sat, CO_2}$ (s)	$T_{bot}$ (K)		$T_{mid}$ (K)		$T_{top}$ (K)	
			Max	Min	Max	Min	Max	Min
Experimental (Asadi et al.)	200	675	327.9	280.7	329.6	290.8	327.4	295
Simulation 1.1 (S1.1)	180	640	331.7	279.6	334.5	286.9	335.4	291
Relative error (%)	10	5.1	1	0.3	1.5	1.3	2.4	1.4

Simulation 1.1 reveals that the breakthrough of CO<sub>2</sub> occurs at  $t_{b, CO_2} = 180$  s and the adsorbent bed becomes saturated at  $t_{sat, CO_2} = 640$  s. These results agree within 5-10% of relative error when compared to the experimental values by Asadi et al., which is still tolerable. Additionally, temperature profiles at different height of the adsorbent bed during adsorption and desorption process were successfully simulated. Adsorption is an exothermic process,

resulting in heat release and causing the adsorbent bed temperature increase, whereas desorption is endothermic thus leading to temperature drop. The maximum and minimum values of  $T_{\text{bot}}$ ,  $T_{\text{mid}}$  and  $T_{\text{top}}$  obtained from the simulation are comparable to the experimental results, with a difference between 0.3-2.4% in relative error. This relatively small error suggests that the choice of mass transfer and isotherm parameters is appropriate for the simulation.

Apart from that, qualitative comparison between simulation results and experimental data from literature could also be made through the goodness of fit between the CO<sub>2</sub> breakthrough profile and the temperature profile, which were obtained from the simulation, with that of the experiments. As could be observed from Figure 5-18-a, the simulated breakthrough profile fits well with experimental results throughout both the adsorption and regeneration steps.

Meanwhile, Figure 5-18-b shows the simulated and experimental temperature profiles at different positions in the column. The experimental results show that the measured temperatures by all thermocouples attained a maximum level, followed by a gradual decrease of until it becomes similar to the temperature of feed gas at the end of adsorption time,  $t_A$ . This decrease results from the cooling of the adsorbent bed by the feed gas flow, thus, it is logic that the cooling at the middle and top sections is slower than the bottom section that is close to the entrance of feed gas. Similarly, the measured temperatures attained a minimum value, followed by a gradual increase until the end of regeneration time,  $t_R$ . This increase in temperature results from the heating of the adsorbent bed by feed gas flow, thus it stands to reason that the heating of the bottom section of the column is much more rapid than the middle and the top sections. Meanwhile, the simulated temperature profiles could be observed to differ slightly from the reported experimental temperature profiles by Asadi et al. [17]. To be more precise, the simulated temperature profiles for middle and top sections of the column are unable to describe well the gradual decrease and increase of temperature observed during  $t_A$  and  $t_R$ , respectively.

It is probable that the adjustment of heat transfer parameters chosen for the simulation would improve the goodness of fitting of the overall temperature profile. To verify this, a sensitivity analysis was performed to investigate the impact of  $h_{f\text{-ads}}$ ,  $h_{f\text{-w}}$  and  $h_{w\text{-ext}}$  on the temperature profiles of the adsorbent bed.

a) Effect of heat transfer coefficient between bulk gas and adsorbent,  $h_{f\text{-ads}}$

As the adsorbent bed heats up/cool down from the heat released/consumed from the adsorption/desorption of the gas constituents, the feed gas stream constantly enters the adsorbent media and passes through it. This gas stream enters the adsorption column at a constant temperature, which can be different from that of the adsorbent bed. This temperature gradient would result in heat transfer between the bulk gas phase and the solid, with the rate dependent on the heat transfer coefficient  $h_{f\text{-ads}}$ . To improve the goodness of fit between the simulated temperature profile and experimental results, new simulations were performed by modifying only the value of  $h_{f\text{-ads}}$  (20 W.m<sup>-1</sup>.K<sup>-1</sup> and 100 W.m<sup>-1</sup>.K<sup>-1</sup>) while keeping other parameters unchanged from Simulation 1.1 (S1.1). Figure 5-19 displays the CO<sub>2</sub> breakthrough profile and temperature profile of the new simulations, whereas Table 5-11 summarizes the impact of  $h_{f\text{-ads}}$  on the simulation results.

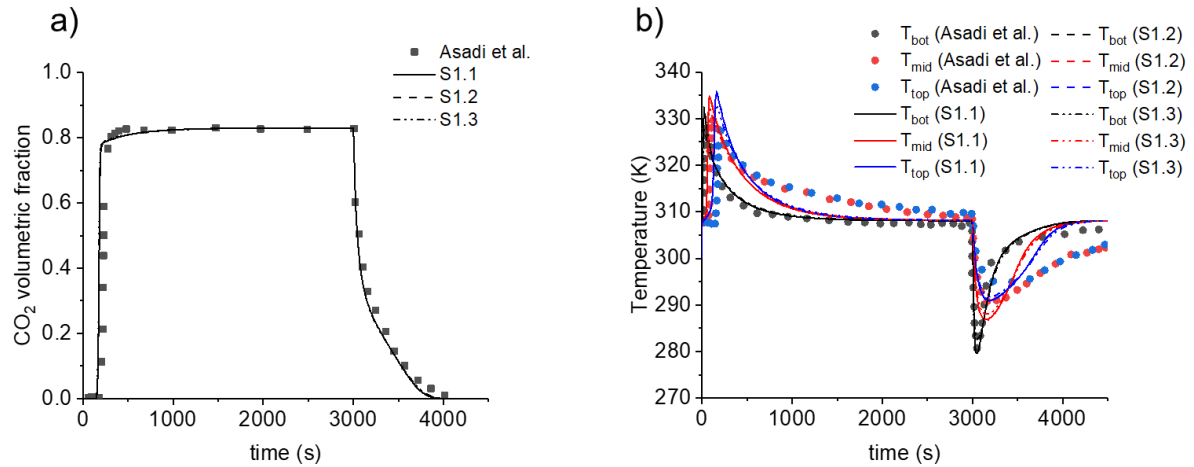


Figure 5-19: (a) Fitting of CO<sub>2</sub> breakthrough profile for different  $h_{f-ads}$  values. (b) Fitting of temperature profile throughout adsorbent bed for different  $h_{f-ads}$  values.

Table 5-11: Impact of  $h_{f-ads}$  on the simulated results

	Variable parameter	Results							
		$t_{b, CO_2}$ (s)	$t_{sat, CO_2}$ (s)	$T_{bot}$ (K)		$T_{mid}$ (K)		$T_{top}$ (K)	
	$h_{f-ads}$ (W.m <sup>-1</sup> .K <sup>-1</sup> )			Max	Min	Max	Min	Max	Min
Experimental (Asadi et al.)	65.3	200	675	327.9	280.7	329.6	290.8	327.4	295.0
Simulation 1.1 (S1.1)		180	640	331.7	279.6	334.5	286.9	335.4	291.0
Simulation 1.2 (S1.2)	100	170	630	332.0	279.1	335.0	286.7	335.9	290.9
Simulation 1.3 (S1.3)	20	170	650	327.7	282.4	332.0	287.9	333.0	291.8

Based on the obtained results, the heat transfer coefficient  $h_{f-ads}$  did not have a significant influence on the performance criteria of the breakthrough process. Additionally, the CO<sub>2</sub> breakthrough and temperature profile of the new simulations (S1.2 and S1.3), which has a different value of  $h_{f-ads}$ , is similar to that of the initial simulation S1.1. These findings allow to conclude that  $h_{f-ads}$  coefficient did not play a significant impact on improving the goodness of fit for the temperature profile.

b) Effect of heat transfer coefficient between bulk gas and wall,  $h_{f-w}$

As the temperature of the feed gas stream traversing the adsorbent bed fluctuates due to the heat released/consumed during adsorption/desorption phenomena, a temperature gradient between the gas phase and the adsorption column wall will inevitably be established, leading to heat transfer between them, with the rate controlled by the heat transfer coefficient  $h_{f-w}$ . Thus, new simulations were carried out by modifying the value of  $h_{f-w}$  (15 W. m<sup>-1</sup>. K<sup>-1</sup> and 35 W. m<sup>-1</sup>. K<sup>-1</sup>) while keeping other parameters constant as in S1.1. Figure 5-20 displays the CO<sub>2</sub> breakthrough

and temperature profiles for the new simulation, whereas Table 5-12 summarizes the impact of  $h_{f-w}$  on the simulation results.

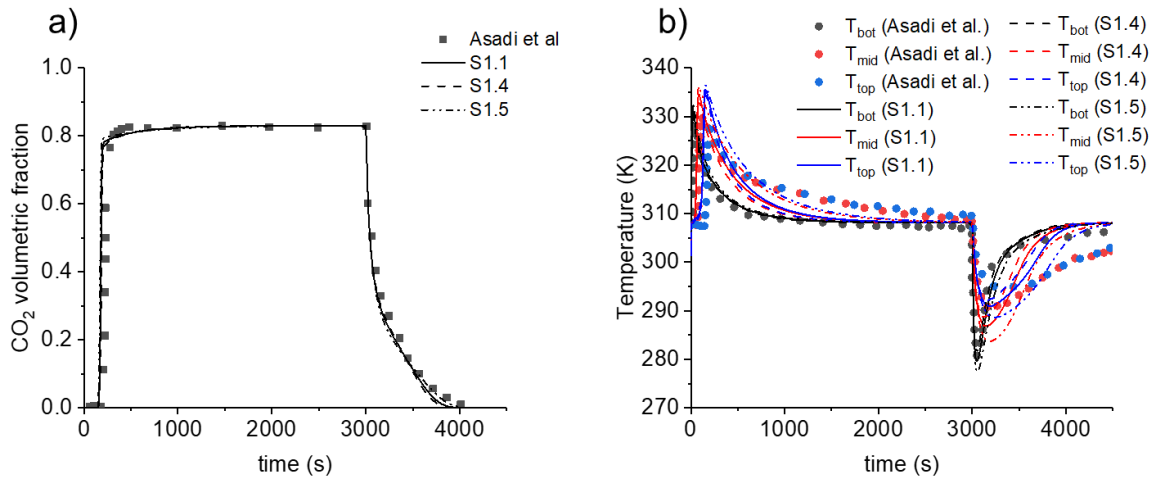


Figure 5-20: (a) Fitting of CO<sub>2</sub> breakthrough profile for different  $h_{f-w}$  values. (b) Fitting of temperature profile throughout adsorbent bed for different  $h_{f-w}$  values.

Table 5-12: Impact of  $h_{f-w}$  on the simulated results

	Variable parameter	Results							
		$t_{b, CO_2}$	$t_{sat, CO_2}$	$T_{bot}$ (K)		$T_{mid}$ (K)		$T_{top}$ (K)	
		(s)	(s)	Max	Min	Max	Min	Max	Min
Experimental (Asadi et al.)	25	200	675	327.9	280.7	329.6	290.8	327.4	295.0
Simulation 1.1 (S1.1)		180	640	331.7	279.6	334.5	286.9	335.4	291.0
Simulation 1.4 (S1.4)	35	180	630	330.7	281.3	333.2	288.6	334.6	292.2
Simulation 1.5 (S1.5)	15	170	650	332.7	277.4	336.1	283.7	336.4	288.6

Simulations S1.4 and S1.5 were carried out by increasing and decreasing the value of  $h_{f-w}$ , respectively. It can be observed that this parameter has a minor impact on the breakthrough time performance criteria ( $t_{b, CO_2}$  and  $t_{sat, CO_2}$ ) as well as the CO<sub>2</sub> breakthrough profile. However, the same cannot be said about the maximum/minimum temperature throughout the bed and the temperature profile. An increase in the value of  $h_{f-w}$  (S1.4) results in an increase in the accuracy for the simulated maximum/minimum temperatures throughout the bed, though the goodness of fit between the simulation and experimental results has notably worsened. Similarly, by decreasing the value of parameter  $h_{f-w}$  (S1.5), the goodness of fit of simulated temperature profile with that of the experiment improved, though it comes at the expense of decreasing accuracy between the simulated maximum/minimum temperatures throughout the bed and that of the experimental results.

c) Effect of heat transfer coefficient between wall and external environment,  $h_{w-ext}$

As the adsorption column used by Asadi et al. for the breakthrough analysis is not insulated [17], a heat transfer between the wall and exterior would occur when there is a temperature gradient between these two media. This heat transfer could contribute to the rate of temperature fluctuation throughout the adsorbent bed. The rate of heat transfer between the wall and the environment depends on the heat transfer coefficient  $h_{f-ext}$ . By analogy with two previous sensitivity analysis case studies, the simulation was done by modifying only the value of  $h_{f-ext}$  ( $5 \text{ W} \cdot \text{m}^{-1} \cdot \text{K}^{-1}$  and  $10 \text{ W} \cdot \text{m}^{-1} \cdot \text{K}^{-1}$ ) while keeping other parameters as in simulation 1 (S1.1), with the aim to determine the impact of this heat coefficient in improving the goodness of fit on the simulated temperature profile with experimental results. Figure 5-21 displays the  $\text{CO}_2$  breakthrough and temperature profile for the new simulation, whereas Table 5-13 summarizes the impact of  $h_{f-w}$  on the simulation results.

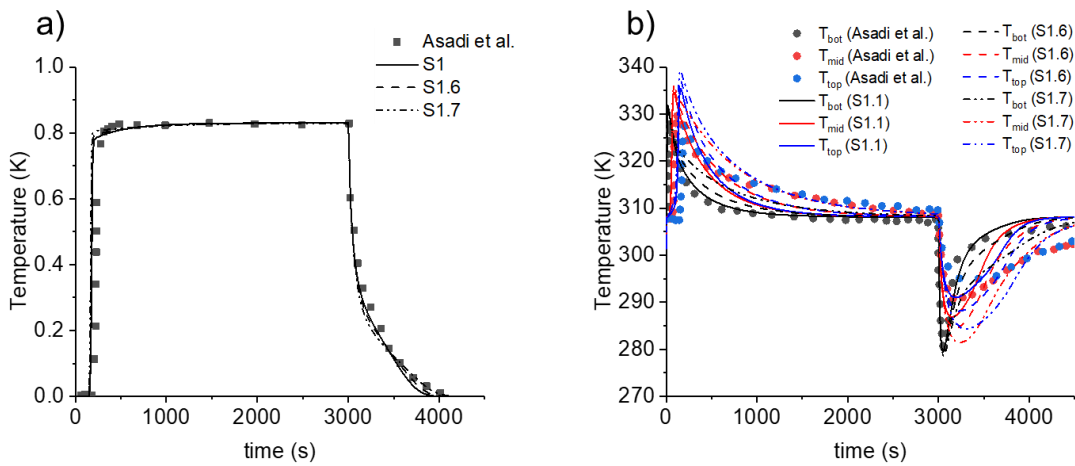


Figure 5-21: (a) Fitting of  $\text{CO}_2$  breakthrough profile for different  $h_{w-ext}$  values. (b) Fitting of temperature profile throughout adsorbent bed for different  $h_{w-ext}$  values.

Table 5-13: Impact of  $h_{w-ext}$  on the simulated results

	Variable parameter	Results							
		$t_{b, \text{CO}_2}$ (s)	$t_{\text{sat}, \text{CO}_2}$ (s)	$T_{\text{bot}}$ (K)		$T_{\text{mid}}$ (K)		$T_{\text{top}}$ (K)	
				Max	Min	Max	Min	Max	Min
Experimental (Asadi et al.)	20	200	675	327.9	280.7	329.6	290.8	327.4	295.0
Simulation 1.1 (S1.1)		180	640	331.7	279.6	334.5	286.9	335.4	291.0
Simulation 1.6 (S1.6)		160	650	331.7	279	335.2	284.4	337.2	288.0

Simulation 1.7 (S1.7)	5	160	580	331.8	278.7	335.9	281.4	339.2	284.3
--------------------------	---	-----	-----	-------	-------	-------	-------	-------	-------

Based on the simulated result, it could be observed that by decreasing the value of  $h_{w-ext}$ , the absolute error between simulated performance criteria and that of the experiments increases. The relative error for  $t_{b, CO_2}$  and  $t_{sat, CO_2}$  could reach up to 15-20%, whereas the error related to the maximum/minimum temperature throughout the bed could reach up to 2.7-3.6%. On another note, the goodness of fit between the simulation and experimental results for breakthrough and temperature profile improves as  $h_{w-ext}$  decreases. Therefore, it could be concluded that the heat transfer coefficient  $h_{w-ext}$  has an impact on the overall goodness of fit between simulation and experimental breakthrough and temperature profile, but it comes at the expense of the accuracy of the simulated results.

d) New breakthrough simulation with modified heat transfer coefficient parameters for  $h_{f-w}$  and  $h_{w-ext}$ .

As the sensitivity analysis conducted on heat transfer coefficient parameters shows that the modification of  $h_{f-w}$  and  $h_{w-ext}$  parameters could improve the goodness of fit between the simulated and the experimental temperature profiles, a new simulation (S1.5 and S1.6) using the adjusted parameter's value was carried out. Table 5-14 summarizes the results of the new simulation and Figure 5-22 displays the new  $CO_2$  breakthrough and temperature profiles.

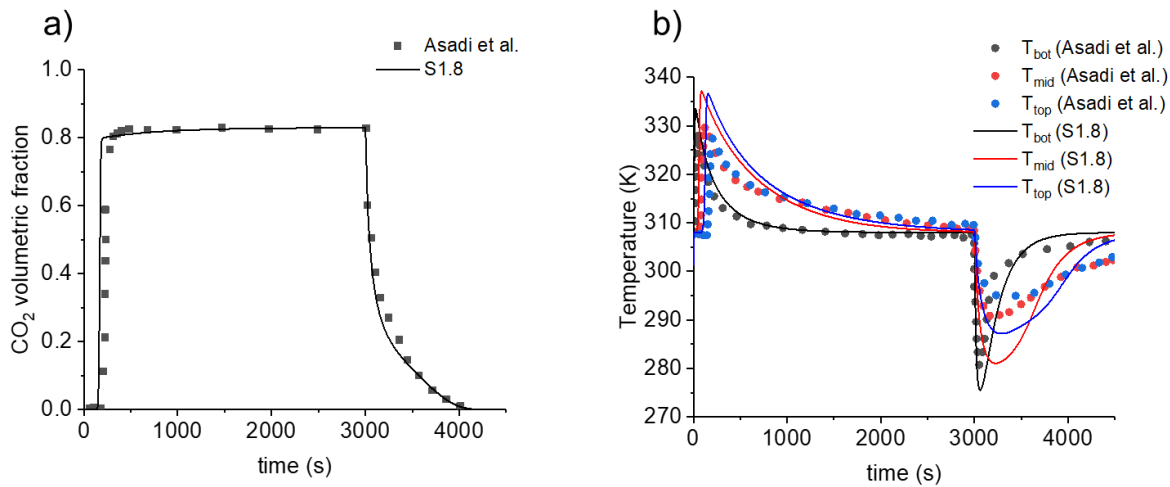


Figure 5-22: (a) Fitting of  $CO_2$  breakthrough profile for simulation with modified heat transfer parameters. (b) Fitting of temperature profile throughout adsorbent bed for simulation with modified heat transfer parameters.

Table 5-14: Comparison between simulation with modified heat transfer parameters, and experimental values of  $CO_2/CH_4$  breakthrough analysis as reported by Asadi et al. [17]

Variable parameter		Results							
$h_{f-w}$ ( $W.m^{-2}.K^{-1}$ )	$h_{w-ext}$ ( $W.m^{-2}.K^{-1}$ )	$t_{b, CO_2}$ (s)	$t_{sat, CO_2}$ (s)	$T_{bot}$ (K)		$T_{mid}$ (K)		$T_{top}$ (K)	
				Max	Min	Max	Min	Max	Min

Experimental (Asadi et al.)	25	20	200	675	327.9	280.7	329.6	290.8	327.4	295
Simulation 1.8 (S1.8)	15	10	160	650	333.5	275.5	337.1	281.1	336.7	287.2
Relative error (%)	-	-	20	3.7	1.7	1.9	2.3	3.3	2.8	2.6

As expected, the overall goodness of fit of the simulated temperature profile improves when compared to earlier simulation S1.1. However, the new simulation S1.8 failed to predict accurately the performance criteria of the breakthrough process, with an absolute error up to 20% could be observed for  $t_{b, CO_2}$ . As we are unable to improve the simulation results without having this trade-off, we decided to prioritize the simulation that yielded the lowest relative error in terms of performance criteria with a somewhat reasonably good fitting of the simulation. The result of the simulation 1.1 (S1.1) carried in this work was able to reasonably reproduce the experimental results of the breakthrough analysis reported by Asadi et al. [17], which validates the model embedded in gPROMS solver. It is however undeniable that the adjustment of several thermophysical properties, which being hard to measure experimentally, would further improve the accuracy of the simulation.

#### 5.4.2. Case 2: PSA cycle for CO<sub>2</sub>/CH<sub>4</sub> separation in the context of biogas upgrading

As previously mentioned, PSA simulation for the separation of equimolar mixture of CO<sub>2</sub>/CH<sub>4</sub> (assuming other contaminants has been removed during biogas cleaning process), was carried out using HKUST-1/PLA as the adsorbent media. This study serves as the preliminary assessment of the efficiency of the shaped HKUST-1 composite in its application as an adsorbent in biogas upgrading. The simulation was made with the constraint condition to obtain an averaged biomethane with purity > 97% under steady state regime (CSS). Prior to the simulation of the whole PSA process, a simple breakthrough profile was generated to ensure that the chosen cycle time for the simulation of the e2<sup>nd</sup> case, specifically,  $t_A$  and  $t_{PS}$ , did not surpass the CO<sub>2</sub> breakthrough time,  $t_{b, CO_2}$ , of the adsorbent bed. The breakthrough simulation was conducted on a single column with the same column design parameters as well as isothermal/mass and heat transfer parameters listed in Table 5-5 and Table 5-9 previously. Furthermore, the single column was assumed to be initially filled with CH<sub>4</sub> at pressure of 4 bar and temperature of 298 K.

Figure 5-23-a illustrates the simplified scheme of a single adsorption column as well as the relevant operational parameters used to simulate the breakthrough profile of HKUST-1/PLA adsorbent bed (Figure 5-23-b). The CO<sub>2</sub> breakthrough of the adsorbent bed would occur at 1010 s and its saturation would take place after around 1200 s. It should be reminded here that this result was based on the assumption that the adsorbent bed was CO<sub>2</sub>-free prior to the start of the adsorption phase, thus breakthrough would occur much earlier if the adsorbent bed is not completely regenerated. Nevertheless, based on the simulation results, the total time of the regenerated adsorbent bed that could come into contact with the feed gas stream (sum of  $t_A$  and  $t_{PS}$ ) should not exceed  $t_{b, CO_2}$ , to avoid the biomethane obtained as the product being contaminated with high concentration of CO<sub>2</sub>, thus reducing its purity.



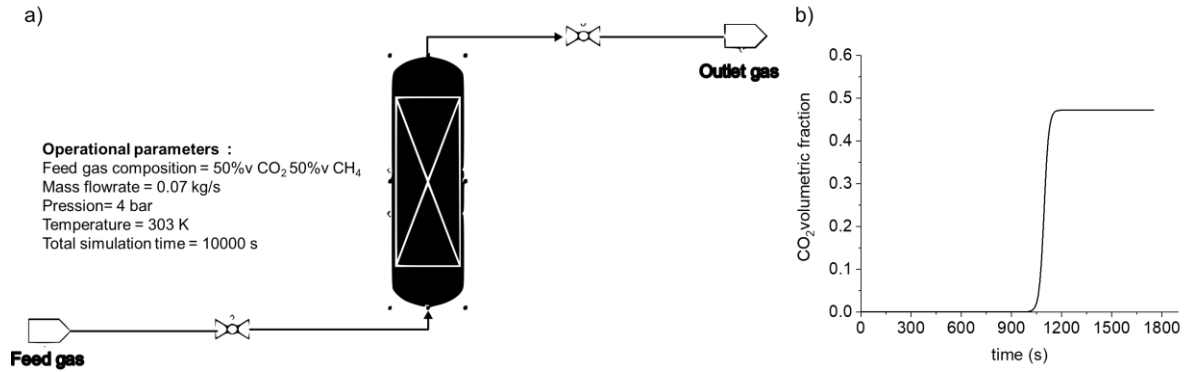


Figure 5-23: CO<sub>2</sub> breakthrough profile using HKUST-1/PLA as adsorbent media.

a) Skarstrom cycle configuration

The PSA simulation for equimolar CO<sub>2</sub>/CH<sub>4</sub> separation was carried out following the Skarstrom cycle configuration. This first simulation was denoted as Simulation 2.1-S (S2.1-S) and Table 5-15 summarizes its simulation variable parameters (cycle step duration) as well as the obtained performance indicators, whereas Figure 5-24 displays the pressure and temperature profile in the column prior before CSS has been achieved.

Table 5-15: Process performance for PSA simulation with Skarstrom configuration

	Simulation variable parameters					Performance indicators	
	t <sub>A</sub> (s)	t <sub>BD</sub> (s)	t <sub>P</sub> (s)	t <sub>PS</sub> (s)	Total cycle time (s)	CH <sub>4</sub> purity (%)	CH <sub>4</sub> recovery (%)
Simulation 2.1-S (S2.1-S)	300	100	300	100	800	98.9	2.5

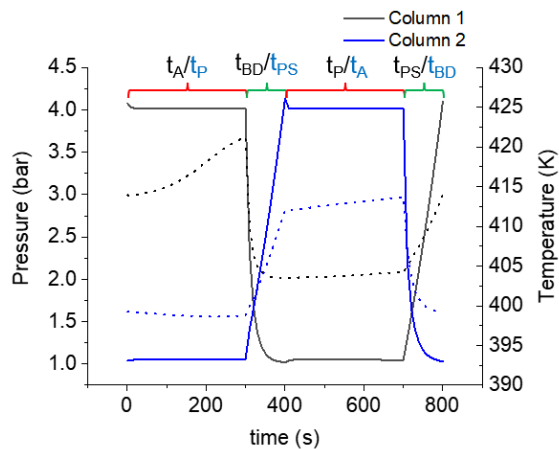


Figure 5-24: Pressure profile (straight lines) and temperature profile (dotted lines), measured in the middle of adsorption column, for simulation 2.1-S.

Simulation 2.1-S was successfully carried out until the CSS condition was achieved. The biomethane obtained as the product during adsorption step has a CH<sub>4</sub> purity up to 98,9%, which exceeds the minimum required purity of 97% set as our objective, though at the same time, it can be observed that resulting recovery of CH<sub>4</sub> is extremely low. Additionally, the pressure and temperature profiles inside the 2 PSA columns provide an interesting information about the overall simulated process. The pressure is able to reach 4 bar during adsorption step and reduce to 1 bar during purge. It can be observed that during one complete simulation cycle, the temperature in the bed fluctuates by  $\pm 15$ K. At CSS condition, the simulated temperature range of the bed is in the range of 400-423 K, which is around 100 K higher than the temperature of feed gas. This result is a bit peculiar and prompted us to further investigate the evolution of temperature and pressure from the start of the cycle until CSS (Figure 5-25).

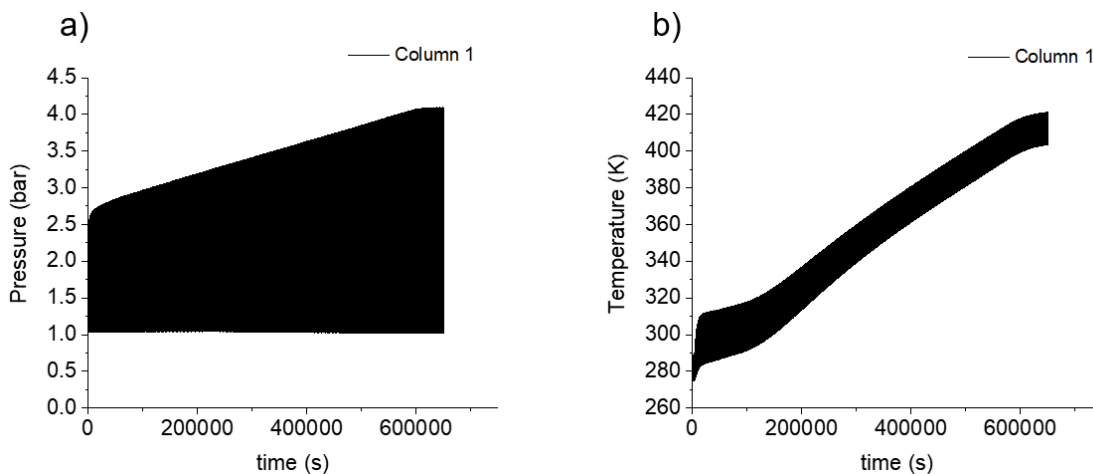


Figure 5-25: (a) Evolution of pressure at the middle of adsorption column 1 from initial simulation cycle (S2.1-S) until CSS. (b) Evolution of temperature at the middle of adsorption column 1 from initial simulation cycle (S2.1-S) until CSS.

Simulation 2.1-S managed to reach the CSS only after 813 cycles, which takes about 645,000 s in total process time. As the adsorption column is considered insulated and there is no heat exchange with the environment, the leftover

excess heat generated from adsorption is accumulating in the column and gradually heats up the adsorbent bed until CCS has been attained. Additionally, it can be observed that the pressure inside the adsorption column at the end of the 1<sup>st</sup> cycle of the simulation (pressurization step) was 2.5 bar, which is lower than the expected adsorption pressure of 4 bar. This makes the valve connecting the column to the product reservoir at the top of the column to remain closed during adsorption step, hence no biomethane was obtained as the product before CSS establishment. After multiple cycles of the simulation ( $\approx 714$  cycle), the pressure inside the column after pressurization step finally approached the expected adsorption pressure of 4 bar thus allowing bio-CH<sub>4</sub> production at the outlet of the process. This information reveals that the chosen pressurization time of 100 s for S2.1-S is not sufficient to ensure the pressure inside the column to reach the expected adsorption pressure at the end of the pressurization phase.

Based on this information, it is clear that the pressurization step in the cycle configuration requires improvement. Thus, new simulation S2.2-S was carried out by increasing the value for  $t_{PS}$  (consequently  $t_{BD}$ ). Figure 5-26 displays the evolution of pressure and temperature in the middle of the column for Simulation 2.2-S and Table 5-16 compares the performance indicators for new PSA simulations 2.2-S (S2.2-S) at CSS, with increased value for  $t_{PS}$  and  $t_{BD}$ .

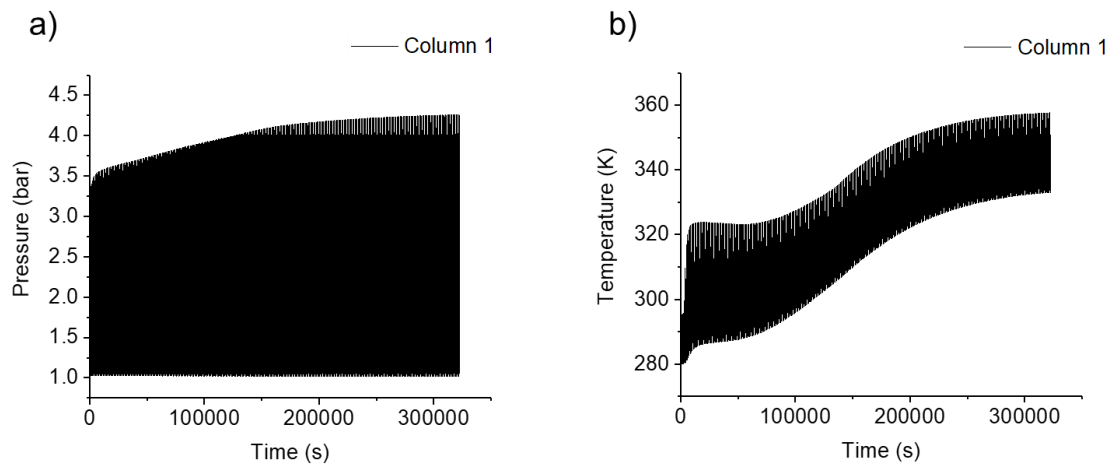


Figure 5-26: (a) Evolution of pressure at the middle of adsorption column 1 from initial simulation cycle (S2.2-S) until CSS. (b) Evolution of temperature at the middle of adsorption column 1 from initial simulation cycle (S2.2-S) until CSS.

Table 5-16: Impact of  $t_{PS}$  to the performance criteria of PSA simulation

	Simulation variable parameters					Performance indicators	
	$t_A$ (s)	$t_{BD}$ (s)	$t_P$ (s)	$t_{PS}$ (s)	Total cycle time (s)	CH <sub>4</sub> purity (%)	CH <sub>4</sub> recovery (%)
Simulation 2.1-S (S2.1-S)	300	100	300	100	800	98.9	2.5
Simulation 2.2-S (S2.2-S)	300	170	300	170	940	99.8	6.2

Simulation 2.2-S corresponds to the same case as Simulation 2.1-S with extended pressurization time  $t_{PS}$  (170 s instead of 100 s) from that of. Once the CSS was obtained for S2.2-S, the  $CH_4$  recovery of the PSA process increases to 6.2%. The increase in  $t_{PS}$  helps to ensure that the pressure inside the column after the pressurization step is able to reach 4 bar at an earlier cycle number than that of Simulation 2.2-S (714 cycles vs. 132 cycles). Furthermore, the temperature inside the column under CCS is 320 K – 350 K, which is significantly lower than that observed in S2.1-S and can be at the origin of the improved purity within this cycle, as lower temperature increase the adsorption capacity of an adsorbent. Unfortunately, the  $CH_4$  recovery for this new simulation still remains very low, as  $CH_4$  in the off gas stream during blowdown and purging steps was sent directly to vent instead of being recycled. Therefore, a new configuration of cycle was simulated with the aim of minimizing the amount of  $CH_4$  being sent to the vent by introducing PE step between adsorption and blowdown steps, which is presented in the next sub-section.

b) Skarstrom + Pressure Equalization cycle

Pressure Equalization (PE) step works by connecting two columns at different pressure to distribute gas according to pressure difference. The addition of this step allows to shorten the pressurization time required to obtain working adsorption pressure inside the column and improve the energy-efficiency of the process. The adsorbent properties, column design parameters as well as operational/isotherms/mass and heat transfer parameters of the modified Skarstrom cycle configuration are similar to those used in S2.1-S (cf. Table 5-5, page 158, and Table 5-9, page 164), with different initial condition as compared to S2.1-S (cf. Table 5-7, page 163) due to the introduction of PE steps.

The new simulation, which is denoted as simulation 2.1-PE, was carried out with the same objective as S2.1-S, that is, to obtain biomethane with  $CH_4$  purity > 97% under steady state regime. Table 4 -17 summarizes the simulated performance indicators and Figure 5-27 displays the simulated pressure and temperature profiles at the CSS of this new PSA configuration.

Table 5-17: Process performance for PSA simulation with Skarstrom+PE configuration

	Simulation variable parameters							Performance indicators	
	$t_A$ (s)	$t_{BD}$ (s)	$t_P$ (s)	$t_{PS}$ (s)	$t_{PE1}$ (s)	$t_{PE2}$ (s)	Total cycle time (s)	$CH_4$ purity (%)	$CH_4$ recovery (%)
Simulation 2.1- PE (S2.1-PE)	971	371	200	400	971	971	3884	99.7	22.6

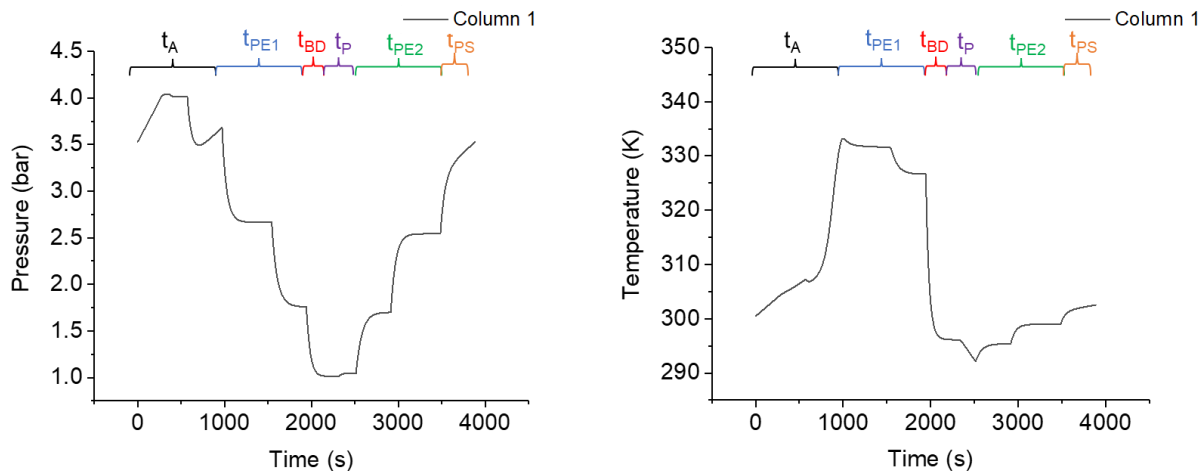


Figure 5-27: (a) Simulated pressure and temperature (in the middle of the bed) profiles for a complete PSA cycle under CSS regime.

The new simulation with modified Skarstrom cycle affords  $\text{CH}_4$  purity of 99.7% recovery of 22.6%. Additionally, the simulated pressure profile at the CSS shows that the pressure inside the column prior to the start of adsorption step reaches the 4 bar level relatively fast (4 complete simulation cycles). Additionally, the pressure inside the column experienced a fluctuation nearing the end of adsorption phase, as at this instant, the first column is connected with a second column that is in pressurization phase, which used the biomethane product from the 1<sup>st</sup> column as the pressurization gas for the 2<sup>nd</sup> column (PS). This is to minimize the amount of  $\text{CO}_2$  adsorbed during pressurization (PS) step. Meanwhile, the simulated temperature profile at the CSS condition demonstrates that at the start of the adsorption phase, the temperature inside the column is in the range of 300 K and it gradually increases up to 335 K nearing the end of this phase. This is significantly better than the result of simulation 2.1-S that predicted the temperature inside the PSA column at the beginning of the adsorption phase to be as high as 400 K under CSS condition.

It is also interesting to observe the evolution of pressure and temperature inside a PSA unit from the start of the simulation until the CSS condition was obtained, which is visualized in Figure 5-28. The impact of the PE step addition in the cycle configuration becomes evident as the pressure inside each adsorption column is able to reach the expected level since the 1<sup>st</sup> complete simulation cycle and continuously to be so until the establishment of CSS, which is a stark contrast to that observed earlier for S2.1-S and S2.2-S. The variation of pressure during a complete PSA cycle is accompanied by temperature fluctuation where it increases during pressure buildup steps (e.g. PE 2, PS, A) and goes down during the pressure decrease steps (e.g. PE 1, BD, P).

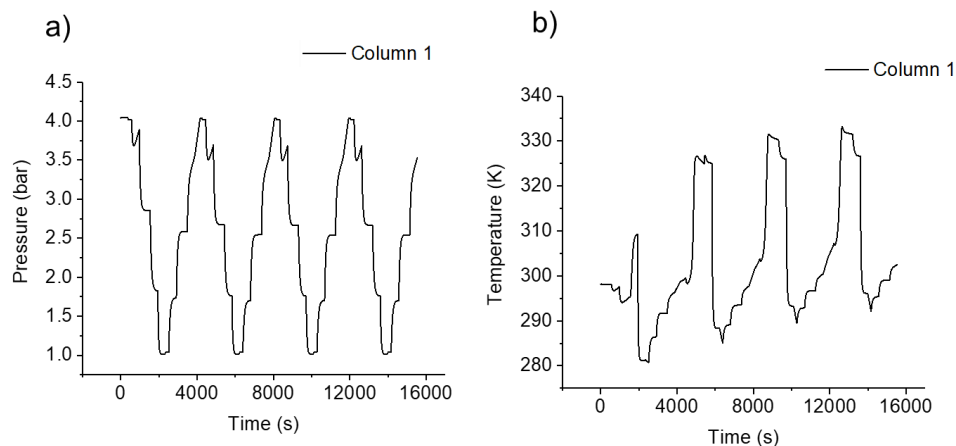


Figure 5-28: (a) Evolution of pressure and temperature (in the middle of adsorption column) from initial simulation cycle (S2.1-PE) until CSS. (b)

The consistency of pressure and temperature evolution inside the adsorption column during the whole simulation cycle, as well as the rapid obtention of CSS for the PSA simulation of the modified Skarstrom configuration, is a good indication that the PSA process is well simulated. To further assess the separation process performances of the CO<sub>2</sub>/CH<sub>4</sub> mixture using HKUST-1/PLA, the productivity and specific energy consumption of Simulation 2.1-PE were determined. The PSA unit of S2.1-PE has CH<sub>4</sub> productivity of 10 kg<sub>CH<sub>4</sub></sub>.m<sup>-3</sup>.h<sup>-1</sup> and a specific energy consumption of 0.15 kWh. Nm<sup>-3</sup><sub>CH<sub>4</sub></sub>. Table 5-18 compares the CH<sub>4</sub> productivity and specific energy consumption for the PSA simulation of the modified Skarstrom cycle in this section with the other examples of PSA/VPSA simulation presented previously in section 4.1:

Table 5-18: Comparison of the operational parameters and CO<sub>2</sub>/CH<sub>4</sub> separation performance of this study with different PSA/VPSA process simulation studies for biogas upgrading.

PSA/VPSA configuration	Adsorbent	Operational parameters				Separation performances		Ref.
		P <sub>ads</sub> (bar)	P <sub>regen</sub> (bar)	Temperature (K)	Biogas flowrate (Nm <sup>3</sup> /h)	CH <sub>4</sub> productivity (kg <sub>CH<sub>4</sub></sub> .m <sup>-3</sup> .h <sup>-1</sup> )	Specific energy consumption (kWh.Nm <sup>3</sup> <sub>CH<sub>4</sub></sub> )	
PSA	HKUST-1/PLA	4	1	298	203	10	0.15	This work
VPSA	CMS	5.8	0.1	308	500	-	0.27	[285]
(V)PSA	CMS	70 <sup>a</sup> 5 <sup>b</sup>	2 <sup>a</sup> 0.5 <sup>b</sup>	313	80-100	56	-	[286]
VPSA	Zeolite 13X	4	0.08	303	2-12	-	0.23	[287]
VPSA	Zeolite 5A	6	0.2	298	100	-	0.23	[288]

VPSA	CMS	8	0.5	305	396-971	80-160	0.28-0.48	[289]
------	-----	---	-----	-----	---------	--------	-----------	-------

<sup>a</sup>First stage. <sup>b</sup>Second stage.

It could be observed that the specific energy consumption for simulation 2.1-PE is lower than that reported in other studies for CO<sub>2</sub>/CH<sub>4</sub> separation using VPSA configuration. This is not surprising as the PSA simulation in this work did not require the usage of vacuum pump for the regeneration of adsorbent bed, hence contributing to less energy requirement for CO<sub>2</sub>/CH<sub>4</sub> separation. On another note, the CH<sub>4</sub> productivity of simulation 2.1-PE is lower when compared with the CO<sub>2</sub>/CH<sub>4</sub> separation simulation of other studies; Grande and Blom [286], Chouikhi et al. [289]. This is logical considering that for simulation 2.1-PE, a grand portion of produced biomethane is redirected to other column as purge gas and pressurization gas, whereas in the study by Grande and Blom [286], the biomethane product was only used for purge step and the study by Chouikhi et al. [289] did not recirculate the produced biomethane. Overall, the simulation of CO<sub>2</sub>/CH<sub>4</sub> separation using the configuration of modified Skarstrom cycle (addition of PE step), shows a promising use of our composite material as the adsorbent media, with a CH<sub>4</sub> purity of biomethane exceeding 97% and a low specific energy consumption of the PSA process. However, the simulated PSA process also yielded a low CH<sub>4</sub> recovery with a relatively low production of CH<sub>4</sub> when compared with other studies concerning the simulation of CO<sub>2</sub>/CH<sub>4</sub> separation.

It should be noted that operational parameters for PSA simulation conducted thus far for CO<sub>2</sub>/CH<sub>4</sub> separation using HKUST-1/PLA are not yet fully optimized, as the initial aim for the simulation was to do a preliminary assessment of the shaped HKUST-1 suitability as adsorbent media for CO<sub>2</sub>/CH<sub>4</sub> separation. This means that there is a possibility of improving the CH<sub>4</sub> recovery and productivity of the simulated PSA process by optimizing parameters such as adsorption pressure and temperature, PSA cycle time, feed biogas flowrate and the product to purge gas flow ratio. Additionally, a more complex cycle configuration for PSA simulation could be investigated to improve the overall performance of CO<sub>2</sub>/CH<sub>4</sub> separation. Furthermore, the accuracy of simulation results could be further verified by executing an experimental analysis on the breakthrough and PSA separation using the shaped HKUST-1 as adsorbent. Finally, a much more comprehensive commercial analysis, ranging from the cost of production of the HKUST-1 composite to the operational cost of the PSA process, could be studied to further assess the viability of the material application in industrial scale.

## 5.5. Conclusion

In this chapter, a preliminary study was conducted to assess the suitability of HKUST-1 composite material, which in this section is represented by HKUST-1/PLA, to be used as an adsorbent media, by means of PSA simulation using a process simulation tool gPROMS. Some relevant parameters required to run the PSA simulation has already been determined from previous chapter such as the adsorbent physical properties and the considered isotherm model, whereas other parameters (mass and heat transfer kinetics) have not been measured in this work and were directly taken from literature.

Prior to the simulation of complete PSA cycle for CO<sub>2</sub>/CH<sub>4</sub> separation, the capability of gPROMS was assessed by executing the simulation of breakthrough analysis experiment reported in the work Asadi et al. [17], providing the most complete spectrum of parameters for the modeling of mass and heat transfer phenomena. The simulation of CO<sub>2</sub>/CH<sub>4</sub> breakthrough is comparable to the experimental results reported by Asadi et al., with a relative error between the simulation and experimental results less than 10% for the CO<sub>2</sub> breakthrough/saturation time of adsorbent bed and absolute error less than 2.4% for the maximum/minimum temperature along the adsorbent bed. In addition to that, the overall goodness of fit between simulated results with experimental breakthrough and temperature profile is satisfactory, which verified the reliability of the embedded models in gPROMS solver to predict the CO<sub>2</sub>/CH<sub>4</sub> separation using adsorption.

Next, the PSA simulation using HKUST-1/PLA as adsorbent media for the separation of equimolar CO<sub>2</sub>/CH<sub>4</sub> mixture was carried out by using conventional Skarstrom configuration. The results of the simulation show that biomethane with CH<sub>4</sub> purity of 98.9% could be obtained, but with an extremely low CH<sub>4</sub> recovery of 6.2%. Additionally, the CCS condition of the Skarstrom scheme could only be obtained after 343 complete cycles, which take around 322,000 s in total process time. To improve the PSA process and produce a more reliable results, the Skarstrom cycle was modified with an addition of pressure equalization step. The modified Skarstrom cycle results in the obtention of CSS after only 4 complete cycles and the temperature inside the adsorption column did not differ significantly from the temperature of feed gas. This new simulation predicts the biomethane purity of 99.7% and specific energy consumption of 0.15 kWh. Nm<sup>-3</sup> CH<sub>4</sub>. Additionally, the CH<sub>4</sub> recovery of the modified Skarstrom cycle is 22.6%, which, although could still be considered low in comparison to the best cases reported in literature, it is significantly better than that obtained for simple Skarstrom configuration simulated earlier in our work.

Several perspectives for the improvement of the PSA simulation in this work could be envisioned, such as optimizing the operating parameters, adding the off gas treatment step in the cycle configuration to obtain better CH<sub>4</sub> recovery and conducting experimental PSA separation to verify the accuracy of the simulation. Nevertheless, the simulated results show a promising possibility of the shaped HKUST-1 to be applied for the separation of CO<sub>2</sub>/CH<sub>4</sub> contains inside biogas using PSA.



# GENERAL CONCLUSION AND PERSPECTIVES

Biogas production has been increasing in recent years thanks to the implementation of multiple renewable energy policies motivated by economic and environmental benefits in order to reduce GHG emission. Biogas is produced from the anaerobic digestion of various organic wastes, such as sewage sludge, agricultural and crop residues, and animal dung, as well as industrial organic wastes and wastewater. Biogas consists of two main components: methane (50–80%), carbon dioxide (20–50%). Other gases that are present in biogas composition are water vapor, oxygen, hydrogen sulfide, ammonia, nitrogen, carbon monoxide, and traces of halogenated hydrocarbons, siloxanes, and toluene. Biogas can be burned directly on-site to produce heat and electricity. However, biogas energy density is low compared to natural gas (NG) since it contains a large fraction of carbon dioxide in addition to other secondary contaminants. Therefore, biogas needs to be purified to produce biomethane, having a composition matching the specifications for injections into gas grids.

Biogas upgrading can be achieved via numerous technologies, such as water/physical/chemical scrubbing, cryogenic separation, membrane separation and pressure swing adsorption (PSA)/vacuum pressure swing adsorption (VPSA). In the context of this study, we are interested in the removal of CO<sub>2</sub> from biogas via PSA, avoiding the use of a vacuum in the desorption step that would then be replaced with desorption in atmospheric pressure. Because vacuum desorption is mainly responsible for the high energy costs of VPSA processes, better energy performances by PSA separation are foreseen. The choice of adsorbent is one of the key factors in designing such a process.

Recently, metal–organic frameworks (MOFs) have been gaining attention for their potential application in gas separation owing to their inherent properties, such as high specific surface area, large porosity, and tunable pore size. However, the application of MOF in industrial scale is still limited as the production of this material is often under powder form, therefore it requires to undergo a shaping process to be used inside an adsorption column. The present study was devoted to the shaping of HKUST-1, which is the model MOF chosen in this study, and examine its CO<sub>2</sub> adsorption performances and separation ability from CH<sub>4</sub>. The aim was to fabricate an adsorbent with a good mechanical and moisture stability, as well as suitable CO<sub>2</sub>/CH<sub>4</sub> separation performance to be used in PSA process.

HKUST-1 powder was mixed with 10% by mass of PLA or TPU, followed by extrusion of the mixture to produce composites, designated as HKUST-1/PLA and HKUST-1/TPU, respectively. Characterization by X-ray diffraction (XRD), scanning electron microscopy (SEM), and thermogravimetric analysis (TGA) confirmed the preservation of the MOF's crystalline structure and the absence of thermal degradation of the composites. CO<sub>2</sub>/CH<sub>4</sub> adsorption isotherm measurements up to 10 bars at 298 K highlighted an increase in CO<sub>2</sub> and CH<sub>4</sub> adsorption capacities of the two composites, by approximately 16–30% compared to HKUST-1. The IAST model prediction of co-adsorption equilibria for an equimolar CO<sub>2</sub>/CH<sub>4</sub> mixture at 298 K allowed for the evaluation of their selectivity over a pressure range up to 10 bar. It was found that the selectivity of the composites was slightly degraded compared to pure HKUST-1 adsorbent.

HKUST-1 is known for its sensitivity to moisture, which decreases its adsorption capacity. The study of the stability of the composite materials under humid conditions showed that the addition of TPU imparts a hydrophobic character to the composite, improving its resistance to degradation in the presence of water. After prolonged storage of the materials in humid conditions, HKUST-1/TPU and HKUST-1/PLA showed decreases in CO<sub>2</sub> adsorption capacities of 10% and 25%, respectively, compared to 54% for pure HKUST-1.

A simulation of the pressure swing adsorption (PSA) process applied to an equimolar CO<sub>2</sub>/CH<sub>4</sub> mixture representative of biogas composition was carried out using the gPROMS software, taking into account the equilibrium properties measured for the composite adsorbent material. The simulation was initially carried out based on Skarstrom cycle configuration for an industrial-sized unit, comprising two adiabatic columns, containing an adsorbent volume of 3.6 m<sup>3</sup> for a CO<sub>2</sub>-CH<sub>4</sub> feed flow rate of 0.07 kg/s at 298 K. The adsorption pressure value applied was defined based on the highest predicted IAST selectivity of the adsorbent for equimolar mixture of CO<sub>2</sub>/CH<sub>4</sub>. The desorption pressure was set to be at atmospheric pressure as to avoid using a vacuum, which is energetically costly.

Optimizing the cycle parameters leads to the production of a CH<sub>4</sub>-enriched raffinate with a purity of 99.7%, but associated with a very low methane recovery rate, less than 7%. To improve the performance of the PSA unit, an additional pressure equalization step was introduced into the cycle, and this new simulation was conducted using 4 columns. Under these conditions, CH<sub>4</sub> recovery rates can be significantly improved, up to 22.6%, but still remain insufficient compared to the expected performance specifications of the unit.

The results obtained in this study demonstrate the viability of using shaped HKUST-1 as an adsorbent in the context of biogas upgrading. As the studies are completed, there are several perspectives that can be highlighted. First, in terms of the shaping method, it is possible to further develop the use of 3D printing as alternative technology for the MOF shaping, as the binding agent materials used in this work is thermoplastics, which often used as feed material for 3D printer. Several shaping tests are currently being studied for the 3D printing of HKUST-1, using FGF technology. Additionally, the use of more hydrophobic thermoplastic binder could be investigated to minimize or even eliminate the inherent moisture sensitivity of pristine HKUST-1.

Secondly, in terms of the adsorption equilibria and kinetics, several other analyses could be conducted to further improve the accuracy of this work. As an example, equilibrium adsorption of CO<sub>2</sub> and CH<sub>4</sub> gas mixture can be performed directly to obtain the co-adsorption isotherms so that we do not only depend on the IAST system to evaluate the selectivity and working capacity of the adsorbent in gas mixture condition. The analysis on the adsorption kinetics, which was not conducted in this study, could be done in future study such as the zero-length column (ZLC) method.

Lastly, in terms of the real application of shaped HKUST-1 in CO<sub>2</sub>/CH<sub>4</sub> separation process, experimental process such as breakthrough analysis and PSA separation process must be conducted to be compared with the PSA simulation conducted in this work. The installation of this equipment is currently ongoing at Universiti Teknologi PETRONAS as well at IMT Atlantique. Furthermore, the parameters optimization of the PSA simulation presented in this work could be further explored, as well as complexifying the PSA cycle configuration, to increase the low CH<sub>4</sub> recovery and productivity obtained from the simulation. Overall, we believe that the findings of this work can contribute to

some extent in the development and application of MOFs as an adsorbent in PSA process in the context of biogas upgrading,

## References

- [1] H. L. a. J. R. (. Core Writing Team, "Climate Change 2023: Synthesis Report," IPCC, Geneva, 2023.
- [2] Dhakal, S., J.C. Minx, F.L. Toth, A. Abdel-Aziz, M.J. Figueroa Meza, K. Hubacek, I.G.C. Jonckheere, Yong-Gun Kim, G.F. Nemet, , "Climate Change 2022: Mitigation of Climate Change. Chapter 2: Emissions Trends and Drivers," Cambridge University Press, Cambridge and New York, 2022.
- [3] UNFCCC, "What is the United Nations Framework Convention on Climate Change," [Online]. Available: <https://unfccc.int/process-and-meetings/what-is-the-united-nations-framework-convention-on-climate-change>. [Accessed 25 July 2024].
- [4] Horowitz, C. A., "Paris Agreement," *International Legal Materials*, vol. 55, no. 4, p. 740–755, 2016.
- [5] Fawzy, Samer, Ahmed I. Osman, John Doran, and David W. Rooney, "Strategies for mitigation of climate change: a review," *Environmental Chemistry Letters*, vol. 18, pp. 2069-2094, 2020.
- [6] Chen, Xiao Yuan, Hoang Vinh-Thang, Antonio Avalos Ramirez, Denis Rodrigue, and Serge Kaliaguine, "Membrane gas separation technologies for biogas upgrading," *RSC advances*, vol. 5, no. 31, pp. 24399-24448, 2015.
- [7] Hernández, J. R, "Biogas cleaning and conditioning: a requirement for optimal operation of CHP systems," *Biogas Dir*, vol. 4, pp. 18-21, 2017.
- [8] Kapoor, Rimika, Pooja Ghosh, Madan Kumar, and Virendra Kumar Vijay, "Evaluation of biogas upgrading technologies and future perspectives: a review," *Environmental Science and Pollution Research*, vol. 26, pp. 11631-11661, 2019.
- [9] European Biogas Association (EBA), Gas Infrastructure Europe (GIE), "EBA-GiE biomethane map 2020," 2020. [Online]. Available: [https://www.europeanbiogas.eu/wp-content/uploads/2020/06/GIE\\_EBA\\_BIO\\_2020\\_AO\\_FULL\\_FINAL.pdf](https://www.europeanbiogas.eu/wp-content/uploads/2020/06/GIE_EBA_BIO_2020_AO_FULL_FINAL.pdf). [Accessed 4 2024].
- [10] Atelge, Muhamed Rasit, Halil Senol, Mohammed Djaafri, Tulin Avci Hansu, David Krisa, Abdulaziz Atabani, Cigdem Eskicioglu et al, "A critical overview of the state-of-the-art methods for biogas purification and utilization processes," *Sustainability*, vol. 13, no. 20, p. 11515, 2021.
- [11] Loiseau, Thierry, Ludovic Lecroq, Christophe Volkringer, Jérôme Marrot, Gérard Férey, Mohamed Haouas, Francis Taulelle, Sandrine Bourrelly, Philip L. Llewellyn, and Michel Latroche, "MIL-96, a porous aluminum trimesate 3D structure constructed from a hexagonal network of 18-membered rings and  $\mu$  3-oxo-centered trinuclear units," *Journal of the American Chemical Society*, vol. 128, no. 31, pp. 10223-10230, 2006.

- [12] Bourrelly, Sandrine, Philip L. Llewellyn, Christian Serre, Franck Millange, Thierry Loiseau, and Gérard Férey, "Different adsorption behaviors of methane and carbon dioxide in the isotopic nanoporous metal terephthalates MIL-53 and MIL-47," *Journal of the American Chemical Society*, vol. 127, no. 39, pp. 13519-13521, 2005.
- [13] Furukawa, Hiroyasu, Kyle E. Cordova, Michael O'Keeffe, and Omar M. Yaghi, "The chemistry and applications of metal-organic frameworks," *Science*, vol. 341, no. 6149, p. 1230444, 2013.
- [14] Dey, Chandan, Tanay Kundu, Bishnu P. Biswal, Arijit Mallick, and Rahul Banerjee, "Crystalline metal-organic frameworks (MOFs): synthesis, structure and function," *Acta Crystallographica Section B: Structural Science, Crystal Engineering and Materials*, vol. 70, no. 1, pp. 3-10, 2014.
- [15] Horcajada, Patricia, Ruxandra Gref, Tarek Baati, Phoebe K. Allan, Guillaume Maurin, Patrick Couvreur, Gérard Férey, Russell E. Morris, and Christian Serre, "Metal-organic frameworks in biomedicine," *Chemical reviews*, vol. 112, no. 2, pp. 1232-1268, 2012.
- [16] Teo, How Wei Benjamin, Anutosh Chakraborty, and Sibnath Kayal, "Evaluation of CH<sub>4</sub> and CO<sub>2</sub> adsorption on HKUST-1 and MIL-101 (Cr) MOFs employing Monte Carlo simulation and comparison with experimental data," *Applied Thermal Engineering*, vol. 110, pp. 891-900, 2017.
- [17] Asadi, Tahereh, Mohammad R. Ehsani, Ana M. Ribeiro, Jose M. Loureiro, and Alirio E. Rodrigues, "CO<sub>2</sub>/CH<sub>4</sub> Separation by Adsorption using Nanoporous Metal organic Framework Copper-Benzene-1, 3, 5-tricarboxylate Tablet," *Chemical Engineering & Technology*, vol. 35, no. 7, pp. 1231-1239, 2013.
- [18] Ren, Jianwei, Xoliswa Dyosiba, Nicholas M. Musyoka, Henrietta W. Langmi, Mkhulu Mathe, and Shijun Liao, "Review on the current practices and efforts towards pilot-scale production of metal-organic frameworks (MOFs)," *Coord. Chem. Rev.*, vol. 352, pp. 187-219, 2017.
- [19] Chui, Stephen S-Y., Samuel M-F. Lo, Jonathan PH Charmant, A. Guy Orpen, and Ian D. Williams, "A chemically functionalizable nanoporous material [Cu<sub>3</sub>(TMA)<sub>2</sub>(H<sub>2</sub>O)<sub>3</sub>]<sub>n</sub>," *Science*, vol. 283, no. 5405, pp. 1148-1150, 1999.
- [20] Xue, Wenjuan, Zhengqing Zhang, Hongliang Huang, Chongli Zhong, and Donghai Mei., "Theoretical insights into the initial hydrolytic breakdown of HKUST-1," *J. Phys. Chem. C*, vol. 124, no. 3, pp. 1991-2001, 2019.
- [21] Yeskendir, Bakytzhan, Jean-Philippe Dacquin, Yannick Lorgouilloux, Christian Courtois, Sébastien Royer, and Jérémy Dhainaut, "From metal-organic framework powders to shaped solids: recent developments and challenges," *Materials Advances*, vol. 2, no. 22, pp. 7139-7186, 2021.
- [22] INTERNATIONAL ENERGY AGENCY, "IEA," October 2023. [Online]. Available: <https://origin.iea.org/reports/world-energy-outlook-2023#overview>. [Accessed July 2024].

- [23] Bruckner T., I.A. Bashmakov, Y. Mulugetta, H. Chum, A. de la Vega Navarro, J. Edmonds, A. Faaij, B. Fungtammasan, A. Garg, , "Energy Systems," Cambridge University Press, Cambridge, New York, 2014.
- [24] Sawyerr, Nathaniel, Cristina Trois, Tilahun Workneh, and Vincent Okudoh, "An overview of biogas production: Fundamentals, applications and future research," *International Journal of Energy Economics and Policy*, vol. 9, no. 2, pp. 105-116, 2019.
- [25] Jewitt, G. P. W., H. W. Wen, R. P. Kunz, and A. M. Van Rooyen, "Scoping Study on Water Use of Crops/Trees," Water Research Commission (WRC), 2009.
- [26] Balagurusamy, Nagamani, and Anuj Kumar Chandel, eds., Biogas production, Cham: Springer , 2020.
- [27] Kulichkova, Ganna I., Tetiana S. Ivanova, Mihael Köttner, Oleksiy I. Volodko, Svitlana I. Spivak, Sergiy P. Tsygankov, and Yaroslav B. Blume, "Plant feedstocks and their biogas production potentials," *The Open Agriculture Journal* , vol. 14, no. 1, 2020.
- [28] Pavičić, Josipa, Karolina Novak Mavar, Vladislav Brkić, and Katarina Simon, "Biogas and Biomethane Production and Usage: Technology Development, Advantages and Challenges in Europe," *Energies*, vol. 15, no. 8, p. 2940, 2022.
- [29] IEA, "Outlook for biogas and biomethane: Prospects for organic growth," 3 2020. [Online]. Available: <https://www.iea.org/reports/outlook-for-biogas-and-biomethane-prospects-for-organic-growth>. [Accessed 3 1 2024].
- [30] (SDES), Le service des données et études statistiques, "Chiffres clés des énergies," Paris, 2023.
- [31] Sacha Alberici, Wouter Grimme and G. Toop, "Biomethane production potentials in EU: Feasibility of REPowerEU 2030 targets, production potentials in the Member States and outlook to 2050," Guidehouse, 2022.
- [32] Shafie, Shafini Mohd, Zakirah Othman, Norsiah Hami, and Shipra Omar., "The potential of using biogas feeding for fuel cells in Malaysia," *International Journal of Energy Economics and Policy*, 2020.
- [33] Amin, Muhd Arshad, Hafiza Shukor, L. S. Yin, Farizul Hafiz Kasim, Noor Fazliani Shoparwe, Muaz Mohd Zaini Makhtar, and Abu Zahrim Yaser, "Methane biogas production in Malaysia: challenge and future plan," *International Journal of Chemical Engineering*, 2022.
- [34] Energy Data and Research Unit, "MALAYSIA ENERGY STATISTICS HANDBOOK," SURUHANJAYA TENAGA (ENERGY COMMISSION), Putrajaya, 2020.
- [35] Hoo, Poh Ying, Haslenda Hashim, and Wai Shin Ho, "Opportunities and challenges: Landfill gas to biomethane injection into natural gas distribution grid through pipeline," *Journal of Cleaner Production*, vol. 175, pp. 409-419, 2018.

- [36] CAMARA, Khadidiatou., "Techniques de l'ingénieur," 13 Jun 2024. [Online]. Available: <https://www.techniques-ingenieur.fr/fiche-pratique/energies-th4/reussir-sa-transition-energetique-dt139/reinjecter-le-biogaz-dans-le-reseau-gazier-1801/>. [Accessed July 2024].
- [37] Chen, Wei-Hsin, Shu-Mi Chen, and Chen-I. Hung, "Carbon dioxide capture by single droplet using Selexol, Rectisol and water as absorbents: A theoretical approach," *Applied energy*, vol. 111, pp. 731-741, 2013.
- [38] Adnan, Amir Izzuddin, Mei Yin Ong, Saifuddin Nomanbhay, Kit Wayne Chew, and Pau Loke Show, "Technologies for biogas upgrading to biomethane: A review," *Bioengineering*, vol. 6, no. 4, p. 92, 2019.
- [39] Bauer, Fredric, Tobias Persson, Christian Hulteberg, and Daniel Tamm, "Biogas upgrading–technology overview, comparison and perspectives for the future," *Biofuels, Bioproducts and Biorefining*, vol. 7, no. 5, pp. 499-511, 2013.
- [40] Rinprasertmeechai, Supitcha, Sumaeth Chavadej, Pramoch Rangsunvigit, and Santi Kulprathipanja, "Carbon dioxide removal from flue gas using amine-based hybrid solvent absorption," *International Journal of Chemical and Molecular Engineering*, vol. 6, no. 4, pp. 284-288, 2012.
- [41] Yuan, Xueling, Xiaochun Chen, Jinming Xing, Jiawei Fang, Xianhang Jin, and Weidong Zhang, "Enhanced research of absorption by mass transfer promoters," *Separation and Purification Technology*, vol. 253, p. 117465, 2020.
- [42] Li, Feng, Abbas Hemmati, and Hamed Rashidi, "Industrial CO<sub>2</sub> absorption into methyl-diethanolamine/piperazine in place of monoethanolamine in the absorption column," *Process Safety and Environmental Protection*, vol. 142, pp. 83-91, 2020.
- [43] Yusuf, Noor, and Fares Almomani, "Recent advances in biogas purifying technologies: Process design and economic considerations," *Energy*, vol. 265, p. 126163, 2023.
- [44] Baena-Moreno, Francisco M., Mónica Rodríguez-Galán, Fernando Vega, Luis F. Vilches, and Benito Navarrete, "Recent advances in biogas purifying technologies," *International Journal of Green Energy*, vol. 16, no. 5, pp. 401-412, 2019.
- [45] Benoît BOULINGUIEZ, Pierre LE CLOIREC, "Techniques de L'Ingénieur," 10 October 2011. [Online]. [Accessed <https://www.techniques-ingenieur.fr/en/resources/article/ti142/biogaz-purification-be8560/v1/biogaz-background-1> July 2024].
- [46] Vilardi, Giorgio, Claudia Bassano, Paolo Deiana, and Nicola Verdone, "Exergy and energy analysis of biogas upgrading by pressure swing adsorption: Dynamic analysis of the process," *Energy conversion and management*, vol. 226, p. 113482, 2020.
- [47] Awe, Olumide Wesley, Yaqian Zhao, Ange Nzihou, Doan Pham Minh, and Nathalie Lyczko, "A review of biogas utilisation, purification and upgrading technologies," *Waste and Biomass Valorization*, vol. 9, pp. 267-283, 2017.

- [48] C. W. Skarstrom, "Method and apparatus for fractionating gaseous mixtures by adsorption". United States of America Patent 2,944,627, 12 July 1960.
- [49] Ruthven, Douglas M., Shamsuzzaman Farooq, and Kent S. Knaebel, Pressure swing adsorption, John Wiley & Sons, 1996.
- [50] Broom, Darren, "Characterizing adsorbents for gas separations," *Chem. Eng. Prog*, vol. 114, no. 3, pp. 30-37, 2018.
- [51] Dusselier, Michiel, and Mark E. Davis, "Small-pore zeolites: synthesis and catalysis," *Chemical reviews*, vol. 118, no. 11, pp. 5265-5329, 2018.
- [52] Lai, Jia Yen, Lock Hei Ngu, and Siti Salwa Hashim, "A review of CO<sub>2</sub> adsorbents performance for different carbon capture technology processes conditions," *Greenhouse Gases: Science and Technology*, vol. 11, no. 5, pp. 1076-1117, 2021.
- [53] Langmi, H. W., Allan Walton, M. M. Al-Mamouri, S. R. Johnson, David Book, J. D. Speight, P. P. Edwards, I. Gameson, P. A. Anderson, and I. R. Harris, "Hydrogen adsorption in zeolites A, X, Y and RHO," *Journal of Alloys and Compounds*, vol. 356, pp. 710-715, 2003.
- [54] E. S. H. a. A. S. M. Kianfar, "Zeolite-based catalysts for methanol to gasoline process: a review," *Microchemical Journal*, vol. 156, p. 104822, 2020.
- [55] Ullah, Ruh, Mohammed Ali H. Salah Saad, Santiago Aparicio, and Mert Atilhan, "Adsorption equilibrium studies of CO<sub>2</sub>, CH<sub>4</sub> and N<sub>2</sub> on various modified zeolites at high pressures up to 200 bars," *Microporous and Mesoporous Materials*, vol. 262, pp. 49-58, 2018.
- [56] Bahrun, Mohd Hardyianto Vai, Awang Bono, Norasikin Othman, and Muhammad Abbas Ahmad Zaini, "Carbon Dioxide Removal from Biogas through Pressure Swing Adsorption—A Review," *Chemical Engineering Research and Design*, vol. 183, pp. 285-306, 2022.
- [57] Chen, Yi-Fang, Po-Wei Lin, Wen-Hua Chen, Fong-Yu Yen, Hong-Sung Yang, and Cheng-Tung Chou, "Biogas upgrading by pressure swing adsorption with design of experiments," *Processes*, vol. 9, no. 8, p. 1325, 2021.
- [58] Jiang, Yangyang, Jianghua Ling, Penny Xiao, Yingdian He, Qinghu Zhao, Zheng Chu, Yingshu Liu, Ziyi Li, and Paul A. Webley, "Simultaneous biogas purification and CO<sub>2</sub> capture by vacuum swing adsorption using zeolite NaUSY," *Chemical Engineering Journal*, vol. 334, pp. 2593-2602, 2018.
- [59] Arya, A., Divekar, S., Rawat, R., Gupta, P., Garg, M.O., Dasgupta, S., Nanoti, A., Singh, R., Xiao, P. and Webley, P.A., "Upgrading biogas at low pressure by vacuum swing adsorption," *Industrial & Engineering Chemistry Research*, vol. 54, no. 1, pp. 404-413, 2015.
- [60] García-Villén, Fátima, Eduardo Flores-Ruíz, Cristóbal Verdugo-Escamilla, and F. Javier Huertas, "Hydrothermal synthesis of zeolites using sanitary ware waste as a raw material," *Applied Clay Science*, vol. 160, pp. 238-248, 2018.



- [61] dos Santos Barbosa, Antonielly, Antusia dos Santos Barbosa, Tellys Lins A. Barbosa, and Meiry GF Rodrigues, "Synthesis of zeolite membrane (NaY/alumina): Effect of precursor of ceramic support and its application in the process of oil–water separation," *Separation and Purification Technology*, vol. 200, pp. 141-154, 2018.
- [62] Meng, Yanrui, Bin Zhao, Hongqi Zhang, Xiuwu Liu, and Jilin Cao, "Synthesis of Zeolite W from Potassic Rocks Activated by KOH Sub-molten Salt Method," *Crystal Research and Technology*, vol. 53, no. 6, p. 1700216, 2018.
- [63] Bai, Shu-xia, Ling-mei Zhou, Zhi-bing Chang, Chao Zhang, and Mo Chu, "Synthesis of Na-X zeolite from Longkou oil shale ash by alkaline fusion hydrothermal method," *Carbon Resources Conversion*, vol. 1, no. 3, pp. 245-250, 2018.
- [64] Król, M., J. Minkiewicz, and W. Mozgawa, "IR spectroscopy studies of zeolites in geopolymeric materials derived from kaolinite," *Journal of Molecular Structure*, vol. 1126, pp. 200-206, 2016.
- [65] Król, Magdalena, Piotr Rożek, Damian Chlebda, and Włodzimierz Mozgawa, "ATR/FT-IR studies of zeolite formation during alkali-activation of metakaolin," *Solid State Sciences*, vol. 94, pp. 114-119, 2019.
- [66] Makgabutlane, Boitumelo, Lebea N. Nthunya, Nicholas Musyoka, Bongumusa S. Dladla, Edward N. Nxumalo, and Sabelo D. Mhlanga, "Microwave-assisted synthesis of coal fly ash-based zeolites for removal of ammonium from urine," *RSC Advances*, vol. 10, no. 4, pp. 2416-2427, 2020.
- [67] Tanaka, Hidekazu, Hajime Eguchi, Satoshi Fujimoto, and Ryozi Hino, "Two-step process for synthesis of a single phase Na–A zeolite from coal fly ash by dialysis," *Fuel*, vol. 85, no. 10-11, pp. 1329-1334, 2005.
- [68] G. J. McDougall, "The physical nature and manufacture of activated carbon," *Journal of the Southern African Institute of Mining and Metallurgy*, vol. 91, no. 4, pp. 109-120, 1991.
- [69] S. M. Manocha, "Porous carbons," *Sadhana*, vol. 28, no. 1, pp. 335-348, 2003.
- [70] Jeguirim, Mejdj, Meriem Belhachemi, Lionel Limousy, and Simona Bennici, "Adsorption/reduction of nitrogen dioxide on activated carbons: textural properties versus surface chemistry—a review," *Chemical Engineering Journal*, vol. 347, pp. 493-504, 2018.
- [71] G. G. a. A. A. Z. Stavropoulos, "Minimizing activated carbons production cost," *Fuel processing technology*, vol. 90, no. 7-8, pp. 952-957, 2009.
- [72] W. J. F. X. M. Q. K. C. R. Y. L. H. Z. e. a. Ao, "Microwave assisted preparation of activated carbon from biomass: A review," *Renewable and Sustainable Energy Reviews*, vol. 92, pp. 958-979, 2018.
- [73] V. K. a. E. A. K. Singh, "Measurement and analysis of adsorption isotherms of CO<sub>2</sub> on activated carbon," *Applied Thermal Engineering*, vol. 97, pp. 77-86, 2016.

- [74] N. P. a. M. J. Wickramaratne, "Activated carbon spheres for CO<sub>2</sub> adsorption," *ACS applied materials & interfaces*, vol. 5, no. 5, pp. 1849-1855, 2013.
- [75] Peredo-Mancilla, Deneb, Camelia Matei Ghimbeu, Bich-Ngoc Ho, Mejdi Jeguirim, Cecile Hort, and David Bessieres, "Comparative study of the CH<sub>4</sub>/CO<sub>2</sub> adsorption selectivity of activated carbons for biogas upgrading," *Journal of Environmental Chemical Engineering*, vol. 7, no. 5, p. 103368, 2019.
- [76] Ioannidou, O., and Anastasia Zabaniotou, "Agricultural residues as precursors for activated carbon production—a review," *Renewable and sustainable energy reviews*, vol. 11, no. 9, pp. 1966-2005, 2007.
- [77] Ahmedna, M. O. H. A. M. E. D., W. E. Marshall, and R. M. Rao, "Production of granular activated carbons from select agricultural by-products and evaluation of their physical, chemical and adsorption properties," *Bioresource technology*, vol. 71, no. 2, pp. 113-123, 2000.
- [78] Hui, Tang Shu, and Muhammad Abbas Ahmad Zaini, "Potassium hydroxide activation of activated carbon: a commentary," *Carbon letters*, vol. 16, no. 4, pp. 275-280, 2015.
- [79] Tsai, Wei-Tek, C. Y. Chang, and S. L. Lee, "A low cost adsorbent from agricultural waste corn cob by zinc chloride activation," *Bioresource Technology*, vol. 64, no. 3, pp. 211-217, 1998.
- [80] Girgis, Badie S., Samya S. Yunis, and Ashraf M. Soliman, "Characteristics of activated carbon from peanut hulls in relation to conditions of preparation," *Materials Letters*, vol. 57, no. 1, pp. 164-172, 2002.
- [81] El-Hendawy, Abdel-Nasser A., S. E. Samra, and B. S. Girgis, "Adsorption characteristics of activated carbons obtained from corncobs," *Colloids and Surfaces A: Physicochemical and Engineering Aspects*, vol. 180, no. 3, pp. 209-221, 2001.
- [82] Tsai, W. T., C. Y. Chang, S. Y. Wang, C. F. Chang, S. F. Chien, and H. F. Sun, "Cleaner production of carbon adsorbents by utilizing agricultural waste corn cob," *Resources, conservation and recycling*, vol. 32, no. 1, pp. 43-53, 2001.
- [83] Lozano-Castello, D., J. M. Calo, D. Cazorla-Amorós, and A. Linares-Solano, "Carbon activation with KOH as explored by temperature programmed techniques, and the effects of hydrogen," *Carbon*, vol. 45, no. 13, pp. 2529-2536, 2007.
- [84] Rashidi, Nor Adilla, and Suzana Yusup, "An overview of activated carbons utilization for the post-combustion carbon dioxide capture," *Journal of CO<sub>2</sub> utilization*, vol. 13, pp. 1-16, 2016.
- [85] Kumar, Sunil, M. M. Malik, and Rajesh Purohit, "Synthesis methods of mesoporous silica materials," *Materials Today: Proceedings*, vol. 4, no. 2, pp. 350-357, 2017.

- [86] Cashin, Veronica B., Daniel S. Eldridge, Aimin Yu, and Dongyuan Zhao, "Surface functionalization and manipulation of mesoporous silica adsorbents for improved removal of pollutants: a review," *Environmental Science: Water Research & Technology*, vol. 4, no. 2, pp. 110-128, 2018.
- [87] Belmabkhout, Youssef, Rodrigo Serna-Guerrero, and Abdelhamid Sayari, "Adsorption of CO<sub>2</sub> from dry gases on MCM-41 silica at ambient temperature and high pressure. 1: Pure CO<sub>2</sub> adsorption," *Chemical Engineering Science*, vol. 64, no. 17, pp. 3721-3728, 2009.
- [88] Jang, Hyun Tae, YoonKook Park, Yong Sig Ko, Ji Yun Lee, and Bhagiyalakshmi Margandan, "Highly siliceous MCM-48 from rice husk ash for CO<sub>2</sub> adsorption," *International Journal of Greenhouse Gas Control*, vol. 3, no. 5, pp. 545-549, 2009.
- [89] Yan, Xinlong, Lei Zhang, Ying Zhang, Guidong Yang, and Zifeng Yan, "Amine-modified SBA-15: effect of pore structure on the performance for CO<sub>2</sub> capture," *Industrial & Engineering Chemistry Research*, vol. 50, no. 6, pp. 3220-3226, 2011.
- [90] Liu, Yamin, Xiaoying Lin, Xiaohang Wu, Minyi Liu, Ronghui Shi, and Xiaojing Yu, "Pentaethylenhexamine loaded SBA-16 for CO<sub>2</sub> capture from simulated flue gas," *Powder Technology*, vol. 318, pp. 186-192, 2017.
- [91] Wei, Lijuan, Shuai Yan, Huanhuan Wang, and Hengquan Yang, "Fabrication of multi-compartmentalized mesoporous silica microspheres through a Pickering droplet strategy for enhanced CO<sub>2</sub> capture and catalysis," *NPG Asia Materials*, vol. 10, no. 9, pp. 899-911, 2018.
- [92] Ette, Pedda Masthanaiah, Karuppiah Selvakumar, Sakkarapalayam Murugesan Senthil Kumar, and Kannadka Ramesha, "Silica template assisted synthesis of ordered mesoporous  $\beta$ -MnO<sub>2</sub> nanostructures and their performance evaluation as negative electrode in Li-ion batteries," *Electrochimica Acta*, vol. 292, pp. 532-539, 2018.
- [93] Díaz de Greñu, Borja, Ruth de Los Reyes, Ana M. Costero, Pedro Amorós, and Jose Vicente Ros-Lis, "Recent progress of microwave-assisted synthesis of silica materials," *Nanomaterials*, vol. 10, no. 6, p. 1092, 2020.
- [94] Rosu, Cornelia, Andrew J. Gorman, Rafael Cueto, Kerry M. Dooley, and Paul S. Russo, "Sculpting the internal architecture of fluorescent silica particles via a template-free approach," *Journal of colloid and interface science*, vol. 467, pp. 321-334, 2016.
- [95] Rodríguez-Reinoso, Francisco, and Antonio Sepúlveda-Escribano, "Porous carbons in adsorption and catalysis," in *Handbook of surfaces and interfaces of materials*, Academic Press, 2001, pp. 309-355.
- [96] Alcañiz-Monge, J., J. P. Marco-Lozar, and D. Lozano-Castelló, "Monolithic Carbon Molecular Sieves from activated bituminous coal impregnated with a slurry of coal tar pitch," *Fuel processing technology*, vol. 95, pp. 67-72, 2012.

- [97] Song, Xue, Xu Ma, and Yunmin Zeng, "Adsorption equilibrium and thermodynamics of CO<sub>2</sub> and CH<sub>4</sub> on carbon molecular sieves," *Applied Surface Science*, vol. 396, pp. 870-878, 2017.
- [98] Jia, Xinyu, Shaoping Xu, and Yuanyuan Cong, "Kinetics of spontaneous liquid-gas imbibition in carbon molecular sieves used for O<sub>2</sub>/N<sub>2</sub> separation," *Microporous and Mesoporous Materials*, vol. 241, pp. 185-191, 2017.
- [99] Demiral, Hakan, and İlknur Demiral, "Preparation and characterization of carbon molecular sieves from chestnut shell by chemical vapor deposition," *Advanced Powder Technology*, vol. 29, no. 12, pp. 3033-3039, 2018.
- [100] Carrott, P. J. M., I. P. P. Cansado, and MML Ribeiro Carrott, "Carbon molecular sieves from PET for separations involving CH<sub>4</sub>, CO<sub>2</sub>, O<sub>2</sub> and N<sub>2</sub>," *Applied surface science*, vol. 252, no. 17, pp. 5948-5952, 2006.
- [101] Jones, Cheryl W., and William J. Koros, "Carbon molecular sieve gas separation membranes-I. Preparation and characterization based on polyimide precursors," *Carbon*, vol. 32, no. 8, pp. 1419-1425, 1994.
- [102] Bello, G., R. Garcia, R. Arriagada, A. Sepulveda-Escribano, and F. Rodriguez-Reinoso, "Carbon molecular sieves from Eucalyptus globulus charcoal," *Microporous and mesoporous materials*, vol. 56, no. 2, pp. 139-145, 2002.
- [103] Arriagada, Renán, Germán Bello, Rafael García, Francisco Rodríguez-Reinoso, and Antonio Sepúlveda-Escribano, "Carbon molecular sieves from hardwood carbon pellets. The influence of carbonization temperature in gas separation properties," *Microporous and mesoporous materials*, vol. 81, no. 1-3, pp. 161-167, 2005.
- [104] Gomez-de-Salazar, C., A. Sepúlveda-Escribano, and F. Rodriguez-Reinoso, "Preparation of carbon molecular sieves by controlled oxidation treatments," *Carbon*, vol. 38, no. 13, pp. 1889-1892, 2000.
- [105] Ahmad, M. A., "Preparation of carbon molecular sieves from palm shell: effect of benzene deposition conditions," *Adsorption*, vol. 15, no. 5, pp. 489-495, 2009.
- [106] Adinata, Donni, Wan Mohd Ashri Wan Daud, and Mohd Kheireddine Aroua, "Production of carbon molecular sieves from palm shell based activated carbon by pore sizes modification with benzene for methane selective separation," *Fuel processing technology*, vol. 88, no. 6, pp. 599-605, 2007.
- [107] Hu, Zhonghua, and E. F. Vansant, "Carbon molecular sieves produced from walnut shell," *Carbon*, vol. 33, no. 5, pp. 561-567, 1995.
- [108] Kawabuchi, Yuji, Masahiro Kishino, Shizuo Kawano, D. Duayne Whitehurst, and Isao Mochida, "Carbon deposition from benzene and cyclohexane onto active carbon fiber to control its pore size," *Langmuir*, vol. 12, no. 17, pp. 4281-4285, 1996.

- [109] Zhang, Tengyan, Walter P. Walawender, and L. T. Fan, "Preparation of carbon molecular sieves by carbon deposition from methane," *Bioresource technology*, vol. 96, no. 17, pp. 1929-1935, 2005.
- [110] Peña-Rodríguez, Rodolfo, Elizabeth Márquez-López, Adrián Guerrero, Lidia E. Chiñas, Dario F. Hernández-González, and José María Rivera, "Hydrothermal synthesis of cobalt (II) 3D metal-organic framework acid catalyst applied in the transesterification process of vegetable oil," *Materials Letters*, vol. 217, pp. 117-119, 2018.
- [111] Wu, Yihan, Hongwei Pang, Wen Yao, Xiangxue Wang, Shujun Yu, Zhimin Yu, and Xiangke Wang, "Synthesis of rod-like metal-organic framework (MOF-5) nanomaterial for efficient removal of U (VI): batch experiments and spectroscopy study," *Science bulletin*, vol. 63, no. 13, pp. 831-839, 2018.
- [112] Mandegarzad, Sakineh, Jahan Bakhsh Raouf, Sayed Reza Hosseini, and Reza Ojani, "MOF-derived Cu-Pd/nanoporous carbon composite as an efficient catalyst for hydrogen evolution reaction: A comparison between hydrothermal and electrochemical synthesis," *Applied Surface Science*, Vols. 451-459, p. 436, 2018.
- [113] Li, Yujie, Jinpeng Miao, Xuejiao Sun, Jing Xiao, Yingwei Li, Haihui Wang, Qibin Xia, and Zhong Li, "Mechanochemical synthesis of Cu-BTC@ GO with enhanced water stability and toluene adsorption capacity," *Chem. Eng. J.*, vol. 298, pp. 191-197, 2016.
- [114] Singh, N. K., S. Gupta, V. K. Pecharsky, and V. P. Balema, "Solvent-free mechanochemical synthesis and magnetic properties of rare-earth based metal-organic frameworks," *Journal of Alloys and Compounds*, vol. 696, pp. 118-122, 2017.
- [115] Cho, Hye-Young, Da-Ae Yang, Jun Kim, Soon-Yong Jeong, and Wha-Seung Ahn, "CO<sub>2</sub> adsorption and catalytic application of Co-MOF-74 synthesized by microwave heating," *Catalysis Today*, vol. 185, no. 1, pp. 35-40, 2012.
- [116] Samuel, Melvin S., Jayanta Bhattacharya, C. Parthiban, Gayathri Viswanathan, and ND Pradeep Singh, "Ultrasound-assisted synthesis of metal organic framework for the photocatalytic reduction of 4-nitrophenol under direct sunlight," *Ultrasonics sonochemistry*, vol. 49, pp. 215-221, 2018.
- [117] Garzon-Tovar, Luis, Mary Cano-Sarabia, Arnau Carné-Sánchez, C. Carbonell, Inhar Imaz, and D. Maspoch, "A spray-drying continuous-flow method for simultaneous synthesis and shaping of microspherical high nuclearity MOF beads," *Reaction Chemistry & Engineering*, vol. 1, no. 5, pp. 533-539, 2016.
- [118] Avci-Camur, Ceren, Javier Troyano, Javier Pérez-Carvajal, Alexandre Legrand, David Farrusseng, Inhar Imaz, and Daniel Maspoch, "Aqueous production of spherical Zr-MOF beads via continuous-flow spray-drying," *Green chemistry*, vol. 20, no. 4, pp. 873-878, 2018.
- [119] Polyzoidis, Angelos, T. Altenburg, M. Schwarzer, Stefan Löbbecke, and S. Kaskel, "Continuous microreactor synthesis of ZIF-8 with high space-time-yield and tunable particle size," *Chemical Engineering Journal*, vol. 283, pp. 971-977, 2016.

- [120] Baerlocher, Ch, Lynne B. McCusker, and David H. Olson, Atlas of zeolite framework types, Elsevier, 2007.
- [121] Janiak, Christoph, and Jana K. Vieth, "MOFs, MILs and more: concepts, properties and applications for porous coordination networks (PCNs)," *New Journal of Chemistry*, vol. 34, no. 11, pp. 2366-2388, 2010.
- [122] Wong-Foy, Antek G., Adam J. Matzger, and Omar M. Yaghi, "Exceptional H<sub>2</sub> saturation uptake in microporous metal-organic frameworks," *Journal of the American Chemical Society*, vol. 128, no. 11, pp. 3494-3495, 2006.
- [123] Chong, Kok Chung, Soon Onn Lai, Shee Keat Mah, Hui San Thiam, Woon Chan Chong, Siew Hoong Shuit, Sze Shin Lee, and Wan Erl Chong, "A Review of HKUST-1 Metal-Organic Frameworks in Gas Adsorption," *IOP C Ser Earth Env*, vol. 1135, no. 1, p. 012030, 2023.
- [124] Hamon, Lomig, Elsa Jolimaître, and Gerhard D. Pirngruber., "CO<sub>2</sub> and CH<sub>4</sub> separation by adsorption using Cu-BTC metal-organic framework," *Industrial & Engineering Chemistry Research*, vol. 49, no. 16, pp. 7497-7503, 2010.
- [125] O'Neill, Laura D., Haifei Zhang, and Darren Bradshaw, "Macro-/microporous MOF composite beads," *Journal of materials Chemistry*, vol. 20, no. 27, pp. 5720-5726, 2010.
- [126] Yu, Decai, A. Ozgur Yazaydin, Joseph R. Lane, Pascal DC Dietzel, and Randall Q. Snurr, "A combined experimental and quantum chemical study of CO<sub>2</sub> adsorption in the metal-organic framework CPO-27 with different metals," *Chem Sci*, vol. 4, no. 9, pp. 3544-3556, 2013.
- [127] Millward, Andrew R., and Omar M. Yaghi, "Metal-organic frameworks with exceptionally high capacity for storage of carbon dioxide at room temperature," *J. Am. Chem. Soc.*, vol. 127, no. 51, pp. 17998-17999, 2005.
- [128] Wu, Hui, Wei Zhou, and Taner Yildirim, "High-capacity methane storage in metal-organic frameworks M2 (dhtp): the important role of open metal sites," *J. Am. Chem. Soc.*, vol. 131, no. 13, pp. 4995-5000, 2009.
- [129] Ye, Sheng, Xin Jiang, Lin-Wei Ruan, Bei Liu, Yi-Min Wang, Jun-Fa Zhu, and Ling-Guang Qiu, "Post-combustion CO<sub>2</sub> capture with the HKUST-1 and MIL-101 (Cr) metal-organic frameworks: Adsorption, separation and regeneration investigations," *Microporous Mesoporous Mater.*, vol. 179, pp. 191-197, 2013.
- [130] Xian, Shikai, Junjie Peng, Zhijuan Zhang, Qibin Xia, Haihui Wang, and Zhong Li, "Highly enhanced and weakened adsorption properties of two MOFs by water vapor for separation of CO<sub>2</sub>/CH<sub>4</sub> and CO<sub>2</sub>/N<sub>2</sub> binary mixtures," *Chem. Eng. J.*, vol. 270, pp. 385-392, 2015.
- [131] Chanut, Nicolas, Andrew D. Wiersum, U-Hwang Lee, Young Kyu Hwang, Florence Ragon, Hubert Chevreau, Sandrine Bourrelly et al, "Observing the Effects of Shaping on Gas Adsorption in Metal-

- Organic Frameworks," *European Journal of Inorganic Chemistry*, vol. 2016, no. 27, pp. 4416-4423, 2016.
- [132] Kayal, Sibnath, and Anutosh Chakraborty, "Activated carbon (type Maxsorb-III) and MIL-101 (Cr) metal organic framework based composite adsorbent for higher CH<sub>4</sub> storage and CO<sub>2</sub> capture," *Chem. Eng. J.*, vol. 334, pp. 780-788, 2018.
- [133] Yuan, Daqiang, Dan Zhao, Daofeng Sun, and Hong-Cai Zhou, "An isorecticular series of metal–organic frameworks with dendritic hexacarboxylate ligands and exceptionally high gas-uptake capacity," *Angew. Chem.*, vol. 122, no. 31, pp. 5485-5489, 2010.
- [134] Lv, Daofei, Renfeng Shi, Yongwei Chen, Yang Chen, Houxiao Wu, Xin Zhou, Hongxia Xi, Zhong Li, and Qibin Xia, "Selective adsorptive separation of CO<sub>2</sub>/CH<sub>4</sub> and CO<sub>2</sub>/N<sub>2</sub> by a water resistant zirconium–porphyrin metal–organic framework," *Ind. Eng. Chem. Res.*, vol. 57, no. 36, pp. 12215-12224, 2018.
- [135] Awadallah-F, Ahmed, Febrian Hillman, Shaheen A. Al-Muhtaseb, and Hae-Kwon Jeong, "Adsorption equilibrium and kinetics of nitrogen, methane and carbon dioxide gases onto ZIF-8, Cu10%/ZIF-8, and Cu30%/ZIF-8," *Ind. Eng. Chem. Res.*, vol. 58, no. 16, pp. 6653-6661, 2019.
- [136] Rocha, Luis AM, Kari Anne Andreassen, and Carlos A. Grande, "Separation of CO<sub>2</sub>/CH<sub>4</sub> using carbon molecular sieve (CMS) at low and high pressure," *Chem. Eng. Sci.*, vol. 164, pp. 148-157, 2017.
- [137] Cavenati, Simone, Carlos A. Grande, and Alírio E. Rodrigues., "Adsorption equilibrium of methane, carbon dioxide, and nitrogen on zeolite 13X at high pressures," *J. Chem. Eng. Data*, vol. 49, no. 4, pp. 1095-1101, 2004.
- [138] Wiersum, Andrew D., Jong-San Chang, Christian Serre, and Philip L. Llewellyn, "An adsorbent performance indicator as a first step evaluation of novel sorbents for gas separations: application to metal–organic frameworks," *Langmuir*, vol. 29, no. 10, pp. 3301-3309, 2013.
- [139] Todaro Michela, Alessi A., Sciortino Luisa, Agnello Simonpietro, Cannas Marco, Gelardi Franco and Buscarino Gianpiero., "Investigation by Raman Spectroscopy of the Decomposition Process of HKUST-1 upon Exposure to Air," *J. Spectrosc. (Hindawi)*, pp. 1-7, 2016.
- [140] Álvarez, J. Raziél, Elí Sánchez-González, Eric Pérez, Emilia Schneider-Revueltas, Ana Martínez, Adriana Tejeda-Cruz, Alejandro Islas-Jácome, Eduardo González-Zamora, and Ilich A. Ibarra, "Structure stability of HKUST-1 towards water and ethanol and their effect on its CO<sub>2</sub> capture properties," *Dalton Transactions*, vol. 46, no. 28, pp. 9192-9200, 2017.
- [141] Ma, Qinglang, Teng Zhang, and Bo Wang, "Shaping of metal-organic frameworks, a critical step toward industrial applications," *Matter*, vol. 5, no. 4, pp. 1070-1091, 2022.
- [142] Ribeiro, Rui PPL, Christine L. Antunes, Aiala U. Garate, Andre F. Portela, Marta G. Plaza, Jose PB Mota, and Isabel AAC Esteves, " Binderless shaped metal-organic framework particles: Impact on carbon dioxide adsorption," *Microporous and Mesoporous Materials*, vol. 275, pp. 111-121, 2019.

- [143] Taddei, Marco, Matthew J. McPherson, Abel Gougsa, Jamie Lam, Jack Sewell, and Enrico Andreoli, "An optimised compaction process for zr-fumarate (MOF-801)," *Inorganics*, vol. 7, no. 9, p. 110, 2019.
- [144] Ntouros, Vasileios, Ioannis Kousis, Anna Laura Pisello, and Margarita Niki Assimakopoulos, "Binding Materials for MOF Monolith Shaping Processes: A Review towards Real Life Application," *Energies*, vol. 15, no. 4, p. 1489, 2022.
- [145] Liu, Binbin, Jiamiao Wang, Jia Zeng, Lijie Zhao, Youjie Wang, Yi Feng, and Ruofei Du, "A review of high shear wet granulation for better process understanding, control and product development," *Powder Technology*, vol. 381, pp. 204-223, 2021.
- [146] Valekar, Anil H., Kyung-Ho Cho, U-Hwang Lee, Ji Sun Lee, Ji Woong Yoon, Young Kyu Hwang, Seung Gwan Lee, Sung June Cho, and Jong-San Chang, "Shaping of porous metal–organic framework granules using mesoporous  $\gamma$ -alumina as a binder," *RSC advances*, vol. 7, no. 88, pp. 55767-55777, 2017.
- [147] Sumida, Kenji, Kang Liang, Julien Reboul, Ilich A. Ibarra, Shuhei Furukawa, and Paolo Falcaro, "Sol-gel processing of metal–organic frameworks," *Chemistry of Materials*, vol. 29, no. 7, pp. 2626-2645, 2017.
- [148] Madden, David G., Robin Babu, Ceren Çamur, Nakul Rampal, Joaquin Silvestre-Albero, Teresa Curtin, and David Fairen-Jimenez, "Monolithic metal–organic frameworks for carbon dioxide separation," *Faraday discussions*, vol. 231, pp. 51-65, 2021.
- [149] Zhang, Bingxing, Jianling Zhang, Chengcheng Liu, Li Peng, Xinxin Sang, Buxing Han, Xue Ma, Tian Luo, Xiuniang Tan, and Guanying Yang, "High-internal-phase emulsions stabilized by metal-organic frameworks and derivation of ultralight metal-organic aerogels," *Scientific reports*, vol. 6, no. 1, pp. 1-9, 2016.
- [150] Gao, Yuanyuan, Jacques Lalevée, and Angélique Simon-Masseron, "An overview on 3D printing of structured porous materials and their applications," *Advanced Materials Technologies*, vol. 8, no. 17, p. 2300377, 2023.
- [151] Evans, Kent A., Zachary C. Kennedy, Bruce W. Arey, Josef F. Christ, Herbert T. Schaefer, Satish K. Nune, and Rebecca L. Erikson, "Chemically active, porous 3D-printed thermoplastic composites," *ACS applied materials & interfaces*, vol. 10, no. 17, pp. 15112-15121, 2018.
- [152] Thakkar, Harshul, Stephen Eastman, Qasim Al-Naddaf, Ali A. Rownaghi, and Fateme Rezaei, "3D-printed metal–organic framework monoliths for gas adsorption processes," *ACS applied materials & interfaces*, vol. 9, no. 41, pp. 35908-35916, 2017.
- [153] Lahtinen, Elmeri, Rafaella LM Precker, Manu Lahtinen, Evamarie Hey-Hawkins, and Matti Haukka, "Selective laser sintering of metal-organic frameworks: production of highly porous filters by 3D printing onto a polymeric matrix," *ChemPlusChem*, vol. 84, no. 2, pp. 222-225, 2019.



- [154] Halevi, Oded, Joel MR Tan, Pooi See Lee, and Shlomo Magdassi, "Hydrolytically stable MOF in 3D-printed structures," *Advanced Sustainable Systems*, vol. 2, no. 2, p. 1700150, 2018.
- [155] Qian, Dan, Cheng Lei, Guang-Ping Hao, Wen-Cui Li, and An-Hui Lu, "Synthesis of hierarchical porous carbon monoliths with incorporated metal–organic frameworks for enhancing volumetric based CO<sub>2</sub> capture capability," *ACS applied materials & interfaces*, vol. 4, no. 11, pp. 6125-6132, 2012.
- [156] Rezaei, Fateme, Shane Lawson, Hooman Hosseini, Harshul Thakkar, Amit Hajari, Saman Monjezi, and Ali A. Rownaghi, "MOF-74 and UTSA-16 film growth on monolithic structures and their CO<sub>2</sub> adsorption performance," *Chemical Engineering Journal*, vol. 313, pp. 1346-1353, 2017.
- [157] D. A. L. L. V. H. B. & F. V. Bazer-Bachi, "Towards industrial use of metal-organic framework: Impact of shaping on the MOF properties," *Powder technology*, vol. 255, pp. 52-59, 2014.
- [158] J. A.-C. C. T. J. L. A. C. J. I. I. .. & F. D. Dhainaut, "Systematic study of the impact of MOF densification into tablets on textural and mechanical properties," *CrystEngComm*, vol. 19, no. 29, pp. 4211-4218, 2017.
- [159] A. M. G. B. P. M. L. W. B. Y. A. K. .. & E. M. Mallick, "Advances in shaping of metal–organic frameworks for CO<sub>2</sub> capture: understanding the effect of rubbery and glassy polymeric binders," *Industrial & Engineering Chemistry Research*, vol. 57, no. 49, pp. 16897-16902, 2018.
- [160] J. F. A. L. J. C. B. G. V. & D. J. F. Cousin-Saint-Remi, "Selection of binder recipes for the formulation of MOFs into resistant pellets for molecular separations by fixed-bed adsorption," *Microporous and Mesoporous Materials*, vol. 304, p. 109322., 2020.
- [161] J. R. M. Y. M. M. C. S. J. Y. J. J. H. K. .. & Z. H. C. Li, "Carbon dioxide capture-related gas adsorption and separation in metal-organic frameworks," *Coordination Chemistry Reviews*, vol. 255, no. 15-16, pp. 1791-1823, 2011.
- [162] L. & Y. R. T. Wang, "Significantly increased CO<sub>2</sub> adsorption performance of nanostructured templated carbon by tuning surface area and nitrogen doping," *The Journal of Physical Chemistry C*, vol. 116, no. 1, pp. 1099-1106., 2012.
- [163] D. L. S. H. Z. W. & K. R. Chen, "Reprint of: Transient breakthroughs of CO<sub>2</sub>/CH<sub>4</sub> and C<sub>3</sub>H<sub>6</sub>/C<sub>3</sub>H<sub>8</sub> mixtures in fixed beds packed with Ni-MOF-74," *Chemical Engineering Science*, vol. 124, pp. 109-117, 2015.
- [164] Hong, Wan Yun, Semali P. Perera, and Andrew D. Burrows, "Manufacturing of metal-organic framework monoliths and their application in CO<sub>2</sub> adsorption," *Microporous and Mesoporous Materials*, vol. 214, pp. 149-155, 2015.
- [165] Rivera-Torrente, Miguel, Danny Kroon, Marie-Vanessa Coulet, Carlos Marquez, Nikolaos Nikolopoulos, Rifan Hardian, Sandrine Bourrelly, Dirk De Vos, Gareth T. Whiting, and Bert M. Weckhuysen., "Understanding the Effects of Binders in Gas Sorption and Acidity of Aluminium Fumarate Extrudates," *Chemistry—A European Journal*, vol. 28, no. 5, p. e202103420, 2022.

- [166] Biron, Michel, Thermoplastics and thermoplastic composites: technical information for plastics users, Elsevier, 2007.
- [167] Traore, Brahiman., Elaboration et caractérisation d'une structure composite (sable et déchets plastiques recyclés): Amélioration de la résistance par des charges en argiles, Abidjan: Université Bourgogne Franche-Comté; Université Félix Houphouët-Boigny, 2018.
- [168] Tangram Technology Ltd, "Tangram Technologies," December 2021. [Online]. Available: <https://tangram.co.uk/wp-content/uploads/Plastics-Topics-Periodic-Table-Full-December-2021.pdf>. [Accessed 25 June 2024].
- [169] Tangram Technology Ltd., "Tangram Technology," [Online]. Available: <https://tangram.co.uk/wp-content/uploads/Plastics-Topics-Introduction-to-thermoplastics.pdf>. [Accessed 26 June 2024].
- [170] Hartmann, M. H., "High molecular weight polylactic acid polymers," in *Biopolymers from renewable resources*, Berlin, Heidelberg: Springer Berlin Heidelberg, 1998, pp. 367-411.
- [171] Frick, Achim, and Arif Rochman, "Characterization of TPU-elastomers by thermal analysis (DSC).," *Polymer testing*, vol. 23, no. 4, pp. 413-417, 2004.
- [172] Jašo, Vladislav, Miroslav Cvetinovic, Srđan Rakić, and Zoran S. Petrović, "Bio-plastics and elastomers from polylactic acid/thermoplastic polyurethane blends," *Journal of Applied Polymer Science*, vol. 131, no. 22, 2014.
- [173] Yazdaninia, Anoosha, Seyed Hassan Jafari, Morteza Ehsani, Ramin Khajavi, and Hossein Ali Khonakdar., "An assessment on the effect of trifluoropropyl-POSS and blend composition on morphological, thermal and thermomechanical properties of PLA/TPU," *Journal of Thermal Analysis and Calorimetry*, vol. 139, pp. 279-292, 2020.
- [174] Sin, Lee Tin, Polylactic acid: PLA biopolymer technology and applications, William Andrew, 2012.
- [175] Nampoothiri, K. Madhavan, Nimisha Rajendran Nair, and Rojan Pappy John, "An overview of the recent developments in polylactide (PLA) research," *Bioresource technology*, vol. 101, no. 22, pp. 8493-8501, 2010.
- [176] Olabisi, Olagoke, and Kolapo Adewale, eds, Handbook of thermoplastics, CRC press, 2016.
- [177] Bhowmick, Anil K., and Howard Stephens, eds, Handbook of elastomers, CRC Press, 2000.
- [178] Datta, Janusz, and Paulina Kasprzyk, "Thermoplastic polyurethanes derived from petrochemical or renewable resources: A comprehensive review," *Polymer Engineering & Science*, vol. 58, no. S1, pp. E14-E35, 2018.
- [179] Khabzina, Yoldes, Jeremy Dhainaut, Matthias Ahlhelm, Hans-Juergen Richter, Helge Reinsch, Norbert Stock, and David Farrusseng, "Synthesis and shaping scale-up study of functionalized UiO-66 MOF for ammonia air purification filters," *Ind. Eng. Chem. Res.*, vol. 57, no. 24, pp. 8200-8208, 2018.

- [180] Rouquerol, Jean, Françoise Rouquerol, Philip Llewellyn, Guillaume Maurin, and Kenneth Sing, Adsorption by powders and porous solids: principles, methodology and applications, Academic press, 2013.
- [181] W.S. Rasband, " J. Image," U. S. National institutes of health, Bethesda, Maryland, , [Online]. Available: <https://imagej.nih.gov/ij/>.
- [182] Stalder, Aurélien F., Tobias Melchior, Michael Müller, Daniel Sage, Thierry Blu, and Michael Unser, "Low-bond axisymmetric drop shape analysis for surface tension and contact angle measurements of sessile drops," *Colloids and Surfaces A: Physicochemical and Engineering Aspects*, vol. 364, no. 1-3, pp. 72-81, 2010.
- [183] Dai, Xiu, Yu Cao, Xiaowei Shi, and Xinlong Wang, "Non-isothermal crystallization kinetics, thermal degradation behavior and mechanical properties of poly (lactic acid)/MOF composites prepared by melt-blending methods," *RSC Adv.*, vol. 6, no. 75, pp. 71461-71471, 2016.
- [184] Singh, Narendra K., Sunil K. Singh, Debabrata Dash, Prasad Gonugunta, Manjusri Misra, and Pralay Maiti, "CNT induced  $\beta$ -phase in polylactide: unique crystallization, biodegradation, and biocompatibility," *The Journal of Physical Chemistry C*, vol. 117, no. 19, pp. 10163-10174, 2013.
- [185] Muñoz-Chilito, José, José A. Lara-Ramos, Lorena Marín, Fiderman Machuca-Martínez, Juan P. Correa-Aguirre, Miguel A. Hidalgo-Salazar, Serafín García-Navarro et al, "Morphological Electrical and Hardness Characterization of Carbon Nanotube-Reinforced Thermoplastic Polyurethane (TPU) Nanocomposite Plates," *Molecules* , vol. 28, no. 8, p. 3598, 2023.
- [186] Kumar, S., Tejendra K. Gupta, and K. M. Varadarajan, "Strong, stretchable and ultrasensitive MWCNT/TPU nanocomposites for piezoresistive strain sensing," *Composites Part B: Engineering*, vol. 117, p. 107285, 2019.
- [187] Silva, FWM da, G. M. Magalhães, Erika de Oliveira Jardim, Joaquín Silvestre-Albero, Antonio Sepúlveda-Escribano, D. C. S. de Azevedo, and S. M. P. de Lucena, "CO<sub>2</sub> adsorption on ionic liquid—modified Cu-BTC: experimental and simulation study," *Adsorp. Sci. Technol.*, vol. 33, no. 2, pp. 223-242, 2015.
- [188] Denning, Shuraya, Ahmad AA Majid, Jolie M. Lucero, James M. Crawford, Moises A. Carreon, and Carolyn A. Koh, "Metal–organic framework HKUST-1 promotes methane hydrate formation for improved gas storage capacity," *ACS Appl. Mater. Interfaces*, vol. 12, no. 47, pp. 53510-53518, 2020.
- [189] Kabir, Shahbaj, Hyelim Kim, and Sunhee Lee, "Physical property of 3D-printed sinusoidal pattern using shape memory TPU filament," *Textile Research Journal*, vol. 90, no. 21-22, pp. 2399-2410, 2020.
- [190] Domínguez-Robles, Juan, Emilia Utomo, Victoria A. Cornelius, Qonita Kurnia Anjani, Anna Korelidou, Zoilo Gonzalez, Ryan F. Donnelly et al., "TPU-based antiplatelet cardiovascular

- prostheses prepared using fused deposition modelling," *Materials & Design*, vol. 220, p. 110837, 2022.
- [191] Segura González, Edwin A., Dania Olmos, Miguel Ángel Lorente, Itziar Vélaz, and Javier González-Benito, "Preparation and characterization of polymer composite materials based on PLA/TiO<sub>2</sub> for antibacterial packaging," *Polymers*, vol. 10, no. 12, p. 1365, 2018.
- [192] Feng, Yafei, Heng Jiang, Songnan Li, Jun Wang, Xiaoyan Jing, Yuren Wang, and Meng Chen, "Metal-organic frameworks HKUST-1 for liquid-phase adsorption of uranium," *Colloids. Surf. A Physicochem. Eng. Asp.*, vol. 431, pp. 87-92, 2013.
- [193] Singbumrung, Kamonthip, Kanjana Motina, Penwisa Pisitsak, Pisutsaran Chitichotpanya, Sujitra Wongkasemjit, and Thitirat Inprasit, "Preparation of Cu-BTC/PVA fibers with antibacterial applications," *Fibers and Polymers*, vol. 19, no. 7, pp. 1373-1378, 2018.
- [194] Nivetha, Ravi, Aparna Sajeev, Aleena Mary Paul, Kannan Gothandapani, Subashini Gnanasekar, Preetam Bhardwaj, George Jacob et al, "Cu based Metal Organic Framework (Cu-MOF) for electrocatalytic hydrogen evolution reaction," *Mater. Res. Express.*, vol. 7, no. 11, p. 114001, 2020.
- [195] Boubakri, A., K. Elleuch, N. Guermazi, and H. F. Ayedi, "Investigations on hygrothermal aging of thermoplastic polyurethane material," *Materials & Design*, vol. 30, no. 10, pp. 3958-3965, 2009.
- [196] Vega-Baudrit, Jose, María Sibaja-Ballester, Patricia Vázquez, Rosa Torregrosa-Maciá, and José Miguel Martín-Martínez., "Properties of thermoplastic polyurethane adhesives containing nanosilicas with different specific surface area and silanol content," *International journal of Adhesion and Adhesives*, vol. 27, no. 6, pp. 469-479, 2007.
- [197] Gwardiak, Sylwia, Barbara Szcześniak, Jerzy Choma, and Mietek Jaroniec, "Benzene adsorption on synthesized and commercial metal-organic frameworks," *J. Porous Mater.*, vol. 26, no. 3, pp. 775-783, 2019.
- [198] Bhorja, Nidhika, Georgia Basina, Jeewan Pokhrel, K. Suresh Kumar Reddy, Stavroula Anastasiou, Vaithilingam V. Balasubramanian, Yasser Fowad AlWahedi, and Georgios N. Karanikolos, "Functionalization effects on HKUST-1 and HKUST-1/graphene oxide hybrid adsorbents for hydrogen sulfide removal," *Journal of hazardous materials*, vol. 394, p. 122565, 2020.
- [199] Cortés-Suárez, Jonathan, Vanessa Celis-Arias, Hiram I. Beltrán, Adriana Tejeda-Cruz, Ilich A. Ibarra, Josué E. Romero-Ibarra, Elí Sánchez-González, and Sandra Loera-Serna, "Synthesis and characterization of an SWCNT@ HKUST-1 composite: enhancing the CO<sub>2</sub> adsorption properties of HKUST-1," *ACS omega*, vol. 4, no. 3, pp. 5275-5282, 2019.
- [200] Domán, Andrea, János Madarász, and Krisztina László, "In situ evolved gas analysis assisted thermogravimetric (TG-FTIR and TG/DTA-MS) studies on non-activated copper benzene-1, 3, 5-tricarboxylate," *Thermochimica Acta*, vol. 647, pp. 62-69, 2017.

- [201] Zou, Hantao, Changhai Yi, Luoxin Wang, Hongtao Liu, and Weilin Xu, "Thermal degradation of poly (lactic acid) measured by thermogravimetry coupled to Fourier transform infrared spectroscopy.," *Journal of thermal analysis and calorimetry*, vol. 97, pp. 929-935, 2009.
- [202] Woolley, W. D., "Nitrogen-containing products from the thermal decomposition of flexible polyurethane foams," *British Polymer Journal*, vol. 4, no. 1, pp. 27-43, 1972.
- [203] Herrera, M., G. Matuschek, and A. Kettrup, "Thermal degradation of thermoplastic polyurethane elastomers (TPU) based on MDI," *Polymer degradation and stability*, vol. 78, no. 2, pp. 323-331, 2002.
- [204] Kanbur, Yasin, and Umit Tayfun, "Investigating mechanical, thermal, and flammability properties of thermoplastic polyurethane/carbon nanotube composites," *Journal of Thermoplastic Composite Materials*, vol. 31, no. 12, pp. 1661-1675, 2018.
- [205] Wu, Wei, Wenjie Huang, Yizhang Tong, Jingshu Huang, Junchen Wu, Xianwu Cao, Qunchao Zhang, Bin Yu, and Robert KY Li, "Self-assembled double core-shell structured zeolitic imidazole framework-8 as an effective flame retardant and smoke suppression agent for thermoplastic polyurethane," *Applied Surface Science*, vol. 610, p. 155540, 2023.
- [206] Zhang, Jing, Zhi Li, Xiaolin Qi, Wen Zhang, and De-Yi Wang, "Size tailored bimetallic metal-organic framework (MOF) on graphene oxide with sandwich-like structure as functional nano-hybrids for improving fire safety of epoxy," *Composites Part B: Engineering*, vol. 188, p. 107881, 2020.
- [207] Shah, Bhuvan B., Tanay Kundu, and Dan Zhao, "Mechanical properties of shaped metal-organic frameworks," *Top Curr Chem (Cham)*, vol. 377, no. 5, p. 25, 2019.
- [208] Nandasiri, Manjula I., Sachin R. Jambovane, B. Peter McGrail, Herbert T. Schaef, and Satish K. Nune, "Adsorption, separation, and catalytic properties of densified metal-organic frameworks," *Coordination Chemistry Reviews*, vol. 311, pp. 38-52, 2016.
- [209] Purewal, J. J., D. Liu, J. Yang, A. Sudik, D. J. Siegel, S. Maurer, and U. Müller, "Increased volumetric hydrogen uptake of MOF-5 by powder densification," *International Journal of Hydrogen Energy*, vol. 37, no. 3, pp. 2723-2727, 2012.
- [210] Tian, Tian, Zhixin Zeng, Diana Vulpe, Mirian E. Casco, Giorgio Divitini, Paul A. Midgley, Joaquin Silvestre-Albero, Jin-Chong Tan, Peyman Z. Moghadam, and David Fairen-Jimenez, "A sol-gel monolithic metal-organic framework with enhanced methane uptake," *Nature materials*, vol. 17, no. 2, pp. 174-179, 2018.
- [211] Hindocha, S., and S. Poulston., "Study of the scale-up, formulation, ageing and ammonia adsorption capacity of MIL-100 (Fe), Cu-BTC and CPO-27 (Ni) for use in respiratory protection filters," *Faraday Discussions*, vol. 201, pp. 113-125, 2017.
- [212] ASTM International, "D4058 – 96: Standard Test Method for Attrition and Abrasion of Catalysts and Catalyst Carriers," June 2020. [Online]. Available:

<https://cdn.standards.iteh.ai/samples/106318/a492c4a01209459d9360238fc303bc0f/ASTM-D4058-96-2020-.pdf>. [Accessed July 2024].

- [213] Cychosz, Katie A., Rémy Guillet-Nicolas, Javier García-Martínez, and Matthias Thommes, "Recent advances in the textural characterization of hierarchically structured nanoporous materials," *Chemical Society Reviews*, vol. 46, no. 2, pp. 389-414, 2017.
- [214] Mallick, Arijit, Georges Mouchaham, Prashant M. Bhatt, Weibin Liang, Youssef Belmabkhout, Karim Adil, Aqil Jamal, and Mohamed Eddaoudi, "Advances in shaping of metal–organic frameworks for CO<sub>2</sub> capture: understanding the effect of rubbery and glassy polymeric binders," *Industrial & Engineering Chemistry Research*, vol. 57, no. 49, pp. 16897-16902, 2018.
- [215] Lee, Daniel W., Terje Didriksen, Unni Olsbye, Richard Blom, and Carlos A. Grande, "Shaping of metal-organic framework UiO-66 using alginates: Effect of operation variables," *Separation and Purification Technology*, vol. 235, p. 116182, 2020.
- [216] Grande, Carlos A., Vicente I. Águeda, Aud Spjelkavik, and Richard Blom, "An efficient recipe for formulation of metal-organic Frameworks," *Chemical Engineering Science*, vol. 124, pp. 154-158, 2015.
- [217] Chua, Hui T., Kim C. Ng, Anutosh Chakraborty, Nay M. Oo, and Mohamed A. Othman, "Adsorption characteristics of silica gel+ water systems," *Journal of Chemical & Engineering Data*, vol. 47, no. 5, pp. 1177-1181, 2002.
- [218] Law, Kock-Yee, "Definitions for hydrophilicity, hydrophobicity, and superhydrophobicity: getting the basics right," *The Journal of Physical Chemistry Letters*, vol. 5, no. 4, pp. 686-688, 2014.
- [219] Lis-Bartos, Anna, Agnieszka Smieszek, Kinga Frańczyk, and Krzysztof Marycz, "Fabrication, characterization, and cytotoxicity of thermoplastic polyurethane/poly (lactic acid) material using human adipose derived mesenchymal stromal stem cells (hASCs)," *Polymers*, vol. 10, no. 10, p. 1073, 2018.
- [220] Oliaei, Erfan, Babak Kaffashi, and Saeed Davoodi, "Investigation of structure and mechanical properties of toughened poly (l-lactide)/thermoplastic poly (ester urethane) blends," *Journal of Applied Polymer Science*, vol. 133, no. 15, 2016.
- [221] Chae, Yun Seok, Sookyung Park, Dong Won Kang, Dae Won Kim, Minjung Kang, Doo San Choi, Jong Hyeak Choe, and Chang Seop Hong, "Moisture-tolerant diamine-appended metal–organic framework composites for effective indoor CO<sub>2</sub> capture through facile spray coating," *Chemical Engineering Journal*, vol. 433, p. 133856, 2022.
- [222] DeCoste, Jared B., Michael S. Denny Jr, Gregory W. Peterson, John J. Mahle, and Seth M. Cohen, "Enhanced aging properties of HKUST-1 in hydrophobic mixed-matrix membranes for ammonia adsorption," *Chemical science*, vol. 7, no. 4, pp. 2711-2716, 2016.
- [223] Park, Jinkyong, Yun Seok Chae, Dong Won Kang, Minjung Kang, Jong Hyeak Choe, Saemi Kim, Jee Yeon Kim, Yong Won Jeong, and Chang Seop Hong, "Shaping of a metal–organic framework–

- polymer composite and its CO<sub>2</sub> adsorption performances from humid indoor air," *ACS Applied Materials & Interfaces*, vol. 13, no. 21, pp. 25421-25427, 2021.
- [224] Králik, Milan, "Adsorption, chemisorption, and catalysis," *Chemical Papers*, vol. 68, no. 12, pp. 1625-1638, 2014.
- [225] Sing, Kenneth SW., "Physisorption of gases by carbon blacks," *Carbon*, vol. 32, no. 7, pp. 1311-1317, 1994.
- [226] Nuhnen, Alexander, and Christoph Janiak, "A practical guide to calculate the isosteric heat/enthalpy of adsorption via adsorption isotherms in metal-organic frameworks, MOFs," *Dalton Transactions*, vol. 49, no. 30, pp. 10295-10307, 2020.
- [227] Buttersack, Christoph, "Modeling of type IV and V sigmoidal adsorption isotherms," *Physical Chemistry Chemical Physics*, vol. 21, no. 10, pp. 5614-5626, 2019.
- [228] Donohue, Marc D., and Grigoriy L. Aranovich, "Classification of Gibbs adsorption isotherms," *Advances in colloid and interface science*, vol. 76, pp. 137-152, 1998.
- [229] Do Duong, D., *Adsorption analysis: equilibria and kinetics.*, Imperial College Press, 1998.
- [230] Henry, William., "III. Experiments on the quantity of gases absorbed by water, at different temperatures, and under different pressures.," *Philosophical Transactions of the Royal Society of London*, vol. 93, pp. 29-274, 1803.
- [231] Al-Ghouti, Mohammad A., and Dana A. Da'ana, "Guidelines for the use and interpretation of adsorption isotherm models: A review.," *Journal of hazardous materials*, vol. 393, p. 122383, 2020.
- [232] Foo, Keng Yuen, and Bassim H. Hameed., "Insights into the modeling of adsorption isotherm systems.," *Chemical engineering journal*, vol. 156, no. 1, pp. 2-10, 2010.
- [233] Langmuir, Irving, "The constitution and fundamental properties of solids and liquids. Part I. Solids.," *Journal of the American chemical society*, vol. 38, no. 11, pp. 2221-2295, 1916.
- [234] Zito, Pasquale F., Alessio Caravella, Adele Brunetti, Enrico Drioli, and Giuseppe Barbieri, "Estimation of Langmuir and Sips models adsorption parameters for NaX and NaY FAU zeolites," *Journal of Chemical & Engineering Data*, vol. 60, no. 10, pp. 2858-2868, 2015.
- [235] Saha, Dipendu, and Shuguang Deng, "Adsorption equilibria and kinetics of carbon monoxide on zeolite 5A, 13X, MOF-5, and MOF-177," *Journal of Chemical & Engineering Data*, vol. 54, no. 8, pp. 2245-2250, 2009.
- [236] Brunauer, Stephen, Paul Hugh Emmett, and Edward Teller, "Adsorption of gases in multimolecular layers," *Journal of the American chemical society*, vol. 60, no. 2, pp. 309-319, 1938.
- [237] LLEWELLYN, Philip, Jean ROUQUEROL, Laurent LUCIANI, Renaud DENOYEL, and Françoise ROUQUEROL, *Texture des matériaux pulvérulents ou poreux*, Ed. Techniques Ingénieur, 2003.

- [238] Van Erp, Titus S., and Johan A. Martens, "A standardization for BET fitting of adsorption isotherms," *Microporous and Mesoporous Materials*, vol. 145, no. 1-3, pp. 188-193, 2011.
- [239] Ambroz, Filip, Thomas J. Macdonald, Vladimir Martis, and Ivan P. Parkin, "Evaluation of the BET Theory for the Characterization of Meso and Microporous MOFs," *Small methods*, vol. 2, no. 11, p. 1800173, 2018.
- [240] Freundlich, H. M. F., "Over the adsorption in solution," *J. Phys. chem*, vol. 57, no. 385471, pp. 1100-1107, 1906.
- [241] Sips, Robert. , "On the structure of a catalyst surface," *The journal of chemical physics*, vol. 16, no. 5, pp. 490-495, 1948.
- [242] Gargiulo, Nicola, Antonio Peluso, Paolo Aprea, Francesco Pepe, and Domenico Caputo, "CO<sub>2</sub> adsorption on polyethylenimine-functionalized SBA-15 mesoporous silica: isotherms and modeling," *Journal of chemical & engineering data*, vol. 59, no. 3, pp. 896-902, 2014.
- [243] J. Toth, "State equation of the solid-gas interface layers," *Acta Chim. Hung.*, vol. 69, pp. 311-328, 1971.
- [244] Azizian, Saied, and Setareh Eris, "Adsorption isotherms and kinetics," *Interface science and technology*, vol. 33, pp. 445-509.
- [245] Wang, Y., Mohammed Hashim, C. Ercan, Anwar Khawajah, and Rashid Othman, "High pressure methane adsorption on granular activated carbons," *Catalysts in Petroleum Refining & Petrochemicals*, Vols. 1-8, 2011.
- [246] Simon, Cory M., Berend Smit, and Maciej Haranczyk., "pyIAST: Ideal adsorbed solution theory (IAST) Python package," *Computer Physics Communications*, vol. 200, pp. 364-380, 2016.
- [247] Chowdhury, Pradip, Chaitanya Bikina, and Sasidhar Gumma, "Gas adsorption properties of the chromium-based metal organic framework MIL-101," *The Journal of Physical Chemistry C*, vol. 113, no. 16, pp. 6616-6621, 2009.
- [248] Dubinin, M., "The potential theory of adsorption of gases and vapors for adsorbents with energetically nonuniform surfaces," *Chemical reviews*, vol. 60, no. 2, pp. 235-241, 1960.
- [249] Polanyi, M, "Adsorption aus Lösungen beschränkt löslicher Stoffe," *Zeitschrift für Physik*, vol. 2, no. 1, pp. 111-116, 1920.
- [250] Carrasco-Marin, F., M. V. Lopez-Ramon, and C. Moreno-Castilla, "Applicability of the Dubinin-Radushkevich equation to carbon dioxide adsorption on activated carbons," *Langmuir*, vol. 9, no. 11, pp. 2758-2760, 1993.
- [251] Černý, Slavoj, and Vladimír Ponec, "Determination of heat of adsorption on clean solid surfaces," *Catalysis Reviews*, vol. 2, no. 1, pp. 249-322, 1969.



- [252] Sircar, S., R. Mohr, C. Ristic, and M. B. Rao., "Isotheric heat of adsorption: theory and experiment," *The Journal of Physical Chemistry B*, vol. 103, no. 31, pp. 6539-6546, 1999.
- [253] Tian, Yun, and Jianzhong Wu., "Differential heat of adsorption and isosteres," *Langmuir*, vol. 33, no. 4, pp. 996-1003, 2017.
- [254] Orsquo; Neil, Matthew, Rex Lovrien, and Jonathan Phillips, "New microcalorimeter for the measurement of differential heats of adsorption of gases on high surface area solids," *Review of scientific instruments*, vol. 56, no. 12, pp. 2312-2318, 1985.
- [255] Du, Zhenyu, Xianhua Nie, Shuai Deng, Li Zhao, Shuangjun Li, Yue Zhang, and Jie Zhao, "Comparative analysis of calculation method of adsorption isotheric heat: Case study of CO<sub>2</sub> capture using MOFs.," *Microporous and Mesoporous Materials*, vol. 298, p. 110053, 2020.
- [256] Wang, H., Z. G. Qu, W. Zhang, Q. N. Yu, and Y. L. He, "Experimental and numerical study of CO<sub>2</sub> adsorption on copper benzene-1, 3, 5-tricarboxylate (Cu-BTC) metal organic framework," *International Journal of Heat and Mass Transfer*, vol. 92, pp. 859-863, 2016.
- [257] Wang, Qing Min, Dongmin Shen, Martin Bülow, Miu Ling Lau, Shuguang Deng, Frank R. Fitch, Norberto O. Lemcoff, and Jessica Semanscin., "Metallo-organic molecular sieve for gas separation and purification," *Microporous and mesoporous materials*, vol. 55, no. 2, pp. 217-230, 2002.
- [258] Shen, Dongmin, Martin Bülow, Flor Siperstein, Maximilian Engelhard, and Alan L. Myers, "Comparison of experimental techniques for measuring isotheric heat of adsorption," *Adsorption*, vol. 6, pp. 275-286, 2000.
- [259] Llewellyn, Philip L., Sandrine Bourrelly, Christian Serre, Alexandre Vimont, Marco Daturi, Lomig Hamon, Guy De Weireld et al, "High uptakes of CO<sub>2</sub> and CH<sub>4</sub> in mesoporous metal organic frameworks mil-100 and mil-101," *Langmuir*, vol. 24, no. 14, pp. 7245-7250, 2008.
- [260] Zhang, Zhijuan, Sisi Huang, Shikai Xian, Hongxia Xi, and Zhong Li, "Adsorption equilibrium and kinetics of CO<sub>2</sub> on chromium terephthalate MIL-101," *Energy & Fuels*, vol. 25, no. 2, pp. 835-842, 2011.
- [261] Liang, Zhijian, Marc Marshall, and Alan L. Chaffee, "CO<sub>2</sub> adsorption-based separation by metal organic framework (Cu-BTC) versus zeolite (13X)," *Energy & Fuels*, vol. 23, no. 5, pp. 2785-2789, 2009.
- [262] Möllmer, Jens, Andreas Möller, Frieder Dreisbach, Roger Gläser, and Reiner Staudt, "High pressure adsorption of hydrogen, nitrogen, carbon dioxide and methane on the metal-organic framework HKUST-1," *Microporous and Mesoporous Materials* 138, Vols. 1-3, pp. 140-148, 2011.
- [263] Liu, Yuanyuan, Pramila Ghimire, and Mietek Jaroniec., "Copper benzene-1, 3, 5-tricarboxylate (Cu-BTC) metal-organic framework (MOF) and porous carbon composites as efficient carbon dioxide adsorbents.," *Journal of colloid and interface science*, vol. 535, pp. 122-132, 2019.

- [264] Myers, Alan L., and John M. Prausnitz, "Thermodynamics of mixed-gas adsorption," *AIChE journal*, vol. 11, no. 1, pp. 121-127, 1965.
- [265] Broom, Darren P., and Darren P. Broom, "Gas sorption measurement techniques," *Hydrogen Storage Materials: The Characterisation of Their Storage Properties*, pp. 117-139, 2011.
- [266] Span, Roland, and Wolfgang Wagner, "A new equation of state for carbon dioxide covering the fluid region from the triple-point temperature to 1100 K at pressures up to 800 MPa," *Journal of physical and chemical reference data*, vol. 25, no. 6, pp. 1509-1596, 1996.
- [267] Rouquerol, Jean, Françoise Rouquerol, Philip Llewellyn, Guillaume Maurin, and Kenneth Sing, *Adsorption by powders and porous solids: principles, methodology and applications.*, Academic press, 2013.
- [268] Myers, A. L., "Thermodynamics of adsorption in porous materials," *AIChE journal*, vol. 48, no. 1, pp. 145-160, 2002.
- [269] Gumma, Sasidhar, and Orhan Talu, "Net adsorption: a thermodynamic framework for supercritical gas adsorption and storage in porous solids," *Langmuir*, vol. 26, no. 22, pp. 17013-17023, 2010.
- [270] Gibbs, Josiah Willard, "The Collected Works of J. Willard Gibbs...," in *Thermodynamics*, vol. 1, Longmans, Green and Company,, 1928.
- [271] Talu, Orhan, "Net adsorption of gas/vapor mixtures in microporous solids," *The Journal of Physical Chemistry C*, vol. 117, no. 25, pp. 13059-13071, 2013.
- [272] Broom, Darren P., and K. Mark Thomas., "Gas adsorption by nanoporous materials: Future applications and experimental challenges.," *MRS bulletin*, vol. 38, no. 5, pp. 412-421, 2013.
- [273] Rowley, H. H., and W. B. Innes, "Application of the Van't Hoff Equation to Adsorption Equilibria," *In Proceedings of the Iowa Academy of Science*, vol. 47, no. 1, pp. 165-170, 1940.
- [274] Lee, Sangwon, Jay H. Lee, and Jihan Kim, "User-friendly graphical user interface software for ideal adsorbed solution theory calculations," *Korean Journal of Chemical Engineering*, vol. 35, pp. 214-221, 2018.
- [275] Saha, Arindom, and Danny Strickland., "Adsorption microcalorimetry of small molecules on various metal-organic frameworks," *Journal of Thermal Analysis and Calorimetry*, vol. 126, pp. 1747-1755, 2016.
- [276] Kloutse, F. A., A. Hourri, S. Natarajan, P. Benard, and R. Chahine, "Hydrogen separation by adsorption: Experiments and modelling of H<sub>2</sub>-N<sub>2</sub>-CO<sub>2</sub> and H<sub>2</sub>-CH<sub>4</sub>-CO<sub>2</sub> mixtures adsorption on CuBTC and MOF-5," *Microporous and Mesoporous Materials*, vol. 271, pp. 175-185, 2018.
- [277] Rother, J., and T. Fieback, "Multicomponent adsorption measurements on activated carbon, zeolite molecular sieve and metal-organic framework," *Adsorption*, vol. 19, pp. 1065-1074, 2013.

- [278] Supronowicz, Barbara, Andreas Mavrandonakis, and Thomas Heine, "Interaction of small gases with the unsaturated metal centers of the HKUST-1 metal organic framework," *The Journal of Physical Chemistry C*, vol. 117, no. 28, pp. 14570-14578, 2013.
- [279] García-Pérez, Elena, Jorge Gascón, Víctor Morales-Flórez, Juan Manuel Castillo, Freek Kapteijn, and Sofía Calero, "Identification of adsorption sites in Cu-BTC by experimentation and molecular simulation," *Langmuir*, vol. 25, no. 3, pp. 1725-1731, 2009.
- [280] Krishna, Rajamani, "Adsorptive separation of CO<sub>2</sub>/CH<sub>4</sub>/CO gas mixtures at high pressures," *Microporous and Mesoporous Materials*, vol. 156, pp. 217-223, 2012.
- [281] Chowdhury, Pradip, Samuel Mekala, Frieder Dreisbach, and Sasidhar Gumma, "Adsorption of CO, CO<sub>2</sub> and CH<sub>4</sub> on Cu-BTC and MIL-101 metal organic frameworks: Effect of open metal sites and adsorbate polarity," *Microporous and Mesoporous Materials*, vol. 152, pp. 246-252, 2012.
- [282] Bharathiraja, B., T. Sudharsana, J. Jayamuthunagai, R. Praveenkumar, S. Chozhavendhan, and J. Iyyappan, "Biogas production—A review on composition, fuel properties, feed stock and principles of anaerobic digestion," *Renewable and sustainable Energy reviews*, vol. 90, pp. 570-582, 2018.
- [283] Mulgundmath, V. P., F. H. Tezel, T. Saatcioglu, and T. C. Golden, "Adsorption and separation of CO<sub>2</sub>/N<sub>2</sub> and CO<sub>2</sub>/CH<sub>4</sub> by 13X zeolite," *The Canadian Journal of Chemical Engineering*, vol. 90, no. 3, pp. 730-738, 2012.
- [284] Boulinguez, Benoit, and Pierre Le Cloirec, *Biogas purification - Eliminating VOCs and siloxanes*, Ed. Techniques Ingénieur, 2011.
- [285] Barbera, Elena, Silvia Menegon, Donatella Banzato, Chiara D'Alpaos, and Alberto Bertucco, "From biogas to biomethane: A process simulation-based techno-economic comparison of different upgrading technologies in the Italian context," *Renewable Energy*, vol. 135, pp. 663-673, 2019.
- [286] Grande, Carlos A., and Richard Blom, "Utilization of dual-PSA technology for natural gas upgrading and integrated CO<sub>2</sub> capture," *Energy Procedia*, vol. 26, pp. 2-14, 2012.
- [287] Khunpolgrang, Jatupol, Songwut Yosantea, Aroon Kongnoo, and Chantaraporn Phalakornkule, "Alternative PSA process cycle with combined vacuum regeneration and nitrogen purging for CH<sub>4</sub>/CO<sub>2</sub> separation," *Fuel*, vol. 140, pp. 171-177, 2015.
- [288] Augelletti, Rosaria, Maria Conti, and Maria Cristina Annesini, "Pressure swing adsorption for biogas upgrading. A new process configuration for the separation of biomethane and carbon dioxide," *Journal of Cleaner Production*, vol. 140, pp. 1390-1398, 2017.
- [289] Chouikhi, Najib, Federico Brandani, Pluton Pullumbi, Patrick Perre, and Francois Puel, "Biomethane production by adsorption technology: New cycle development, adsorbent selection and process optimization," *Adsorption*, vol. 26, no. 8, pp. 1275-1289, 2020.

- [290] Kärger, Jörg, Douglas Morris Ruthven, and Doros Nicolas Theodorou, Diffusion in nanoporous materials, Weinheim: Wiley-VCH., 2012.
- [291] Wakao, N., S. Kaguei, and T. Funazkri., "Effect of fluid dispersion coefficients on particle-to-fluid heat transfer coefficients in packed beds: correlation of Nusselt numbers," *Chemical engineering science*, vol. 34, no. 3, pp. 325-336, 1979.
- [292] R. Byron Bird, Warren E. Stewart, Edwin N. Lightfoot , Transport Phenomena, Revised 2nd Edition, Wiley, 2006.
- [293] Kapoor, A., R. T. Yang, and C. Wong, "Surface diffusion," *Catalysis Reviews—Science and Engineering* , vol. 31, no. 1-2, pp. 129-214, 1989.
- [294] Barrer, R. M., Intracrystalline Diffusion, AMERICAN CHEMICAL SOCIETY, 1971.
- [295] Glueckauf, E., and J. I. Coates., "41. Theory of chromatography. Part IV. The influence of incomplete equilibrium on the front boundary of chromatograms and on the effectiveness of separation," *Journal of the Chemical Society (Resumed)*, pp. 1315-1321, 1947.
- [296] Specchia, Vito, and Silvio Sicardi, "Modified correlation for the conductive contribution of thermal conductivity in packed bed reactors," *Chemical Engineering Communications*, vol. 6, no. 1-3, pp. 131-139, 1980.
- [297] Kloutse, F.A., Zacharia, R., Cossement, D. and Chahine, R., "Specific heat capacities of MOF-5, Cu-BTC, Fe-BTC, MOF-177 and MIL-53 (Al) over wide temperature ranges: Measurements and application of empirical group contribution method," *Microporous and Mesoporous Materials*, vol. 217, pp. 1-5, 2015.
- [298] Islamov, Meiirbek, Hasan Babaei, and Christopher E. Wilmer, "Influence of missing linker defects on the thermal conductivity of metal–organic framework HKUST-1," *ACS Applied Materials & Interfaces* , vol. 12, no. 50, pp. 56172-56177, 2020.
- [299] Lemmer, Andreas, Wolfgang Merkle, Katharina Baer, and Frank Graf, "Effects of high-pressure anaerobic digestion up to 30 bar on pH-value, production kinetics and specific methane yield," *Energy*, vol. 138, pp. 659-667, 2017.
- [300] Liang, Z., D. W. Wilkinson, C. Wang, and S. J. Wilkinson, "Pressurised Anaerobic Digestion for Reducing the Costs of Biogas Upgrading," *BioEnergy Research*, vol. 16, no. 4, pp. 2539-2548, 2023.
- [301] Gaz Réseau Distribution France-GRDF, "CONTRAT RELATIF A L'INJECTION DE BIOMETHANE DANS LE RESEAU DE DISTRIBUTION DE GAZ," 1 1 2022. [Online]. Available: <https://projet-methanisation.grdf.fr/cms-assets/2021/12/GRDF-Contrat-dinjection-Conditions-Generales-Janvier22.pdf>. [Accessed 29 5 2024].



**Titre :** Elaboration de composites MOF-polymères pour la capture de CO<sub>2</sub> par adsorption modulée en pression dans le contexte de l'enrichissement de biométhane

**Mots clés :** adsorption, MOF, matériaux composites, simulation, procédés PSA, biométhane

**Résumé :** HKUST-1 est l'un des MOFs fréquemment étudiés comme adsorbant pour la séparation CO<sub>2</sub>/CH<sub>4</sub> compte tenu de sa disponibilité commerciale et de grande capacité d'adsorption du CO<sub>2</sub>. Néanmoins, les voies de synthèse actuelles mises en œuvre à l'échelle industrielle conduisent à l'obtention de poudres auxquelles des post-traitements de mise en forme sont nécessaires. La mise en forme de HKUST-1 par extrusion en utilisant deux liants thermoplastiques : TPU, (thermoplastic polyurethane) et PLA (polylactic acid) a été réalisé, dans le but de fabriquer un adsorbant avec une bonne tenue mécanique et une stabilité à l'humidité améliorée en vue de sa mise en œuvre dans un procédé PSA. La caractérisation par DRX, MEB et ATG a confirmé la préservation de la structure cristalline du HKUST-1, ainsi que l'absence de dégradation thermique des composites jusqu'à 523 K.

Les mesures d'isothermes d'adsorption CO<sub>2</sub>/CH<sub>4</sub> mettent en évidence une augmentation des capacités d'adsorption en CO<sub>2</sub> et CH<sub>4</sub> des deux composites, de l'ordre de 16-30% par rapport au HKUST-1. Après un stockage prolongé des matériaux en conditions humides, HKUST-1/TPU et HKUST-1/PLA présentent respectivement des diminutions de 10% et 25% des capacités d'adsorption de CO<sub>2</sub>, contre 54% pour le HKUST-1 pur. Enfin, Une simulation du procédé PSA en utilisant HKUST-1/PLA comme adsorbant, a été appliquée à un mélange équimolaire CO<sub>2</sub>/CH<sub>4</sub>. La simulation montre que la production d'un raffinat enrichi en CH<sub>4</sub> avec une pureté de 99,7%, est associé à un taux de récupération faible en CH<sub>4</sub> de 22,6% et consommation d'énergie de 0,15 kWh. Nm<sup>-3</sup> CH<sub>4</sub>, ce qui doit être amélioré en optimisant les paramètres du procédé.

**Title :** Elaboration of Metal Organic Framework - polymer composites for CO<sub>2</sub> capture by Pressure Swing Adsorption in the context of bio-CH<sub>4</sub> enrichment.

**Keywords :** adsorption, MOF, composite materials, simulation, PSA, biomethane

**Abstract :** HKUST-1 is one of MOFs frequently studied as an adsorbent for CO<sub>2</sub>/CH<sub>4</sub> separation thanks to its high CO<sub>2</sub> adsorption capacities and commercial availability. It is often produced in powder form and thus requires a post-shaping process for use as an adsorbent in fixed-bed separation processes. Powdered HKUST-1, was extruded into pellets using two thermoplastic binders: TPU, (thermoplastic polyurethane) and PLA (polylactic acid), with the aim to fabricate an adsorbent with a good mechanical and moisture stability for use in PSA process. The characterization of the HKUST-1 composites (HKUST-1/PLA and HKUST-1/TPU) was determined via XRD, TGA, SEM-EDS, and N<sub>2</sub> adsorption isotherm analysis. The gas-separation performances of the materials were measured from CO<sub>2</sub> and CH<sub>4</sub> isotherms. The composites preserved the HKUST-1's crystalline structure and they are also thermally stable under 523 K,

whilst their textural properties were not significantly modified compared with the pristine HKUST-1. Furthermore, both composites exhibited larger CO<sub>2</sub> and CH<sub>4</sub> adsorption capacities in comparison to the pristine HKUST-1. After three months of storage under atmospheric humid conditions, CO<sub>2</sub> adsorption capacities were reduced to only 10% for HKUST-1/TPU, whereas reductions of about 25% and 54% were observed for HKUST-1/PLA and the pristine HKUST-1, respectively. Finally, PSA simulation for CO<sub>2</sub>/CH<sub>4</sub> separation was carried out to assess the viability of using the composite as adsorbent media. The process simulation, which was performed using HKUST-1/PLA as the adsorbent predicts biomethane production with CH<sub>4</sub> purity of 99.7% and specific energy consumption of 0.15 kWh. Nm<sup>-3</sup> CH<sub>4</sub>. However, the simulated CH<sub>4</sub> recovery rate remains low at 22.6%, which requires improvement by optimizing the process parameters.